



High temperature and toughened bismaleimide composite materials for aeronautics

Guillaume Fischer

► To cite this version:

Guillaume Fischer. High temperature and toughened bismaleimide composite materials for aeronautics. Materials. Université de Lyon, 2015. English. NNT: . tel-01299359

HAL Id: tel-01299359

<https://hal.science/tel-01299359>

Submitted on 7 Apr 2016

HAL is a multi-disciplinary open access archive for the deposit and dissemination of scientific research documents, whether they are published or not. The documents may come from teaching and research institutions in France or abroad, or from public or private research centers.

L'archive ouverte pluridisciplinaire **HAL**, est destinée au dépôt et à la diffusion de documents scientifiques de niveau recherche, publiés ou non, émanant des établissements d'enseignement et de recherche français ou étrangers, des laboratoires publics ou privés.

N° d'ordre 2015ISAL0117
Année 2015

Thèse

Matériaux composites aéronautiques hautes températures à matrice bismaléimide renforcée

Présentée devant
L’Institut National des Sciences Appliquées de Lyon

Pour obtenir
Le grade de docteur

Formation doctorale
Matériaux polymères
École doctorale Matériaux de Lyon

Par
Guillaume Fischer
(Ingénieur)

Soutenue le 11 décembre 2015 devant la Commission d'examen

Jury MM.

O. Allix	Professeur (ENS Cachan) - Président
M. Bauer	Professeur (Fraunhofer PYCO) - Rapporteur
M. Cicotti	Professeur (ESPCI ParisTech) - co-directeur
J. Cinquin	Docteur (Airbus Group Innovations) - Examinateur
J.-F. Gérard	Professeur (INSA de Lyon) - Directeur
L. Laiarinandrasana	Maître de recherches (Mines ParisTech) - Rapporteur
F. Lortie	Maître de conférences (INSA de Lyon) - Examinateur

Laboratoires de recherche : IMP INSA de Lyon, SIMM ESPCI ParisTech

INSA Direction de la Recherche - Ecoles Doctorales - Quinquennal 2011-2015

SIGLE	ECOLE DOCTORALE	NOM ET COORDONNEES DU RESPONSABLE
CHIMIE	CHIMIE DE LYON http://www.edchimie-lyon.fr Sec : Renée EL MELHEM Bat Blaise Pascal 3 ^e etage 04 72 43 80 46 Insa : R. GOURDON secretariat@edchimie-lyon.fr	M. Jean Marc LANCELIN Université de Lyon – Collège Doctoral Bât ESCPE 43 bd du 11 novembre 1918 69622 VILLEURBANNE Cedex Tél : 04.72.43.13.95 directeur@edchimie-lyon.fr
E.E.A.	ELECTRONIQUE, ELECTROTECHNIQUE, AUTOMATIQUE http://edea.ec-lyon.fr Sec : M.C. HAVGOUDOUKIAN Ecole-doctorale.eea@ec-lyon.fr	M. Gérard SCORLETTI Ecole Centrale de Lyon 36 avenue Guy de Collongue 69134 ECULLY Tél : 04.72.18.60.97 Fax : 04 78 43 37 17 Gerard.scorletti@ec-lyon.fr
E2M2	EVOLUTION, ECOSYSTEME, MICROBIOLOGIE, MODELISATION http://e2m2.universite-lyon.fr Sec : Safia AIT CHALAL Bat Atrium- UCB Lyon 1 04.72.44.83.62 Insa : S. REVERCHON Safia.ait-chalal@univ-lyon1.fr	M. Fabrice CORDEY Laboratoire de Géologie de Lyon Université Claude Bernard Lyon 1 Bât Géode – Bureau 225 43 bd du 11 novembre 1918 69622 VILLEURBANNE Cédex Tél : 04.72.44.83.74 Sylvie.reverchon-pescheux@insa-lyon.fr fabricce.cordey@univ-lyon1.fr
EDISS	INTERDISCIPLINAIRE SCIENCES-SANTE http://www.ediss-lyon.fr Sec : Safia AIT CHALAL Bat Atrium – UCB Lyon 1 04 72 44 83 62 Insa : Safia.ait-chalal@univ-lyon1.fr	Mme Emmanuelle CANET-SOULAS INSERM U1060, CarMeN lab, Univ. Lyon 1 Bâtiment IMBL 11 avenue Jean Capelle INSA de Lyon 696621 Villeurbanne Tél : 04.72.11.90.13 Emmanuelle.canet@univ-lyon1.fr
INFOMATHS	INFORMATIQUE ET MATHÉMATIQUES http://infomaths.univ-lyon1.fr Sec : Renée EL MELHEM Bat Blaise Pascal 3 ^e etage infomaths@univ-lyon1.fr	Mme Sylvie CALABRETTA LIRIS – INSA de Lyon Bat Blaise Pascal 7 avenue Jean Capelle 69622 VILLEURBANNE Cedex Tél : 04.72. 43. 80. 46 Fax 04 72 43 16 87 Sylvie.calabretta@insa-lyon.fr
Matériaux	MATERIAUX DE LYON http://ed34.universite-lyon.fr Sec : M. LABOUNE PM : 71.70 -Fax : 87.12 Bat. Direction 1 ^{er} et. Ed.materiaux@insa-lyon.fr	M. Jean-Yves BUFFIERE INSA de Lyon MATEIS Bâtiment Saint Exupéry 7 avenue Jean Capelle 69621 VILLEURBANNE Cedex Tél : 04.72.43.71.70 Fax 04 72 43 85 28 Ed.materiaux@insa-lyon.fr
MEGA	MECANIQUE, ENERGETIQUE, GENIE CIVIL, ACOUSTIQUE http://mega.universite-lyon.fr Sec : M. LABOUNE PM : 71.70 -Fax : 87.12 Bat. Direction 1 ^{er} et. mega@insa-lyon.fr	M. Philippe BOISSE INSA de Lyon Laboratoire LAMCOS Bâtiment Jacquard 25 bis avenue Jean Capelle 69621 VILLEURBANNE Cedex Tél : 04.72 .43.71.70 Fax : 04 72 43 72 37 Philippe.boisse@insa-lyon.fr
ScSo	ScSo* http://recherche.univ-lyon2.fr/scso/ Sec : Viviane POLSINELLI Brigitte DUBOIS Insa : J.Y. TOUSSAINT viviane.polsinelli@univ-lyon2.fr	Mme Isabelle VON BUELTINGLOEWEN Université Lyon 2 86 rue Pasteur 69365 LYON Cedex 07 Tél : 04.78.77.23.86 Fax : 04.37.28.04.48 isavonb@dbmail.com

*ScSo : Histoire, Géographie, Aménagement, Urbanisme, Archéologie, Science politique, Sociologie, Anthropologie

**Matériaux composites aéronautiques
hautes températures à matrice
bismaléimide renforcée**

**High temperature and toughened
bismaleimide composite materials for
aeronautics**

À Dominique Briez

Remerciements

Je remercie d'abord Monika Bauer et Lucien Laiarinandrasana pour avoir accepté d'être rapporteurs de mes travaux. J'ai pu apprécier les échanges et les discussions apportant des ouvertures et un regard nouveaux sur les résultats obtenus. Je remercie également Olivier Allix dont l'expertise mais aussi la curiosité ont pu enrichir les discussions.

Je dois également beaucoup à chacune des quatre personnes qui ont participé à mon encadrement et qui ont ainsi pu évaluer et confirmer mon travail. Je remercie Jacques d'abord pour m'avoir offert l'opportunité de réaliser cette thèse, ensuite pour m'avoir fourni des conditions exceptionnelles dont il a souvent été le seul garant, enfin pour m'avoir guidé tout au long de ces trois années. Je remercie Frédéric pour l'investissement dont il a fait preuve, ce qu'il ne semble pas toujours réaliser. Il n'aurait pas été possible de coordonner ces travaux à distance sans son implication. Les discussions que nous avons pu avoir ont souvent dépassé le simple cadre de la recherche. Je remercie Jean-François pour avoir accordé de la valeur à mon travail et pour avoir si judicieusement orienté mes réflexions lorsque le besoin s'en faisait sentir. Je remercie Matteo pour m'avoir permis de partager l'aventure d'exploration que devient la recherche à ses côtés.

Il y aussi trois personnes qui ont posé des jalons au cours de ces trois années de pérégrinations, à travers des discussions bien souvent cruciales. C'est à ce titre que je remercie Jean-Louis Halary pour m'avoir guidé dès mes premiers pas dans le monde de la recherche et pour avoir suivi le déroulement de mes travaux avec une fidélité indéfectible. Je remercie Jean-Pierre Pascault qui a permis de jeter un éclairage nouveau sur certains résultats. Je remercie Didier L. pour son soutien et l'intérêt qu'il a porté à mon devenir.

Je tiens également à remercier Étienne Fleury et Christian Frétigny pour m'avoir accueilli au sein de leurs laboratoires respectifs.

J'ai passé la majorité de mon temps au centre de recherche d'Airbus Group à Suresnes, y liant des liens particuliers. Mes pensées vont d'abord à Élisa qui m'a supporté pendant plus de trois ans. Elles vont aussi à Didier F., Christophe, Jérôme, Fernand, François M., Laëtitia, Sophie G., Sophie S., Marie-Paule, Catherine, Christine, Claire, Éric et Thierry que j'ai côtoyés longuement. Je me dois de remercier Martine, Christian, Pascal N., Alain R., Alain M., Florian, Albert, Tanguy B., Pascal M., François P., Gilles et Thierry M. qui m'ont aidé à un moment ou à un autre. Bien que jamais très nombreux en simultanément, les années ont vu se succéder les doctorants, je salue donc ceux qui ont occupé le terrain en même temps que moi, Benjamin, Ludovic, Basile et Tanguy.

C'est avec un peu de regrets que je n'ai pas pu davantage fréquenter les membres de l'IMP à l'INSA. Je remercie l'ensemble du laboratoire pour le temps que j'y ai passé, en particulier Fernande, Patrick, Jocelyne, Jannick, Julien et Marion. Mes pensées accompagnent également mes camarades doctorants et post-doctorants Suzanne, Thibaut, Yann, Jean-Charles, Thomas, Marie, Vincent, Julien, Jean-David, Elie, Nour, Sylvain, Loïc, Hélène, Benjamin, Quentin, Camille, Amélie, Arthur, Florence, Aymeric, Mélody, Olivier, Arnaud, Sandra, Maëlis, Luanda, Damien, Nicolas, Noëllie, Johanna, Constance et Margaux.

Si c'est au SIMM que ma thèse m'a laissé passer le moins de temps, j'y ai trouvé mes marques instantanément, l'ESPCI étant mon école. Mes remerciements vont à David, Ludovic, Freddy et Bruno pour leur aide précieuse. Ils vont également à mes pairs et aînés Laure, Romain, Pierre, Paul, Robin, Jennifer, Yannick, Éric, Benjamin, Davide, Quentin, Robert, Thitima, Ekkachai, Richard, Marc, Pauline, Charles, Marine, Victor, Matthieu, Julien, Pascaline, Christopher, Louis, Guillaume, Corentin et Tom.

Enfin il me faut remercier ma famille, qui a le mérite de m'avoir laissé libre de mes choix, accompagné et soutenu jusqu'à la conclusion de mes études.

Je ne pourrais pas terminer le chapitre des remerciements sans évoquer celle qui partage ma vie et qui, depuis des années, est une source de réconfort et un soutien irremplaçable. Mais elle est aussi celle qui a le plus guidé mes pas et fait naître cette vocation qui est aujourd'hui la mienne.

Matériaux composites aéronautiques hautes températures à matrice bismaléimide renforcée

Le domaine aéronautique fait de plus en plus appel aux matériaux composites pour alléger les structures dans le but d'améliorer leurs performances et de limiter la consommation de carburant. Les composites à matrices organiques représentent aujourd'hui plus de 50% de la structure des avions civils de dernière génération (A350 et B787). Les matériaux utilisés sont essentiellement des composites à matrice époxy avec des températures d'utilisation en service continu pour de longues durées ne dépassant pas 110°C. Continuer à augmenter cette part de matériaux composites passe par leur introduction dans des zones plus chaudes, proches des réacteurs ou des turbines.

Les matériaux composites à matrice bismaléimides sont compatibles avec des températures d'application d'au moins 200°C, mais sont très sensibles aux impacts et présentent une fragilité beaucoup trop importante pour des pièces de structure. Les composites à matrice époxy ont fait l'objet de développements pour améliorer ces propriétés, en incorporant dans les formulations des thermoplastiques solubles et insolubles qui ont pour effet de freiner la propagation des délaminages induits par des impacts.

En s'inspirant des méthodologies et des connaissances acquises sur les formulations époxys, l'objectif de ces travaux est de développer des systèmes réactifs de type bismaléimide à propriétés optimisées et d'identifier les paramètres clés pour y parvenir.

Mots clés : composite, thermodurcissable, bismaléimide, ténacité.

High temperature and toughened bismaleimide composite materials for aeronautics

Aeronautics use more and more composite materials to reduce structures weight, in order to improve performance and to limit fuel consumption. Polymer matrix composite materials represent today more than 50% of last generation civil aircrafts structure (A350, B787). Most of thermoset matrices are epoxies with service temperatures below 110°C for long time services. To further optimize the composite part ratio, it is now necessary to use those materials in structural parts exposed to higher temperatures, for instance, near engines.

Among high performance thermoset matrices, bismaleimides offer potential in service temperature up to at least 200°C, but their brittleness makes them non-suitable for structural applications. Epoxy-based composite materials have gone through improvements, increasing their toughness by mixing with soluble and non-soluble thermoplastics to hold in delamination crack propagation.

Starting with methods and knowledge from epoxies toughening strategies, this work is dedicated to develop toughened bismaleimide systems and to identify relevant parameters to reach this aim.

Key words : composite, thermoset, bismaleimide, toughness.

Résumé étendu

Introduction

Le domaine aéronautique est très exigeant, tant en aérodynamique qu'en électronique, en mécanique et en chimie. Les sciences des matériaux demeurent un élément fondamental dont l'ingénierie aéronautique ne saurait se passer. Les matériaux utilisés pour la conception des aéronefs ont beaucoup évolué depuis l'apparition des premières machines volantes. Les premiers avions du début du 20^{ème} siècle, étaient principalement faits de bois et de toile, directement hérités de la structure des machines volantes du 19^{ème} siècle. La première moitié du 20^{ème} siècle a vu le perfectionnement des systèmes de propulsion et des structures aller de pair avec un usage grandissant des matériaux métalliques. Pendant la seconde moitié du 20^{ème} siècle, les moteurs plus puissants ont permis le vol à plus haute altitude, engendrant de nouvelles contraintes pour les matériaux et les structures, comme la nécessité de pressuriser les habitacles. Dans les années 1960, l'essor du transport aérien et le développement d'avions plus volumineux pour transporter des passagers a rendu nécessaire la recherche de matériaux plus légers. Les alliages d'aluminium ont rempli ce rôle. A partir des années 1970, les matériaux composites ont été progressivement introduits dans la conception d'appareils volants (Figure I). Même si les premiers radômes à base de fibre de verre sont apparus dès les années 1940, c'est l'utilisation de la fibre de carbone qui a mené au développement d'une nouvelle classe de matériaux à la fois rigides et légers.

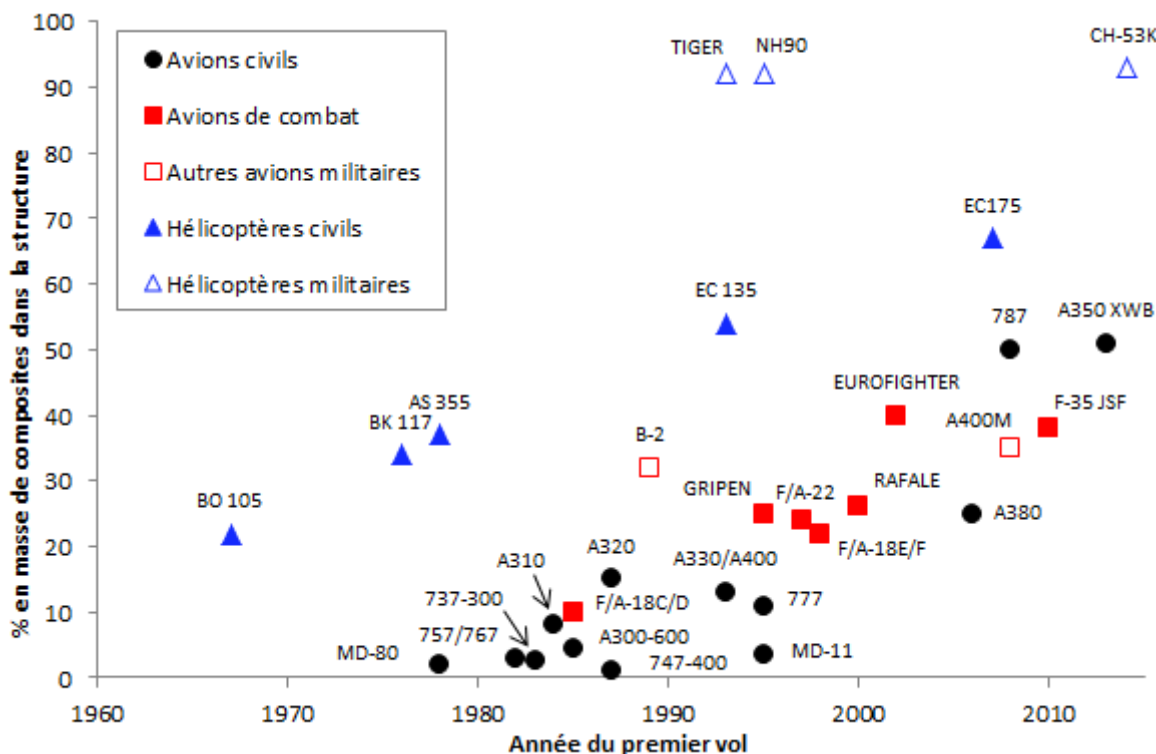


Figure I : part des matériaux composites à matrice organique dans la structure de différents appareils.

Le terme composite désigne l'ensemble des matériaux fait d'au moins deux composants distinguables. Pour un simple composite à deux composants, l'un, appelé matrice, assure

le maintien de l'intégrité du matériau, ainsi que le transfert des efforts. L'autre appelé renfort amène généralement les propriétés d'intérêt. Les matrices peuvent être de diverses natures, comme des métaux, des céramiques ou des polymères. Les renforts les plus communs sont constitués de métaux, de céramiques et de divers types de fibres et de particules. Matrice et renfort peuvent être faits du même matériau, comme dans le cas des composites SiC/SiC ou C/C où fibres et matrice sont fait respectivement de carbure de silicium ou de carbone. Dans ce cas, les propriétés intéressantes sont apportées par la forme du renfort. En général, ce sont deux matériaux de nature différentes qui sont associés.

Les matériaux composites dont il sera question par la suite sont constitués d'une matrice polymère et de renforts en fibres longues. Ce type de composite est largement utilisé dans les structures aéronautiques. Deux classes de matrices polymères sont rencontrées, les thermoplastiques et les thermodurcissables. Les thermoplastiques sont constitués de longues chaînes moléculaires et nécessitent d'être chauffés pour être mis en forme. Les thermodurcissables sont constitués de petites molécules qui réagissent pour former un réseau macromoléculaire tridimensionnel. Ils sont également communément appelés *résines*, un terme ambiguë pouvant désigner à la fois l'état initial non réagi et le matériau polymère solide dans son état final. Les matériaux composites aéronautiques sont principalement fait à partir de résines de type époxy. Les résines phénoliques sont plutôt destinées aux habitacles, en raison de leur résistance au feu. Les thermoplastiques sont encore peu utilisés mais quelques applications ont été retenues, comme le plancher du cockpit de l'A400M à matrice polyéther cétone.

Plusieurs natures de fibres peuvent être rencontrées (Figure II), chacune destinée à des applications précises. Les fibres de carbone sont utilisées dans les structures primaires, les fibres de verre pour les planchers et les structures secondaires. Les radômes contiennent des fibres de quartz ou de verre, alors que les fibres de bore sont de moins en moins utilisées (des parties d'empennage sur de vieux modèles d'avions militaires en contiennent encore).



Figure II : fibres communément rencontrées dans les matériaux composites à matrice organique. A) carbone ; B) verre ; C) aramide.

Les propriétés mécaniques des matériaux composites dépendent de l'orientation spatiale des fibres. Les laminés sont constitués de couches de fibres et de matrice appelées plis. La séquence d'empilement détermine les propriétés suivant les différents axes. L'empilement le plus simple est constitué de plis dont toutes les fibres sont parallèles (uni-directionnel). Les propriétés dans l'axe d'alignement des fibres sont excellentes mais au détriment de l'axe latéral. Les plis de fibres parallèles peuvent être orientés différemment, de sorte à obtenir des fibres alignées dans plusieurs directions. Un tel empilement est appelé quasi-isotrope. Des plis de fibres tissées sont également souvent utilisés.



Figure III : séquences d'empilement. A) unidirectionnel ; B) quasi-isotrope ; C) tissus.

Le succès des matériaux composites dans un domaine aussi exigeant que celui de l'aéronautique s'explique par les nombreux avantages qu'ils offrent. Avec une faible densité, ils permettent d'alléger les structures en se substituant aux matériaux métalliques. Ceci impose de nouvelles conceptions pour adapter la géométrie et la structure composite à la distribution des efforts. Un gain non négligeable peut être accompli grâce à des procédés de fabrication efficaces. Les pièces composites sont en effet réalisées à partir d'ébauches très proches de leur forme définitive, réduisant les usinages nécessaires et la perte de matière. Ces pièces peuvent d'ailleurs être de très grande taille, réduisant le nombre de raccords (rivetage ou boulonnage). Ces matériaux composites sont de plus très résistant à la fatigue et à la corrosion.

Un nombre conséquent de limites accompagne ces avantages. Si l'usage intensif des composites en aéronautique a entraîné une dynamique de production de masse, réduisant le coût des matières premières, les matériaux de haute performance demeurent assez chers. De plus, par certains aspects, leur mise en forme est coûteuse (hautes températures, cycles de cuisson longs...). Un des problèmes majeurs apparaissant lorsqu'une pièce métallique est remplacée par une homologue composite, est la différence de conductivité électrique. Bien que les fibres de carbone conduisent le courant, les matières plastiques constituant les matrices sont de bons isolants. L'impossibilité d'évacuer convenablement les charges provoque l'endommagement du matériau en cas d'impact de foudre. La faible conductivité électrique va de pair avec une faible conductivité thermique et l'accumulation de chaleur est néfaste pour des matériaux limités à une gamme de faibles températures (les composites à base époxy ne peuvent en général pas dépasser 140°C). Tout comme le vieillissement thermique, l'humidité nuit au maintien de bonnes propriétés. Enfin, les matériaux composites sont assez sensibles aux impacts et résistent mal à l'endommagement.

Un des axes de développement des composites à matrice organique pour l'aéronautique concerne l'introduction de pièces dans des zones chaudes. Les matériaux doivent alors pouvoir subir des températures élevées pendant toute la durée de vie de l'appareil. Parmi les matrices satisfaisant ce critère, les résines bismaléimides ont déjà connu plusieurs applications en environnement moteur. Cependant presque aucune ne concerne des structures primaires, devant supporter des contraintes mécaniques importantes, la raison étant la trop grande fragilité de ces matériaux.

Ces travaux visent à développer des matériaux composites à matrice bismaléimide, ayant une ténacité augmentée. La stratégie adoptée est celle qui a porté ses fruits pour les matrices époxy, à savoir l'introduction de thermoplastiques dans les formulations.

Chimie des bismaléimides

Trois générations de résines bismaléimides ont été employées. La première n'implique pas d'autre composant que des molécules de la classe des bismaléimides. En effet, portés au-dessus de leur point de fusion, celles-ci réagissent entre elles (homopolymérisation) pour former un réseau tridimensionnel densément réticulé. Leurs difficiles conditions de mise en forme (réaction rapide, fusion au-delà de 150°C) et leur grande fragilité ont amené à mélanger les bismaléimides avec d'autres composés. La deuxième génération de bismaléimides a introduit l'usage d'amines qui copolymérisent avec les bismaléimides par réaction de Michael. L'amine écartant les nœuds de réticulation, le réseau formé est moins fragile. La troisième génération de résines reprend le même principe en remplaçant les amines par des bisallyles. Les résines alors obtenues ont une facilité de mise en forme similaire à celle des époxys, rendant possible l'utilisation des mêmes outils pour la fabrication de pièces composites. C'est un de ces systèmes qui a été sélectionné pour cette étude (Figure IV).

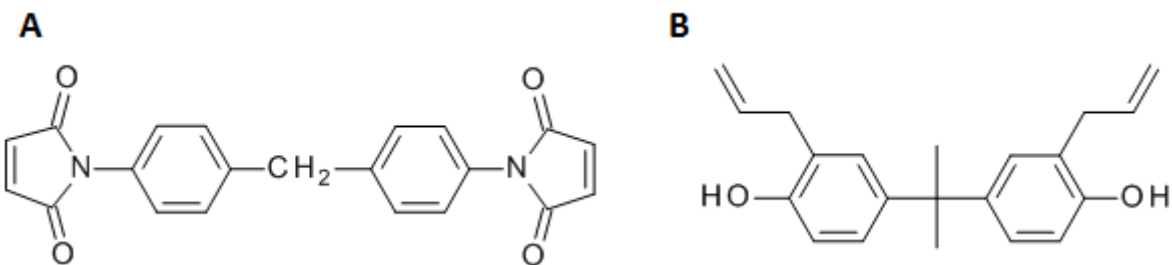


Figure IV : composants de la résine bismaléimide sélectionnée.

A) 1,1'-(methyldi-4,1-phényl)bismaleimide (BMI) ; B) 2,2'-diallylbisphénol A (DBA).

La réactivité des résines bismaléimides/bisallyles a fait l'objet de nombreuses études, desquelles se dégagent deux principaux mécanismes réactionnels. La première étape est commune aux deux, il s'agit d'une réaction de type Alder-ène entre les deux monomères pour allonger linéairement les chaînes polymères. La seconde étape, celle responsable de la réticulation du réseau, est soit l'homopolymérisation des groupements maléimides, soit un ensemble de réactions d'addition (Diels-Alder ou Wagner-Jauregg) et de réarrangements, impliquant les fonctions maléimides et l'adduit de la réaction d'Alder-ène.

La première étape a été confirmée par RMN en solution de systèmes modèles reproduisant la réactivité des monomères tout en évitant la réticulation. Les produits de réaction de la seconde étape n'ont pas été identifiés avec précision à cause de leur trop faible solubilité. L'étude des systèmes modèles permet cependant de suggérer que les deux mécanismes sont possibles dans la résine choisie. Les analyses chimiques n'ont pas été poussées plus loin, mais de nouveaux éléments sont apparus lors de l'étude physico-chimique du mélange réactif. La mesure du temps de gel en condition isotherme, avec et sans inhibiteur de radicaux, a mis en évidence un retard conséquent du gel lorsque les réactions radicalaires sont inhibées (Figure V). Ceci tend à prouver que le mécanisme de réticulation (lié à l'obtention du gel) est de nature radicalaire.

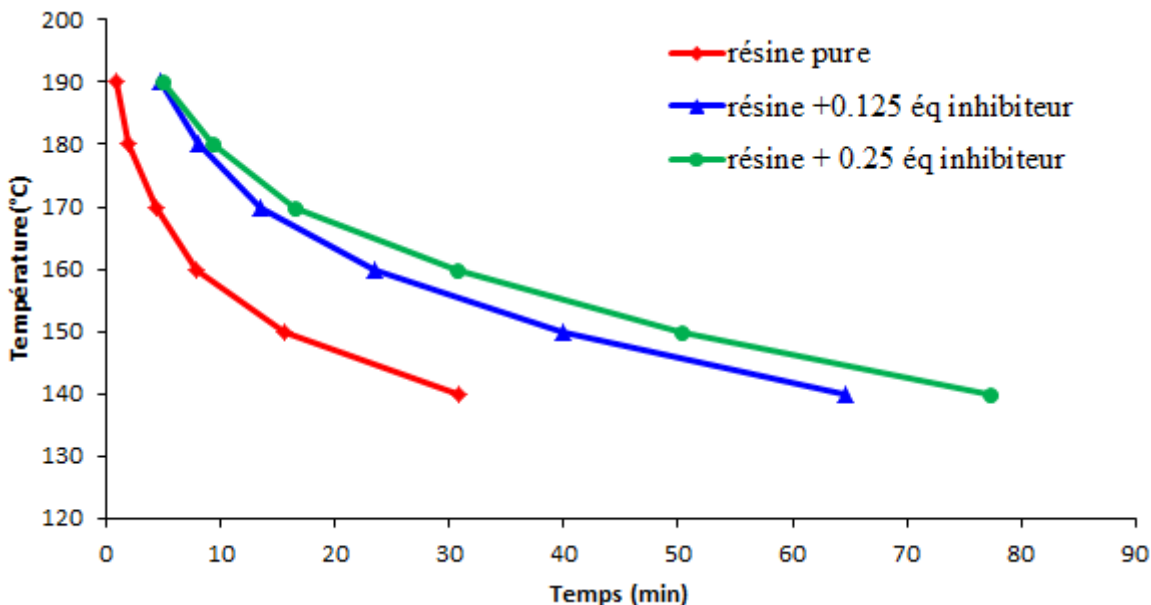


Figure V : courbes de gel du système réactif BMI/DBA avec et sans inhibiteur de radicaux.

Les conséquences de cette observation sont multiples. Les résines bismaléimides-bisallyles se distinguent par cette réactivité radicalaire en chaîne, des résines époxys qui ont un mécanisme de croissance par étapes. Comme conséquence directe, les paramètres de contrôle des cinétiques de réaction ne seront pas les mêmes. Le mécanisme radicalaire amène également une inhomogénéité dans le réseau, notamment en terme de densité de réticulation. En effet, la polymérisation est active autour des radicaux, formant rapidement des micro-gels réticulés baignant dans des monomères n'ayant pas encore réagi. Ces inhomogénéités peuvent être limitées par l'ajout d'inhibiteurs de radicaux, permettant ainsi un contrôle relatif sur la structure du réseau, à travers les différents mécanismes réactionnels.

Modification par des thermoplastiques

Les mélanges bismaléimides/thermoplastiques ont été étudiés pour des polyéthersulfones (PES), des polyétherimides (PEI), des polyesters, des polyimides et des polyaryléther cétones. Seuls les PES et les PEI ont été retenus pour cette étude, pour leur haute température de transition vitreuse (225°C), leur disponibilité à l'échelle industrielle et leur utilisation connue dans des mélanges avec des résines époxy/amine. La littérature prévoit des morphologies particulières à faible taux de thermoplastique, puis des morphologies co-continues et en phase-inverse, en augmentant ce taux. Seules les morphologies de particules de thermoplastique dans une matrice réticulée sont souhaitables, pour une bonne conservation des propriétés thermomécaniques.

Le suivi par microscopie optique à platine chauffante des différents mélanges, a mis en évidence une séparation de phase pendant la cuisson, suivant un mécanisme de décomposition spinodale. Ce mécanisme n'est pas modifié par le taux de thermoplastique ou la vitesse de chauffage. Les morphologies particulières sont obtenues jusqu'à des taux de 5 à 10 pcr (parts pour cent parts de résine), selon le thermoplastique utilisé. Lorsque la concentration de thermoplastique augmente, des objets plus complexes apparaissent,

d'abord de grosses particules à morphologie en phase-inverse, puis des globules plus gros, puis de multiples échelles de séparations de phases (Figure VI).

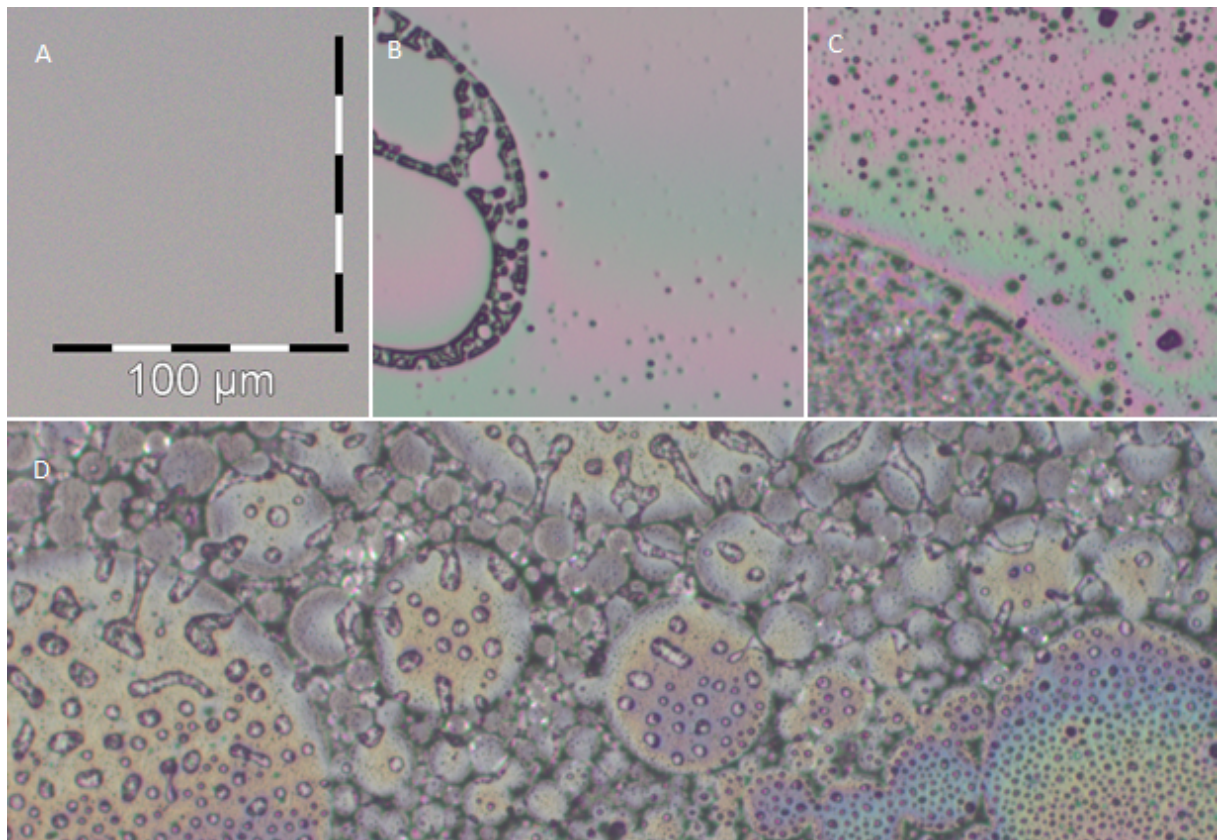


Figure VI : morphologie d'un mélange BMI/DBA/PEI à différents taux de PEI.
A) résine pure ; B) 1 pcr ; C) 5 pcr ; D) 10 pcr. Échelle commune 100 μ m.

Dans le cas des morphologies particulières, l'observation à petite échelle a révélé des sous-structures au sein des particules, même des plus petites. Celles-ci sont particulièrement visibles dans le cas du PES, où les particules ont une morphologie en phase-inverse.

En plus des PES et PEI qui sont initialement solubles dans les monomères de la résine bismaléimide, des thermoplastiques non solubles tels que le polyamide-imide (PAI) et un polyimide (PI) ont également été utilisés pour améliorer la ténacité du matériau thermodurcissable. Les particules de thermoplastic sont alors simplement dispersées dans la matrice.

Rupture des bismaléimides

Un dispositif expérimental original a été utilisé pour étudier les comportements à petite échelle lors de la rupture de la matrice thermodurcie. Une géométrie de test mécanique permettant de propager de manière contrôlée une fissure en mode I (DCDC) est associée à la microscopie à force atomique (AFM). La propagation de fissure peut alors être observée à une échelle inférieure au micromètre. Ce dispositif a permis de mettre en évidence une propagation lente de la fissure dans le matériau, les vitesses d'avancée de fissure allant du micromètre par seconde (dans ce cas le suivi par caméra optique est substitué à l'AFM) à la dizaine de picomètres par seconde.

Une mesure du facteur d'intensité de contrainte peut être réalisée à partir du profil d'ouverture de la fissure. La variation de ce facteur est associée à la relaxation de la force appliquée à l'échantillon. Sur les sept décades de vitesse explorées, le facteur d'intensité de contrainte varie d'environ 10%. Un modèle reliant la vitesses de propagation de fissure au taux de déformation à la pointe, met en relation cette faible variation avec la faible dépendance de la loi de comportement du matériau au taux de déformation.

Un phénomène de propagation saccadée est visible lorsque la vitesse de propagation de fissure est suffisamment faible. Des phases de très faible vitesse (pratiquement nulle) succèdent à des avancées brutales (instantanées à l'échelle d'observation) sur environ 250 nm. Pendant les phases lentes, la pointe de fissure s'arrondit progressivement, alors que la propagation brutale génère une pointe très effilée. Ce phénomène peut avoir deux origines, la première étant un phénomène mécanique semblable à du *stick-slip* à petite échelle. La seconde provient de l'inhomogénéité du réseau polymère, où l'alternance de zones plus ou moins densément réticulées est associée à l'alternance de phases lentes et rapides. L'utilisation d'un réseau homogénéisé à l'aide d'un inhibiteur de radicaux modifie cette séquence de propagation. Les avancées brutales disparaissent et sont remplacées par des phases d'accélération et de ralentissement de la pointe de fissure.

Rupture des matrices modifiées

Les différentes matrices modifiées ont été classées selon leur ténacité. Le PAI est relativement efficace pour augmenter la ténacité (+25%), alors que le PI est le moins efficace. Les PES et PEI sont d'efficacité équivalente à celle du PAI (+18-28%). Le PES et le PAI ont été retenus pour poursuivre l'étude sur les mécanismes de renforcement.

La méthode d'observation utilisée sur la matrice bismaléimide pure a été adaptée pour observer la propagation de fissure dans les matrices modifiées par ajout de thermoplastique. Ce protocole permet de suivre avec une résolution temporelle les phénomènes ayant lieu lorsque la pointe de fissure rencontre une particule renforçante (Figure VII).

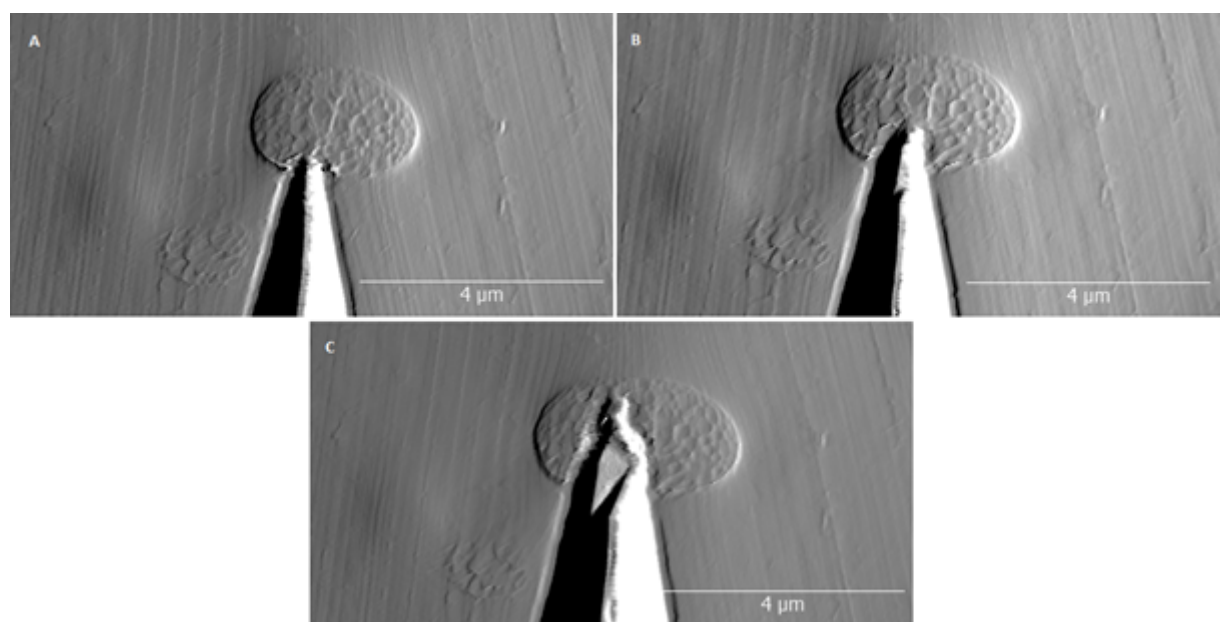


Figure VII : images AFM d'une fissure propageant dans un mélange BMI/DBA/PES à 10 pcr. A) t_0 ; B) $t_0 + 413$ min ; C) $t_0 + 1102$ min. Propagation vers le haut.

Les mécanismes liés aux différents types de particules ont été ainsi identifiés. Si la fissure traverse les particules de PES (Figure VII), elle a plutôt tendance à contourner celles de PAI (Figure VIII).

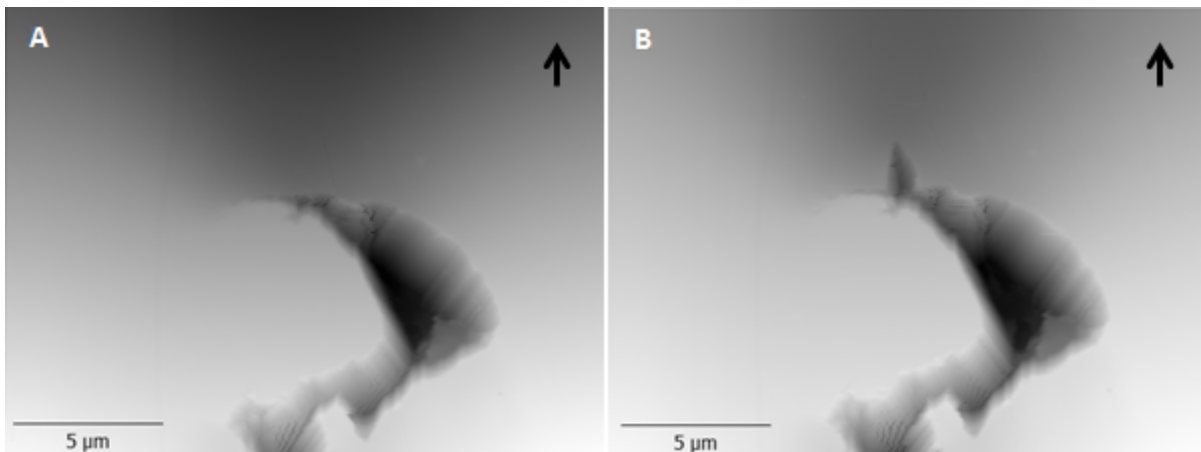


Figure VIII : images AFM d'une fissure propageant dans un mélange BMI/DBA/PAI à 7 pcr. A) t_0 ; B) $t_0 + 25$ min. Propagation vers le haut.

Les surfaces de rupture des différents échantillons ont été analysées en microscopie électronique à balayage. Les différents évènements observés pendant la propagation sous AFM ont été mis en relation avec des marques particulières sur les surfaces de rupture. Chaque évènement permet ainsi de remonter à la formation des différents reliefs observés.

Ainsi il est possible d'établir une relation entre la structure du matériau (dépendant de ses constituants), les mécanismes de propagation de fissure et l'efficacité du renforcement. Dans le cas du PES, la fissure traverse les particules en étant peu déviée, mais celles-ci montrent une forte déformation plastique, entraînant une dissipation d'énergie supplémentaire par rapport à la matrice pure. Dans le cas du PAI, la déviation de la fissure (engendrant des modes mixtes locaux) et la création de surface supplémentaire (contour des particules) coûtent de l'énergie. De plus, des mécanismes de déformation du front de fissure (*crack-pinning*) semblent également être impliqués.

Rupture des composites

Quatre formulations de matrices ont été retenues pour la conception de matériaux composites à fibre de carbone : matrice bismaléimide pure, matrice modifiée avec 5 pcr de PES, matrice modifiée avec 7 pcr de PAI et matrice modifiée avec 5 pcr de PES et 7 pcr de PAI. Les contraintes du procédé d'injection, notamment sur la viscosité de la résine, empêchent de mélanger les thermoplastiques aux monomères, par conséquent il sont placés directement entre les plis de la préforme, dans laquelle la résine non modifiée est injectée.

La mesure de l'énergie nécessaire au délaminage en mode I du composite montre une augmentation de la résistance à la propagation de fissure pour les composites à matrice modifiées. Le meilleur renforcement est obtenu avec le PES et le plus faible avec le PAI, le mélange des deux étant intermédiaire (Figure IX).

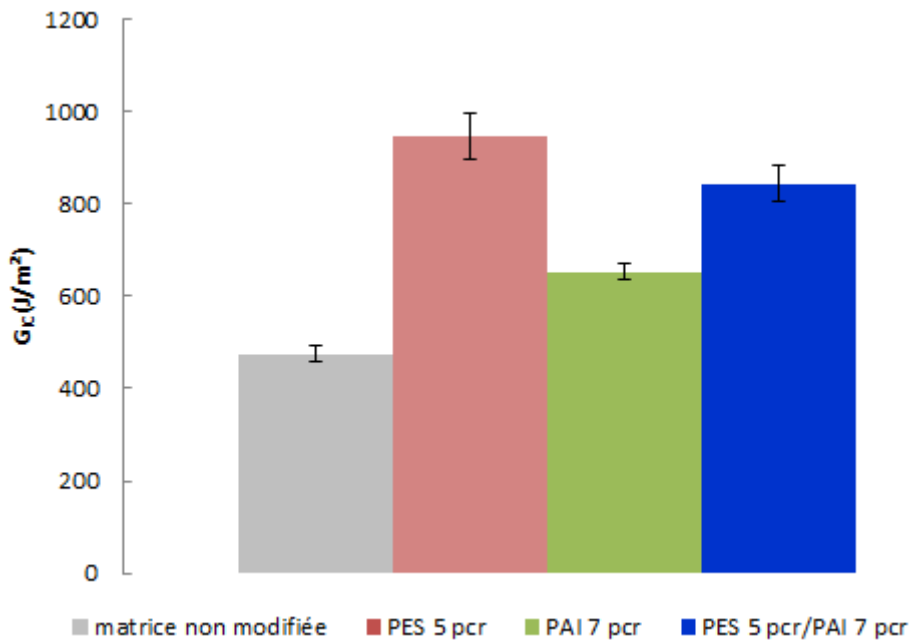


Figure IX : énergie surfacique de délaminaison en mode I pour les différents composites.

L'efficacité du PES ne peut pas être simplement mise en regard de l'étude sur les matrices. Le procédé de fabrication des composites ayant nécessité d'introduire les thermoplastiques dans la préforme, le PES n'a pas été pré-solubilisé dans la résine. De fait, des coupes microscopiques dans le composite révèlent la présence de morphologies en phase-inverse, qui n'apparaissent pas dans la matrice au même taux de thermoplastique. L'étude des surfaces de rupture des composites délamínés montre que les zones en phase-inverse introduisent de la ductilité dans le processus de rupture. Ce nouveau mécanisme permet d'expliquer la plus grande efficacité du PES (+99%) dans le composite par rapport au PAI (+37%), situation inverse au cas des matrices. Le fait que combinaison des deux types de thermoplastiques n'est pas aussi efficace que le PES seul peut s'expliquer par une hypothèse de maillon le plus faible, où la présence de PAI renforce la matrice pure mais amoindrit la résistance des zones de morphologie en phase-inverse.

Conclusions

Cette étude aborde de multiples aspects liés aux résines bismaléimides, allant de leur chimie à la caractérisation fine de leurs mécanismes de rupture.

La chimie des résines bismaléimide/bisallyles est très complexe, avec plusieurs étapes de polymérisation de natures différentes et de possibles réactions parallèles. La première étape de réaction identifiée est conforme aux observations de la littérature scientifique, avec un allongement des chaînes par réaction d'Alder-ène entre les fonctions maléimides et allyles. La seconde étape, menant à la réticulation du réseau polymère, est beaucoup plus difficile à caractériser. Les méthodes d'analyse chimique ont souvent été mises en défaut par la rapide formation de composés insolubles. L'utilisation d'inhibiteurs de radicaux et la mesure rhéologique du temps de gel, discriminant les mécanismes de réticulation, a permis de mettre en évidence le caractère radicalaire de cette seconde étape. Les autres réactions d'addition de type Diels-Alder ne sont cependant pas à exclure complètement.

Elles peuvent d'ailleurs constituer un mécanisme alternatif dans le cas où la polymérisation radicalaire est inhibée. La chimie même de ces résines suggère une structure de réseau polymère profondément différente de celle des époxy, référence en matière de matrice pour les composites aéronautiques. L'étape de polymérisation radicalaire engendre des inhomogénéités, en particulier dans la densité de réticulation.

La stratégie d'amélioration de la ténacité de la matrice bismaléimide par l'ajout de thermoplastiques nécessite une connaissance et une maîtrise des phénomènes de séparation de phases pendant la cuisson des thermodurcissables modifiés. Le paramètre ayant la plus grande influence sur les morphologies obtenues est la concentration en thermoplastique. Pour préserver au maximum les bonnes propriétés thermomécaniques de la matrice, les morphologies doivent se limiter à des dispersions de particules riches en thermoplastiques dans une phase principale riche en thermodurcissable. Les formulations retenues sont donc celles aux plus faibles taux de thermoplastiques (5-10 pcr).

L'étude des mécanismes de rupture de la matrice non modifiée a été poussée jusqu'à une échelle sub-micrométrique. À l'échelle macroscopique, le matériau est fragile (verre organique), mais la dissipation d'énergie a majoritairement lieu dans une zone plastique en pointe de fissure. Dans le cas des résines bismaléimides, cette zone a une taille de l'ordre de quelques micromètres. La technique d'observation par AFM a donc permis d'étudier les phénomènes contrôlant la résistance à la propagation de fissure. Le comportement lors de la propagation à faible vitesse d'avancée de fissure est cohérent avec celui d'autres polymères vitreux, bien que jamais mis en évidence sur ces systèmes auparavant. Un modèle en loi d'échelle, issu de réflexions plus générales, pour prédire ce comportement à partir des courbes contrainte-déformation est suggéré. L'analyse fine de la propagation a révélé des variations non monotones de la vitesse d'avancée de fissure. Celles-ci sont liées à la structure inhomogène du réseau polymère, mis en évidence par l'étude de la chimie et de la physico-chimie de la résine.

Le même dispositif expérimental a été utilisé pour observer les phénomènes de propagation de fissure dans les matrices hétérogènes modifiées. Cette méthode apporte une résolution temporelle qui n'existe pas dans l'analyse fractographique conventionnelle. Les divers événements observés ont été mis en relation avec les caractéristiques des surfaces de rupture, apportant des informations sur leur origine, tout en confirmant la pertinence de la méthode. Chaque type de formulation sélectionnée est associé à des mécanismes renforçants particuliers, bien identifiés à l'aide de cette technique.

L'analyse de la rupture des laminés composites a permis de confirmer l'efficacité de la stratégie de renforcement mise en place, l'énergie associée au délamination pouvant être multipliée par deux. L'analyse fractographique a cependant révélé de nombreuses différences entre les matrices et les composites associés, tant sur le plan des morphologies que sur les mécanismes de résistance à la propagation de fissure. À cause des contraintes liées aux procédés de fabrication des laminés, les morphologies de la matrice dans le composite ne sont pas identiques à celles dans la matrice seule. Ceci entraîne l'apparition de nouveaux mécanismes renforçants.

Cette étude apporte une connaissance plus profonde des résines bismaléimides et montre la possibilité de concevoir des matériaux composites à ténacité augmentée pour des applications structurelles hautes températures.

Contents

Résumé étendu	i
Introduction	i
Chimie des bismaléimides	iv
Modification par des thermoplastiques	v
Rupture des bismaléimides	vi
Rupture des matrices modifiées	vii
Rupture des composites	viii
Conclusions	ix
Introduction	6
Composite materials for aeronautics	6
Materials	7
Interesting properties	8
Limiting properties	9
Going further with composite materials	9
Bismaleimide resins	10
Preamble to the study	11
1 Bismaleimide resins	12
1.1 Development of bismaleimide resins	12
1.1.1 Evolution of the BMI-based thermoset	12
1.1.2 A whole history of chemical investigation	13
1.2 Experimental details	16
1.2.1 Selected materials	16
1.2.2 Experimental procedures	17
1.2.2.1 Mixing protocol	17
1.2.2.2 Spectroscopy	17
1.2.2.3 Calorimetry	18
1.2.2.4 Rheological analysis	18
1.2.2.5 Degradation	19
1.3 Thermal properties	19
1.3.1 Thermal degradation	20
1.3.2 Mechanical properties preservation	21
1.3.3 Thermomechanical behaviour	21
1.3.4 Conclusion	23
1.4 Reactivity	24
1.4.1 Phenol reactivity	24
1.4.2 Maleimide/allyl reactivity	24
1.4.2.1 Alder-ene reaction	24
1.4.2.2 Addition reactions	27
1.4.3 Standard resin reactivity	30
1.5 Kinetics elements	30
1.5.1 Gelation	30
1.5.1.1 Theoretical considerations	30
1.5.1.2 Rheology of bismaleimide resins	31

1.5.2	Time-Temperature-Transformation diagram	34
1.5.3	Vitrification	36
1.6	Network structure	39
1.6.1	Inhomogeneity in thermosetting polymers	39
1.6.2	Network architecture analysis	41
1.6.3	Simulated networks	42
1.7	Conclusions	46
2	Morphologies of bismaleimide thermoset and thermoplastics blends	47
2.1	Phase separation in thermosetting polymers	47
2.1.1	Flory-Huggins theory	47
2.1.2	Flory parameter	49
2.1.3	Reaction-induced phase separation	49
2.1.3.1	Reactive solvent	50
2.1.3.2	Pseudo-ternary thermoset	50
2.2	Literature on bismaleimide/thermoplastic blends	52
2.2.1	Polyethersulfones	52
2.2.2	Polyetherimides	52
2.2.3	Polyesters	53
2.2.4	Polyimides	54
2.2.5	Polyether ketones	55
2.2.6	Other polymers	55
2.2.7	Conclusion	55
2.3	Experimental details	56
2.3.1	Selected materials	56
2.3.1.1	Thermoset	56
2.3.1.2	Thermoplastics	56
2.3.2	Methods	57
2.3.2.1	Blend preparation	57
2.3.2.2	In situ temperature controlled microscopy	58
2.3.2.3	Cured samples preparation	60
2.3.2.4	Optical microscopy on cured samples	60
2.3.2.5	Electron Dispersive X-ray Spectroscopy	60
2.3.2.6	Dynamic Mechanical Analysis	61
2.3.2.7	Rheology	61
2.4	Phase separation in bismaleimide/solubilised thermoplastic blends	61
2.4.1	Phase separation behaviours	61
2.4.1.1	Polyetherimide	62
2.4.1.2	Polyethersulfone	63
2.4.2	Final morphologies	65
2.4.2.1	Influence of curing conditions	65
2.4.2.2	Comparison between thermoplastics	67
2.4.2.3	Deeper look on morphologies	70
2.4.3	Thermomechanical analysis	72
2.4.4	First conclusions on solubilised thermoplastics	75
2.5	Bismaleimide/thermoplastic particles blends	76
2.5.1	Soluble particles	76
2.5.1.1	Experimental considerations	76
2.5.1.2	Influence of the curing conditions	76

2.5.1.3	Conclusion on morphological control	79
2.5.2	Non-soluble particles	79
2.6	Conclusion	79
3	Fracture of bismaleimide resins	81
3.1	Polymer fracture	81
3.1.1	Fracture mechanics	81
3.1.1.1	Linear elastic fracture mechanics	81
3.1.1.2	Crack propagation	82
3.1.1.3	Fracture modes	83
3.1.1.4	Stress limitation at a crack-tip	83
3.1.2	Failure of thermosets	84
3.1.3	Crack propagation in glassy polymers	85
3.2	Experimental details	88
3.2.1	Materials	88
3.2.2	Methods	88
3.2.2.1	Mechanical characterisation	88
3.2.2.2	Compact tension	88
3.2.2.3	Double Cantilever Drilled Compression	90
3.2.2.4	Optical Imaging	91
3.2.2.5	Interferometry	93
3.2.2.6	Atomic force microscopy	94
3.2.2.7	SEM Fractography	95
3.3	Neat bismaleimide network fracture	95
3.3.1	Mechanical properties	95
3.3.1.1	Uniaxial tension	95
3.3.1.2	Uniaxial compression	96
3.3.1.3	Extrapolated microscopic behaviour	97
3.3.1.4	Molecular behaviour	98
3.3.2	Failure at the macroscopic scale	99
3.3.3	Crack propagation kinetics	100
3.3.3.1	Evaluation of the stress intensity factor	100
3.3.3.2	Considerations on the crack opening measurement	102
3.3.3.3	Velocity measurements and $K(v)$ curves	104
3.4	Influence of the network architecture	108
3.4.1	Non-monotonic crack propagation	108
3.4.2	Network modification	110
3.5	Modelling toughness	112
3.5.1	Steady state toughness	112
3.5.2	Material behaviour at the crack-tip	112
3.5.3	Steady state crack propagation	114
3.6	Conclusion	116
4	Fracture in heterogeneous materials	117
4.1	Material toughness	117
4.1.1	Toughening of thermosetting polymers	117
4.1.1.1	Modifiers for thermosets	117
4.1.1.2	Toughening mechanisms	118
4.1.2	Toughness in composite laminates	121

4.2	Experimental details	123
4.2.1	Materials	123
4.2.1.1	Modified resins	123
4.2.1.2	Composites	123
4.2.2	Methods	124
4.2.2.1	Tension	124
4.2.2.2	Compact tension	124
4.2.2.3	Double Cantilever Drilled Compression	125
4.2.2.4	Composite delamination	125
4.2.2.5	Atomic force microscopy	126
4.2.2.6	Fractography	126
4.3	Fracture behaviour in matrices	127
4.3.1	Mechanical properties	127
4.3.2	Toughening	128
4.3.3	Crack path in modified matrices	129
4.3.3.1	Particles from phase separation	129
4.3.3.2	Initially insoluble particles	134
4.3.4	Conclusions	138
4.4	Composite materials properties	139
4.4.1	Selected formulations	139
4.4.2	Morphologies	140
4.4.2.1	Neat bismaleimide-based composite	140
4.4.2.2	Polyethersulfone-modified composite	140
4.4.2.3	Polyamide-imide-modified composite	141
4.4.2.4	PES/PAI-modified composite	142
4.4.2.5	Conclusions	143
4.4.3	Toughening	144
4.4.4	Crack path	145
4.4.4.1	Neat bismaleimide-based composite	145
4.4.4.2	Polyethersulfone-modified composite	146
4.4.4.3	Polyamide-imide-modified composite	148
4.4.4.4	PES/PAI-modified composite	148
4.4.4.5	Matrix-composite comparison	149
4.5	Conclusions	150
4.5.1	On crack propagation in modified resins	150
4.5.2	On composite processing and toughening	150
5	Suggestions for further work and general conclusion	151
5.1	Reactivity of bismaleimides	151
5.1.1	Chemical characterisations	151
5.1.2	Simulated network architecture	151
5.2	Fracture mechanics of bismaleimides	153
5.3	Failure of modified resins	153
5.4	Composites properties	154
5.4.1	Fracture of composites	154
5.4.2	Compression after impact	156
5.4.3	Other types of alteration	157
5.5	Conclusions	157

Abbreviations	159
Bibliography	161
Appendix A: NMR spectra	176
Appendix B: Modulus loss calculation	196
Appendix C: Epoxy TTT diagram	197
Appendix D: Simulation program	198
Appendix E: Solubility parameters	213
Appendix F: Thermoplastics TGA	214
Appendix G: Edge detection tools	215

Introduction

Composite materials for aeronautics

Aeronautic is an extremely demanding field from aerodynamic and electronic to mechanic and chemistry. Material science remains a fundamental element, which engineering and aeronautic design have to comply with. Huge changes have occurred since the beginning of flying machines history. First aircrafts in the early 20th century made an extensive use of wood and fabric, directly inherited from the 19th century flying machines. During the first half of the 20th century, constant innovation in thrust, and structures went hand in hand with an increasing use of metallic components. In the second half of the 20th century, more powerful engines enabled high altitude flight, which lead to new requirements and needs for materials and structures such as pressurization. In the 1960s, the development of bigger planes to carry passengers made the search for strong and light designs a necessity. Aluminium alloys were employed to this end. From the 1970s, composite materials have been progressively more and more used (Figure 1). Even if the first glass fibre-based radomes had been introduced in the 1940s, the use of carbon fibres lead to a new class of low density and stiff materials.

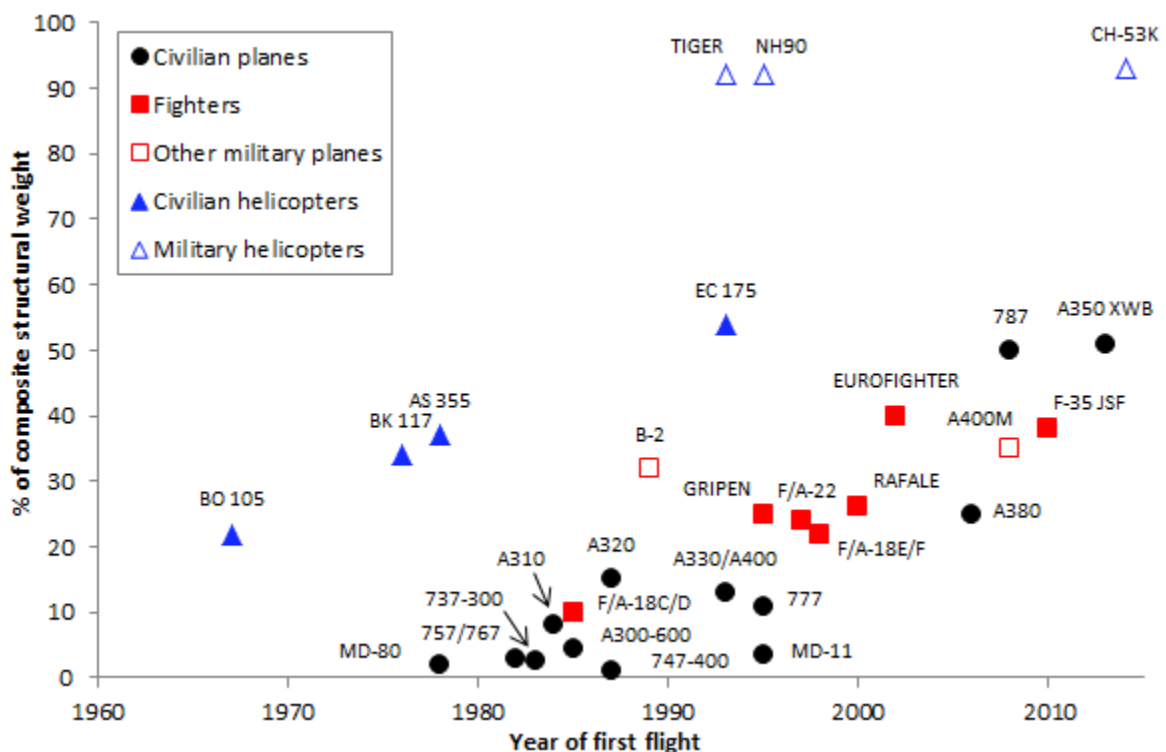


Figure 1: polymer matrix composite materials used as structural parts for different aircrafts.

Military aircrafts are often those which include the highest proportion of composite materials of their time, the exception being the last generation of civilian planes, with a composite structural weight over 50%. The reasons are the great potential of composite technologies (for instance with the stealth bomber B-10), the differences in certifications between civilian and military technologies and the military funding programs. Helicopters have applied composite technologies very early at a wide extent. This reflects different

dynamics in material development and certifications. In any case, the global trend for the use of these materials is an increasing curve.

Materials

Composite is a general designation for materials that are made from at least two non-miscible components. For a simple two components composite, one of the materials is the matrix, which keeps the whole part together and ensure the load transfer, the other one being the reinforcement, which brings interesting mechanical properties. Common matrices are made of metal, ceramic or polymer. Common reinforcement are based on metal, ceramic, various kinds of fibres or particles [1]. Matrix and reinforcement can be made from the same material, such as SiC/SiC or C/C composites in which fibres and matrix are respectively made of silicon carbide or carbon. In that case, strong properties result from the shape of the reinforcement. Generally, different materials are combined. Metal matrix composites (MMC) comprehend metallic or ceramic fillers or fibres, ceramic matrix composites usually comprehend ceramic fillers.

Composite materials considered here consist into a polymer matrix with long fibre reinforcement. This class of composite materials is well represented in modern aeronautic structures. There are two kinds of matrices used which are thermosetting polymers and thermoplastic polymers. Thermosets are low molecular weight species that create macro-molecular networks by reacting [2,3]. They are also commonly called *resins*, a term that can designate either the unreacted compounds or the reacted and solid polymer material. Thermoplastics are polymer species that have to be heated to reach a fluid state. Thermoplastic systems similar to thermosetting resins can also be found. They are based on reactive precursors of thermoplastics, easier to handle for material processing. Composite structural aeronautic parts are mainly designed from epoxy resins composites. Phenolic resins are also used for non-critical structures in passenger compartments according to their good fire resistance behaviour. Thermoplastic matrices are not as commonly used as thermosets, but some applications, such as the A400M cockpit floor, made of carbon fibre reinforced polyether ketone ketone (PEEK), have been successful.

Several kinds of fibres are used for such composite materials [2] (Figure 2). Carbon fibres are used for primary structures, glass fibres for floors and secondary structures. Radomes can be made with quartz or glass fibres, boron fibres can still be found in tail units of some old military aircrafts.



Figure 2: different types of fibres used as reinforcement for polymer matrix composites.
A) carbon ; B) E-glass ; C) aramid.

Properties of the composite are strongly dependent on the spatial orientation of fibres [2,4] (Figure 3). For laminates, in which fibres layers are stacked in plies, the stacking sequence determines the properties along spatial axis. For an unidirectional (UD)

laminate, every fibres have the same direction, resulting into very strong longitudinal properties at the cost of transverse performance. Unidirectional layers can also be stacked with different directions to distribute the reinforcement effect all over the plane. Such a sequence is called quasi-isotropic. Instead of unidirectional tapes, woven fibres can be used, this also lead to isotropic properties.



Figure 3: stack sequences. A) unidirectional ; B) quasi-isotropic ; C) fabrics.

More complex structures involving honeycomb-like designs are commonly employed [5]. Honeycomb cores made of aluminium, carbon or aramid fibres are held between two rigid sides that can be aluminium or composite slabs. In this later case, adhesion between the two sides and the core can be achieved by the resin impregnating fibres. Those panels, called sandwich structures, combine high strength with low density, *i.e.* used as lightweight materials.

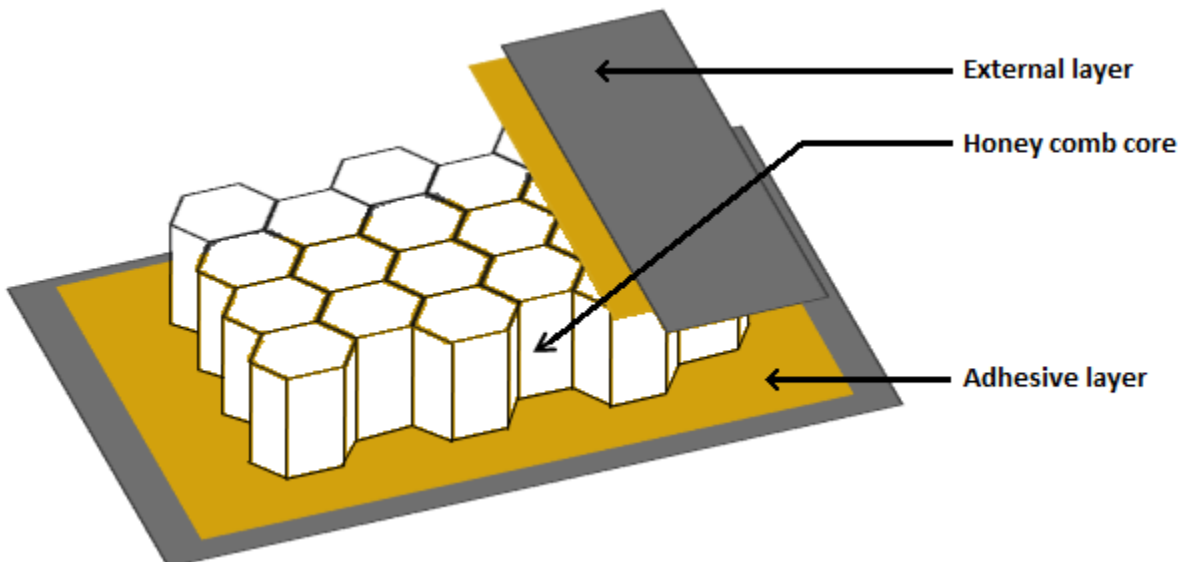


Figure 4: sandwich structure including a honeycomb core.

Desirable properties

The main advantage of using organic matrices composite materials, is that a reduction of weight can be achieved by replacing metallic parts. This usually requires to redesign parts, to adapt the geometry and the composite structure to the expected mechanical stresses.

Fabrication costs can also be reduced thanks to effective processes. Parts can be constructed very closed to their final shape, which can be very complicated. As a consequence,

leaving aside additive layer manufacturing (ALM), very few material is lost compared to classical machining of metallic parts (cut and drilling). It is also possible to design very large parts and panels, which removes some assembling steps.

More than low density, composite materials have desirable physical properties such as resistance to fatigue and lack of corrosion. Carbon fibres exhibit a negative longitudinal thermal expansion coefficient, whereas matrices usually exhibit a positive one. Adjusting the materials and the structure of the laminates, a nearly zero expansion coefficient can be obtained. This is particularly useful for spatial applications, where the range of temperatures of uses varies from -180°C to 160°C [6].

Limiting properties

The extensive use of composite materials in aeronautics has resulted in a mass production decreasing the cost of raw materials. Some high performance polymer matrices composites are still quite expensive because of raw materials prices and processing conditions (high temperature, long curing cycles...).

On several aspects, general properties of composite materials are highly limited. One of the most worrisome drawbacks is the quite low electrical conductivity through the thickness of laminates. Even if carbon fibres are prone to conduct charges, composite laminates are alternated layers including insulating polymers. As a result, a lightning strike generating local electrical charges would highly damage the material. Usually the low electrical conductivity comes with low thermal conductivity which is also a problem, most matrices having a limited range of compatible temperatures. For instance most epoxy-based composites are not used above 140°C. As for thermal ageing, water uptake alters the materials' properties. Polymers usually absorb small amounts of water from ambient atmosphere, this makes their attributes to vary until a saturation is reached. A massive exposition to water might deteriorate the composite part. Thermoset matrices often lead to materials sensitive to impacts. Lack of precaution while handling those parts may result to damaging such as delamination.

Other considerations appear during machining or assembling. Drilling holes is a needed operation for assembling and it causes huge loss of mechanical properties to composite panels. Galvanic corrosion is also a problem when using carbon fibres and aluminium [7]. Both materials have to be isolated from each other.

Going further with composite materials

Intrinsic limitations of current composite materials point out that innovation is a necessity if they were to be used to a larger extent. Thermal stability appears to be a crucial key to new applications. Different kinds of thermoset matrices, such as bismaleimides, cyanate esters, high temperature epoxies or benzoxazines, and high performance thermoplastic matrices, such as polyaryletherketones (PAEK) or polyimides (PI), have been developed for that purpose.

Design of materials integrating several functions (multi-functional materials) fits well composites because of their multi-material nature. This route of development relies on the necessity to simplify structures and to overcome limitations. Here, thermally stable

composites would enable to use them in hot parts of structures, without the constrain to add a thermal shield.

Bismaleimide resins

The US Air Force F-22 fighter jet is the first use of BMI resins at an industrial scale in aeronautics. Among the 24% of thermoset composite materials, half is made of carbon fibre with bismaleimide resins. These are mainly located on the wings. Some other kinds of composite parts have been designed, relying on the thermal stability of these resins. Aft flap hinge fairing structure of the US Air Force C-17 heavy carrier, that are located under the wings (Figure 5A) and the helicopter tail boom of the Bell 429 have integrated BMI composite structures. These are exposed to engine exhausts, so that service temperatures of 200°C are required. The nacelles surrounding engines are also exposed to high temperatures. On Airbus A330 aircrafts, BMI composites are used in the inner cowls of thrust reverser structures [8] (Figure 5B). On Airbus A340, the pre-cooler ducts in the inner fixed structure of thrust reverser are also made of BMI composites. Composites are also integrated directly on motors. In the SaM146, an engine for regional aircrafts, the mixed flow nozzle is mainly made of an epoxy/bismaleimide-based composite.

Bismaleimides are also used as adhesives with a high temperature stability for numerous aircrafts [8].

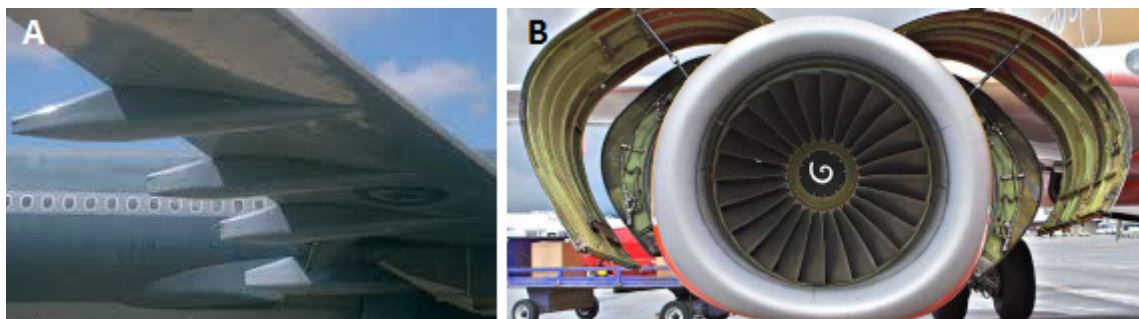


Figure 5: A) hinge fairing. B) open engine cowl, from [9].

By comparison with epoxy based composites, bismaleimides are not widely used in aeronautic primary structures (an exception being the supporting structure of auxiliary power units on Airbus planes). Those critical parts require materials that can sustain stresses, function that is usually fulfilled with carbon fibre-based composites, but also resist damaging and damage propagation. Bismaleimide resins are quite brittle materials and bismaleimide composites may experience micro-cracking during thermal aging [10–13]. There is therefore a need to improve their toughness to offer a wider range of high temperature applications.

Preamble to the study

Different aspects of bismaleimide-based composites for aeronautics will be addressed in the following study. The outline is the toughening of bismaleimide-based composites for structural applications, compatible with temperatures of uses up to 200°C. For this purpose, the thermoplastic modification strategy, successfully applied on epoxy-based composites, was selected.

Chapter 1 starts with a general introduction to bismaleimide resins composition and chemistry. The suitability for targeted high temperature applications is put to the test. This chapter then focuses on the complex chemistry of these systems. From discussions around the possible reaction paths, specific chemical mechanisms are identified. Differences with epoxy-based thermosets, the reference for structural aeronautics composites, arise, especially about their polymer network structure.

Chapter 2 is dedicated to obtaining controlled morphologies from thermoplastic-modified bismaleimide systems. The phase separation mechanisms are identified and morphologies are investigated at different scales. The influence of key parameters (chemical structure of thermoplastics, thermal history, blend composition...) are also discussed.

Chapter 3 focuses on the fracture behaviour of a neat bismaleimide matrix. A multi-scale approach is applied, investigating the classic macroscopic properties, down to micro-scale mechanisms, using an uncommon experimental observation procedure. The relationship between the thermoset network structure and the micro-scale fracture behaviour is also considered.

Chapter 4 deals with the fracture behaviour of thermoplastic-modified systems. The observation method introduced in chapter 3 is transposed to selected modified matrices developed in chapter 2. Different mechanisms are identified, depending on the type of modification. In a second part, failure of modified composites is investigated to determine the most effective toughening strategy.

Chapter 5 summarises the results from different parts of the study. Suggestions for further work are also detailed.

Chapter 1

Bismaleimide resins

After an introduction of the bismaleimide resins history and chemistry, main properties of a standard material will be looked over, under the scope of high temperature applications. The complex reactivity will then be examined, a chemical investigation highlighting key questions, answers being brought by physico-chemistry. The last part focuses on the consequences of the reaction path on the resulting polymer network structure.

1.1 Development of bismaleimide resins

1.1.1 Evolution of the BMI-based thermoset

Bismaleimide-based resins have been known for over 40 years and have come through three generations, each one with a different chemistry. Maleimides can be prepared from maleic anhydride (Figure 6A) or maleic acid (Figure 6B) reacting with a primary amine. The maleimide chemical function is a five-atoms ring containing a nitrogen atom, a carbon-carbon double bond conjugated with two carbonyl groups (Figure 6C). Using a primary diamine leads to a bismaleimide, bearing two maleimide groups (Figure 6D). In that case, the chemical backbone of the bismaleimide is determined by the original chemical structure of the diamine: carbon aromatic, ester or sulfone [14]. This kind of synthesis was changed rapidly because of low reaction yields. The use of organometallic catalysts made synthesis at an industrial scale possible [15].

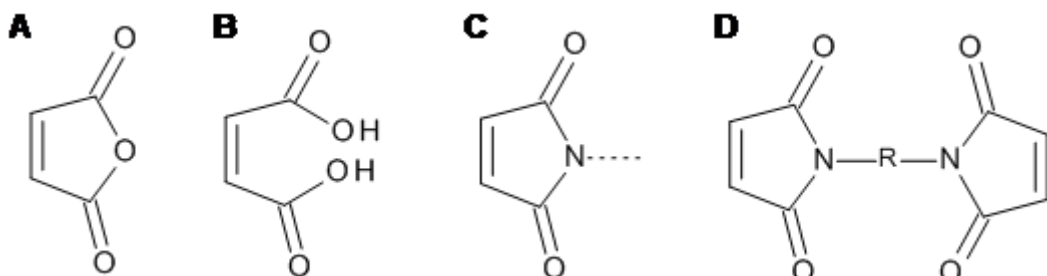


Figure 6: A) maleic anhydride ; B) maleic acid ; C) maleimide group ; D) bismaleimide.

Neat bismaleimides are considered as the first generation of bismaleimide resins. Above their melting point, which depends on their chemical backbone (usually above 150°C [14,16]), they undergo homopolymerization, leading to a cross-linked polymer. One of the main limiting property of these thermosets is their high brittleness, arising from a very high cross-link density. According to the low molecular mobility of polymeric segments and low free volume, only few molecular rearrangements are possible while damaging. As a consequence plasticity and deformation at break are very limited. To reduce this effect, chain extenders have been added to bismaleimides. These are simply co-monomers that increase the molecular weight between cross-links.

Bismaleimide/amine resins have also been employed [17,18] but the last generation of bismaleimide resins involves allyl chain extenders. They have been preferred to amines

for several reasons. To ensure high thermal properties, the polymer chain has to be rigid, the main factor being the chemical structure directly inherited from the monomers. So far, high performance polymers mainly rely on aromatic backbones, but aromatic amines needed for that kind of bismaleimide/amine resins are known to be health hazardous. Furthermore, from a practical point of view, bismaleimide/amine resins still have to be handled at quite high temperature. By comparison, bismaleimides can be solubilized in allyl derivatives, leading to a resin that can be handled in the same range of temperatures as epoxy resins. This is a major advantage not to change the industrial process.

Some other chain extenders were investigated such as bisallylspirolactam^[19], allyl chain extenders derived from epoxide (DGEBA)^[20], allyl liquid crystals^[21], N-allyl^[22], bithiols^[23], N-phenyl-maleimide^[24] or allylamine^[25,26]. Other strategies aimed at modifying the bismaleimide molecular structure by inserting polysiloxane chains^[27] or oxidazol cycles^[28].

1.1.2 A whole history of chemical investigation

Varma and Sharma have examined the curing of pure bismaleimides. These crystalline compounds melt at quite high temperatures (above 150°C) and react in the liquid state. Different monomers indeed behave that way but lead to very different reactivity. They found very different activation energies (based on a n^{th} order kinetic), which shows that the curing behaviour strongly depends on the chemical structure^[14]. Grenier-Loustalot and co-workers have studied the polymerization of sterically hindered bismaleimides. Melting and reaction temperatures both depend on the hindrance of the maleimide group^[29,30]. In this case, homopolymerization follows a radical mechanism (Figure 7). Hopewell and co-workers have examined the involved radical species, which depend on the maleimide chemical structure^[31]. By mixing different bismaleimides, Grenier-Loustalot and co-workers have observed eutectic blends^[32]. By using model compounds, they suggested a first-order kinetic for the homopolymerization^[33], which is consistent with results from an other study based on inverse gas chromatography analyses^[34].

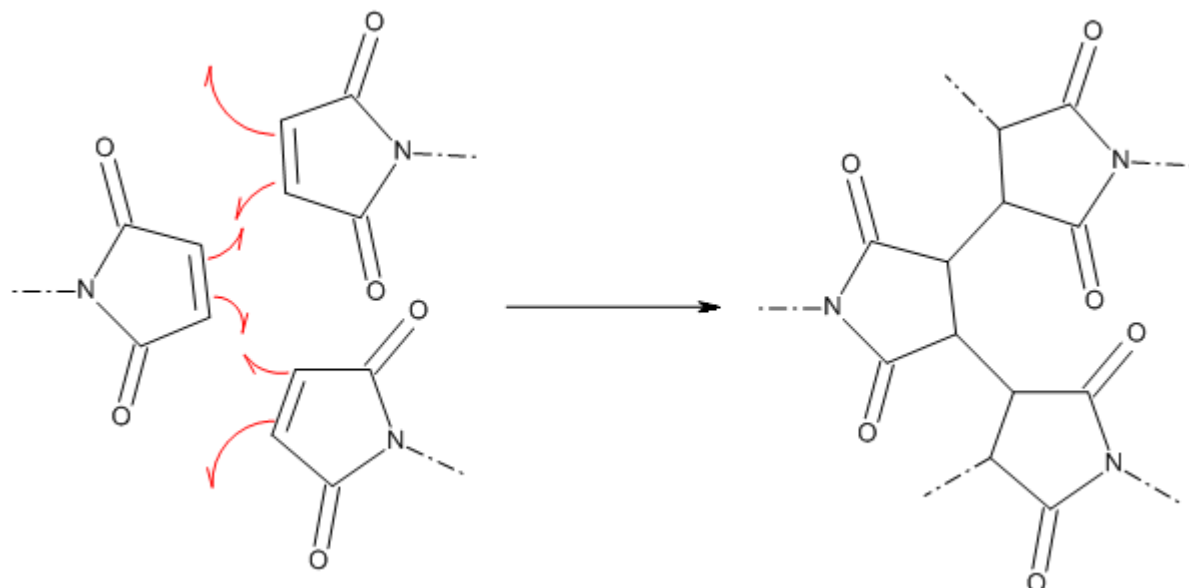


Figure 7: homopolymerization of maleimides.

Introducing amines brings new chemical paths as the amine reacts with the maleimide function through a Michael reaction (Figure 8). The maleimide homopolymerization does not occur at low reaction temperatures [17, 18, 35, 36]. BMI and amine steric hindrance makes both reactions more difficult [36]. The secondary amine formed by the Michael reaction is far less reactive than the primary one. Hopewell and co-workers have suggested that the reaction is first catalyzed by the primary amine then by the secondary amine, involving a BMI/amine complex formed from hydrogen bonds [17, 18]. This can be compared to Boey's kinetics study, which first step is autocatalytic [37]. Other mechanisms are suggested when the mixture is in solution, for instance a succinimide ring opening [38].

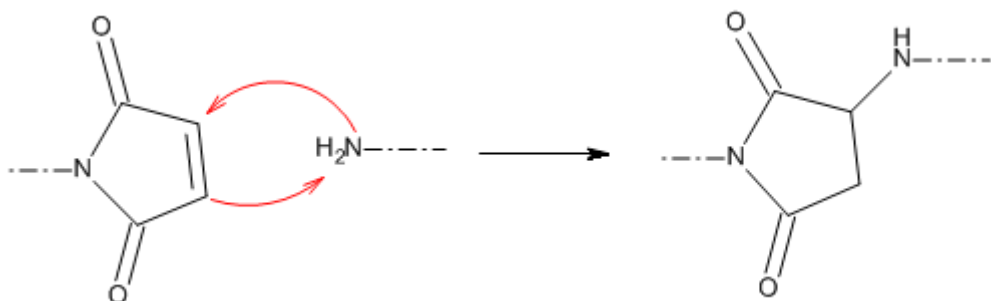


Figure 8: Michael reaction between a primary amine and a maleimide.

The third and last system considered here is bismaleimide blended with an allyl chain extender. In most of the studies, this system is a reactive blend based on 1,1'-(methyldi-4,1-phenyl)bismaleimide (BMI) and 2,2'-diallylbisphenol A (DBA) (Figure 9).

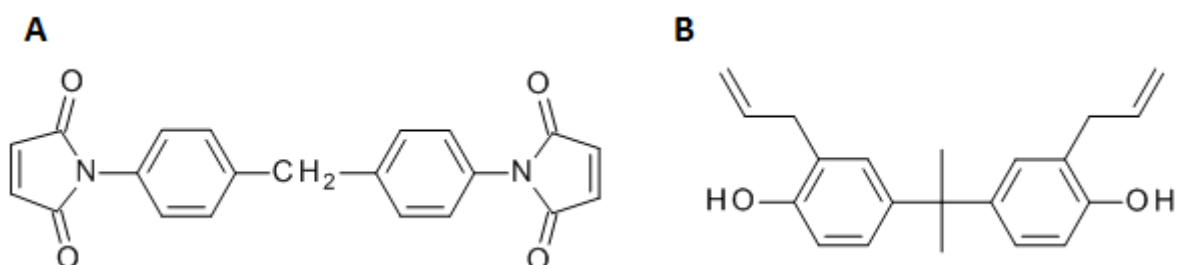


Figure 9: usual components of a bismaleimide resin. A) BMI ; B) DBA.

All studies agree on the fact that at low curing temperatures (<200°C), the predominant reaction is an ene-reaction (or Alder-ene reaction) involving an allyl double-bond and a maleimide double-bond. As a result a prepolymer is formed (Figure 10) [39-51].

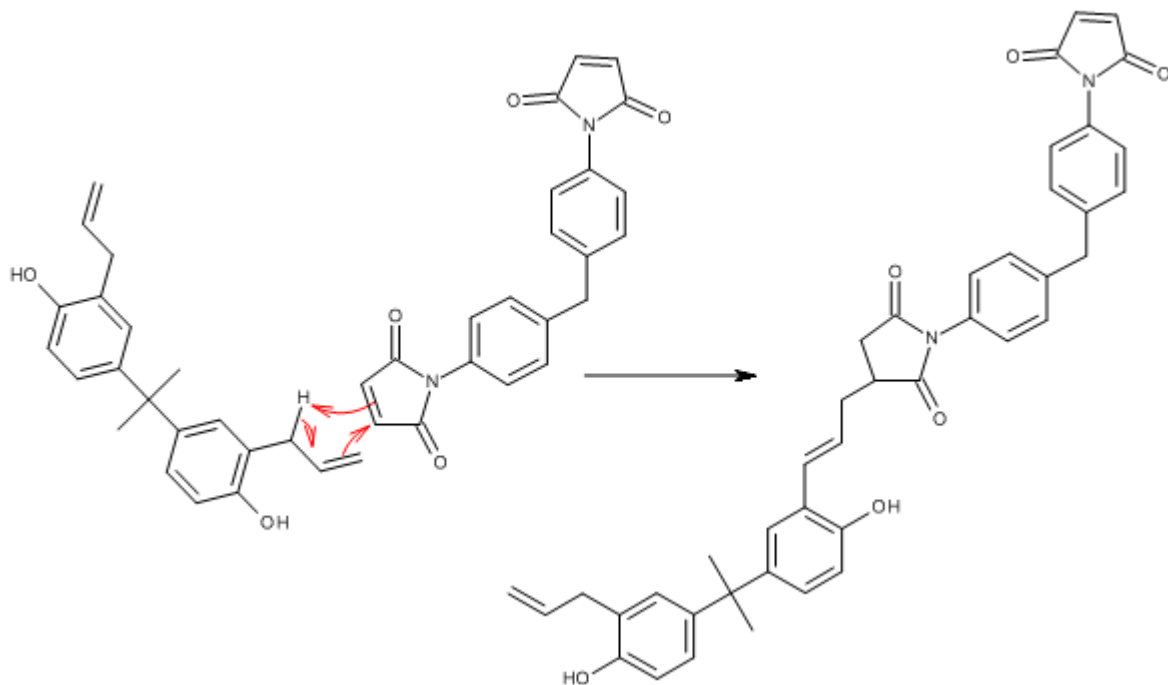


Figure 10: Alder-ene reaction between a diallyl and a bismaleimide.

The following steps of the curing mechanism are more controversial. Some studies using model compounds observe a Diels-Alder reaction followed by a re-aromatization between the maleimide and the prepolymer [39, 44] (Figure 11). A Wagner-Jauregg reaction is sometimes suggested in the same way [40, 50]. This reaction starts like a Diels-Alder reaction but leads to the formation of multiple rings on the same site. In the last curing steps, persistent DBA double-bonds can undergo further cross-linking [45].

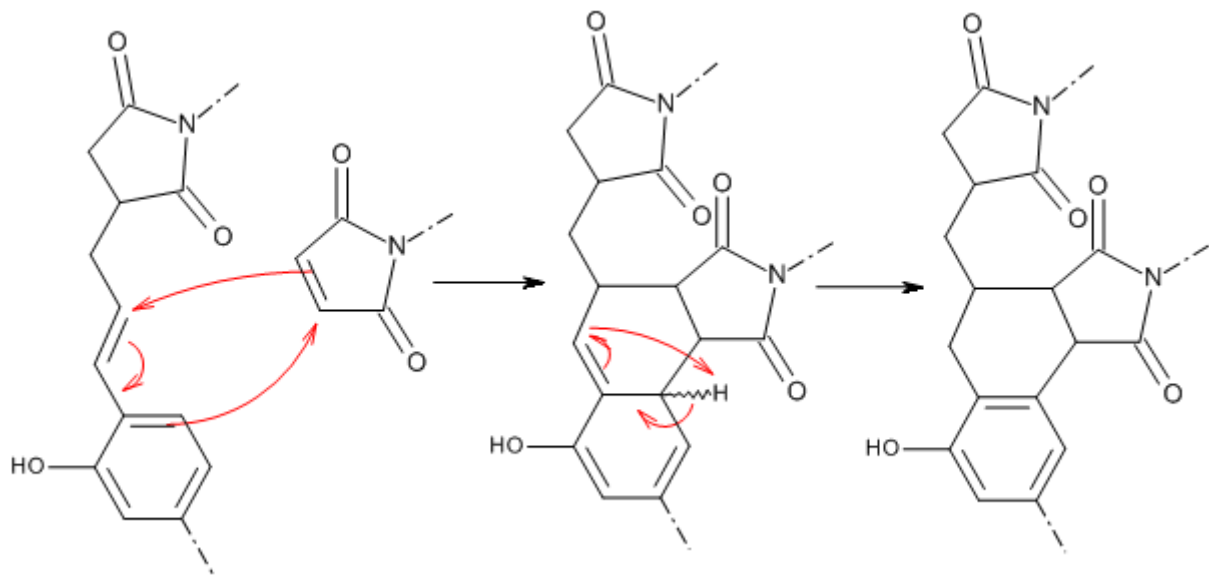


Figure 11: Diels-Alder reaction and re-aromatization of a maleimide group on the resulting product of an Alder-ene reaction between an allyl and a maleimide.

The other possible cross-linking process is the homopolymerization of the maleimide groups (Figure 7) [41, 43, 47, 51]. The maleimide/allyl copolymerization is predominant between 140°C and 200°C. Between 200°C and 250°C, the maleimide homopolymerization

takes place, but only if maleimide functions concentration is still high enough [41]. The Diels-Alder reaction which is observed in model systems is not taken into account because it cannot occur in highly cross-linked networks due to strong steric hindrance and the restricted mobility. The bismaleimide immediately reacts on the prepolymer central double-bond, this molecule creates free radicals from dissociation. The maleimide autocatalytic homopolymerization can then proceed [47,51].

Phenol groups do not seem to react with maleimide functions [39]. On the other hand, they can form ether bonds by dehydration [41,43,47–49,51]. This is observed for temperatures as low as 140°C and it does not happen for the allyl-phenol alone [41]. This process is limited by the vitrification of the system, and these bonds are not stable above 300°C [43]. Other studies suggest that instead of creating ether bonds, phenol groups turn into carbonyl groups [40,50]. This last point requires to lose the phenol ring aromaticity through multiple additions.

Considering this entire set of investigations, various methods and measurements were employed. Most of them use differential scanning calorimetry (DSC) to compare reactive systems and sometimes to determine parameters in kinetic models. When it comes to chemical analysis, ¹H-NMR, ¹³C-NMR, in solid and liquid states, IR and NIR spectroscopies, UV fluorescence and different kinds of chromatographies were involved. None of the works briefly described here were able to provide a fully satisfying reaction path for the maleimide/allyl-phenol blends. The first reason is the high number of possible reactions, the fact that they do not exclude each other and the probability of a dependency on the thermal history. The second reason is more practical, whatever the reaction path suggested, cross-linking leads to insoluble species that cannot be analysed by many spectroscopic and chromatographic methods. This is why many studies are based on model compounds: molecules that exhibit the same chemical groups but with a lower functionality to avoid cross-linking (mono-maleimides and mono-allyls). This strategy indeed enables the use of powerful analysis methods such as NMR in solution, but, as pointed out by Rozenberg and co-workers [47–49,51], steric hindrance and species mobility strongly differs from the real resins.

1.2 Experimental details

1.2.1 Selected materials

The selected monomers were already introduced: 1,1'-(methyldi-4,1-phenyl)bismaleimide and 2,2'-diallylbisphenol A (Figure 9). All monomers used came from a single batch.

Other molecules with a lower functionality were used for mechanistics investigations. Similar reactivity compared to the monomers is expected but leading to more soluble species, suppressing or delaying the cross-linking process. N-phenylmaleimide (MI, Figure 12A) and 1-allylphenol (AP, Figure 12B) copy the reactivity of BMI and DBA respectively. This model system approach has been widely used to study theses reaction paths [39,40]. 1-propenylphenol (PP, Figure 12C) is a mixture of *Z* and *E* isomers. It should partially reproduce the reactivity of the Alder-ene adduct (Figure 10).

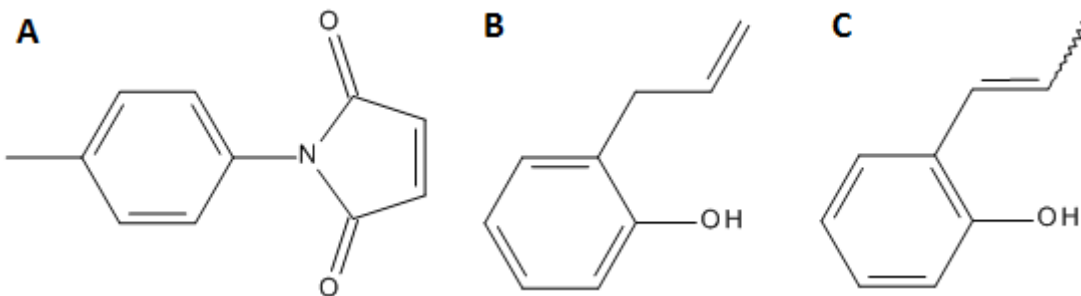


Figure 12: A) *N*-phenylmaleimide ; B) 1-allylphenol ; C) 1-propenylphenol.

To investigate the radical nature of chemical reactions, hydroquinone (HQ) was used as a radical inhibitor.

Main physical properties of these compounds are summarized in Table 1.

Compound	Molecular mass (g/mol)	Aspect	Melting point(°C)
BMI	358.35	yellow powder	156
DBA	308.41	yellowish viscous liquid	-
MI	173.17	green solid	90
AP	134.18	clear liquid	-
PP	134.18	clear liquid	-
HQ	110.11	white powder	172

Table 1: main properties of chemicals.

1.2.2 Experimental procedures

1.2.2.1 Mixing protocol

The standard procedure to prepare the resin was the dissolution of the solid part (BMI) in the liquid part (DBA). Monomers were heated at 130°C and the blend was stirred and degassed under vacuum until an amber clear mixture was obtained. This resin could be stored at low temperature (-18°C). The standard resin composition was chosen with a BMI/DBA molar ratio of 1.145:1. The standard curing cycle was: 3°C/min up to 180°C, isotherm for 1h ; 1°C/min up to 200°C, isotherm for 2h ; 1°C/min up to 250°C, isotherm for 6h. Cooling was performed around 1°C/min (supplier recommendations for aeronautic grade material).

Systems involving model compounds (MI, AP or PP) were prepared at room temperature simply by mixing components together. Dissolution of solids in liquids was achieved during the heating step before reaching the experiment temperature.

1.2.2.2 Spectroscopy

Infrared spectroscopy: Infrared analyses were carried out on an Agilent spectrometer. Powder samples were mixed and ground with potassium bromide. The powder was then compacted, under a 10 tons pressure, to form tablets. These specimens were placed in an infrared ray for transmission analysis. Soft samples were analysed between two potassium bromide tablets. If needed, these samples can be placed in a heating device, allowing

in situ analysis. Characteristic vibrations associated with chemical bonds can be identified with this spectroscopy, providing information on compounds molecular structure. Elongation, in plane and out of plane vibrations will be noted v , δ and ν respectively.

Nuclear Magnetic Resonance spectroscopy: Samples were solubilised in a deuterated dimethyl sulfoxide (DMSO-d6) at a concentration around 30 mg/ml. ^1H analysis was performed with a 32 scans sequence in a Bruker Avance apparatus (400 MHz). Characteristic frequencies can be identified, giving information on the chemical environment of protons. IR and NMR complete each other for chemical identification. For the sake of clarity, relevant NMR signals will conveniently be extracted from spectra, which will be displayed in appendix A.

1.2.2.3 Calorimetry

The Differential Scanning Calorimetry measurements were carried out with a Q2000 apparatus from TA Instruments. Baseline calibration was done with specific sapphires provided by the constructor. The constant cell calibration was done with indium before each set of measurements. Samples were prepared in aluminium pan capsules.

The sample and a reference pan capsule are maintained at the same temperature. The heat flow necessary to maintain this temperature is measured. The difference between the reference and the sample capsules account for the sample material alone (Φ_H). If a transformation is to be associated to an energy, the corresponding mass enthalpy is obtained by:

$$\Delta H_m = \frac{1}{m} \int_{t_a}^{t_b} \Phi_H dt$$

with m the sample mass, t_a and t_b the starting and ending time of the event. For a constant heating rate R_T , the time-temperature dependency is sometimes used:

$$\Delta H_m = \frac{1}{mR_T} \int_{T_a}^{T_b} \Phi_H dT$$

1.2.2.4 Rheological analysis

Rheology: The rheology of the uncured resins has been done with an AR2000EX apparatus from TA instruments. The resin samples were softened by heating and set between two aluminium plates. The lower plate is fixed whereas the upper one sets up an oscillation or a flow. The gap between the two plates (the resin layer thickness) was forced to be constant and equal to 0.5 mm. For isothermal curing conditions, the temperature was set to the aimed one as quickly as possible (around 20°C/min). Experiments were carried out with 40 mm diameter parallel plates.

In an oscillatory test, the elastic and dissipative contributions to shear are measured:

$$G' = \frac{\tau_0}{\gamma_0} \cos(\delta)$$

$$G'' = \frac{\tau_0}{\gamma_0} \sin(\delta)$$

γ_0 is the angular strain amplitude, τ_0 the maximum shear stress and δ the phase shift between oscillatory strain and stress. γ_0 is chosen to remain in the linear visco-elastic domain of the thermoset. In this domain, G' and G'' do not depend on the shear strain amplitude. When it comes to cross-linking, materials evolve from liquids to gels (or soft solids) with a significantly reduced linear domain. Consequently, the previous relations are expected to become invalid above a certain curing extent.

Dynamic Mechanical Analysis: The behaviour of solid samples was studied by dynamic mechanical analysis. Single cantilever tests were carried out with a Q800 apparatus from TA Instruments. The samples $(48(\pm 0.5) \times 10(\pm 0.5) \times 2(\pm 0.1) \text{ mm}^3)$ were cut with an Isomet 5000 linear precision saw from Buehler with low cutting speed (between 1.2 and 2 mm/min) and moderate rotation speed (around 2800 rpm) to avoid burning the surface. The gauge length in clamp is 17 mm.

Three point bending samples were designed the same way with the following dimension: $60(\pm 2) \times 10(\pm 0.5) \times 2(\pm 0.1)$, the gauge length being 50 mm. This test geometry reduces the shear component of the applied stress because the sample edges are not clamped but lie on free cylinder paws. However, modulus values are not as accurate as what would be obtained with traction experiments. Here, oscillatory tests were performed at 1 Hz with a maximum deformation of 0.1%. With this kind of experiment, the storage (E') and loss (E'') moduli are distinguished:

$$E' = \frac{\sigma_0}{\epsilon_0} \cos(\delta)$$

$$E'' = \frac{\sigma_0}{\epsilon_0} \sin(\delta)$$

ϵ_0 is the strain amplitude, σ_0 the maximum stress and δ the phase shift between oscillatory strain and stress ($\tan(\delta)$ being the loss factor). For a pure elastic solid, no phase shift would theoretically be observed ($\delta = 0$). The Young modulus is usually approximated by the DMA elastic modulus as long as energy dissipation can be neglected. E' accounting for the energy conservation and E'' for dissipation, the approximation becomes: $E = E'$ for $E'' \ll E'$ (δ close to 0).

The oscillatory frequency will be noted f and the strain amplitude ϵ_0 . This last parameter is chosen to remain in the linear visco-elastic domain of the material.

1.2.2.5 Degradation

The thermal decomposition of various samples was followed with a Q500 apparatus from TA Instruments. Samples were placed in a platinum crucible and could be heated under air or nitrogen atmosphere up to 900°C. The heating rate is chosen at 10°C/min.

1.3 Thermal properties

High temperature applications require some thermal performance on very basic material properties. Mechanical properties have to keep up when increasing the temperature (remain constant in ideal case). Moreover, the material should not suffer alteration due to long time exposure at high temperature and stress. These alterations can take many forms

such as oxidation, hydrolysis, creep or micro-cracking and often pair up. This section reviews the main properties of the BMI/DBA standard resin, showing its compatibility with the targeted temperature range.

1.3.1 Thermal degradation

Thermogravimetric analysis brings quantitative information about the weight loss of a material during its thermal degradation. As a consequence chemical transformations that do not lead to a gas emission cannot be detected by this method. This kind of experiment is also sensitive to the surface-to-volume ratio of samples that determines the outer surface area (influencing the oxidation and gas release kinetics). With heterogeneous samples such as composite laminates these effects are amplified because the nature of surfaces depends on the sampling procedure [11, 52].

Both the cured and uncured reactive systems were analysed by thermogravimetry under air (Figure 13). Similar features are observed with an onset of weight loss close to 410°C and a maximum weight loss rate close to 440°C. Above 600°C, the weight loss rate remains constant with similar values for both kinds of samples. The main difference is located in the temperature range under 200°C, *i.e.* the curing temperature range. Uncured samples usually loss around 5% weight before the main degradation (this also explain why the initial weight on Figure 13B is not 100%, the sample being cured directly in the TGA crucible). This effect is often attributed to the phenol groups reactivity and will be discussed in the following section.

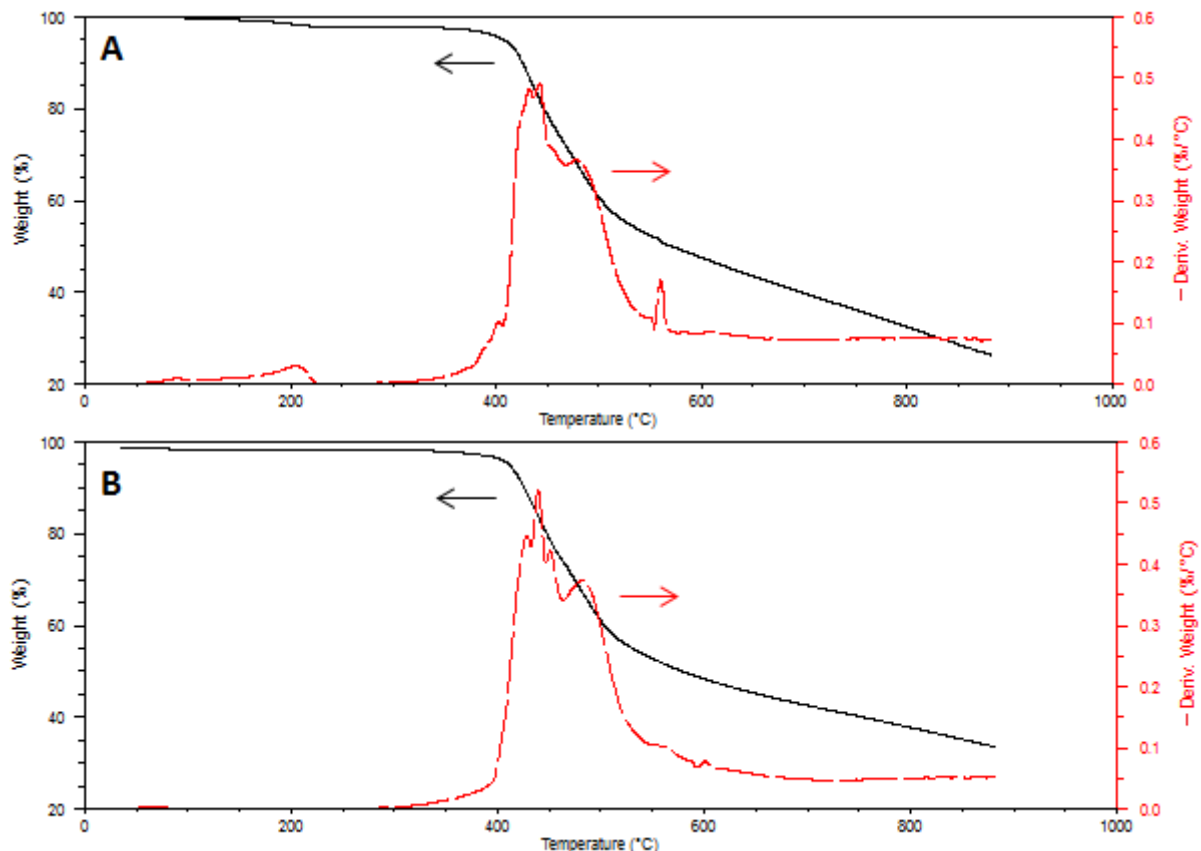


*Figure 13: weight loss of the standard BMI/DBA resin heated at 10 °C/min under air.
A) uncured ; B) cured.*

The cured system starts loosing significant weight at 400°C, which is in accordance with the targeted applications requirements.

1.3.2 Mechanical properties preservation

Three point bending DMA was used to follow the evolution of the modulus on a wide temperature range, each point being measured after reaching temperature equilibrium (Figure 14). Between 40°C and 260°C, E'' is lower than E' by more than an order of magnitude, E' will then be considered as an estimation for E . At 200°C, E' has decreased by nearly 25% but it still remains close to a few GPa, which is the typical value for aeronautic thermosetting resins.

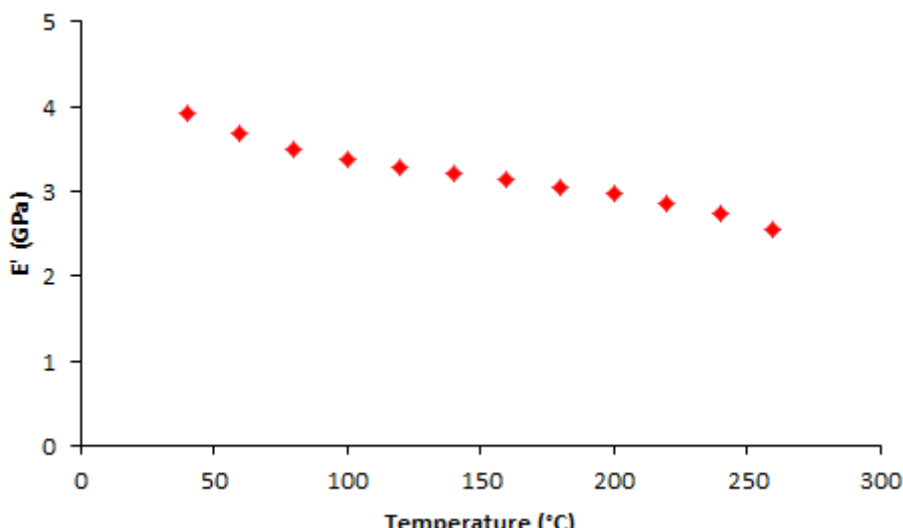


Figure 14: storage modulus of the standard BMI/DBA resin at different temperatures.

In composite materials the interesting mechanical properties such as the Young modulus are mainly inherited from the carbon fibres. The effect of such a modulus variation can be estimated with a simple calculation, that leads to a modulus loss of only 0.3% in the fibre direction (see Appendix B for calculation details).

1.3.3 Thermomechanical behaviour

DMA also gives a full overview of the material behaviour while increasing the temperature. For samples cured with the standard cycle, the α -relaxation is measured at 310°C, the E'' peak at 300°C and the onset of the E' decrease at 290°C (Figure 15). Correspondence between the α -relaxation and the glass transition gives a glass transition temperature (T_g) around 300°C. The β -relaxation is wide, as it can be seen on the inset of Figure 15 it ranges from -50°C to 200°C. This suggests that several kinds of chain and side groups relaxations are involved. From a practical point of view, targeted service temperatures are contained within the β -relaxation domain.

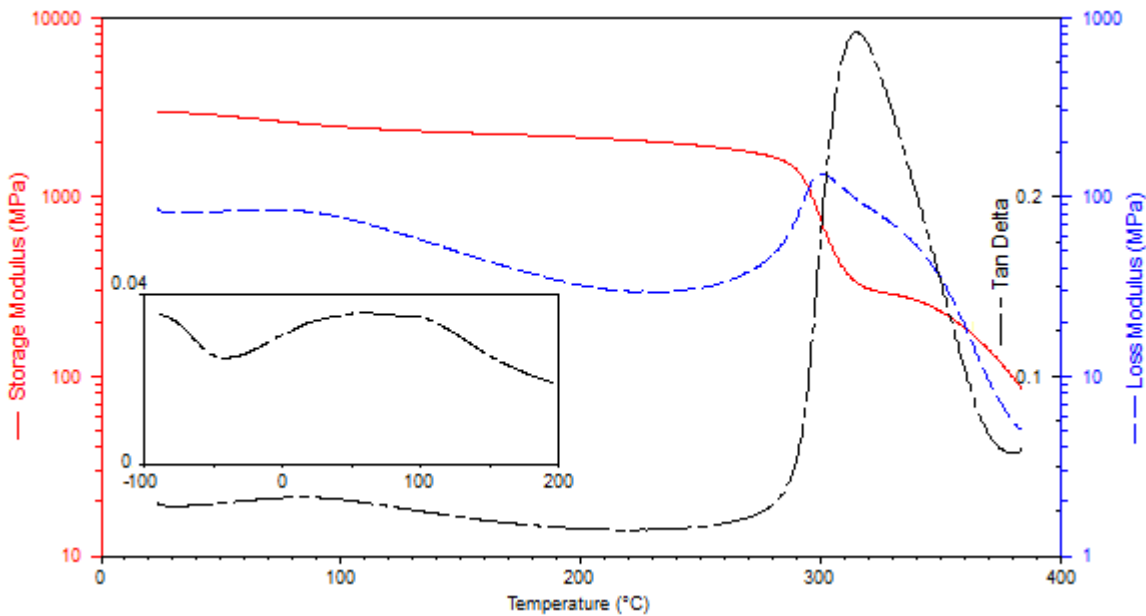


Figure 15: Dynamic Mechanical analysis of the cured BMI/DBA system. $3\text{ }^{\circ}\text{C/min}$, $f=1\text{Hz}$, $\epsilon_0=0.1\%$.

Above the glass transition temperature, a rubbery plateau is expected. In this state, the material is a soft elastic solid. In this case, the storage modulus decreases quickly after the glass transition without a real plateau. In the meantime, the loss modulus relaxation peak remains quite broad. A decrease zone of E' is usually encountered when the material starts to flow, which is the case for a thermoplastic whereas it cannot occur for a polymer network, due to chemical bonds between the polymer chains. This points out a probable evolution of the material at high temperatures, where a decrease of E' could be correlated with a thermal degradation.

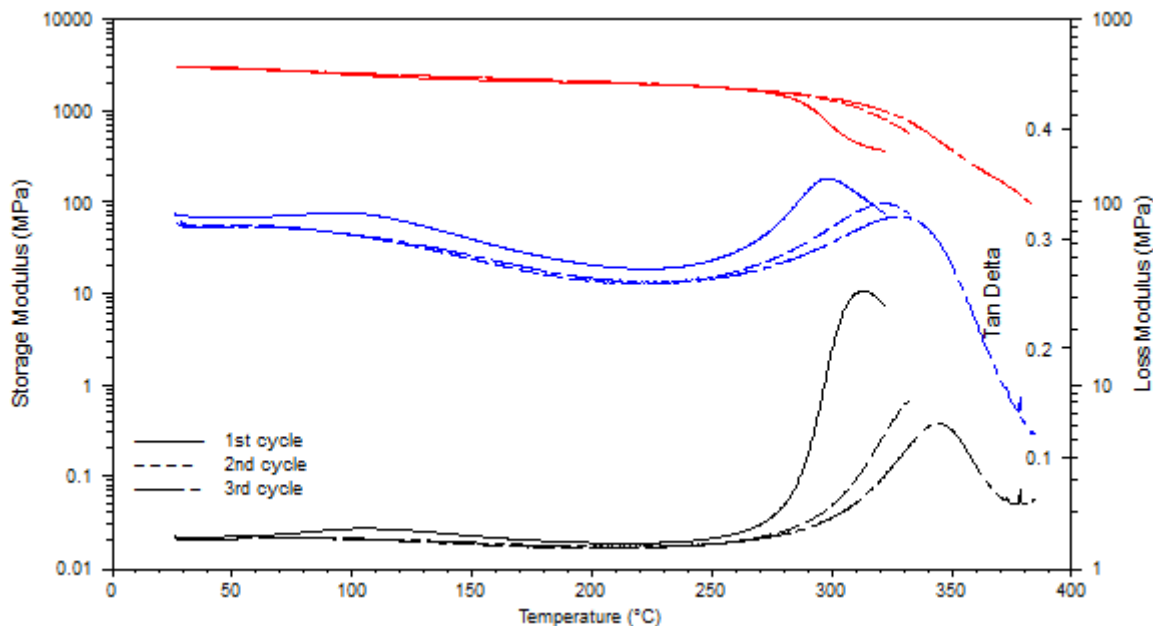


Figure 16: Dynamic Mechanical analysis of the cured BMI/DBA system with successive cycles. $3\text{ }^{\circ}\text{C/min}$, $f=1\text{Hz}$, $\epsilon_0=0.1\%$.

Successive heating ramps were applied to the same sample ; the first ramp stops immediately after the glass transition ; the second ramp stops to a slightly higher temperature

and the latter one at 400°C. It can be seen on Figure 16 that after each heating phase, the glass transition is shifted to higher temperatures. Once the material is softened, unreacted chemical functions gain enough mobility to carry on additional cross-linking which considerably increases the T_α (here by 50°C). Visual control revealed slightly blackened samples after the first two heating cycles. After the last cycle, samples are ash-black, suggesting occurrence of oxidation.

The BMI/DBA resin cured with the standard cycle appears to undergo chemical transformations above its T_g region. First a post-curing phase is observed, significantly increasing the T_g , similarly to epoxy-based systems [53]. At higher temperatures oxidation seems to occur, this event is correlated with the very beginning of the weight loss during thermal degradation (between 300°C and 350°C on Figure 13). The decreasing elastic modulus above T_g can be a consequence of oxidation. These two alterations of the material had been attributed by Morgan and co-workers to a competition between cross-linking by phenol forming ether bonds and ether bonds breakage because of thermal instability (Figure 17A) [43]. For degradation at higher temperatures, Torrecillas and co-workers suggested breakage of cross-link points through formation of isocyanate species (Figure 17B).

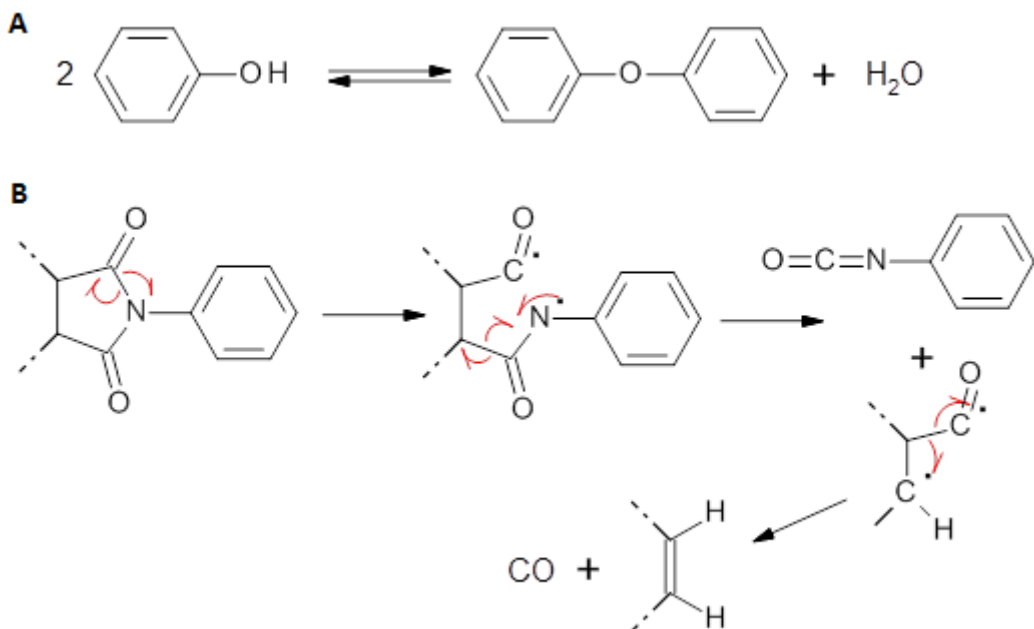


Figure 17: suggested degradation mechanisms in a bismaleimide resin. A) ether bonding/debonding ; B) cross-link degradation.

1.3.4 Conclusion

The BMI/DBA system exhibits a high T_g close to 300°C and is thermally stable up to 200°C, chemically and mechanically. Alteration occurs above T_g . An evolving material is not desirable for aeronautics perspectives, but this bismaleimide resin starts to be altered nearly 100°C above the maximum targeted service temperature. By comparison epoxy composites used up to 100°C usually exhibit a T_g around 200°C, *i.e.* the same gap is met here. Nevertheless, possible chemical transformations have to be kept in mind for long term ageing.

1.4 Reactivity

1.4.1 Phenol reactivity

A Michael addition between phenols and maleimides has been observed at moderate temperature using a base to help deprotonation of the intermediate adduct [54]. The reaction is still possible without any base, at higher temperature. Nevertheless, Zahir and co-workers did not observe such adducts in a BMI/DBA reactive blend [39]. As pointed out previously, the main phenol reactivity is here considered to be etherification through dehydration [41, 43, 47, 51]. The initial weight loss observed by TGA can be attributed to water elimination. Mijović and Andjelić found that this etherification does not occur when the bisphenol (DBA) is heated alone. Comparatively, TGA of DBA did not show such an initial weight loss. The occurrence of such a condensation reaction is not desirable because water would act as a plasticizer, lowering T_g , if it remained trapped within the polymer network. In case of evaporation, porosity could also be generated with highly harmful consequences for composite structures.

Morgan and co-workers found this reaction to be partial and limited by vitrification and ether bonds unstable above 350°C [43]. They followed the ether bond appearance by IR spectroscopy with a characteristic C–O band at 1183 cm⁻¹. It was not possible to reproduce such observations (see Figure 18), as using *in situ* measurements does not allow a sufficient accuracy, and because several absorption peaks are overlapping in this area. In fact, the maleimide C–N–C band can still be distinguished at 1150 cm⁻¹ but the succinimide C–N–C band, located at 1185 cm⁻¹ [30], is expected to increase during the Alder-ene reaction.

1.4.2 Maleimide/allyl reactivity

1.4.2.1 Alder-ene reaction

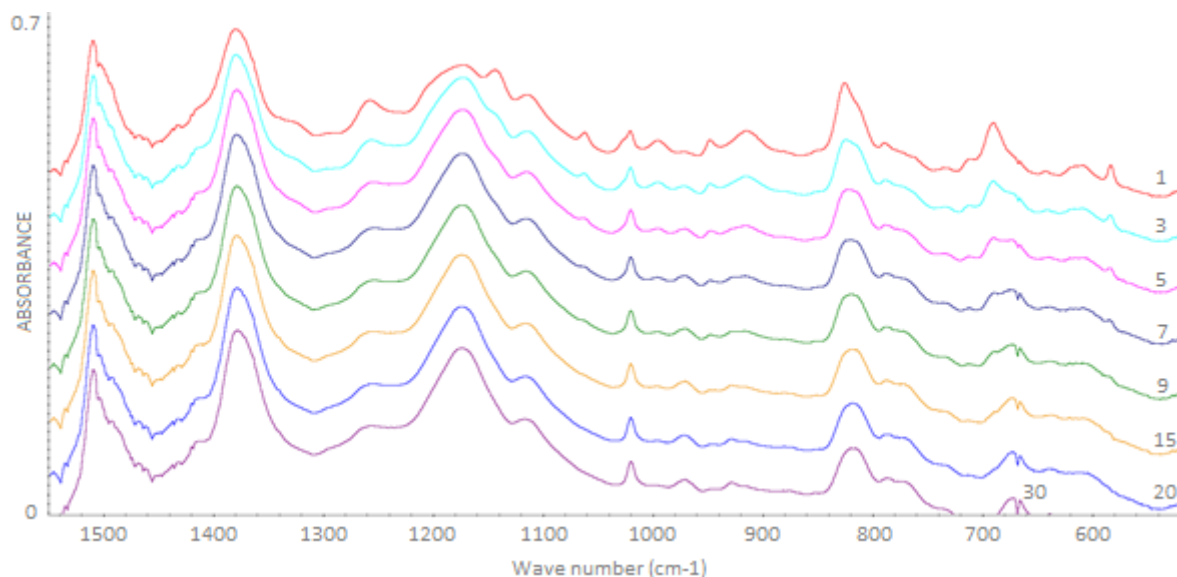


Figure 18: infrared spectra of a BMI/DBA 1:1 model blend during curing at 150 °C. Curves obtained after 1, 3, 5, 7, 9, 15, 20 and 30 min, from up to down.

The first step of the reaction path, the Alder-ene reaction, involves the consumption of allyl and maleimide functions with the creation of succinimide rings. These were evidenced

with IR spectroscopy on a BMI/DBA model system during curing at 150°C (Figure 18). Among the disappearing peaks, allyl C=C–H (δ) and C=CH₂ (ν) are located at 692 cm⁻¹ and 915 cm⁻¹ respectively. The maleimide C=C–H (δ) and C–N–C (ν) vibrations are measured at 827 cm⁻¹ and 1150 cm⁻¹ respectively. The succinimide C–N–C (ν) expected at 1185 cm⁻¹ brings its contribution to the broad band around 1180 cm⁻¹.

Further investigations were carried out with model compounds with the same maleimide to allyl proportions as in the standard BMI/DBA system consider a representative reactivity. NMR attributions for starting materials can be found in Table 2.

Compound	Attribution	Signal (ppm)	Shape	Integration
BMI/MI	Maleimide double bond	7.15	s	4/2H
BMI	Central methyl	4.04	s	2H
MI	Methyl	3.32	s	3H
DBA/AP	Allyl –CH=	5.9	m	2/1H
DBA/AP	Allyl =CH ₂	4.95	m	4/2H
DBA/AP	Allyl –CH ₂ –	3.2	d	4/2H
DBA/AP	Phenol	9.05	s	2/1H
DBA	Central methyl	7.36	s	6H
PP	Propenyl –CH=	6.45-6.6	d	0.15+0.85H
PP	Propenyl =CH–	5.7-6.2	m	0.15+0.85H
PP	Propenyl –CH ₃	1.8-1.85	d	0.45+2.55H
PP	Phenol	9.4	s	1H

Table 2: NMR signals for monomers and model compounds (s=singlet, d=doublet and m=multiplet). From [29, 30, 32, 36, 55–57].

Model compounds mixtures were heated in isothermal conditions and sampled at different curing times. Chemical transformations in a MI/DBA blend cured at 175°C were observed by ¹H NMR (Figure 19).

Characteristic resonances show the progressive consumption of allyl, turning into the Alder-ene adduct. Next to the central proton of the DBA allyl group, a new multiplet similar in shape appears around 6.16 ppm. This one is attributed to the central proton of propenyl chain bonding the succinimide ring with the phenol ring (c). At 7.25 ppm a signal that might be a doublet also appears. Proximity to the maleimide and aromatic peaks made proper integration impossible, it is attributed to the –CH= next to the phenol ring side (b). The remaining propenyl –CH₂– can be seen as a shoulder of the water peak at 3.3 ppm (d). The corresponding phenol is located at 9.38 ppm (a). These attributions are consistent compared to the propenylphenol spectrum (see Table 2).

The succinimide protons can be evidenced at 2.95 ppm and 2.65 ppm (e and f). Integration gives values slightly too high compared to the propenyl chain. If succinimide ring formation by other means, such as homopolymerization, is not totally excluded, the proximity of strong signals from water (3.3 ppm) and DMSO-d6 (2.5 ppm) is expected to increase the integral value.

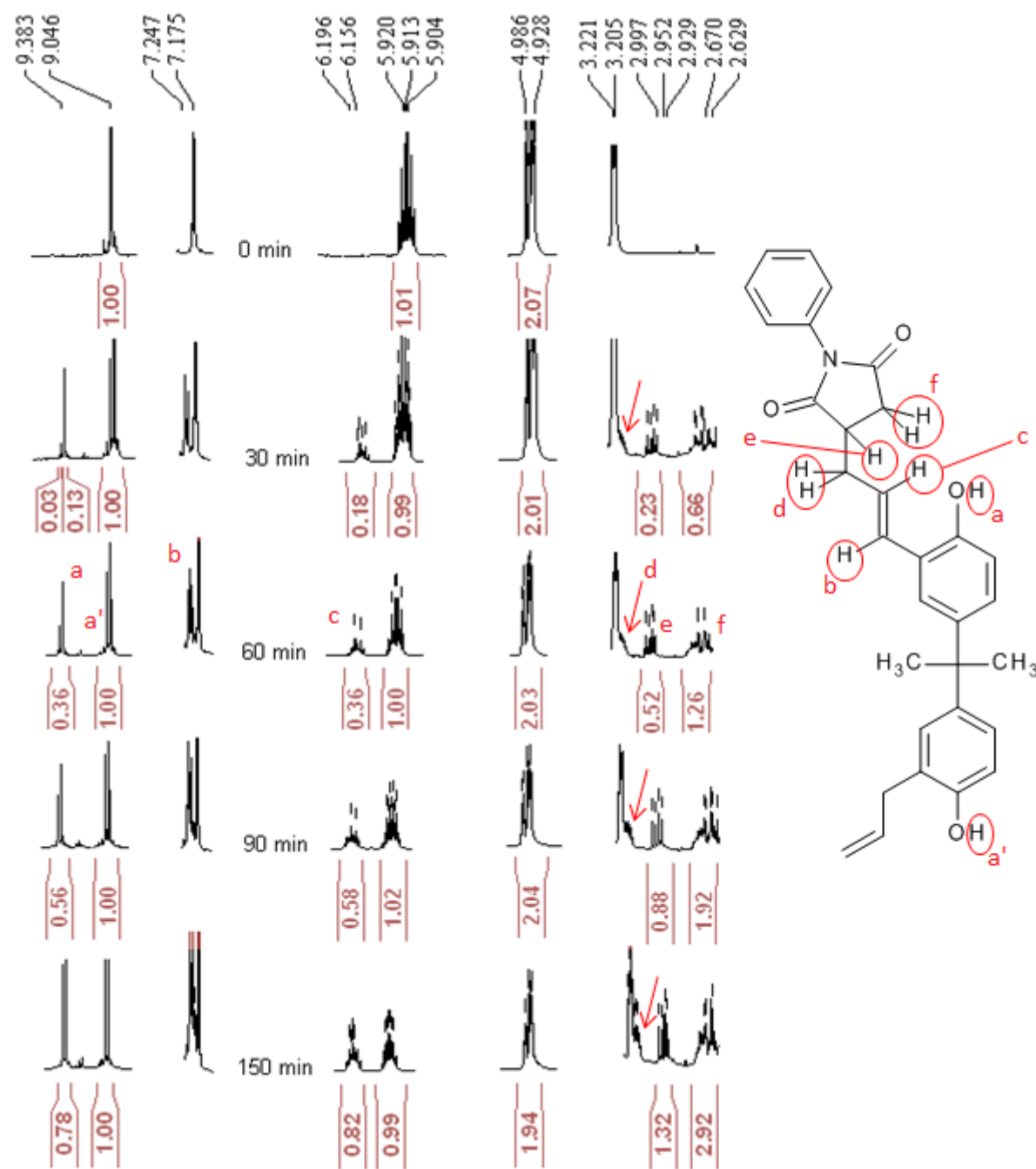


Figure 19: resonance signals extracted from NMR spectra of a MI/DBA 2.28:1 model systems cured at 175 °C, at different reaction times. DMSO-d₆, 400 MHz.

The same experiment carried out with BMI/AP and MI/AP blends lead to similar observations.

Most studies consider 200°C to be a transition temperature from which new reactions may occur. Curing model systems blends at 200°C confirmed that the Alder-ene reaction is still observed. Figure 20 shows the characteristic =CH– and phenol NMR signal of the Alder-ene adduct for the three model systems.

As expected, at this temperature, reactive systems become insoluble much more quickly than at 175°C. Moreover comparing Figure 19 with Figure 20, the Alder-ene adduct proportion appears to be slightly higher for the MI/DBA mixture cured at 175°C.

This suggests a consumption of the adduct, leading to insoluble species, that were not analysed by ^1H NMR. The Alder-ene reaction alone cannot explain this phenomenon.

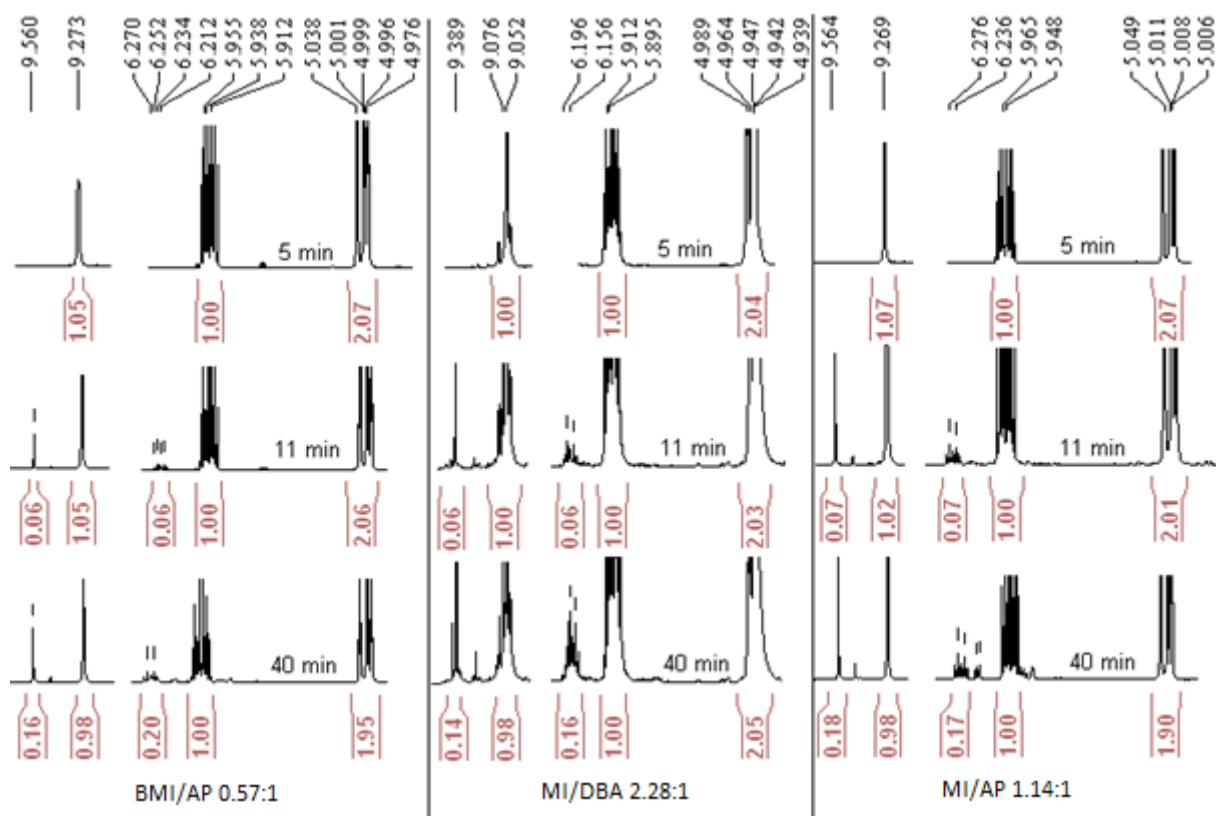


Figure 20: resonance signals extracted from NMR spectra of BMI/AP, MI/DBA and MI/AP model systems cured at 200 °C, at different reaction times. DMSO-d6, 400 MHz.

1.4.2.2 Addition reactions

DMSO-d6 was preferred as NMR solvent to deuterated chloroform because it offers a better solubility to the analysed reaction products. Nevertheless insoluble species are always formed, probably because of branching. As mentioned previously, solid state analysis from the literature did not bring a full comprehension of the cross-linking process.

To get a better understanding of the possible reactivity of maleimide functions with the Alder-ene adduct, propenylphenol (PP) was used. Zahir and co-workers had already suggested that maleimides have a higher reactivity with propenyls than with allyls^[39]. This was confirmed by the impossibility to use the same curing conditions for BMI/PP model systems as for BMI/AP. At 175°C, BMI/PP becomes a glassy hard solid in less than five minutes whereas the BMI/AP mixture can still be solubilised after more than two hours. Consequently, for further studies, the curing temperature was lowered at 150°C.

Analysis of such a BMI/PP 1:2 system leads to the same difficulties as depicted in the literature. Difficult to solubilise and to separate, reaction products were not identified precisely. It can be seen on Figure 21 that products are only traces to the initial compounds. In these conditions, integration is nearly irrelevant and peak shapes hard to determine. Nevertheless different molecular structures attributions are suggested. The Wagner-Jauregg product is suggested by Reyx and co-workers^[40]. The Diels-Alder adduct

is also quite suitable and suggested by both analysis from Reyx and Zahir [39, 40]. The polymer form is not to exclude [58], protons from the carbon backbone would be located under the PP methyl protons. Each of these compounds leaves several unidentified peaks that can come from a mixture or from impurities. The presence of a single new methyl signal (doublet o) and the apparent change in the isomeric ratio (based on the methyls) suggests a preferential addition reaction such as the Diels-Alder one.

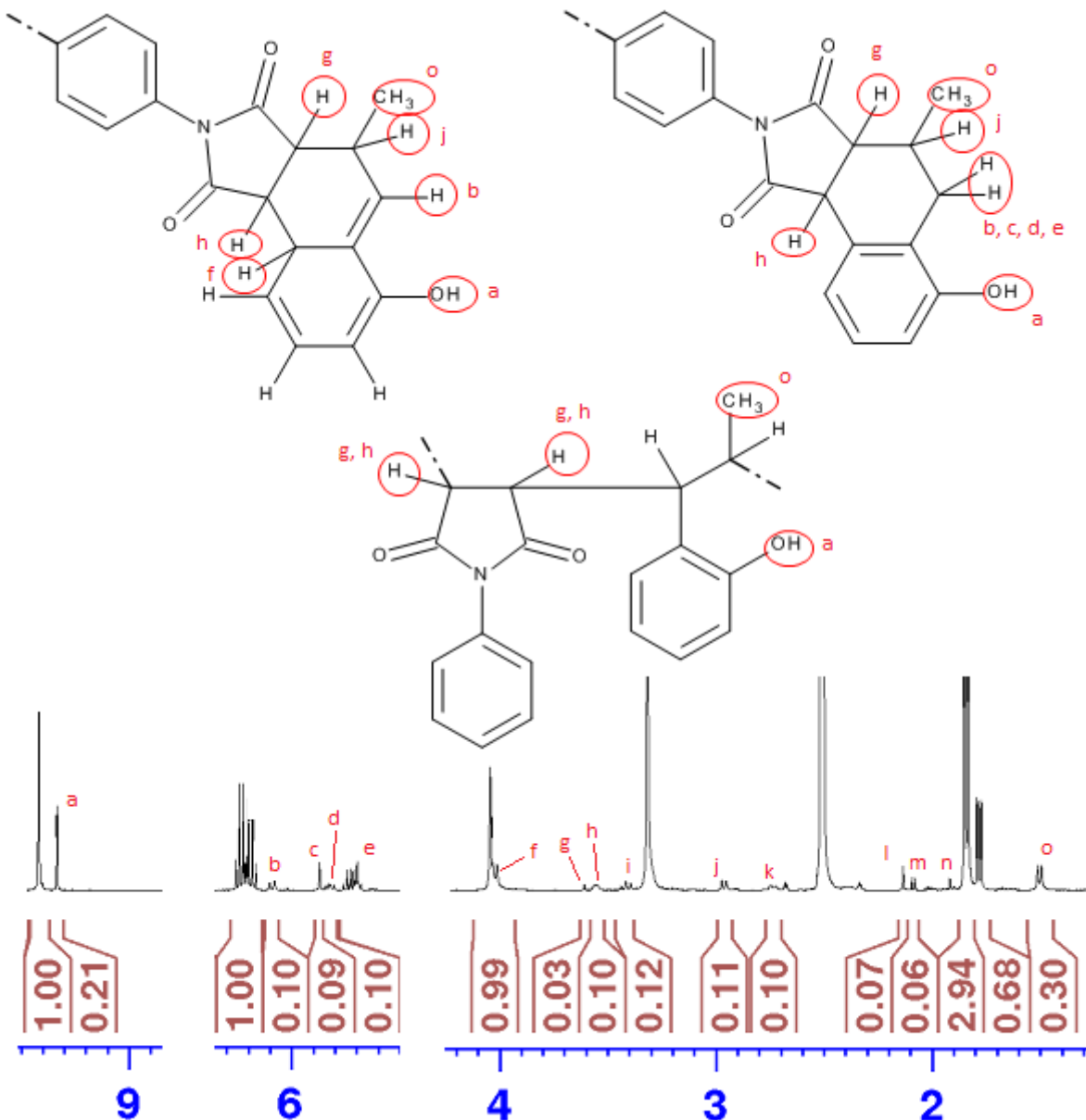


Figure 21: resonance signals extracted from the NMR spectrum of a BMI/PP 1:2 mixture after 6 min curing at 150 °C. Attribution suggestions for different adducts.
DMSO-d₆, 400 MHz.

Remark: the g and h signals on Figure 21 are also found on NMR spectra from long time curing or high temperature curing of BMI/AP, MI/DBA and MI/AP systems.

Thermal analysis of BMI/AP/PP systems, varying from AP:PP proportion and keeping the maleimide/(allyl + propenyl) ratio constant, gives more information on the allyl/propenyl competing to react with maleimide functions (Figure 22). Three main reaction peaks are evidenced around 115°C, 160°C and 220°C. The latter enthalpy peak is

identified as BMI homopolymerization whereas the central peak stands for the Alder-ene reaction. Both can be found on a BMI/DBA blend thermogram as displayed on Figure 23 (for a better comparison, the BMI:DBA proportion was chosen at 1:1 and BMI was not solubilised in DBA before the experiment). The lower temperature enthalpy peak stands for the maleimide/propenylphenol reaction.

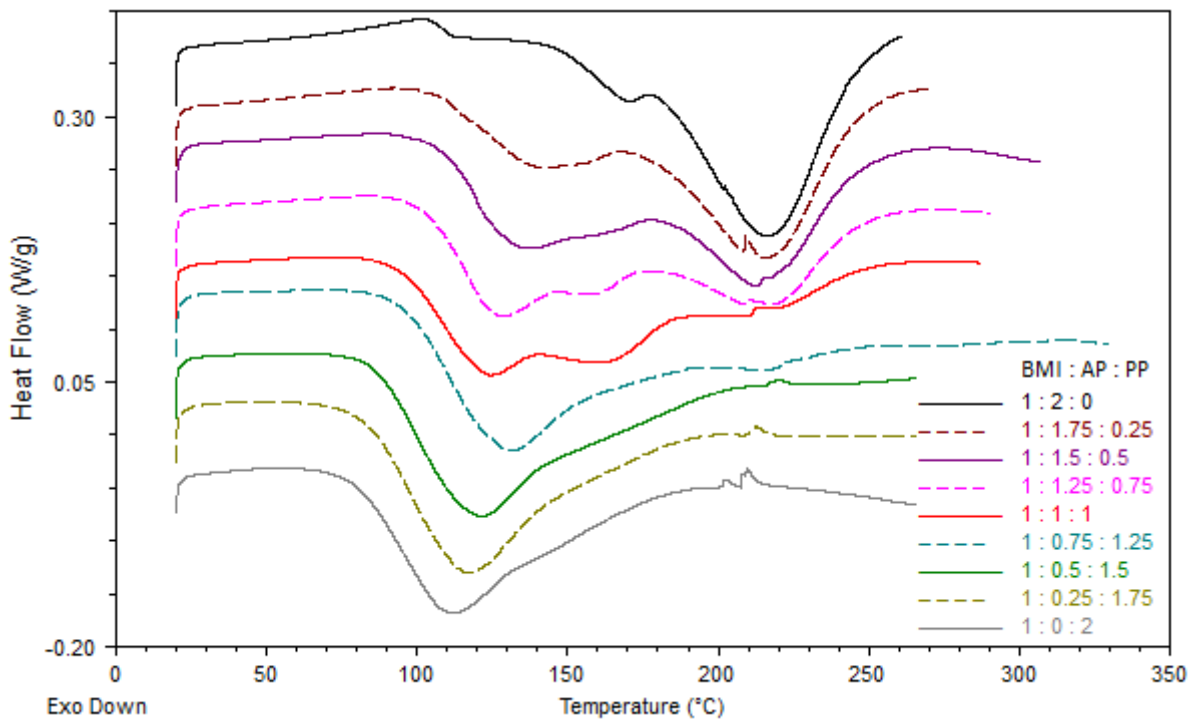


Figure 22: thermograms for BMI/AP/PP mixtures at 2 °C/min.

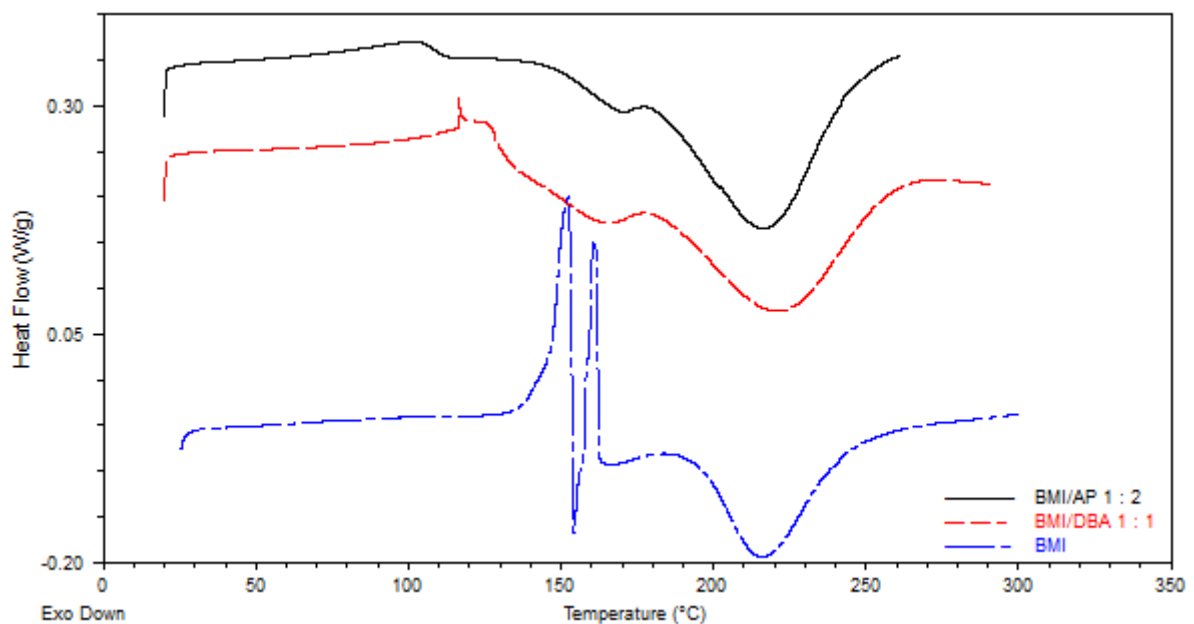


Figure 23: thermograms for BMI/AP, BMI/DBA mixtures and BMI alone at 2 °C/min.

Increasing the PP content first suppresses the BMI homopolymerization then the Alder-ene reaction. When the PP to BMI ratio reaches 1.5, with still 25% of allyl double-bonds, only the maleimide/propenylphenol reaction is detected. This transformation

appears to be predominant and to consume maleimide functions beyond stoichiometry. This demonstrate the high reactivity of maleimides with aryl-propenyl groups, pointing out that the reaction between maleimide groups and the central double bond of Alder-ene adducts is a plausible polymerization path.

1.4.3 Standard resin reactivity

From practical and theoretical points of view, bismaleimide resins chemistry has always proved to be difficult to investigate. Some reactions are observed with little doubt, such as the Alder-ene reaction, responsible for the chain-extension, and maleimide polymerization. Other addition reactions such as Wagner-Jauregg and Diels-Alder are strongly supported by studying model compounds reactivity. Using physico-chemistry investigation instead of chemical analysis will give more information about the nature of reactions involved in key steps such as gelation. This last point will be developed in the following part.

1.5 Kinetics elements

1.5.1 Gelation

1.5.1.1 Theoretical considerations

A gel is a state in which a material (polymer solution and/or architecture, particle dispersion...) develops a macroscopic structure. The gel state is usually characterised by two fractions: the *gel*, made of a percolated structure and the *sol* made of the remaining soluble compounds. The gel rests upon physical or chemical interactions. Physical gels often exhibit possible transitions from and to the gel state because of the reversibility of the involved interactions. For thermosets, gelation is usually defined by the creation of a macromolecular network (percolation). This type of chemical gel can also be preceded by a physical gel state in which unbonded macromolecular species are organized in a network shape. Depending on the polymerization route, the *sol* fraction consists of unreacted monomers, oligomers or branched species.

Gelation of thermosetting polymers is based on the cross-linking process, in which non-linear polymer chains are created. For epoxy/amine resins, chain extension and cross-linking can be achieved by the same chemical reaction. A bifunctional monomer contributes to lengthen polymer chains, whereas a functionality higher than two implies a cross-link node. At this stage, bismaleimide/allyl resins appear to be quite different. The Alder-ene reaction can only lead to chain extension, cross-linking has to go through addition reactions or maleimide homopolymerization. As a consequence, functionality-related gelation phenomena become difficult to define. For instance, the BMI monomer can react twice by Alder-ene reaction but four times by homopolymerization, without considering the new reactive double bond brought by the Alder-ene step. Thus the cross-linking process is directly determined by the chemical reactions reported in the previous part. Furthermore, gelation is a key behaviour for handling the resin, with consequences on the whole processing. Polymerization reaction conversion upon gelation can be predicted by models such as Flory-Stockmayer [59,60] or Macosko-Miller theories [61]. These models are based on monomers functionality and assume equivalent reactivity, which makes them inapplicable to the BMI/DBA system.

Gelation transition in thermosets is associated to a strong increase in viscosity to reach a higher stiffness, with an elastic response (transition from liquid-like to solid-like material). This makes rheology a dedicated method to observe this phenomenon. During isothermal curing, the time at which gelation occurs is denoted as gel time t_{gel} . A first approximation is to consider a liquid to solid transition where the viscosity increases up to the saturation threshold of the rheometer. This method is not accurate because viscosity may rise on wide period. Another widespread criterion is the intersection of the G' and G'' curves. Winter gave a theoretical approach to justify the fact that this method is not the most rigorous one^[62]. Only a few cases are compatible with this approach, for instance stoichiometrically balanced networks, a concept difficult to apply to the BMI/DBA system. The same theoretical background lead to the Winter and Chambon criterion^[63]. In this approach, both $G'(\omega)$ and $G''(\omega)$ at the gel point are proportional to ω^n , resulting to $\tan(\delta)$ not depending on the frequency. The starting point of this mathematical modelling is the time to frequency transformation of a power law for the shear modulus at the gel point:

$$G(t) = St^{-n}$$

S accounts for the gel flexibility. G' and G'' are calculated as follow:

$$G'(\omega) = \omega \int_0^\infty G(t) \sin(\omega t) dt = \Gamma(1 - n) \cos\left(\frac{n\pi}{2}\right) S\omega^n$$

$$G''(\omega) = \omega \int_0^\infty G(t) \cos(\omega t) dt = \Gamma(1 - n) \sin\left(\frac{n\pi}{2}\right) S\omega^n$$

here, Γ is the Gamma function (Euler). This transformation requires the power law to be valid over the whole time range (from short to long times). An underlying molecular theory suggested by Winter and Chambon, to comply with this hypothesis, is the fractal theory^[63]. In fractal networks, objects are similar whatever the considered scale. A noticeable point is the resulting homogeneous topology of such networks.

1.5.1.2 Rheology of bismaleimide resins

Isothermal experiment with combined sinusoidal oscillations containing several frequencies (5 Hz, 10 Hz and 20 Hz) were used to determine the gel time starting from 130°C. The strain amplitude (γ_0) was fixed at 1%. At this strain value, the initial material still follows a linear stress-strain behaviour. Figure 24 displays examples of experimental $\tan(\delta)$ curves for two temperatures. During the first part of the experiment, the viscosity is very low, which results into inaccurate measurements. The shear moduli G'' and especially G' cannot be determined precisely. For longer times, smooth $\tan(\delta)$ curves are obtained. Gelation occurs during the transition at intermediate times. If the crossover point of $\tan(\delta)$ curves can be easily identified at 130°C, it becomes more difficult to locate at higher temperatures.

The BMI/DBA gelation process appears to be fast, with a sharp change from the *sol* to the *gel* state. Attempts to improve the measurement accuracy, by changing the shear strain amplitude, the set of frequencies, the plates diameter and even using another rheometer, were unsuccessful. Not being able to point out the $\tan(\delta)$ crossover, a fair approximation is still possible by considering the liquid to soft solid transition (red line at 150°C on Figure 24). A numerical approach is to determine the onset of a monotonic increase of G' curves. The assessment is that when a consistent signal is being recorded, the gel state has already been reached.

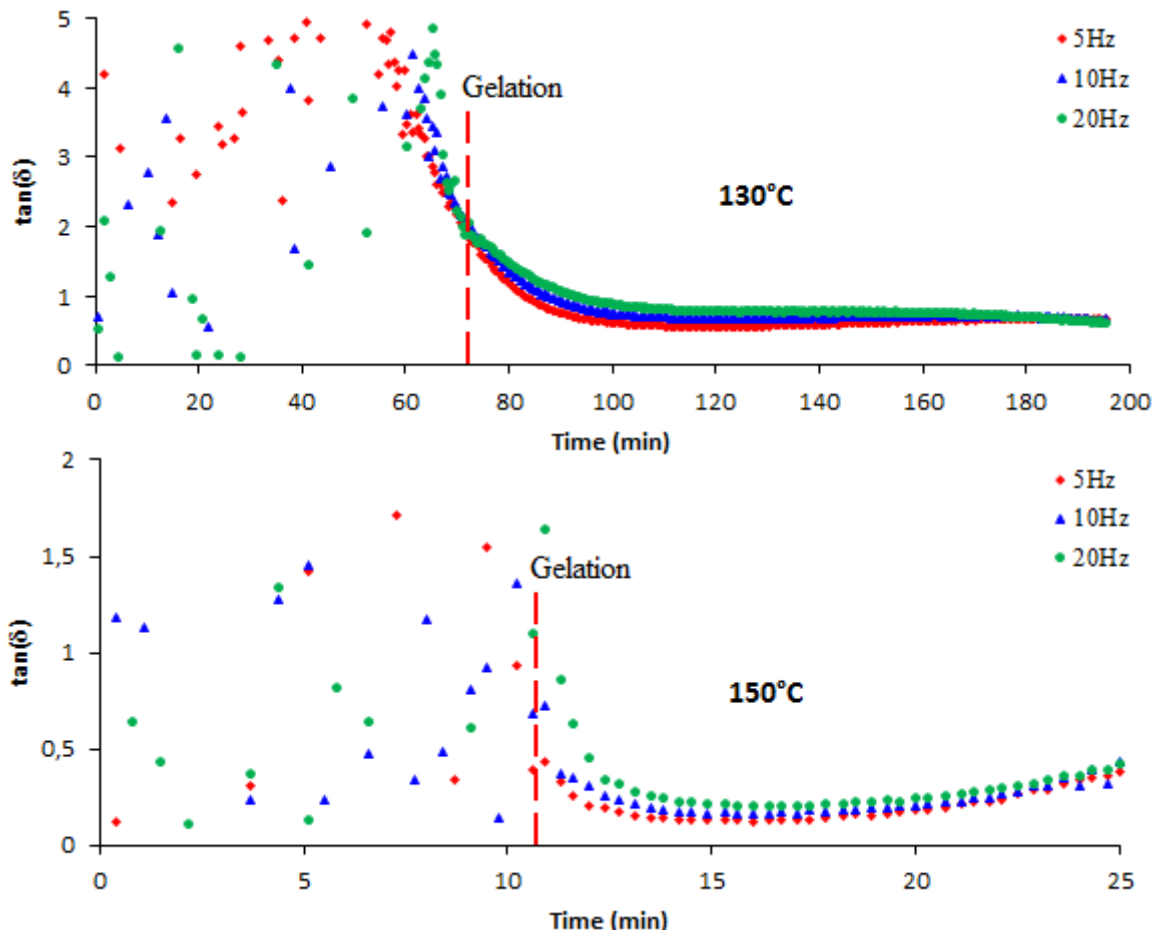


Figure 24: isothermal multifrequency rheology of the standard BMI/DBA resin at 130 °C and 150 °C. $\gamma_0 = 1\%$.

The previous method gives a higher value of t_{gel} that is expected to be close to true t_{gel} because of the sharpness of the transition. To validate this experimental approach, the material state was investigated around the approximated t_{gel} . Solid and liquid behaviours under high level of deformation are strongly different. Here the material recovering after high strains was observed. Regular rheology samples were cured directly in the rheometer oven at 140°C. Curing was stopped before, after and at the approximated gel point by lowering the temperature to 70°C (at this temperature, the resin does not significantly evolve within a few hours). Successive strain sweeps were then applied up to over 100% deformation for a maximum of five cycles. Oscillation procedure was chosen because a flow procedure would not be suitable to a hypothetical chemical gel state.

The resulting stress-strain curves are displayed on Figure 25. Before the determined gelation time, a quasi-linear response of oscillatory stress is observed with a full recovery of mechanical properties between cycles. This is a typical behaviour for a Newtonian fluid. Once the alleged gelation is reached, a limited linear domain, which can be assimilated to an elastic domain, is observed. After the first cycle mechanical properties are altered with a decrease of the initial slope, which means a diminution of the complex shear modulus $|G^*| = \sqrt{G'^2 + G''^2}$. This can be interpreted either as a damaging or as a decohesion between the parallel plates and the resin sample. Strains up to 100% may lead to a degradation of the network, involving breakage of chemical bonds and consequently, a loss of elastic properties. Both damaging and decohesion would mean an increased stiffness, characterizing the *sol* to *gel* transition.

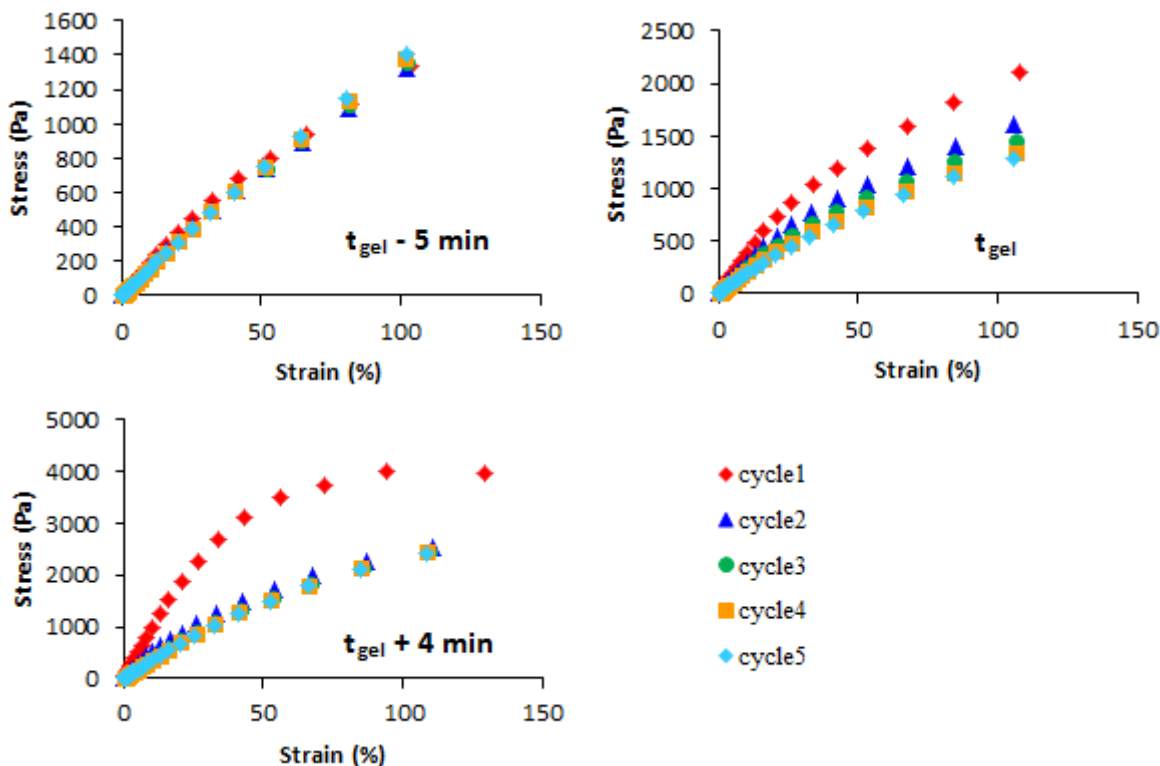


Figure 25: oscillatory strain sweeps of the standard BMI/DBA resin around the approximated gel time. Curing at 140°C , $f = 1 \text{ Hz}$, sweeps at 70°C .

From a practical point of view, at the gel point, the resin is still very soft with no mechanical strength. The bismaleimide resin rheological behaviour is completely different of the case of epoxy resins. Comparison was made with a diglycidylether bisphenol F/4,4'-diaminodiphenylsulfone (DGEBF/DDS) epoxy/amine resin in stoichiometric proportion of reactive functions. The Winter and Chambon criterion can be applied perfectly thanks to an initial pre-gel viscosity higher by one order of magnitude. Upon gelation, the resin is a soft rubber-like solid.

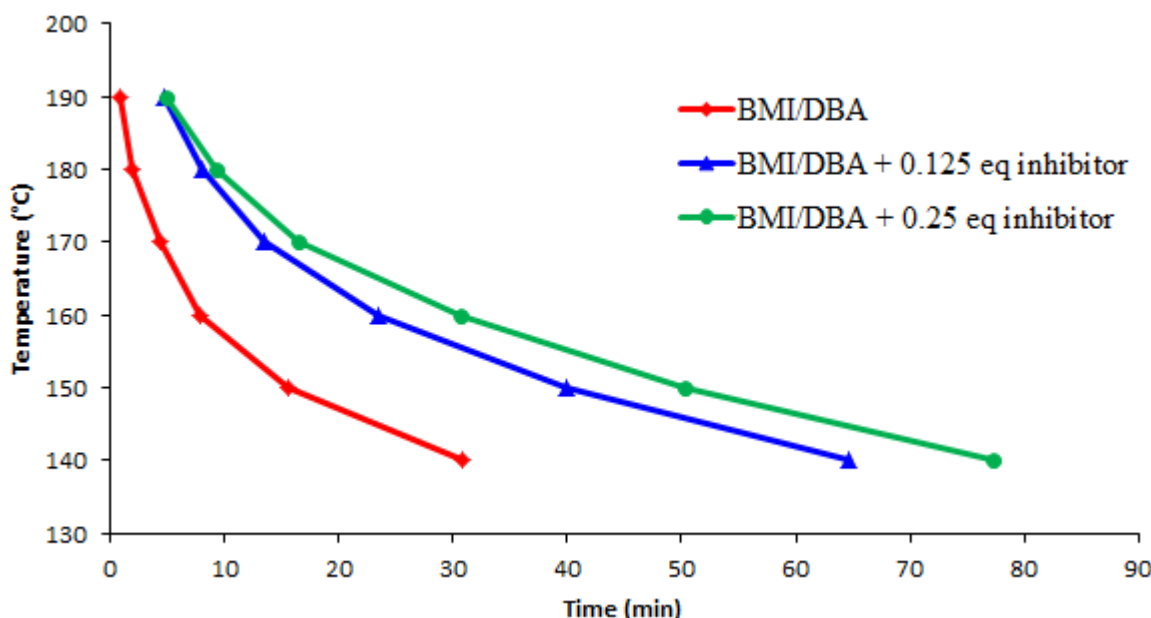


Figure 26: gelation curves for the standard and hydroquinone-modified BMI/DBA resin. Isothermal curing, $\gamma_0 = 1\%$.

On the other hand, Hsu and Lee described a similar sharp gelation transition in unsaturated polyesters copolymerized with styrene [64–67]. Soft diluted gel and similarity with a vinyl-based system send back to the radical-based nature of bismaleimide polymerization.

Using the method described previously, t_{gel} was evaluated for the standard BMI/DBA resin and the same system modified by hydroquinone. The radical inhibitor was added at 0.125 and 0.25 molar equivalents to BMI monomers. It can be seen on Figure 26 that the presence of hydroquinone significantly delayed gelation. This confirms the radical nature of the cross-linking process.

Remark: tracking down gelation by the appearance of an insoluble fraction was unsuccessful because, as for model systems, insoluble species seem to be generated even at short reaction times.

1.5.2 Time-Temperature-Transformation diagram

The use of TTT diagrams for thermosetting polymers was made popular by Gillham [68]. This kind of graphical representation gathers physical and chemical information with an overview of involved kinetics. Events, such as gelation or vitrification, are represented by curves on a time-temperature plot, defining a sort of state diagram. Data relative to the polymerization reaction can be added with isoconversional curves. Defining $\alpha(t, T)$ the reaction conversion, depending on the curing temperature T and the time t , those curves are obtained by sets of coordinates (t, T) for which α is equal to a chosen value (ranging from 0 to 1). TTT-diagrams need to be used along horizontal lines corresponding to isothermal curing.

Experimentally, α is obtained by DSC measurements during isothermal curing. The reaction enthalpy is determined by the integrated heat flow over the whole reaction range during a heating experiment. Here $\Delta_r H = 340\text{J/g}$ at $5^\circ\text{C}/\text{min}$. $\alpha(t, T)$ is then measured during an isothermal curing experiment at T using the partial reaction enthalpy $\Delta_r H^p(t)$:

$$\alpha(t, T) = \frac{\Delta_r H^p(t)}{\Delta_r H} \quad \text{at } T$$

$\Delta_r H^p(t)$ is calculated by the running integral of the heat flow:

$$\Delta_r H^p(t) = \frac{1}{m} \int_{t_0}^t \Phi_H(t') dt'$$

The heat flow Φ_H rises sharply at the beginning of such an experiment, consequently the integral value is extremely sensitive to t_0 . The normalised procedure to calculate t_0 is defined as follow:

- Each isothermal experiment has the same duration t_f .
- After t_f samples are not cooled down but directly heated at $5^\circ\text{C}/\text{min}$ up to 400°C .
- From this last heating phase, a residual reaction enthalpy $\Delta_r H^{res}(T)$ is measured.

- t_0 is chosen to satisfy equation 1.

$$\frac{1}{m} \int_{t_0}^{t_f} \Phi_H(t') dt' = \Delta_r H - \Delta_r H^{res}(T) \quad \text{Eq. 1}$$

The two main hypotheses of this procedure rely on the apparatus sensitivity. The recorded heat flow during the isotherm has to account for all the reaction heat. At long times, the reaction becomes very slow and the resulting heat flow cannot be measured accurately. This can be controlled with t_f , which was fixed here at 3h. On the other hand, the approximation is made that the calorimetric analysis is not dependent on the possible different reaction paths at the different temperatures.

Remark: in this case, for reaction enthalpies, mass values and not molar values are considered.

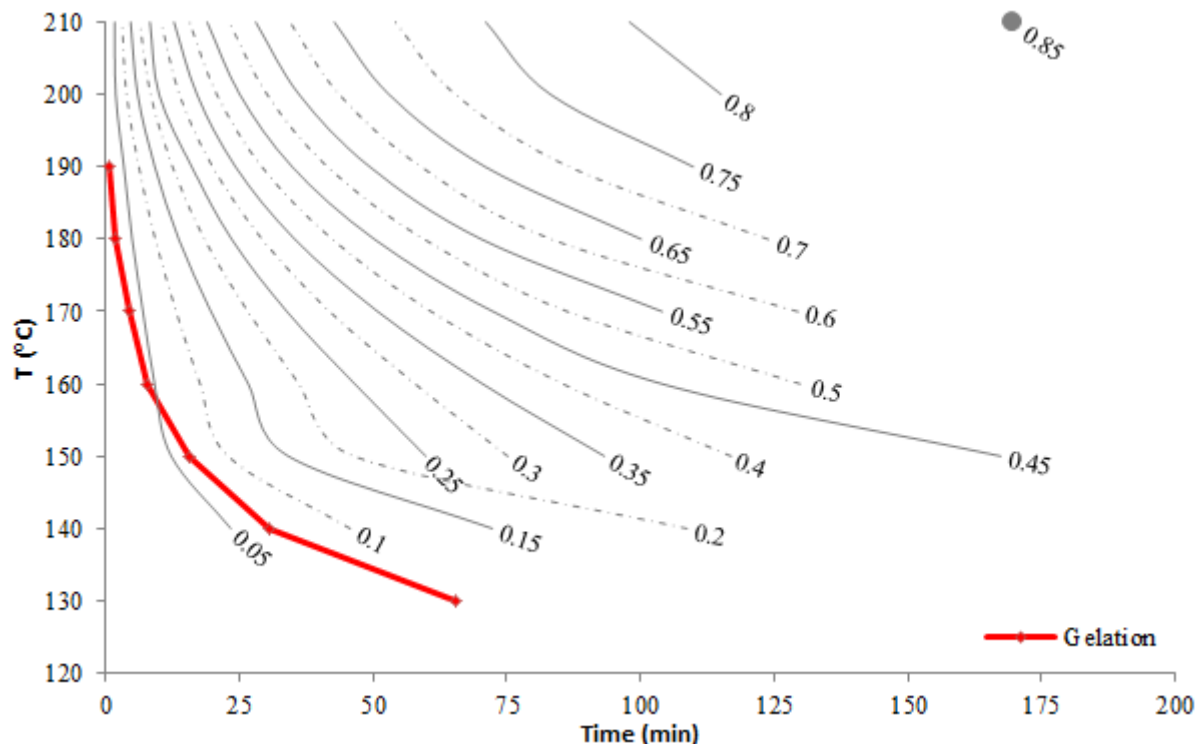


Figure 27: TTT diagram of the standard BMI/DBA resin. Grey curves are isoconversional for given conversions α .

The resulting TTT diagram with the gel curve is shown on Figure 27. The conversion at gel is evaluated close to 5%, which is near the lower detection limit of the method. The same procedure was applied to the DGEBA/DDS epoxy resin (TTT diagram in appendix C). The conversion at gel is in that case evaluated between 60% and 70%, which is slightly higher than the Flory-Stockmayer theory prediction [59, 60], possibly accounting for intra-molecular reactions. This first confirms the validity of the method and further points out a major difference between bismaleimide and epoxy thermosets. The rheological investigation evidenced weak BMI/DBA gels, and the low extent of the polymerization upon gelation suggests a very small *gel* fraction swollen by low molecular weight species, probably mainly monomers. For epoxies, the *sol* fraction is expected to contain much more oligomers and branched species.

Both the Flory-Stockmayer^[59,60] and Macosko-Miller^[61] models are not suitable to predict conversion at gel for such a reactive system. As mentioned previously, the occurrence of several reactions with different rates is not handled well in these theories. Moreover, the equi-reactivity assumption is invalid in the case of radical polymerization, where propagation rates are high compared to initiation. Finally, gel state described for the BMI/DBA system is, on the contrary to the DGEBF/DDS system, difficult to comply with the underlying molecular theories of the Winter and Chambon criterion. As it will be detailed in the next part, radical polymerization usually lead to inhomogeneities, especially in the cross-link density, generating networks that are not well described by a fractal theory.

1.5.3 Vitrification

As gelation, vitrification is a characteristic state change of thermoset polymers. It is the point at which the glass transition temperature of the thermoset, increasing because of the polymerization reaction, reaches the curing temperature. The material moves from a rubbery or liquid state to a glassy state where the molecular mobility drops dramatically. Further reaction is then limited by diffusion. For the standard BMI/DBA resin the final T_g was measured at 300°C for a final curing temperature of 250°C. The last reaction steps, even limited by diffusion, have a significant influence on the T_g .

Three methods were investigated to measure the vitrification time with DSC during isothermal curing. The conventional one consists into measuring the T_g of samples at different curing times during isotherms. Results of this approach are given on Figure 28. The time at which T_g equals the curing temperature can easily be estimated.

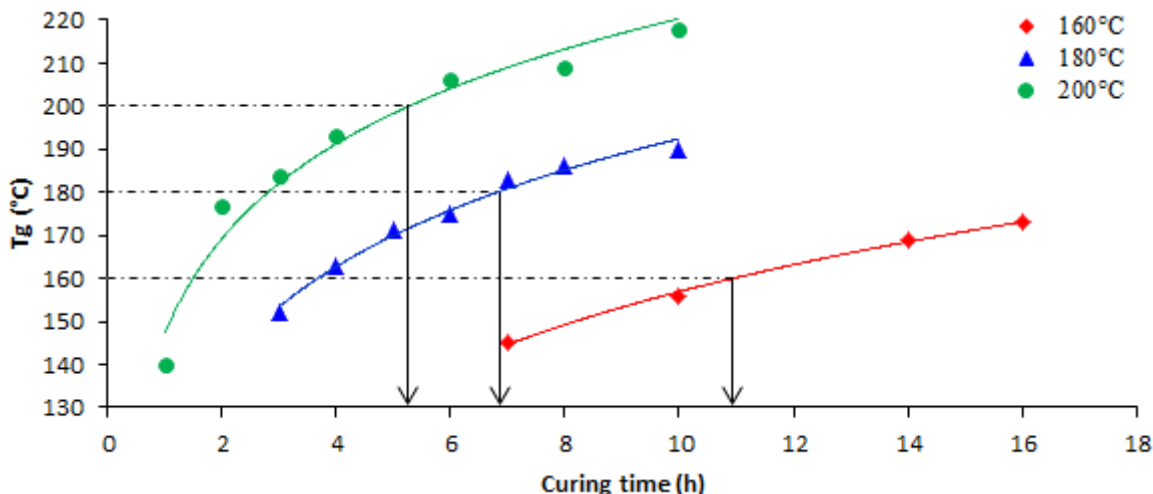


Figure 28: evolution of T_g of the standard BMI/DBA system with the curing time in isothermal conditions (DSC analysis).

This method being very time-consuming, other procedures implying modulated temperature DSC were explored.

Modulated temperature DSC consists into adding a periodic component to a DSC experiment. Van Assche and co-workers developed a procedure to detect vitrification in thermosetting polymers using this method^[69,70].

A temperature modulated around a mean temperature T_0 at an angular frequency ω with an amplitude ΔT_a can be expressed:

$$T(t) = T_0 + \Delta T_a \sin(\omega t) \quad \text{Eq. 2}$$

The heat flow is postulated to be:

$$\Phi_H(t) = C_p \frac{dT}{dt} + f(t, T) \quad \text{Eq. 3}$$

C_p being the sample heat capacity and f a response to a kinetic phenomenon. Combining equations 2 and 3:

$$\Phi_H(t) = C_p \Delta T_a \omega \cos(\omega t) + f(t, T) \quad \text{Eq. 4}$$

A discrete Fourier transform algorithm allows to extract from $\Phi_H(t)$ the cyclic component with an amplitude A_{cy} . From equation 4, a “cyclic” heat capacity is calculated:

$$C_p = \frac{A_{cy}}{\Delta T_a \omega}$$

The transition from rubbery to glassy state goes in pair with a strong reduction of molecular mobility. For thermosets, the network construction reduces the number of available conformations. Vitrification is then expected to go along with a heat capacity decrease. Van Assche and co-worker compare isothermal vitrification of thermosets with through T_g cooling of non reactive polymers [69]. They managed to measure vitrification of epoxies [69, 70] and unsaturated polyesters [71] using this method.

Applied to the BMI/DBA system, the procedure ($\Delta T_a = 1^\circ\text{C}$, $\omega = 0.1 \text{ rad/s}$) revealed a very broad phenomenon with a continuous decrease of C_p (Figure 29). The vitrification detection criterion was not applicable here.

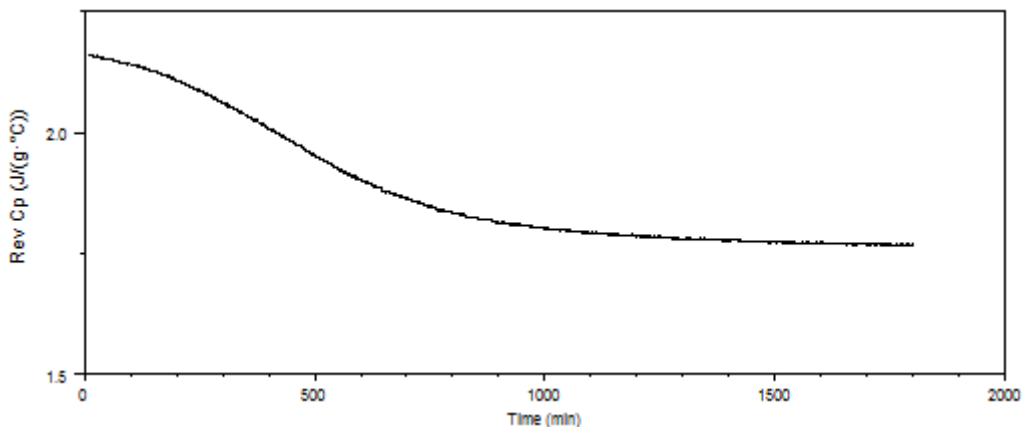


Figure 29: change of “ C_p ” for the standard BMI/DBA system during isothermal curing at 160°C ($\Delta T_a = 1^\circ\text{C}$, $\omega = 0.1 \text{ rad/s}$).

Van Assche and co-workers also explored another theoretical approach of modulated temperature DSC developed by Schawe [72], closer to classic oscillation theories. A complex heat capacity is defined:

$$C^*(\omega) = C'(\omega) + iC''(\omega)$$

C' is interpreted as related to the molecular mobility and, in particular cases, approximated by the regular heat capacity C_p . The physical sense of C'' is more complex, it seems to be related to dissipative phenomena. For a modulated temperature isothermal experiment, the resulting heat flow is expressed as:

$$\Phi_H(t) = \omega\Delta T_a|C^*|\cos(\omega t - \phi)$$

with

$$\tan(\phi) = \frac{C''}{C'}$$

The phase shift ϕ was found to exhibit a maximum when vitrification occurs in epoxies and unsaturated polyesters [69–71]. Isothermal modulated experiments ($\Delta T_a = 1^\circ\text{C}$, $\omega = 0.1 \text{ rad/s}$) were then carried out on the BMI/DBA resin. Maxima were observed on phase shifts (Figure 30).

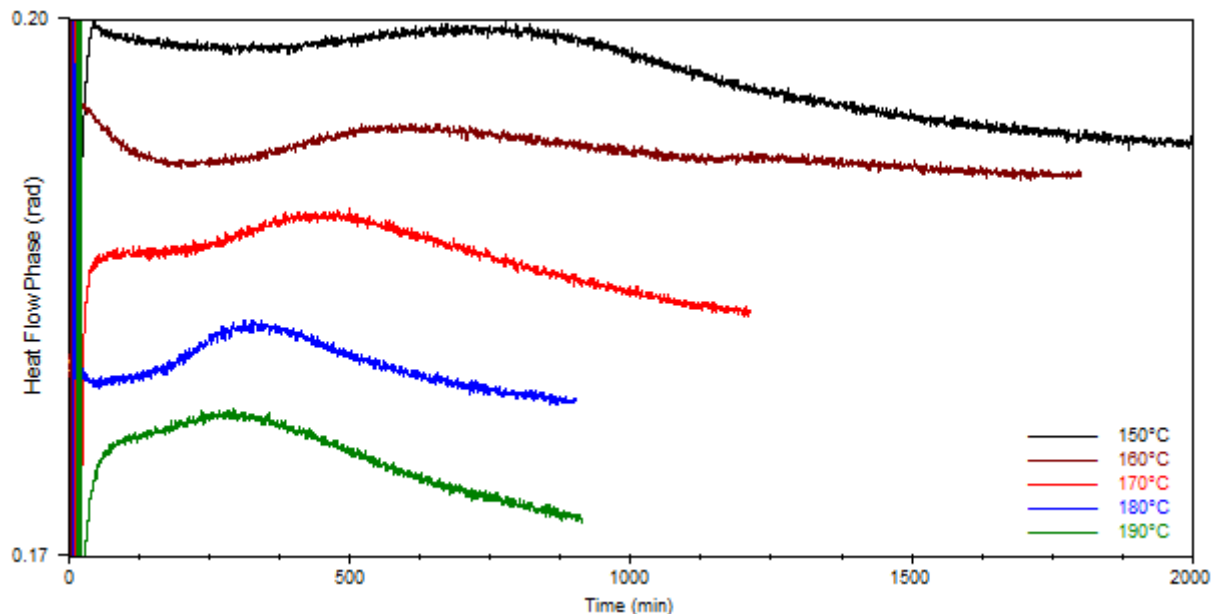


Figure 30: phase shifts for isothermal modulated DSC experiments on the BMI/DBA system ($\Delta T_a = 1^\circ\text{C}$, $\omega = 0.1 \text{ rad/s}$).

From the position of each maximum, the vitrification times are obtained (Figure 31). Comparison between the first (Figure 28) and last methods gives a difference around 45 min at 160°C and 180°C.

Independently of chosen the method, the noticeable point is the time scale for vitrification. With all the precautions on the interpretation of modulated DSC experiments, the evolution of the heat capacity and the broad phase shift peaks suggest a continuous transition over a large range of temperatures. The slow increase of T_g during curing, especially for lower temperatures (Figure 28) tends to confirm this observation.

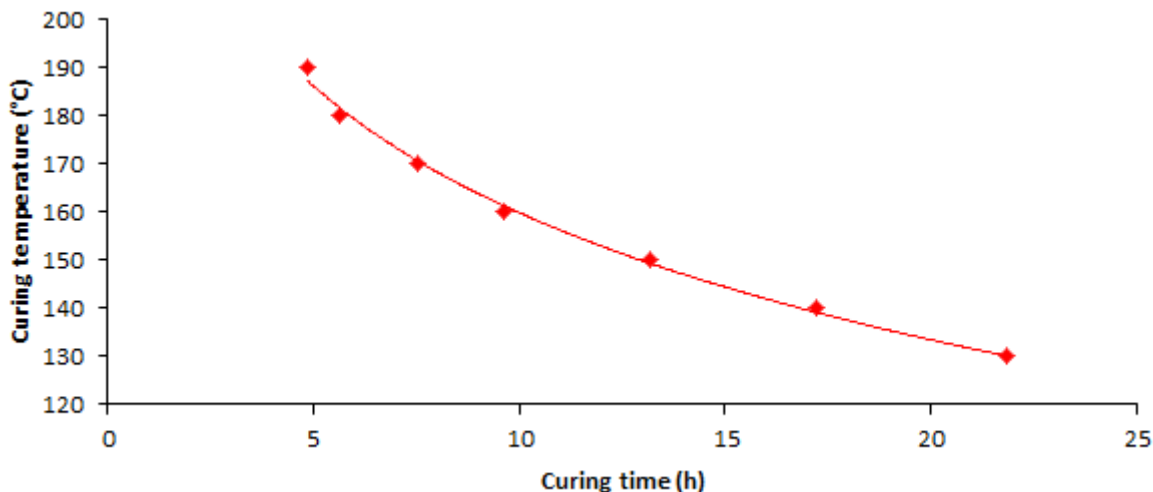


Figure 31: vitrification curve for the standard BMI/DBA resin.

The vitrification curve is usually plotted on the TTT diagram. Here this phenomenon occurs so late that it would be irrelevant. Completely opposite kinetic behaviours are observed for gelation and vitrification. The gel state is reached with a sharp transition within minutes at a low reaction conversion. The glassy state seems to result from a slow process after hours at a high reaction conversion (above 75% at 190°C).

1.6 Network structure

1.6.1 Inhomogeneity in thermosetting polymers

Topological inhomogeneity of thermosets always leads to numerous questions. Dušek reviewed the subject with a critical approach of different kinds of thermosetting polymers, depicting a field where theoretical scenarii are hardly confirmed by, sometimes misleading, observation methods [73]. Characterisations involve electron microscopy, scattering methods (X-rays, neutrons), NMR, EPR... Inhomogeneities of cross-link density find their origin in the network building process but some early-stage inhomogeneities may be eliminated after curing. Consequently, studying the curing process along with the final material brings complementary information.

A conclusion arising from Dušek's review is that topological inhomogeneities are not commonly found in epoxy-based thermosets, synthesized from polyaddition. Using specific conditions, such as stoichiometry imbalance or particular curing agent composition, can promote inhomogeneity, due to change in components compatibility or reaction paths. On the other hand, unsaturated polyester-based networks, building up by free radical polymerization, are prone to develop inhomogeneous structures. At the root of this difference, the polymerization mechanisms are found. For stepwise reactions, polymer products grows up together with a relatively narrow molecular mass distribution. By comparison, chain-wise reactions result in long chains dissolved in a high volume fraction of unreacted monomers. Radicals have a high reactivity, diffusion of reactive species being passed over, reactions proceed in a limited area. In appropriate conditions, this lead to highly cross-linked nodules, called microgels (Figure 32).

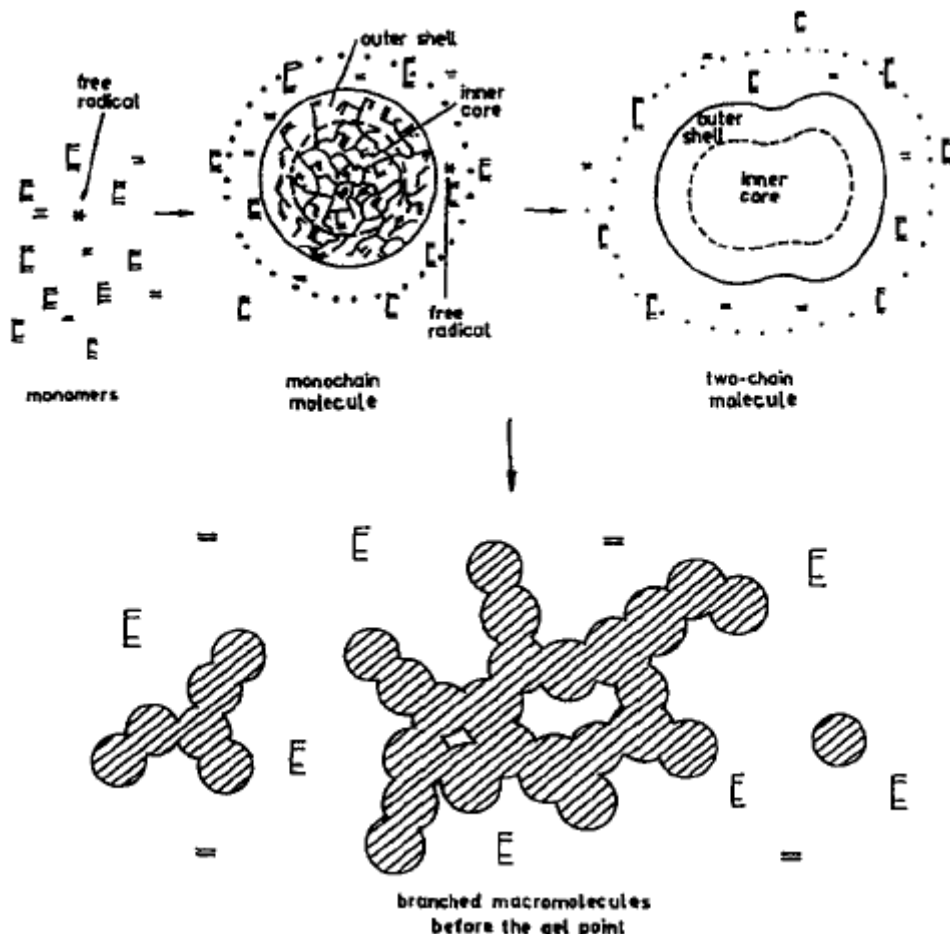


Figure 32: model for network formation by radical copolymerization of a nonovinyl and a divinyl monomer. From [73].

A common consequence of the diffusion control over free radical polymerization is known as the Trommsdorff effect. When the reactivity falls under a limited diffusion of active centres, the radical recombination, quenching reaction, occurs less frequently. As a consequence, the polymerization rate increases.

For a single kind of chemical function, such as double bonds in vinylic systems, several reactions occur during radical polymerization. When an active centre meets a reactive function, the chain lengthens and the active centre is transferred to the new end of chain. This propagation reaction is the linear chain growth process. If the reactive function is born by another polymer chain, a cross-link point is formed. The recombination of two radicals ends the reaction cycle. Intramolecular recombination or propagation (cyclisation) generates a ring. Because of diffusion control effects this last reaction is frequently met. A polymer cycle is an ineffective contribution to the network elasticity. Finally, an active centre can be transferred to another location, depending on the chemical structure of the polymer backbone.

Other limiting effects are expected in free radical polymerization building networks. Some functions may become less reactive because of excluded volume effects, such as steric hindrance. Similarly, radicals can be trapped in highly cross-linked areas with no accessible functions to react with.

1.6.2 Network architecture analysis

In the case of bismaleimide resins, several reactions were identified as theoretically possible paths for building the final network. The first occurring one, the Alder-ene reaction, accounts for linear chain growth. Addition reactions involving maleimide functions and Alder-ene adducts can lead to cross-linking but it was shown in the previous part that the cross-linking mechanism had a major radical contribution. Multiple reactions may lead to chemical function imbalance, promoting inhomogeneities in the polymer network, but adding the radical process is expected to greatly favour this effect.

Control over the radical reaction is a key to modulate the network macromolecular structure. Two parameters were used to that purpose. First, hydroquinone, the radical inhibitor, strongly delayed gelation. Either it only slows down the radical reactions or it partially quenches them. In both cases, more time and reactive functions are available for parallel reactions to proceed. Second, the literature and DSC analysis showed that Alder-ene and addition reactions occurs at lower temperature than BMI homopolymerization. Consequently a low temperature curing step is expected to promote non-radical reactions.

A hydroquinone-modified resin (0.25 equivalent per BMI molecule) was cured with two selected protocols. In the first case, the standard curing cycle was preceded by an isotherm at 140°C during 3h (cycle 1). In the second case, the pre-curing step is 140°C for 12h and the last isotherm at 250°C for 8h, instead of 6h (cycle 2). Dynamic mechanical analysis is displayed on Figure 33.

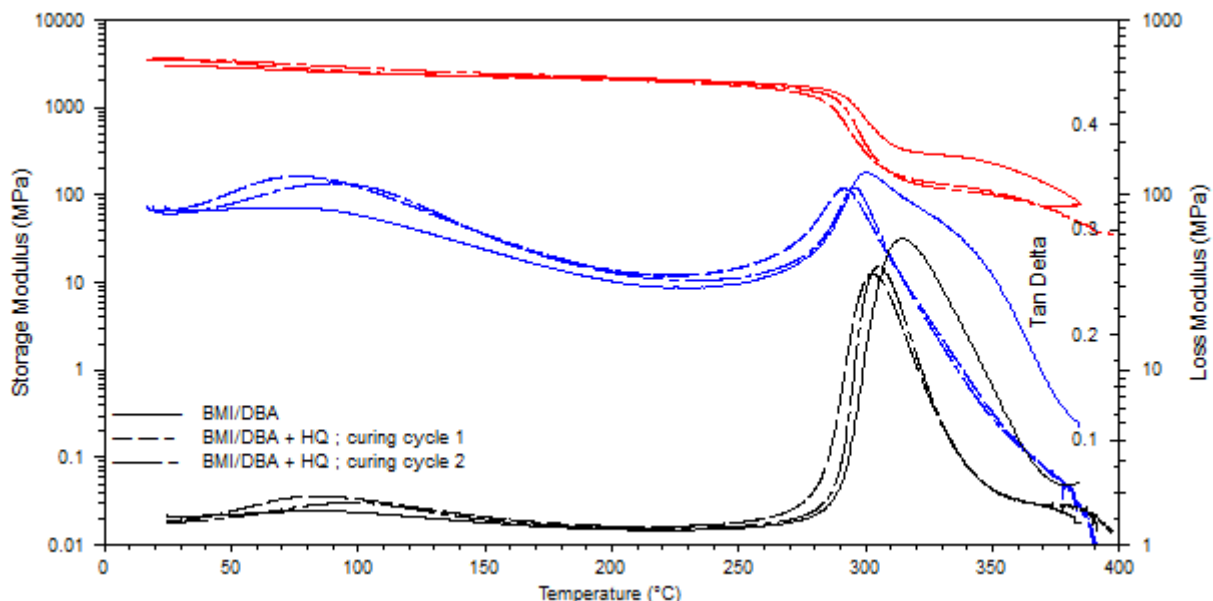


Figure 33: DMA spectra of the standard and hydroquinone-modified BMI/DBA systems.
 $3\text{ }^{\circ}\text{C}/\text{min}$, $f=1\text{Hz}$, $\epsilon_0=0.1\%$.

Spectra for the modified systems are very similar. With the curing cycle 2, the glass transition temperature is slightly higher due to a possible consequence of the longer post-curing time at 250°C. For both modified resins, the glass transition is lower than for the standard resin. Their initial storage modulus is the same but a larger decrease is observed in the T_g region. Lower T_g and lower E' at the rubbery plateau are compatible with a higher molecular weight between cross-links, a consequence of a promoted chain extension reaction against cross-linking. The hydroquinone reaction sub-products may also act as

plasticizers, contributing to lower T_g .

Focusing on the $\tan(\delta)$ curve in the α -relaxation zone, the peak for the modified systems is nearly half as broad as for the standard resin. The α -relaxation is related to the polymer chains configurational changes. A more homogeneous network is expected to exhibit a more restricted number of configurational changes, *i.e.* a narrower relaxation time spectrum, and therefore a thinner α relaxation peak. On the other hand, it was previously shown that the standard resin α -relaxation peak broadness is also due to a post-curing during DMA measurement. Leaving aside the phenol reactivity which is not expected to be different here, unreacted groups can be due to trapping and excluded volume, a consequence of the radical polymerization process and therefore, not unrelated to the network inhomogeneity.

This DMA investigation evidenced differences between standard and hydroquinone-modified BMI/DBA networks and suggests a reduction of inhomogeneity by limiting the radical reactions.

1.6.3 Simulated networks

Computer simulation is a powerful tool to predict architectures as well as construction of thermosetting polymer network construction was often approached by that means. Gelation prediction was achieved for stepwise polymerization through percolation models based on the Flory-Stockmayer theory. As reported previously, such an approach is no longer effective with bismaleimide resins where multiple reactions occurs and where the concept of functionality becomes more difficult to define. A program was developed to generate networks from initial conditions. Neither the model accuracy nor the computing efficiency were targeted here. This program suggests a computer method to obtain networks from chemical structure information and hypothesis on the reaction path. The detailed code can be found in appendix D.

The program was developed for Matlab and is based on oriented object programming (OOP). The computing method follow a Monte-Carlo process, though without using statistic tools. In OOP, objects are elements belonging to a class which defines their properties and some of the functions affecting them. Specific functions can be added directly in the object definition. To call an object property the syntax is simply: `object.property`. Monomers are defined as objects from the `Monomer` superclass. They have four basic properties: `type` (BMI or DBA), `doubleBond` (the number of double bonds), `radical` (the number of radicals) and `AlderEneCount` (a variable to determine if the monomer still has an available double bond for the Alder-ene reaction). Initial properties of both monomers are defined as follow:

For BMI:

```
function obj = BMI()
    obj.type = 'BMI';
    obj.doubleBond = 2;
    obj.radical = 0;
    obj.AlderEneCount = 0;
end
```

For DBA:

```
function obj = DBA()
    obj.type = 'DBA';
    obj.doubleBond = 2;
    obj.radical = 0;
    obj.AlderEneCount = 0;
end
```

Functions for the Monomer superclass are `PropagateRadical` and `TerminateRadical` that account respectively for the creation and the consumption of a radical.

```
function PropagateRadical(monomer)
    if monomer.doubleBond > 0
        monomer.radical = monomer.radical+1;
        monomer.doubleBond = monomer.doubleBond-1;
    end
end

function TerminateRadical(monomer)
    if monomer.radical > 0
        monomer.radical = monomer.radical-1;
    end
end
```

The BMI class has an additional function `initiate` that creates radicals. The assumption is made that radicals only appear on BMI molecules^[31].

```
function initiate(monomer)
    if monomer.doubleBond > 0
        monomer.radical = monomer.radical+1;
        monomer.doubleBond = monomer.doubleBond-1;
    end
end
```

The Alder-ene reaction consumes two double bonds and brings a new one. In this simulation, Diels-Alder and Wagner-Jauregg reaction are neglected and only the Alder-ene reaction and the radical process are taken into account. Consequently the new double bond is set to be available for radical reaction, stocked in the `doubleBond` property but not for another Alder-ene reaction, `AlderEneCount` being the control parameter. This double bond is arbitrarily attributed to the DBA unit in the `AlderEne` function definition:

For BMI:

```
function AlderEne(monomer)
    if monomer.doubleBond > 0 & monomer.AlderEneCount < 2
        monomer.doubleBond = monomer.doubleBond-1;
        monomer.AlderEneCount = monomer.AlderEneCount+1;
    end
end
```

For DBA:

```
function AlderEne(monomer)
    if monomer.doubleBond > 0 & monomer.AlderEneCount < 2
        monomer.AlderEneCount = monomer.AlderEneCount+1;
    end
end
```

Mobility of species is not included in the present simulation. Effects of such a parameter for a free radical polymerization simulation has been studied by Bansil and co-workers [74,75]. Suggestions for its implementation will be discussed in the last chapter.

The initial material for the simulation is a $L \times L \times L$ cell array with a random distribution of BMI and DBA objects with the BMI/DBA standard resin proportion. Each simulation cycle contains several steps, each one corresponding to a chemical reaction. First a recombination phase, where adjacent radicals are linked and quenched. Then a propagation step, where radicals react with an adjacent double bond and are transferred to the new bonded cells. The Alder-ene reaction then proceeds randomly over the whole cell array. Finally new radicals are initiated. This last step follows the mechanism suggested by Hopewell and co-workers, in which two BMI monomers associate to generate a radical on each of them [31]. A random initiation step account for a thermal radical initiation reaction but an initial radical concentration could be used too. A bond matrix contains pairs of bonded cells.

Reactions occurs between neighbouring cells. Neighbours are defined to be the 6, 5, 4 or 3 closest cells, depending on the considered position (inside, side, edge or corner). As a consequence, growth is oriented in six directions but another definition would enable more (for instance using the closest 10 cells add diagonal growth). Some restrictions are applied to avoid non-realistic bonding. Double bonding between two cells is not allowed (condition on the bond matrix), initiation requires two neighbouring BMI cells and Alder-ene requires a BMI next to a DBA, each of them with an available double bond (`AlderEneCount` inferior to 2). In addition, initiation cannot involve bonded BMI cells.

The chemical reactions are controlled by reaction probabilities `pi`, `pp` and `pa` for initiation, propagation and Alder-ene reaction respectively. Radical recombination is assumed to have a probability of 1. With three parameters a simulation derived from Monte-Carlo is not adapted to optimisation. Nevertheless, the effect of each reaction can be illustrated. In the following illustrations, created bonds are displayed and white areas correspond to unreacted monomers.

The Alder-ene reaction alone cannot generate a network but lead to linear polymer chains. Figure 34 shows the result of simulations with $\text{pi} = 0$ and $\text{pa} = 10^{-3}$ after 50 and 100 steps. The extent of the reaction is maintained low enough to illustrate properly the polymeric structure. The polymer growth proceeds with an homogeneous distribution over the whole sample.

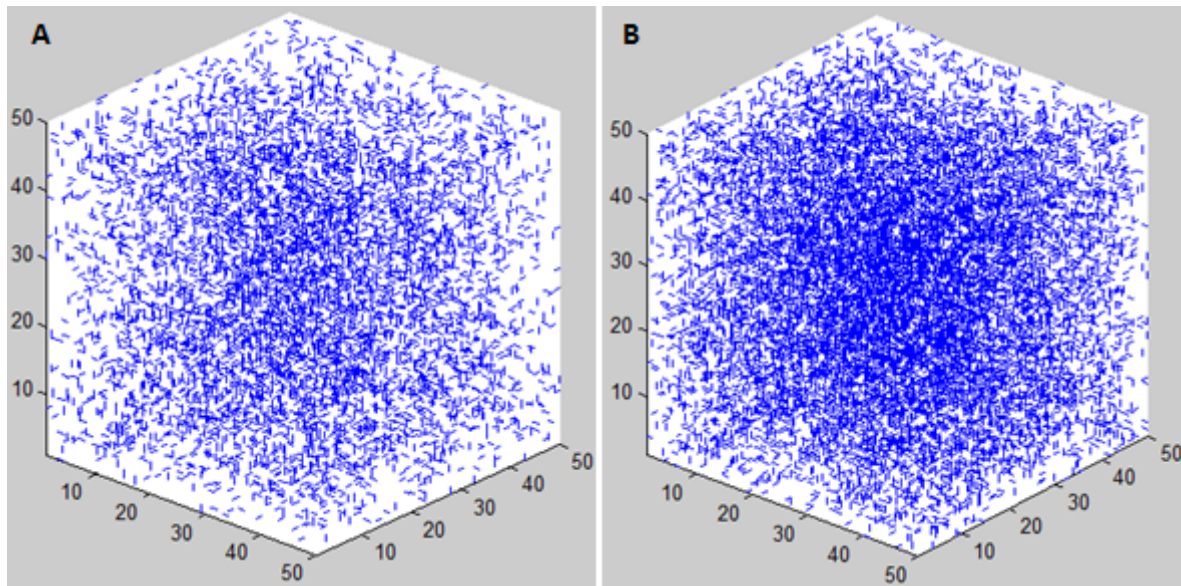


Figure 34: simulated polymers with Alder-ene reaction. A) 50 steps ; B) 100 steps.

The free radical polymerization generates very different structures. Figure 35 shows networks with $p_i = 10^{-3}$ and $p_a = 0$. The propagation probability is purposely set at maximum ($p_p = 1$) to bring out the heterogeneous nature of this polymerization process. It also accounts for the high reactivity of radical species. Simulated networks are indeed quite heterogeneous with created bonds localized around initiation sites.

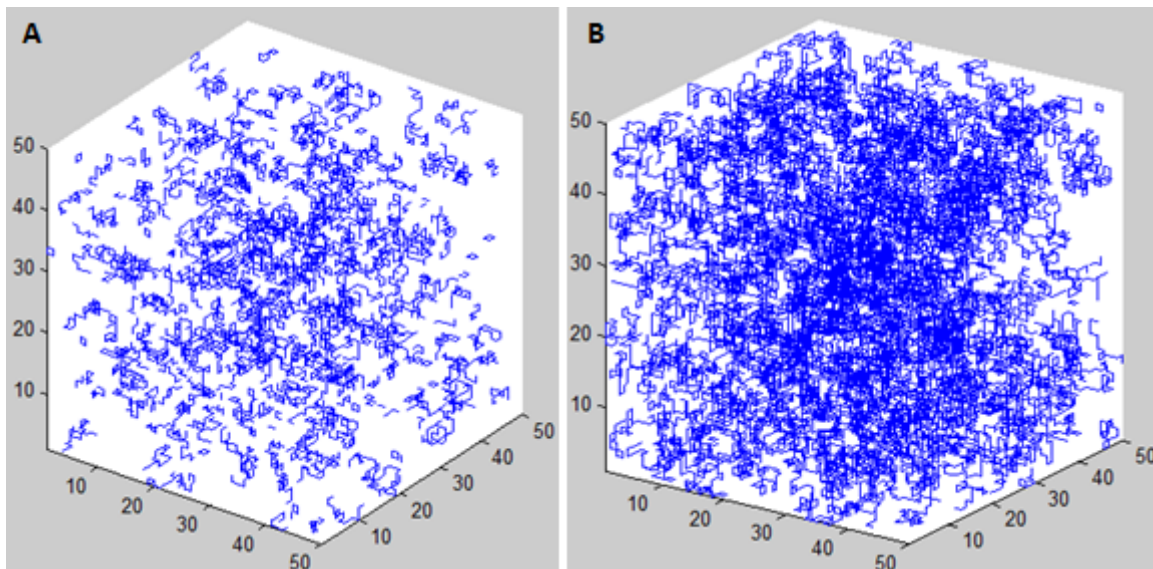


Figure 35: simulated networks with free radical polymerization reaction. A) 20 steps ; B) 40 steps.

This simulated free radical polymerization is subjected to several parameters but any tested combination naturally lead to quite heterogeneous networks (compared to the simulated Alder-ene reaction) with expected features. Figure 36 shows many loops created by monomer bonding, such a cyclisation was predicted by Dušek and co-workers for bismaleimide/styrene networks^[76]. More generally, cyclisation is expected with free radical polymerization as a consequence of local high reactivity of activated species.

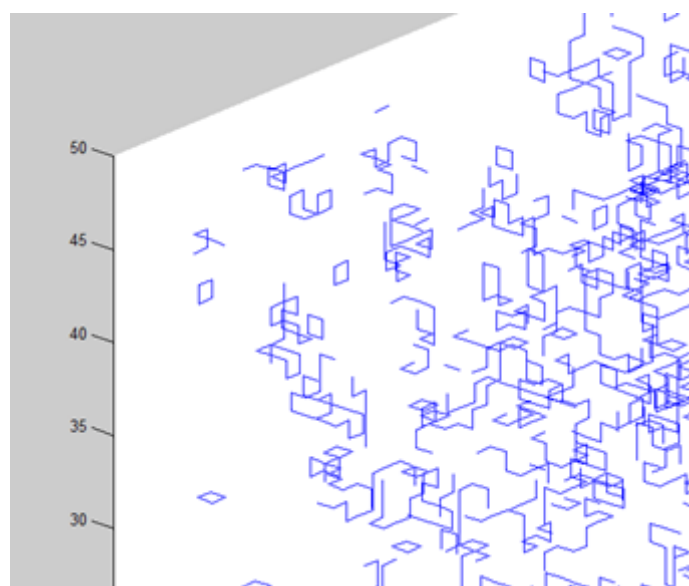


Figure 36: detail of a simulated network with free radical polymerization reaction.

Bismaleimide/bisallyl networks are expected to be an intermediate case, with an homogeneity determined by two opposite forces driven by chain-extension and free radical polymerization.

1.7 Conclusions

From this study on a conventional bismaleimide resin, arise many differences with epoxies, the reference thermosets for aeronautic composite structures. Reaction paths in bismaleimide/bisallyl resins are complex with possible side reactions. However, the cross-linking process appears to imply free radical polymerization. From a practical point of view, these resins are compatible with classic tools used to handle epoxies, but the control parameters are different. Gelation occurs at very short times but the gel displays a poor rigidity. It can be delayed using a radical inhibitor. With such a modifier and adapting the curing cycle, non-radical reactions can be promoted, leading to less inhomogeneous polymer networks. Radical polymerization indeed generates more inhomogeneous networks than stepwise polymerization met with epoxy resins.

Other consequences on thermodynamics and mechanical properties will be addressed in the following chapters.

The cured bismaleimide resin is, in principle, suitable for high temperature applications up to 200°C. However, further investigation on ageing of the resulting networks and composites is required.

Chapter 2

Morphologies of bismaleimide thermoset and thermoplastics blends

Modification of thermosets by thermoplastics is a common strategy to increase their toughness [77,78]. Resulting materials usually exhibit multi-phase morphologies. Theoretical considerations on phase separation process will illustrate a difference between epoxy and bismaleimide resins, consequence of their respective polymerization mechanisms studied in the first chapter. After a review on modified bismaleimide resins, phase separation and morphologies of model matrices will be investigated. Further tests also account for practical limitations arising from composites processing.

2.1 Phase separation in thermosetting polymers

2.1.1 Flory-Huggins theory

Studying polymer blends usually leads to consider their affinity, which is a way to describe how well they can be mixed and remain in a single phase. Many parameters have to be taken into consideration to predict such behaviours. A phase diagram is a graphic construction in which the mixing state is displayed in function of parameters (here, temperature and thermoplastic content). The blend behaviour is described by the mixing free enthalpy $\Delta_m G$ (equal to the mixing free energy $\Delta_m F$ at constant pressure and volume). The Flory-Huggins equation for a polymer solution can be expressed as [59,79]:

$$\frac{\Delta_m G}{k_B TV} = \frac{\Phi_{pol}}{v_{pol}} \ln(\Phi_{pol}) + \frac{\Phi_{sol}}{v_{sol}} \ln(\Phi_{sol}) + \chi \frac{\Phi_{pol} \Phi_{sol}}{v_r} \quad \text{Eq. 5}$$

where k_B is the Boltzmann constant, V the volume, v the molecular volume and Φ the volume fraction. Subscripts *sol* and *pol* refer to solvent and polymer respectively. χ is called Flory parameter and account for the polymer-solvent interactions. v_r is a molecular volume for a specific segment.

$\Delta_m G < 0$ is a necessary condition for a single phase to be observed. The phase diagram shape is calculated from equation 5 and strongly depends on χ . The solubility (or coexistence, or binodal) curve is obtained with the condition:

$$\frac{\partial \Delta_m G}{\partial \Phi_{sol}} = 0$$

Zero to two extrema for $\Delta_m G$ are obtained for each temperature. The temperature at which a single extrema is obtained is the critical temperature T_c . If the solubility curve displays a maximum, T_c is a upper critical solution temperature (UCST, solubility at high temperature) and lower critical solution temperature if it displays a minimum

(LCST, solubility at low temperature). Example is given on Figure 37.

The stability of an equilibrium state can be evaluated with the sign of the second partial derivative of $\Delta_m G$. The spinodal curve, the boundary of the area in which metastable (out of equilibrium single phase mixture) systems are met, is defined by:

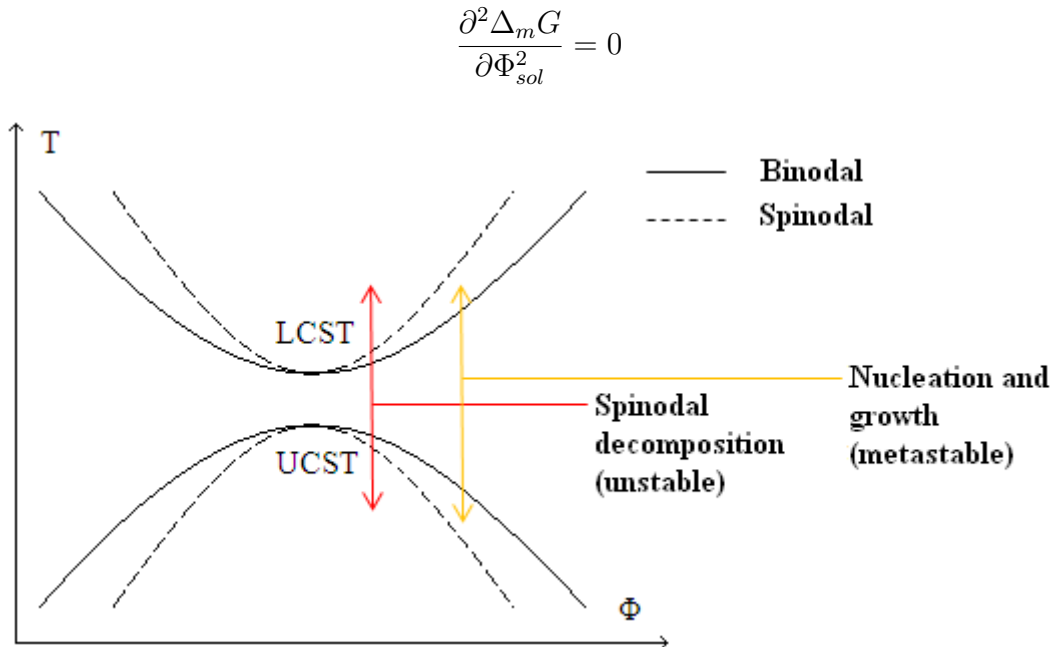


Figure 37: theoretical phase diagrams.

The Flory-Huggins theory which has been commonly used for polymer-solvent interactions can be extended to polymer-polymer interactions under the scope of different hypothesis. Equation 6 is an alternative form of equation 5 for mass-polydispersed polymers.

$$\frac{\Delta_m G}{k_B T V} = \frac{N_A \rho_{TP}}{M_{TP}} \Phi_{TP} \ln(\Phi_{TP}) + N_A \rho_{TS} \sum_i \frac{\Phi_{TS,i}}{M_{TS,i}} \ln(\Phi_{TS,i}) + \frac{\chi}{v_r} \Phi_{TP} \sum_i \Phi_{TS,i} \quad \text{Eq. 6}$$

with ρ_{TP} , M_{TP} and Φ_{TP} being respectively the density, molar mass and volume fraction of thermoplastic. ρ_{TS} , $M_{TS,i}$ and $\Phi_{TS,i}$ being the density, molar mass and volume fraction of thermoset, the subscript i accounting for the different polymer lengths depending on the extent of the polymerization reaction. N_A is the Avogadro constant.

Usual simplifications are made with:

$$\rho_{TP} = \rho_{TS} = \rho$$

$$\chi' = \frac{\chi}{N_A v_r}$$

Finally giving:

$$\frac{\Delta_m G}{\rho R T V} = \frac{\Phi_{TP}}{M_{TP}} \ln(\Phi_{TP}) + \sum_i \frac{\Phi_{TS,i}}{M_{TS,i}} \ln(\Phi_{TS,i}) + \chi' \Phi_{TP} \sum_i \Phi_{TS,i} \quad \text{Eq. 7}$$

A good way to apprehend the multiplicity of phase separation processes in TS/TP blends, is to consider that TS is initially a solvent. In most cases, the thermoset monomers are molecules with molar masses already greater than those of usual solvents, but still low enough to solubilise some thermoplastics. The structure of those monomers also has an influence on the solubilisation force. The χ parameter takes both factors into consideration.

2.1.2 Flory parameter

χ is a crucial parameter to predict polymer-solvent or polymer-polymer blends behaviour. Hildebrand and Scott introduced solubility parameters (δ_i) for a two component blend [80]:

$$\chi' = \frac{1}{RT}(\delta_1 - \delta_2)^2 \quad \text{Eq. 8}$$

This expression assumes only positive values for χ' , favourable interactions, such as hydrogen-bonding, have to be added either with a negative contribution to χ' or with a negative free energy to the Flory-Huggins equation right member.

The single phase condition is often transferred from $\Delta_m G$ to χ' . The solubility parameters δ can be calculated from the chemical structure of compounds. Small [81], Hoy [82] and van Krevelen [83] used the following relationship:

$$\delta = \sum_i \frac{F_i}{V_i} \quad \text{Eq. 9}$$

with F_i an attraction constant and V_i a molar volume. Both are tabulated for different molecular segments. Coleman introduced a correction to take stronger interactions into account [84].

Hansen developed a different approach, separating non-dipolar dispersive (D), polar (P) and hydrogen bond (H) interaction contributions [85]:

$$\delta^2 = \delta_D^2 + \delta_P^2 + \delta_H^2 \quad \text{Eq. 10}$$

For polymer blends, the degree of polymerization is also a discriminant factor. Krause defined a critical value for χ' , above which mixing is no longer achieved without favourable interactions [86]:

$$\chi'_c = \frac{1}{2} \left(\frac{1}{\sqrt{M_1}} + \frac{1}{\sqrt{M_2}} \right)^2 \quad \text{Eq. 11}$$

where M is the polymer molar mass. Polymers with a high degree of polymerization are more difficult to mix.

2.1.3 Reaction-induced phase separation

The Flory-Huggins modified equation (equation 7) can be used to describe a specific kind of phase separation phenomenon: reaction induced phase separation, which is usually the main process considered in thermosetting polymer blends. It is of course clear that other phase separation processes, as in polymer-solvent and other non-thermosetting polymer blends, are also valid here.

2.1.3.1 Reactive solvent

From this point, an uncured TS/TP blend can be understood as a regular solvent-polymer blend. What makes the difference is that the solvent is reactive. Not only temperature but also time will change the properties of the solvent and therefore influence its phase separation behaviour. The molecular weight increase of the thermoset is expressed in the distribution of $M_{TS,i}$. The polymerization reaction often results in the consumption of chemical functions with high polarity so that the chemical nature of the solvent is altered. Consequently, the χ' parameter is expected to be modified. Taking this into consideration, there are at least two terms in equation 7 that depend not only on time and temperature but also on the whole thermal history. From an experimental point of view, a quasi-equilibrium state, which is necessary to the measure, can be very difficult to achieve, especially at high temperatures where the properties of the thermoset evolve quickly.

For a stepwise polymerization, such as in epoxies, a simplification consists into considering a homogeneous chain growth, reducing the molar mass distribution to a single value $M_{TS}(T, t)$. M_{TS} being a growing function of time, the second favourable term in equation 7 decreases (in absolute value), leading to phase-separation for $\Delta_m G > 0$.

The effect on χ' can be estimated with the transformation of reactive functions. For instance, according to Coleman tables^[84], a primary amine turning into a secondary amine increases δ_{TS} . The phase separation condition based on χ' depends on the chemical structure evolution (determined by the chemical reaction) and the polymerization extent:

$$\chi'(T, t) > \chi'_c(T, t) \quad \text{Eq. 12}$$

A critical molar mass $M_{TS,c}(T, t)$ at the onset of phase-separation can be evaluated from equations 11 and 12. Knowledge on the reaction kinetics links $M_{TS,c}(T, t)$ to a critical time t_c or a critical reaction extent α_c .

Remark: branched species and excluded volume effects were not taken into consideration here, but are expected to favour phase-separation.

2.1.3.2 Pseudo-ternary thermoset

The differences between bismaleimide and epoxy resins were described in chapter 1. The free radical polymerization component of the cross-linking mechanism for the BMI/DBA resin has consequences on the phase-separation thermodynamics. BMI and DBA react to quickly form high molecular weight and cross-linked species with a low volume fraction, finally leading to a dilute gel. In the reactive solvent case, the thermoset was considered as a single entity with an increasing molecular weight. Here, BMI, DBA and the BMI-DBA copolymer have to be treated as different species. The separated treatment of BMI and DBA will be experimentally justified in this chapter. Schroeder and co-workers studied the evolution of the phase diagram of a similar system: Styrene/methacrylate/PMMA^[87]. The theoretical basis of their work comes from the Flory-Rehner theory^[88], which adds an elastic contribution to the Flory-Huggins equation. Dušek and Dušková-Smrčková introduced a modification to the Flory-Rehner equation^[89], adapted in equation 13.

$$\frac{\Delta_m G}{\rho RTV} = \frac{\Phi_{TP}}{M_{TP}} \ln(\Phi_{TP}) + \sum_i \frac{\Phi_{TS,i}}{M_{TS,i}} \ln(\Phi_{TS,i}) + \Phi_{TP} \sum_i \chi'_i \Phi_{TS,i} + \nu_e \Phi_g \left(\frac{3}{2} (\Phi_g^{-2/3} - 1) + \frac{2}{f} \ln(\Phi_g) \right) \quad \text{Eq. 13}$$

The last term describes the behaviour after gelation, where an insoluble fraction (Φ_g) appears. The pre-factor ν_e stands for polymer chains between cross-links that contribute to elasticity. Cyclisation reduces ν_e . f is the functionality of a cross-link point.

In the pre-gel state, the last term of equation 13 is discarded. Four species have to be considered: BMI, DBA, copolymer and TP. The form of equation 13 assumes Flory parameters equal to 0 for pairs of thermoset species. During the curing process, phase-separation can be seen as the result of volume transfer from BMI and DBA to the copolymer.

Negative contributions decrease in absolute value under a critical value ($\Phi \simeq 0.37$):

$$\begin{aligned} & \frac{\Phi_{BMI}}{M_{BMI}} \ln(\Phi_{BMI}) \\ & \frac{\Phi_{DBA}}{M_{DBA}} \ln(\Phi_{DBA}) \end{aligned}$$

while for the copolymer, $\Phi_{copo} \ln(\Phi_{copo})$ first increases (becomes more negative) under the critical volume fraction ($\Phi_{copo} < 0.37$) but then decreases in absolute value. Adding the fact that M_{copo} increases, the copolymer contribution ends up decreasing in absolute value:

$$\frac{\Phi_{copo}}{M_{copo}} \ln(\Phi_{copo})$$

Using:

$$\Phi_{TP} + \Phi_{BMI} + \Phi_{DBA} + \Phi_{copo} = 1$$

The third term of equation 13 becomes:

$$\Phi_{TP} [\chi'_{copo,TP}(1 - \Phi_{TP}) + (\chi'_{BMI,TP} - \chi'_{copo,TP})\Phi_{BMI} + (\chi'_{DBA,TP} - \chi'_{copo,TP})\Phi_{DBA}]$$

A simple calculation made with Coleman tables [84] for the Alder-ene reaction shows that $\chi'_{BMI,TP} - \chi'_{copo,TP}$ and $\chi'_{DBA,TP} - \chi'_{copo,TP}$ are expected to be negative (see appendix E for calculation). Consequently this contribution also decreases with Φ_{BMI} and Φ_{DBA} .

From this analysis, it appears that the phase-separation process in bismaleimide resins follows different laws by comparison with epoxy resins. The post-gel phase separation was not treated here because a *gel* phase is already a kind of phase separation. Nevertheless, a *sol* fraction containing the thermoplastic coexisting with a diluted thermoset *gel* fraction could be assumed, with a behaviour predicted by equation 13. Post-gel phase separation is not observed in epoxy resins because gelation implies a strong increase of viscosity. However, molecular mobility being not completely suppressed in a non-glassy biphasic gel, phase enrichment can still occur.

2.2 Literature on bismaleimide/thermoplastic blends

The use of elastomers^[90,91] will not be discussed here. These systems limit the high temperature performances and are efficient only with loosely cross-linked networks^[92,93]. As for epoxy-based systems, some studies have focused on BMI/TP blends. The challenges for these studies lie in the observation of morphology generation and the understanding of structure-properties relationships. Commonly used with epoxies, polyethersulfones (PES) and polyetherimides (PEI) have naturally been added to the list of polymers which could reinforce BMI resins.

2.2.1 Polyethersulfones

Liu and co-workers have studied the phase separation of PES in a BMI/DBA resin. A spinodal decomposition mechanism was identified by time resolved light scattering (TRLS). Based on a Maxwell model, a relaxation time has been calculated. This relaxation time is attributed to the characteristic extraction time of BMI out of the PES phase^[94]. Increasing the TP proportion or its molar mass (Figure 38) yields a range of morphologies from PES particles in a resin phase matrix to phase-inverted structures, including co-continuous morphologies^[95].

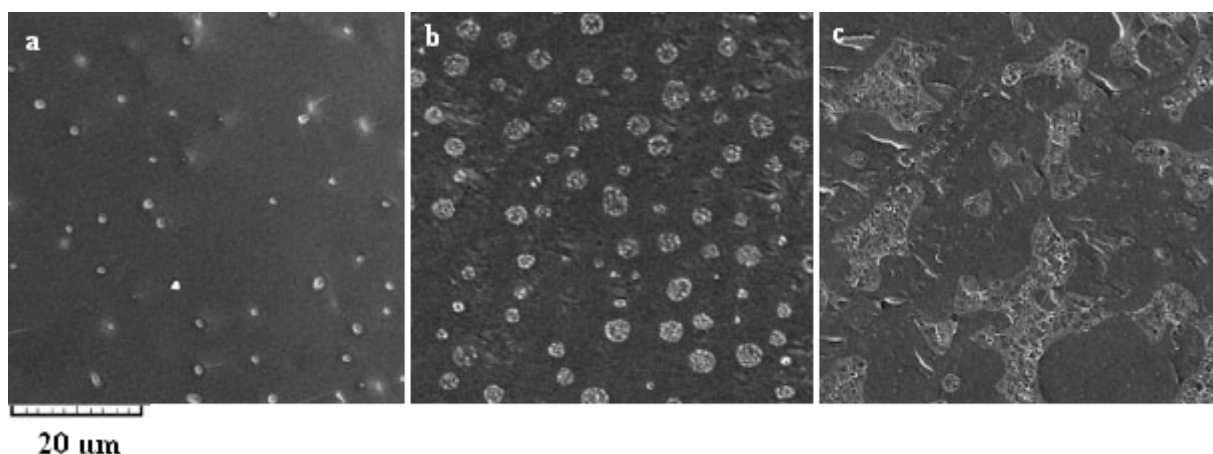


Figure 38: SEM image: morphology of a BMI/DBA/PES blends. a) 5%wt ; b) 10%wt ; c) 15%wt. PES appears as bright domain. From [95].

Using a different approach, Kurdi et Kumar have synthesized BMI/PES films with 90%wt PES, with a solvent-cast method. They obtained inter-penetrated polymer networks (IPNs), excepted when the solvent evaporation is slow. In that case, the morphology consists in BMI spherical particles (10 μm) in a PES-rich phase^[96].

2.2.2 Polyetherimides

Abbate and co-workers have used PEI to toughen a BMI/DDS blend. The 10 phr^a material consists in small (around 2 μm) and bigger (from 50 μm to 100 μm) PEI particles in a BMI continuous phase. Big particles seem to constitute a phase-inverted morphology, therefore containing BMI domains. When the PEI proportion is increased, small particles are replaced by big particles and then by larger domains. With a sufficient proportion of PEI, the whole material exhibits a phase-inverted morphology. Increasing the PEI

^aparts per hundred parts of resin

content leads to an increase of K_{IC} (up to around $0.7 \text{ MPa.m}^{\frac{1}{2}}$) and G_{IC} (up to around 200 J.m^{-2}) [90].

Jin and co-workers have studied the influence of the chemical structure of PEI [97] and the PEI content [98] in a BMI/DBA resin. The resulting morphologies depend on the type of PEI. Once again, phase-inverted and co-continuous structures with PEI inclusions in the BMI phase are obtained. The TP content is also a crucial parameter. At 10 phr a co-continuous structure with TP inclusions in the TS phase and reciprocally is obtained (Figure 39). At 15 and 20 phr, a phase-inverted morphology is obtained. In these cases, the higher the PEI proportion, the smaller the BMI particles. DMTA displays two relaxation peaks, attributed to the cross-linked network T_α and the PEI T_α . At 15 and 20 phr, a spinodal decomposition mechanism has been identified with TRLS. The resulting best properties are $1.64 \text{ MPa.m}^{\frac{1}{2}}$ for K_{IC} and 667 J.m^{-2} for G_{IC} .

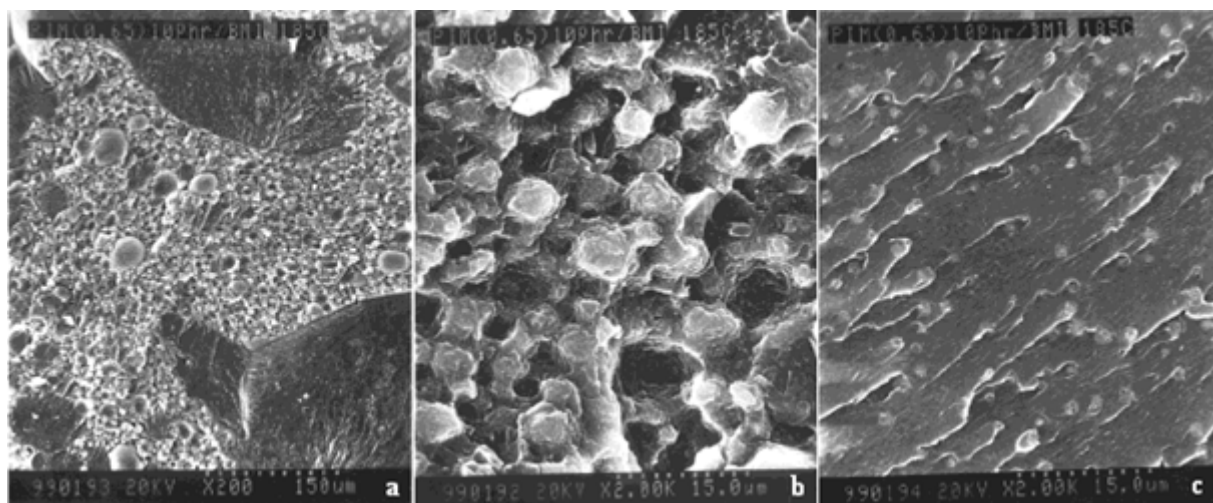


Figure 39: SEM image: morphology of a BMI/DBA blend with 10 phr of PEI. a) global view ; b) PEI-rich phase ; c) BMI-rich phase. From [98].

2.2.3 Polyesters

Iijima and co-workers have paid many efforts to reinforce thermosetting matrices with thermoplastics. They have used copolymerized polyesters and have identified key parameters for tuning properties of a BMI/DBA resin [99,100]. They have shown that K_{IC} increases with the TP concentration or with its weight average molecular mass (M_w). K_{IC} increases from $0.62 \text{ MPa.m}^{\frac{1}{2}}$ to, at best, $1.2 \text{ MPa.m}^{\frac{1}{2}}$ (20 %wt of a $M_w = 18,200$ copolyester). With less flexible aromatic polyesters, a different behavior has been observed. K_{IC} increases up to a maximum before decreasing, while increasing the TP content or its weight average molecular mass. They have also shown that a careful choice of these two parameters allows to maintain the mechanical flexural properties (with aromatic polyesters) and even to enhance them (with flexible polyesters). The decrease of T_g depends on the blend composition. The resulting morphologies are dispersions of TP particles (size around $1 \mu\text{m}$) for flexible polyesters. In the case of rigid polyesters, co-continuous and phase-inverted morphologies can also be obtained when the TP proportion increases (Figure 40). In this particular case, owing to the K_{IC} , the latter morphology is not efficient for toughness improvement. A macroscopic phase separation is observed for a high enough TP content. A third study using polyesterimide copolymers tends to confirm those results [101]. In this case the maximum value of K_{IC} is $1.16 \text{ MPa.m}^{\frac{1}{2}}$ (30 %wt of a $M_w = 13,500$ copolyester).

For all these TP, this group have shown that a transesterification occurs with the DBA phenol functions in the last curing step at 245°C. This leads to a chemical integration of the TP in the TS, which makes the identification of morphologies much more complicated. This also seems to play a positive role for toughness enhancement, possibly because of a plasticizing of the TS network by the TP segments and/or a better TS/TP interface.

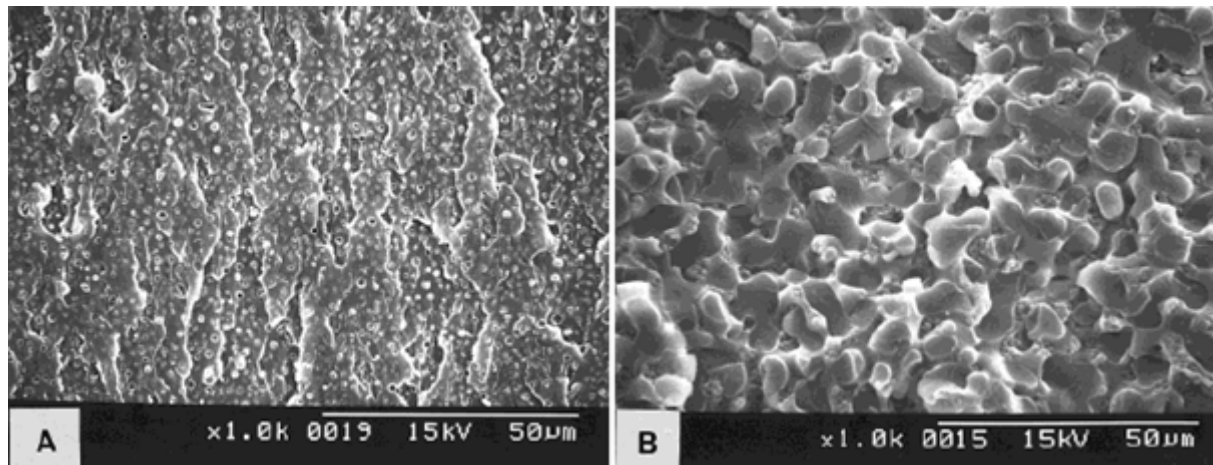


Figure 40: SEM image : morphology of a BMI/DBA blend with 5%wt copolyester.
A) $M_w = 126,000$; B) $M_w = 274,000$. From [99].

Gopala, Xu and co-workers have studied the BMI/DBA system reinforcement with hyperbranched polyesters (similar to small dendrimers) [102,103]. The main advantage of these compounds is that they do not raise the viscosity as much as linear counterparts. The higher the degree of branching, the higher the K_{IC} , with a maximum of 1 MPa.m $^{\frac{1}{2}}$ compared to 0.42 MPa.m $^{\frac{1}{2}}$ for the neat resin. The only observed morphology consists of spherical inclusions of polyester in the resin. These particles are bigger (from 0.2 μm to 15 μm) and more irregular when the degree of branching increases. The suggested reinforcing mechanism is related to the cavitation of TP inclusions.

2.2.4 Polyimides

There are fewer studies on bismaleimide reinforcement with polyimides. Pascal and co-workers have obtained heterogeneous blends of BMI with linear polyimides, described as semi-IPNs [104,105]. Qin and co-workers have used a hyperbranched polyimide with a BMI resin which monomer contains ether bonds. Toughness is only slightly enhanced: 0.55 MPa.m $^{\frac{1}{2}}$ (5 %wt and 15 %wt of polyimide) compared to 0.48 MPa.m $^{\frac{1}{2}}$ [106]. Gopala and co-workers have also prepared polyimide-based BMI by two different strategies. The first one uses DBA as a solvent to generate polyimide oligomers before adding BMI. This method only leads to small improvement in K_{IC} (0.7 MPa.m $^{\frac{1}{2}}$ compared to 0.4 MPa.m $^{\frac{1}{2}}$) [107]. In the second one, a comb-shaped polyimide which ends can be reactive or not. This parameter affects toughness in two ways. On one hand, reactive chain, reactive chain ends makes the TP more soluble in the resin, which does not favour the toughness enhancement. On the other hand, better cohesion between TP and TS is achieved, which raises the toughness. The best compromise (20 %wt) achieves a value of 1.05 MPa.m $^{\frac{1}{2}}$ for K_{IC} (compared to 0.42 MPa.m $^{\frac{1}{2}}$ for the neat resin) [108].

2.2.5 Polyether ketones

Those thermoplastics usually exhibit high T_g and good thermal stability. Iijima and co-workers have reinforced BMI resins with Polyether ketone ketones (PEKK). With a BMI/DBA resin, K_{IC} increases from 0.67 MPa.m $^{\frac{1}{2}}$ to 1.17 MPa.m $^{\frac{1}{2}}$ (10 %wt). Toughness is enhanced with higher M_w and content of TP(Figure 41). By varying these parameters, various morphologies are obtained (particles, co-continuous and phase-inverted) (Figure 41) [109]. With a BMI/DBA/dimethylallyl, similar results are observed, K_{IC} increasing from 0.9 MPa.m $^{\frac{1}{2}}$ to 1.21 MPa.m $^{\frac{1}{2}}$ [110]. In both studies, an IPN has been evidenced around the boundary between TP and TS phases.

Han and co-workers have used polyphthalazinone ether ketone (PPEK) to improve the toughness of a BMI/DBA resin. They have observed a spinodal decomposition mechanism for the phase separation and co-continuous or phase-inverted morphologies. With a 10 phr content of PPEK, the value of K_{IC} is 1.64 MPa.m $^{\frac{1}{2}}$ (compared to 1.36 MPa.m $^{\frac{1}{2}}$ for the neat resin). For this TP content, the suggested reinforcing mechanism is the concentration of stress by the TP domains and the yielding of the TS resin around these domains. With a 20 phr PPEK content, K_{IC} drops, which is correlated with the observation of de-cohesion between the TP and TS phases upon fracture [111].

With a polyether ketone and a BMI/DBA resin, Mai and co-workers have observed co-continuous morphologies [112]. Zhang and co-workers have evidenced the toughening of such a system [113]. Ding and co-workers have reached the same conclusion using PEEK [114].

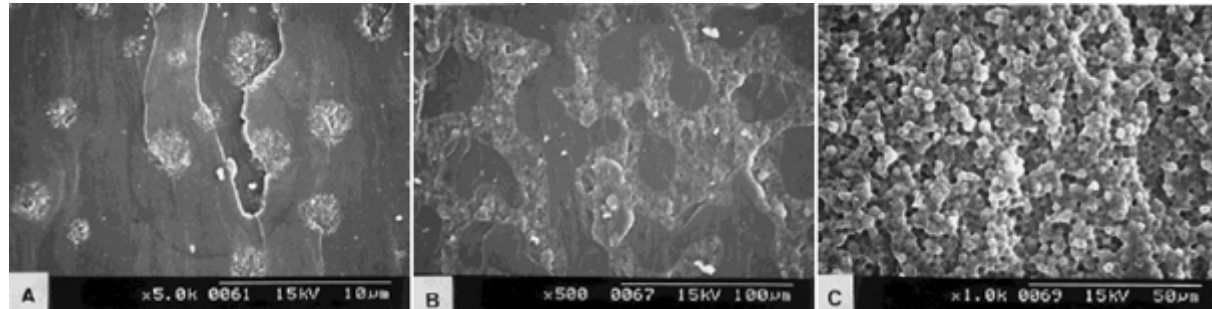


Figure 41: SEM image: morphologies of BMI/DBA blended with PEKK ($M_w = 27,300$). A) 5%wt ; B) 10%wt ; C) 15%wt. From [109].

2.2.6 Other polymers

Iijima and co-workers have also used various copolymers to toughen BMI/DBA resins derivatives. The resulting morphologies and the evolution of the materials properties are similar to those from their studies described previously. Among different conclusions, they exposed that for some systems, an optimal co-continuous morphology for fracture resistance can be found. It requires a control of the extent of the phase separation [115, 116].

2.2.7 Conclusion

Many thermoplastics have been used to enhance the fracture resistance properties. Various morphologies can be obtained by reaction induced phase separation as classically observed for epoxy-based systems. Significant toughness improvements are obtained by tuning the thermoplastic nature, content, molecular weight, and, as a consequence, the

blend morphology. The thermoset/thermoplastic interface is also a key-parameter for reinforcement. However very few studies have reach the composite material stage, including fibres. Furthermore, most of the involved high performance thermoplastic are home-made polymers, which are consequently not commercially available.

2.3 Experimental details

2.3.1 Selected materials

2.3.1.1 Thermoset

The standard BMI/DBA resin that has already been introduced in the first chapter was used here with an adapted blending procedure to include thermoplastics.

2.3.1.2 Thermoplastics

Two kinds of thermoplastics have been selected. The first one gathers families of polymers that are initially soluble in the BMI resin. They fall under the scope of reaction induced phase separation study. They are expected to enhance the fracture resistance of the resin matrix. Many families of thermoplastics have been introduced in the previous part. Only two of them have been selected: PES and PEI. They are compatible with applications up to 200°C and available at an industrial scale.

The second kind of thermoplastics consists in non-soluble thermoplastics. They are expected not to dissolve in the BMI/DBA resin. The role of thermoplastic particles in thermosetting resins toughening has been less investigated than for soluble thermoplastics. Particles are expected to be efficient to toughen laminates with few influence on the resin properties. The selected polymers are polyamide-imide (PAI) and polyimide (PI), which are stable at high temperature.

The main properties of the selected thermoplastics are listed in table 3 and the chemical structures are presented in Figure 42. All of them are amorphous.

Polymer and designation	M_w (g/mol) ^a	Powder size (μm) ^b	T_g (°C)	T_d (°C) ^c
Polyethersulfone (PES ⁱ)	22,000	75	225 ^d	450
Polyethersulfone (PES ^h)	45,000	65	225 ^d	457
Polyetherimide (PEI)	55,000	250	225 ^d	543
Polyamide-imide (PAI)	—	1 to 25	280 ^d	582
Polyimide (PI)	—	5	350 ^a	555

Table 3: selected thermoplastics and their main properties.

a: estimated with supplier technical data ; *b:* measured by optical microscopy ; *c:* measured by TGA ;
d: measured by DSC.

Degradation temperature (T_d) is indicated at the maximum degradation rate under air at 10°C/min. Weight loss curves are displayed in appendix F for degradation under air and nitrogen.

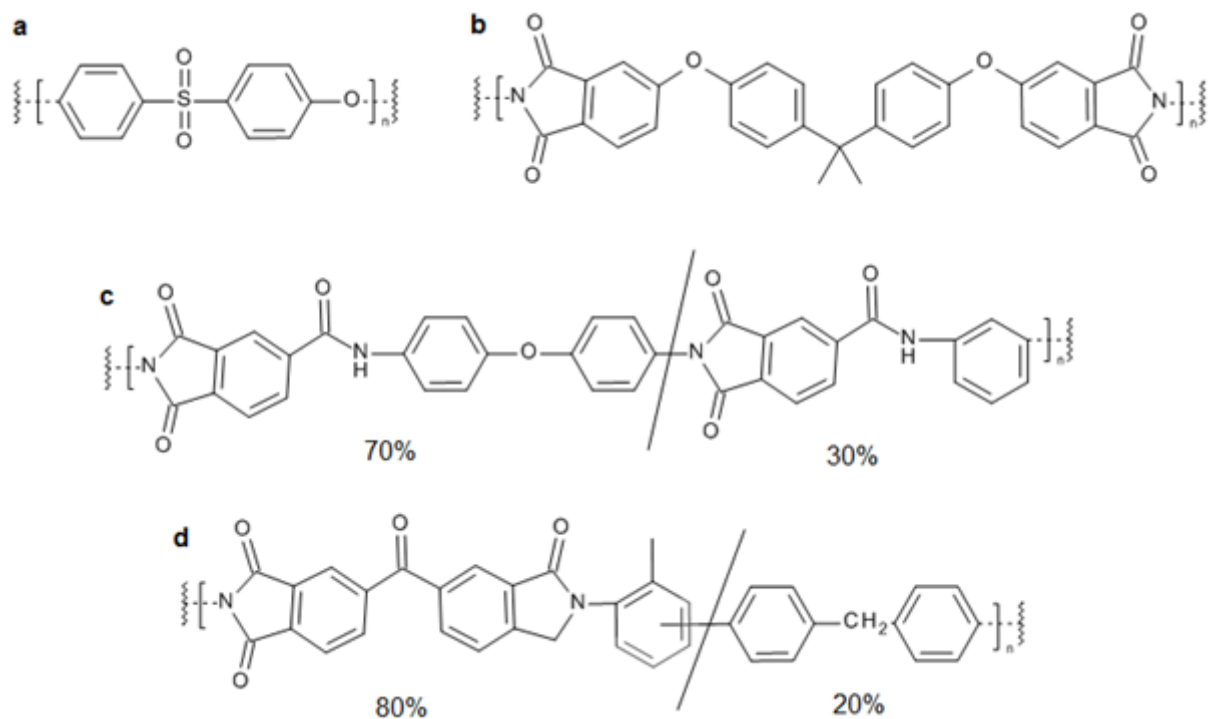


Figure 42: chemical structures of the selected thermoplastics. a) PES ; b) PEI ; c) PAI ; d) PI.

2.3.2 Methods

2.3.2.1 Blend preparation

The resin is made of two parts, among which one is liquid (DBA). Conveniently, the thermoplastics were solubilised in this liquid part before adding BMI. Figure 43 displays a scheme of the experimental device and mixing procedure.

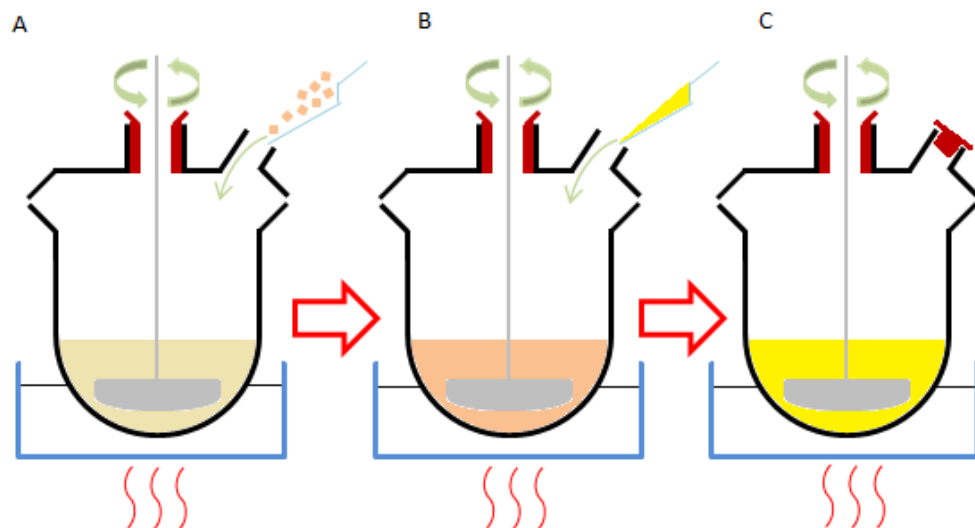


Figure 43: experimental procedure to blend soluble thermoplastics with a bismaleimide resin.

The compounds are blended in a glass reactor heated by an oil bath. The blend is mechanically stirred with a PTFE blade. During step A, DBA is heated up to around

130°C and the TP is added. The blend is stirred until it becomes clear or at least homogeneous. During step B, BMI is added and the blend is mixed until it becomes homogeneous. Usually, BMI is not completely solubilised during the last step (C). For low TP concentrations (under 5 phr), a transparent blend can still be obtained. Nevertheless, at this stage, a suspension has been preferred for several reasons. First, it would be quite difficult to obtain blends with the same initial reaction state. With a suspension, as long as BMI is not solubilised, polymerization is expected not to start. Second, it would be even more difficult considering the fact that the solubilisation time of BMI depends on the nature and the amount of TP previously added. Finally, as it will be explained later, for some blends, phase separation can occur during the solubilisation of BMI.

The thermoplastic content is conveniently expressed in *phr*, which means part per hundred part of resin. This proportion is the ratio of the mass of thermoplastic by the mass of resin multiplied by 100. Here the resin considered is the blend of BMI with DBA. Table 4 gives mass percentage correspondence.

phr content	mass percentage (%)
1	1
5	4.8
10	9.1
15	13
20	16.7

Table 4: correspondence of phr with mass percentage.

2.3.2.2 In situ temperature controlled microscopy

Most morphological investigations use cured samples under optical microscopy or electron microscopy [90, 95, 97–103, 110–116]. This allows to describe the phase structure only in its final state. Even if some methods enable to follow the phase separation at several times [111], these remain observations after the fact. Moreover, if scanning electron microscopy allows to identify finer elements than optical measurements, it requires to cut or fracture samples, which may alter the morphology.

An optical microscopy experiment has been specifically dedicated to following phase separation phenomena directly during curing. A heating stage (red arrow on Figure 44) has been set under a regular optical microscope equipped with a video camera. The heating stage could be controlled to reproduce various classical curing conditions, with ramps up to 20°C/min and temperatures up to 400°C. The microscope is usually used in a transmission mode because the studied blends are transparent.

Samples were prepared by placing a small piece of blend on a glass plate and heating it at sufficient temperature to soften the blend. This temperature is usually between 40°C and 100°C. In this range, neither polymerization reaction nor phase separation are expected to occur. Once softened, the sample was degassed under vacuum to ensure that no bubbles would alter the observation. A glass cover slip was finally pressed on the sample still soft. During the heating phase, the blend spreads between the two glass layers, which requires a constant focus adaptation. When the thickness is stabilized, continuous observation can easily be carried out.

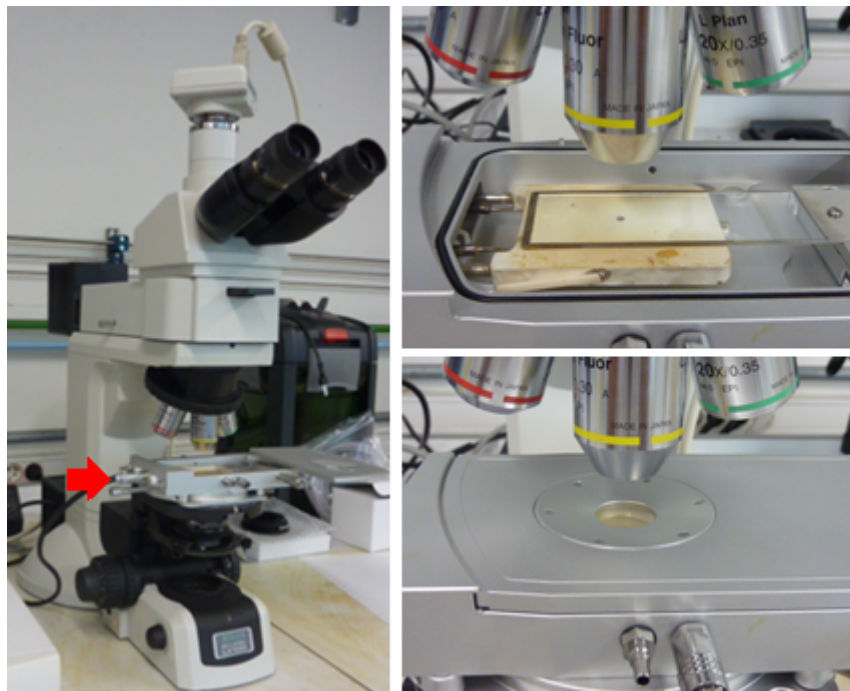


Figure 44: optical microscope with a heating stage.

Because samples are thin layers, superposition of objects has to be questioned. Depending on the depth field, an object that seems to be inside an other one might be above or under it (Figure 45). The depth of field Δz is the thickness of the slice of sample that gives an image. It can be calculated with equation 14.

$$\Delta z = \frac{\lambda \sqrt{n^2 - NA^2}}{NA^2} \quad \text{Eq. 14}$$

λ is the wavelength of the incident light, n the refractive index of the medium between the sample and the objective and NA the numerical aperture of the objective. Choosing 600 nm for λ and 1 for n (air), Table 5 summarises the depth of field values for the available objectives. Assuming that small circles (a few micrometers) on images correspond to spherical objects, with the last three objectives, they can be considered as contained in the same plan.

Objective	NA	$\Delta z(\mu\text{m})$
5x	0.15	26
10x	0.30	6
20x	0.35	5
50x	0.45	3

Table 5: depth of field of different microscope objectives.

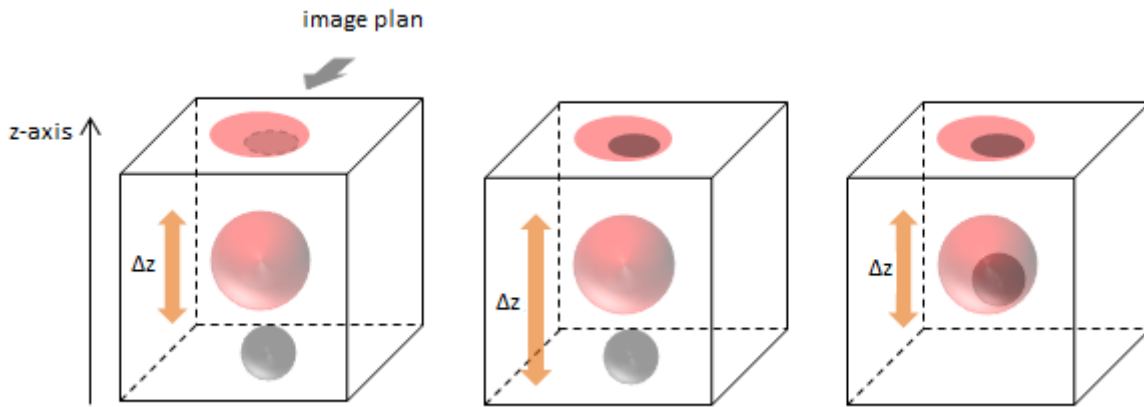


Figure 45: effect of the depth of field (Δz) on the image formed by superimposed or included objects.

2.3.2.3 Cured samples preparation

A mould has been designed for vertical curing of the blends (plan in appendix). The thickness of the sample is determined by the thickness of the central *U-shaped* part *e*. The central part is tightened up between two lateral parts, with six screws.

The general protocol for moulding a resin sample consists in two steps of degassing and moulding. A lateral part of the mould is tightened up to the central part with clips screws. The resin is placed on this lateral part, maintained horizontally. It is then degassed in an oven under vacuum. The flowing resin usually moulds itself during this step. The second preheated lateral part of the mould is pressed on the sample (clips are removed) and the mould is put in a vertical position and tightened up with the screws. The resin is degassed one more time vertically to ensure a correct moulding at the bottom of the mould. Using bare aluminium surfaces, coated only with a demoulding agent leads to samples with a well-controlled average thickness.

The standard curing cycle (see chapter 1) was used for all samples.

2.3.2.4 Optical microscopy on cured samples

Final morphology of cured samples was observed through the thickness on offcuts of DMA samples. They were polished with silicon carbide papers and diamond particle dispersions down to 1 μm . For blends including soluble thermoplastics, they were etched with dichloromethane so that the thermoplastic phases are removed from the surface. The microscope was used in reflection.

2.3.2.5 Electron Dispersive X-ray Spectroscopy

In addition to classic scanning electron microscopy (SEM) observations, spectroscopic analysis can be carried out. The incident electron beam ejects inner shell electrons (energy E_K) from atoms, resulting into a hole. An electron from the outer shell (energy E_L) fills in the hole, the exceeding energy being released by an X photon emission (energy $E_K - E_L$). X-ray emission spectra are characteristic from atoms, giving information on chemical composition.

Polished samples were coated with a thin layer of gold and palladium to avoid surface charging up and subsequent local degradation.

2.3.2.6 Dynamic Mechanical Analysis

Test samples were designed and analysed with the procedure described in chapter 1. Single cantilever tests were carried out with $48(\pm 0.5) \times 10(\pm 0.5) \times 2(\pm 0.1)$ mm³ samples, the length in the clamp being 17 mm. Oscillatory tests parameters were fixed to: $f = 1$ Hz; $\epsilon_0 = 0.1\%$; heating rate: 3°C/min.

2.3.2.7 Rheology

The experimental procedure described in chapter 1 was adapted here to estimate blends viscosity before phase separation. During an oscillatory test at an angular frequency ω , a complex viscosity can be defined by:

$$\eta^* = \eta' - i\eta'' = \frac{G^*}{i\omega} = \frac{G' + iG''}{i\omega}$$

The empirical Cox-Merz rule states [117]:

$$|\eta^*(\omega)| = \eta(\dot{\gamma}) \quad \text{at } \dot{\gamma} = \omega$$

Where η is the viscosity and $\dot{\gamma}$ the shear rate. Limitations are met for high frequency or high shear rate, where flow instability appears. Experimental parameters were fixed here: $f = \omega/(2\pi) = 1$ Hz, $\epsilon_0 = 1\%$.

2.4 Phase separation in bismaleimide/solubilised thermoplastic blends

2.4.1 Phase separation behaviours

As developed in the first part of this chapter, binary blends usually exhibit two kind of phase separation behaviour: LCST and UCST. The UCST-type is commonly met, with polymer solutions requiring heat. For the LCST-type, favourable interactions are needed, for instance hydrogen-bonds. High temperature leads to hydrogen-bonds dissociation and removes a favourable solvent/polymer interaction, possibly triggering phase separation.

For all the investigated bismaleimide/thermoplastic blends, it was not possible to define a LCST or UCST phase behaviour. To obtain a phase diagram such as on Figure 37, blends with different TP concentration have to be heated at different temperatures. Phase separation can be determined by various means, such as light scattering. The phase behaviour is not time-dependent, which brings the main experimental problem. Heating the bismaleimide blends quickly leads to polymerization, promoting phase separation independently from a LCST or UCST behaviour.

2.4.1.1 Polyetherimide

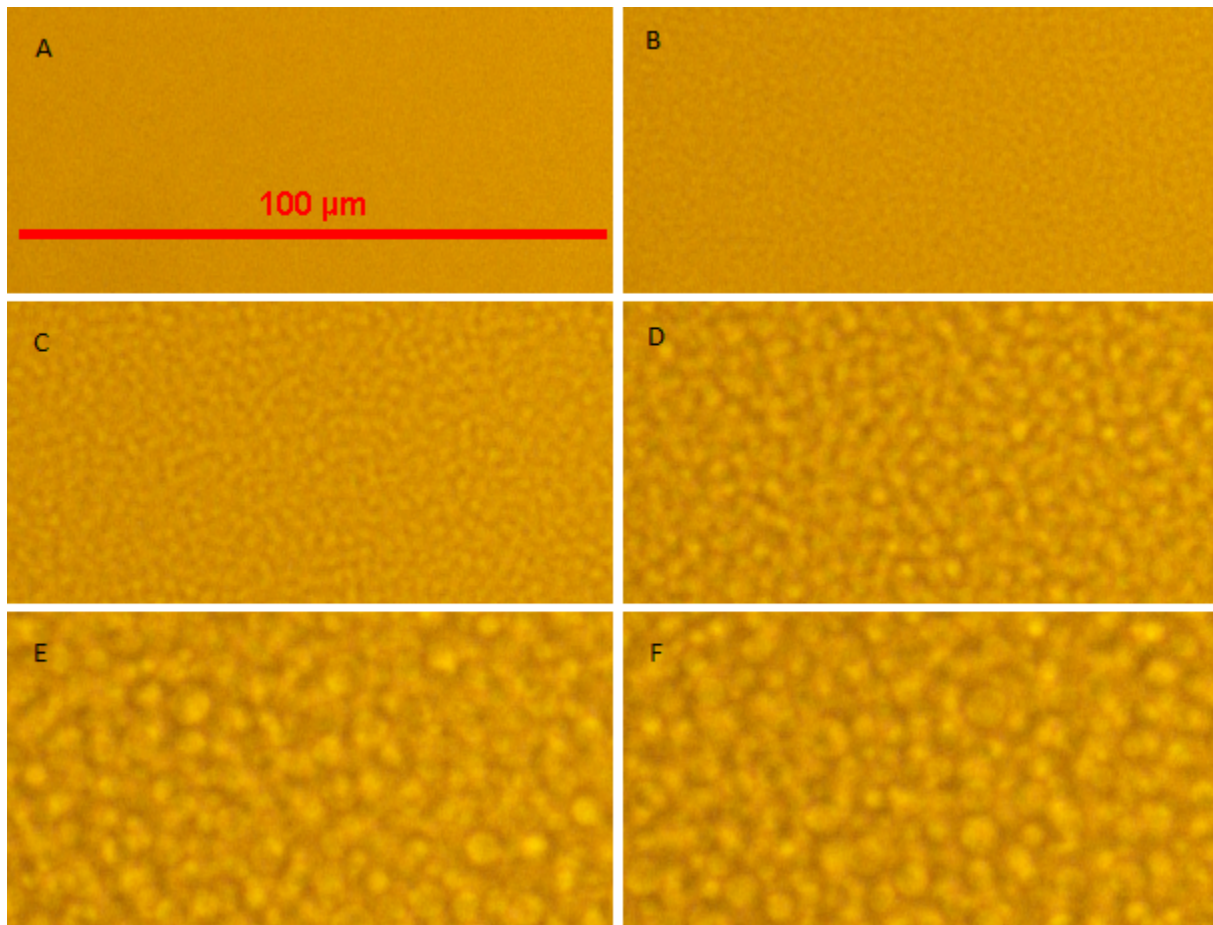


Figure 46: optical microscopy images of a BMI/DBA/PEI 5 phr blend during isothermal curing at 150 °C. A) 3 min ; B) 31 min ; C) 34 min ; D) 44 min ; E) 51 min ; F) 60 min.

Among the different thermoplastics used, PEI leads to the simplest phase separation process. It is indeed highly soluble in the liquid part of the resin and remain solubilised when the solid part is added. Therefore, phase separation is expected to occur only because of the polymerization reaction of the thermoset.

Under dynamic as well as isothermal curing conditions, phase separation seems to proceed the same way. Figure 46 shows different steps of the phase separation of a single sample with 5 phr of PEI. It was heated at 150°C with a rate of 20°C/min and maintained at this temperature for an hour. A fine structure progressively appears after nearly 30 min (Figure 46B). Its characteristic size grows, first quite rapidly (Figure 46B to D) and then stabilises (Figure 46E and F). During the first stage, the morphology seems to be co-continuous, with two interlaced phases. The final morphology displays particles. Considering that phase separation happens on the whole sample at the same time, this description corresponds to a spinodal decomposition process.

The same kind of phase separation takes place even if the proportion of PEI is changed, or in dynamic curing. Figure 47 shows the different steps of the spinodal decomposition of a blend with 10 phr of PEI. The final morphology contains big globules which size lies between 80 μm and 200 μm. A new phenomenon appears in the last stages of curing:

particles formed during spinodal decomposition undergo coalescence to create these bigger globules (Figure 48).

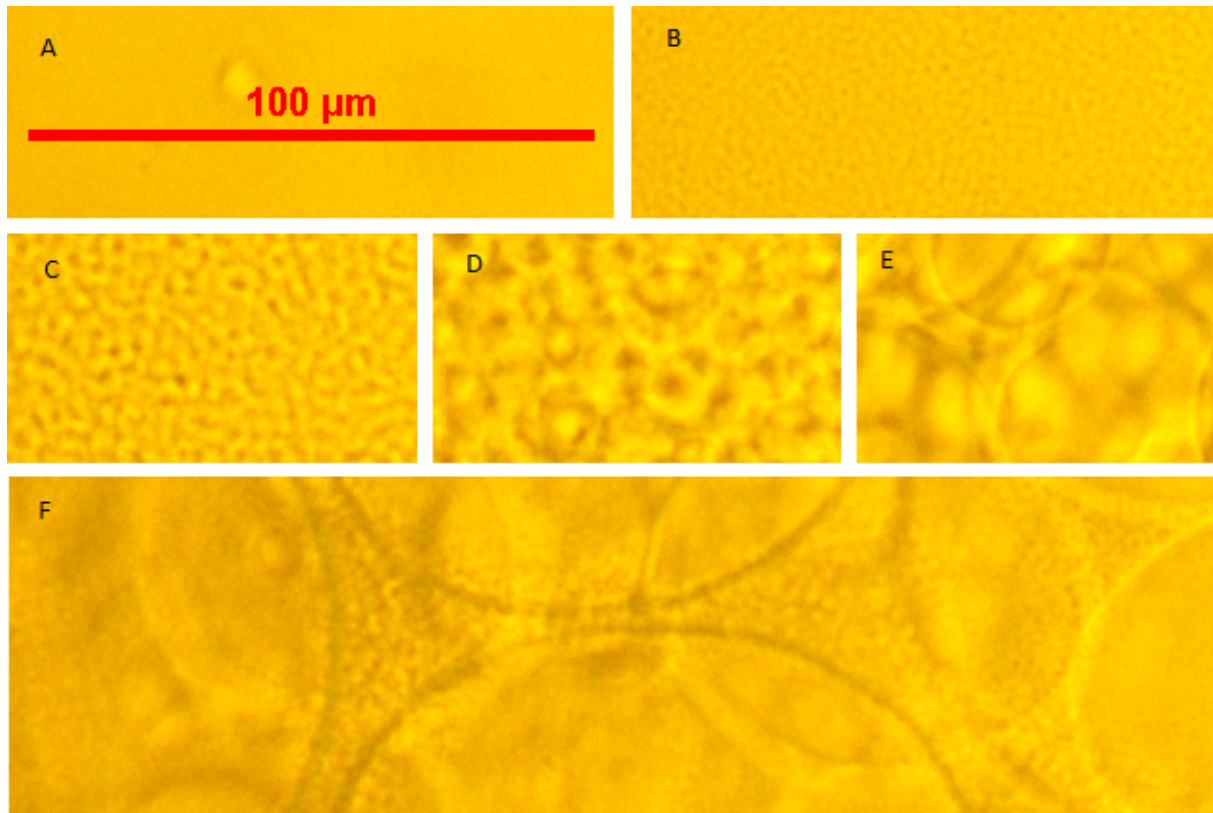


Figure 47: optical microscopy images of a BMI/DBA/PEI 10 phr blend during curing at 5 °C/min. A) 150 °C ; B) 183 °C ; C) 192 °C ; D) 203 °C ; E) 214 °C ; F) 224 °C.
Common scale 100 μm .

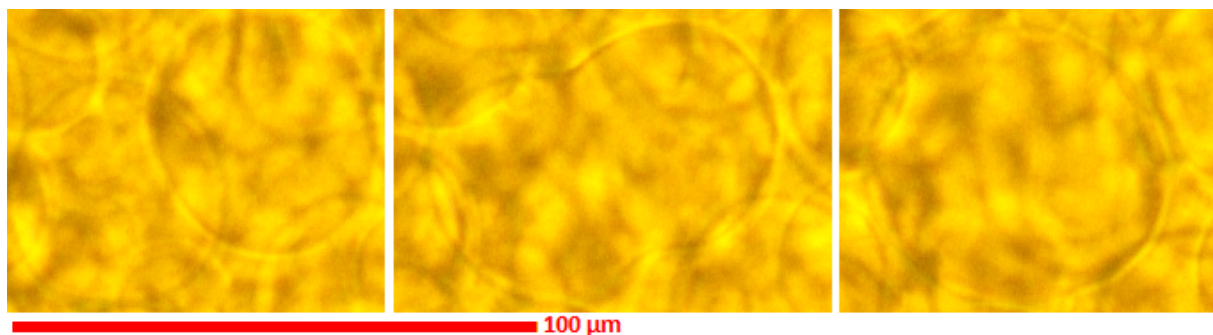


Figure 48: optical microscopy images of a BMI/DBA/PEI 10 phr blend during curing at 5 °C/min. Coalescence of particles around 210 °C. Common scale 100 μm .

2.4.1.2 Polyethersulfone

Two PES have been used in blends with the BMI/DBA resin. The main difference lies in their weight average molecular mass, PES^h having the higher M_w . These polymers having the same chemical structure, the Flory-Huggins equation (equation 7) predicts a greater solubility of PES^l, M_{TP} being the only parameter changed. Both thermoplastics were solubilised in the amount of DBA corresponding to a 5 phr blend in BMI/DBA. Microscopy observations showed no trace of remnant PES. The correct amount of BMI was added to complete the blend. Solubilisation of BMI was then followed by optical microscopy at 140°C. In the case of PES^h, after 20 minutes, small particles appears before BMI crystals

had completely disappeared. They have been attributed to the phase separation of PES. The same phenomenon was observed with PES^l but after 1h20 (Figure 49).

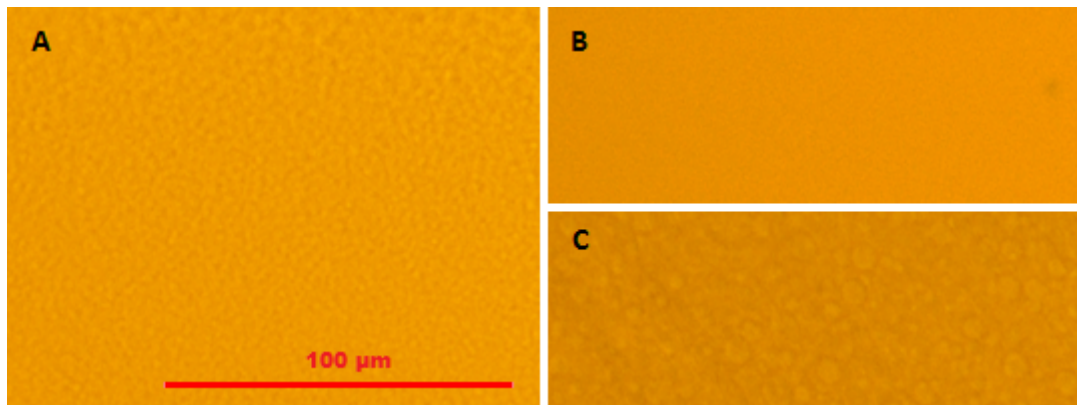


Figure 49: phase separation of PES during BMI solubilisation at 140 °C. A) PES^h after 20 min ; B) PES^l after 20 min ; C) PES^l after 80 min. Common scale 100 μm .

Two aspects have to be taken into consideration with this experiment. PES^l is indeed more soluble in the BMI/DBA resin because its phase separation occurs after a longer time than for PES^h. Furthermore, PES^h undergo a phase separation at a very low conversion rate, and probably before the beginning of polymerization (keeping in mind that BMI is not initially solubilised). This suggests that PES^h is completely soluble in neat DBA but no more in the BMI/DBA blend, a consequence of the critical molecular weight effect (equation 11).

As a result, the phase separation mechanism for PES^h blends is complex. Figure 50 displays the different steps encountered during dynamic curing at 2 °C/min for a blend with 10 phr PES^h. At a very early stage, several phases are distinguishable before the complete solubilisation of BMI crystals (Figure 50A). Phase separation goes on with well defined domains (Figure 50B). A fine structure then appears (Figure 50C and D).

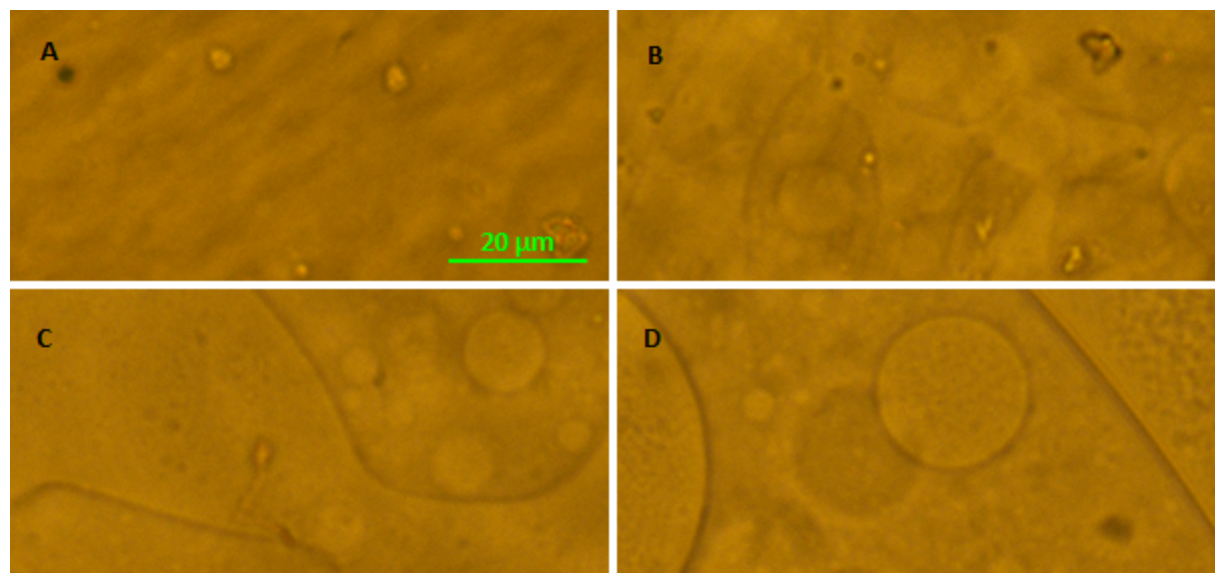


Figure 50: optical microscopy images of a BMI/DBA/PES^h 10 phr blend during curing at 2 °C/min. A) 105 °C ; B) 115 °C ; C) 127 °C ; D) 152 °C.

PES^l blends exhibit a phase separation behaviour very similar to PEI blends.

2.4.2 Final morphologies

2.4.2.1 Influence of curing conditions

Blends with PEI were heated at various heating rates to reach a fixed morphology (between 200°C and 250°C). Figure 51 shows the influence of the heating rate and the PEI content on the final morphology. Thermal conditions seem to have little effect. With 1 phr, small particles (size estimated around 1 µm) are present whatever the conditions. With 10 phr, the final morphology is always the same as introduced on Figure 47F: big globules with a continuous phase that contains smaller particles (around 1 µm). The globules also seem to exhibit a particular morphology. For an intermediate thermoplastic content, 5 phr, particles are formed. They are bigger than in the case of a 1 phr PEI blend (from 3 µm to 10 µm). All these values are estimations performed on a limited number of images without any statistical treatment.

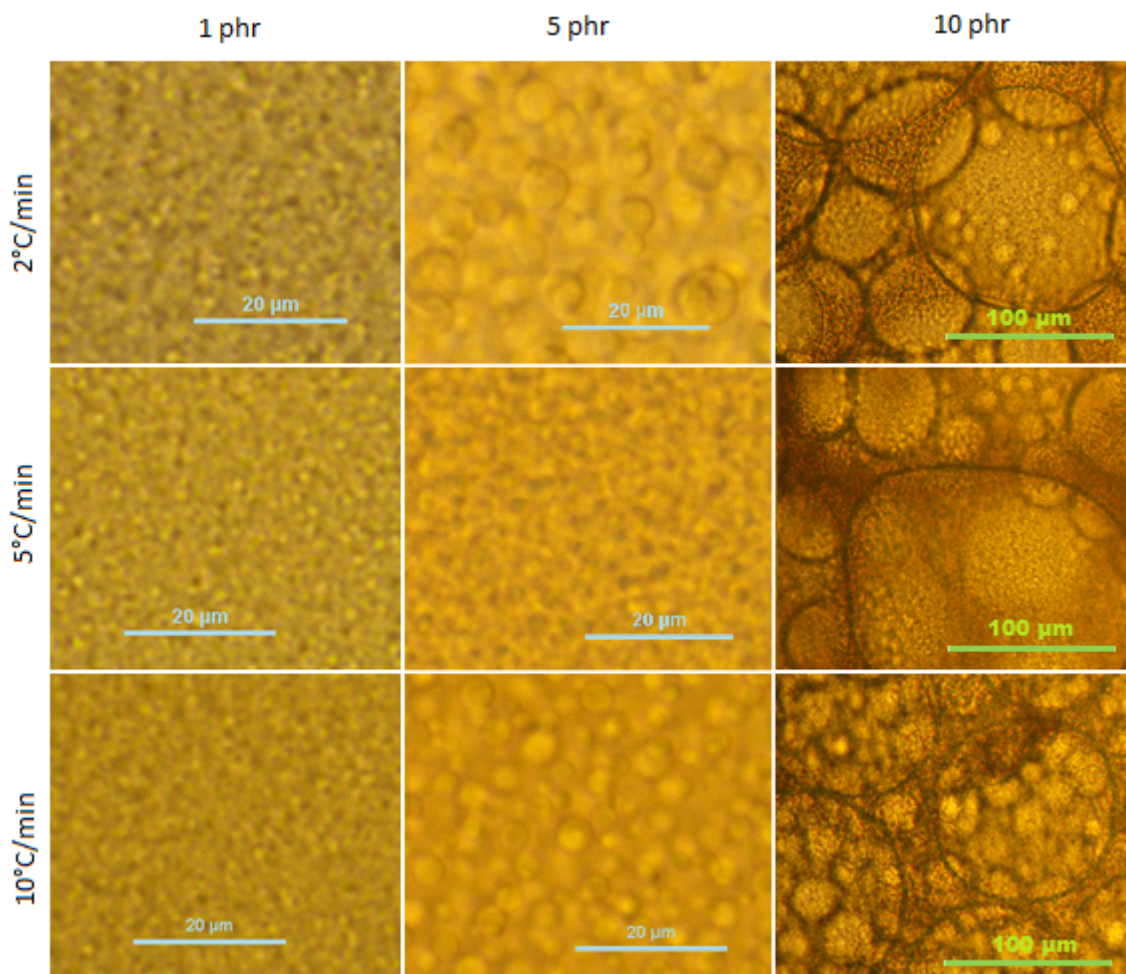


Figure 51: optical microscopy images of BMI/DBA/PEI blends final morphologies for different heating rates.

Blends with PES^l contents of 5, 10 and 15 phr were observed during curing to identify the phase separation mechanism and the final morphologies. These can be seen on Figure 52 for different heating rates. The blend with 5 phr of PES^l exhibits small particles (around 1 µm) whatever the heating rate. With 10 phr, the particles size distribution is wider. After a temperature ramp at 2°C/min, particle size ranges from 5 µm to 15 µm, with a very high proportion of sizes close to 5 µm. At 5°C/min, the minimal particle size remains around 5 µm but some bigger objects are measured around 20 µm. Finally,

at 10°C/min, the bigger particles size is still around 20 µm but the small particles average size slightly increases. For the 15 phr blend, a low heating rate (2°C/min) results into macroscopic phases which contains particles of various sizes up to 50 µm. At higher heating rates, no more macroscopic phases are visible. At 5°C/min, two populations are visible, numerous smaller particles with very various sizes and some bigger ones up to 80 µm. At 10°C/min bigger particles only reach 30 µm.

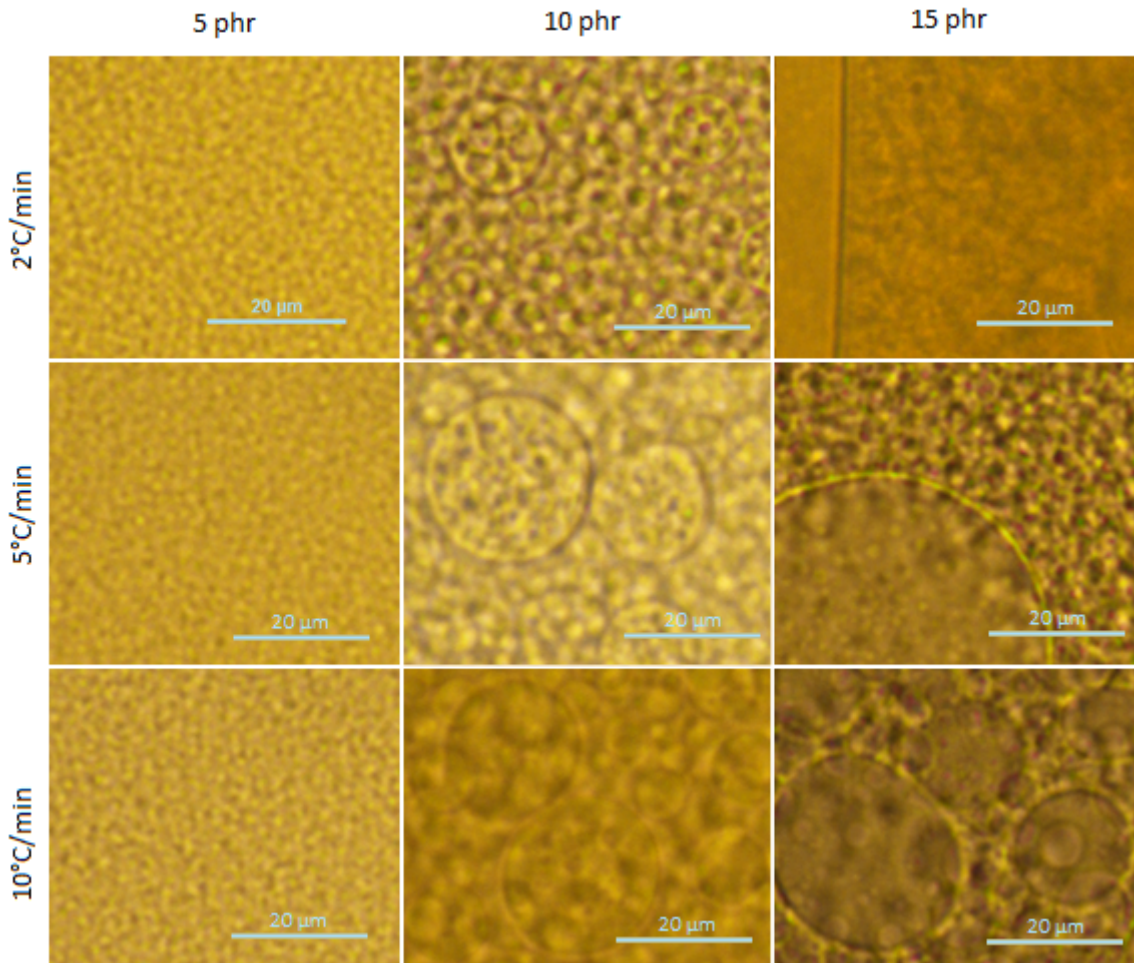


Figure 52: optical microscopy images of BMI/DBA/PES^l blends final morphologies for different heating rates.

The morphologies of blends with 1, 5 and 10 phr of PES^h were investigated at different heating rates (Figure 53). The blend at 1 phr displayed small particles around 2 µm. The contrast being very poor, no image will be presented here. The heating rate does not seem to influence the final morphology. The blend with 5 phr exhibits particles which nearly all have a size under 15 µm. Some very big particles are also present (around 100 µm) and seem to contain a fine substructure (1-5 µm, not shown here). The morphology of the blend with 10 phr is similar to the corresponding blend with PEI. Big phases (millimetre size) containing small particles (under 10 µm) coexist with a phase with a lower density of particles. These later have quite a wide size distribution between 20 µm and 100 µm, bigger ones display a fine structure (a few micrometres, not shown here).

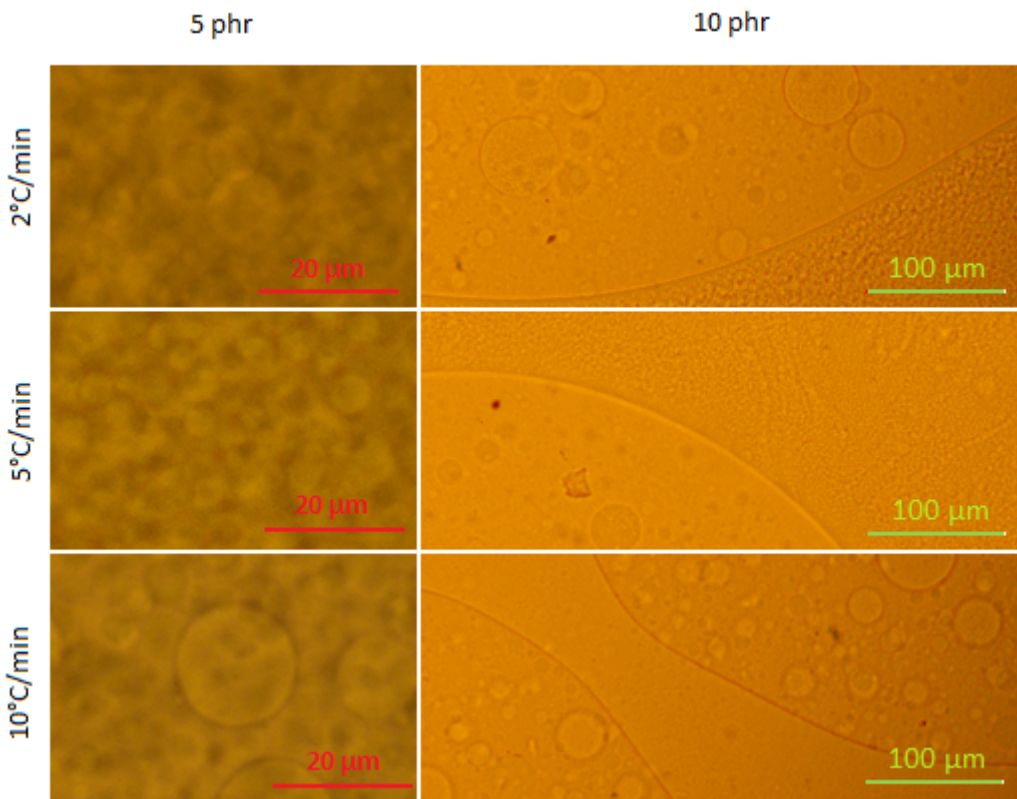


Figure 53: optical microscopy images of BMI/DBA/PES^h blends final morphologies for different heating rates.

Remark: A blend with 20 phr of PES^h has also been observed. It develops a phase-inverted morphology while curing, but it is very difficult to handle (highly viscous and sticky). As a result air bubbles always remain trapped in samples, making impossible to properly observe phase separation. Consequently, this blend has not been further investigated.

2.4.2.2 Comparison between thermoplastics

From the previous observations, similarity arises between the different bismaleimide-thermoplastic blends. The final morphologies resulting from the standard curing procedure were observed on solid samples.

Figure 54 displays the resulting morphologies for PEI blends. At 1 phr, particles around 1-2 μm are spread on the surface. Some isolated structures sometimes appear (see the left side of Figure 54B). They may be the result of local heterogeneities, for instance a high concentration of PEI that would lead to a localised phase inversion. At 5 phr, most of the surface is covered by particles from 2 μm to 10 μm. There are also bigger nodules up to 200 μm which exhibit a phase-inverted structure, containing TS particles with a wide size distribution (between 1 μm and 50 μm). Increasing the PEI content to 10 phr leads to quite a complex morphology. Big particles (200 μm) and macroscopic globules (millimetre size) are formed. The continuous phase also seems to contain smaller particles (from 10 μm to 50 μm). Considering that dark parts stand for the removed thermoplastic, all these particles are made of BMI-rich phases, which would mean a first scale phase-inverted morphology. Bigger particles also exhibit a second scale morphology with co-continuous parts and particles (typical size around 10 μm). Closely looking at these smaller objects reveals even smaller black spots, which would mean fine TP particles

(around 1 μm). At least three levels of phase separation have been observed with this blend.

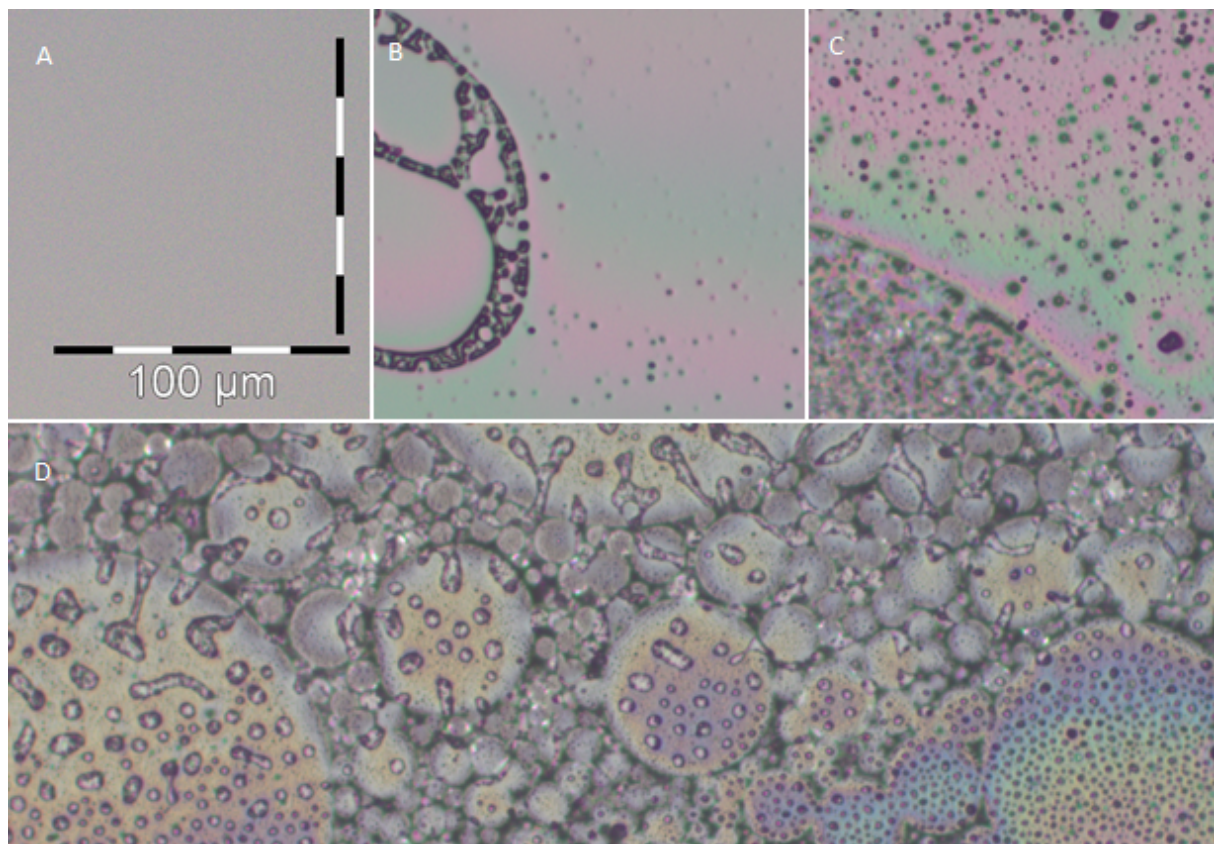


Figure 54: morphologies of BMI/DBA/PEI blends cured with the standard curing cycle.
A) neat resin ; B) 1 phr ; C) 5 phr ; D) 10 phr. Common scale 100 μm .

These observations are consistent with *in situ* microscopy, especially for blends with 1 and 5 phr. The morphology of the 10 phr blend seems more complex on solid samples, which can be explained in two ways. First, structure identification is more difficult with optical microscopy in transmission. The contrast is lower than when etching with dichloromethane and many objects are superimposed. Second, increasing the thickness of samples changes the geometry from nearly two dimensions to three dimensions, which may lead to more available volume for phases reorganisation. Nevertheless, there are common features between these two experiments with at least two levels of phase separation involving globules and fine particles.

Figure 55 shows morphologies for PES^l blends. With 5 phr, small particles (1-2 μm) are visible all over the sample surface. Increasing the PES content up to 10 phr leads to bigger particles (2 to 5 μm). Big inverted phases globules (over 100 μm) also appear. They contain particles of various sizes up to 30 μm . With 15 phr of PES^l, big globules are spread all over the sample surface in a continuous phase that contains particles up to 10 μm . The internal morphology of globules is not visible which may be a consequence of a very low contrast. Remembering that the heating rate was here chosen at 3°C/min, these observations are in good agreement with the previous investigation for blends at 5 and 15 phr. The minimal particle size for the 10 phr blend is lower than expected. This may be explained by a mis-evaluation of this characteristic on samples for microscopy in transmission. The superposition of numerous particle layers makes the estimation more

difficult. The big objects observed here are not visible on the previous images. This difference might be due to a volume or thermal effect.

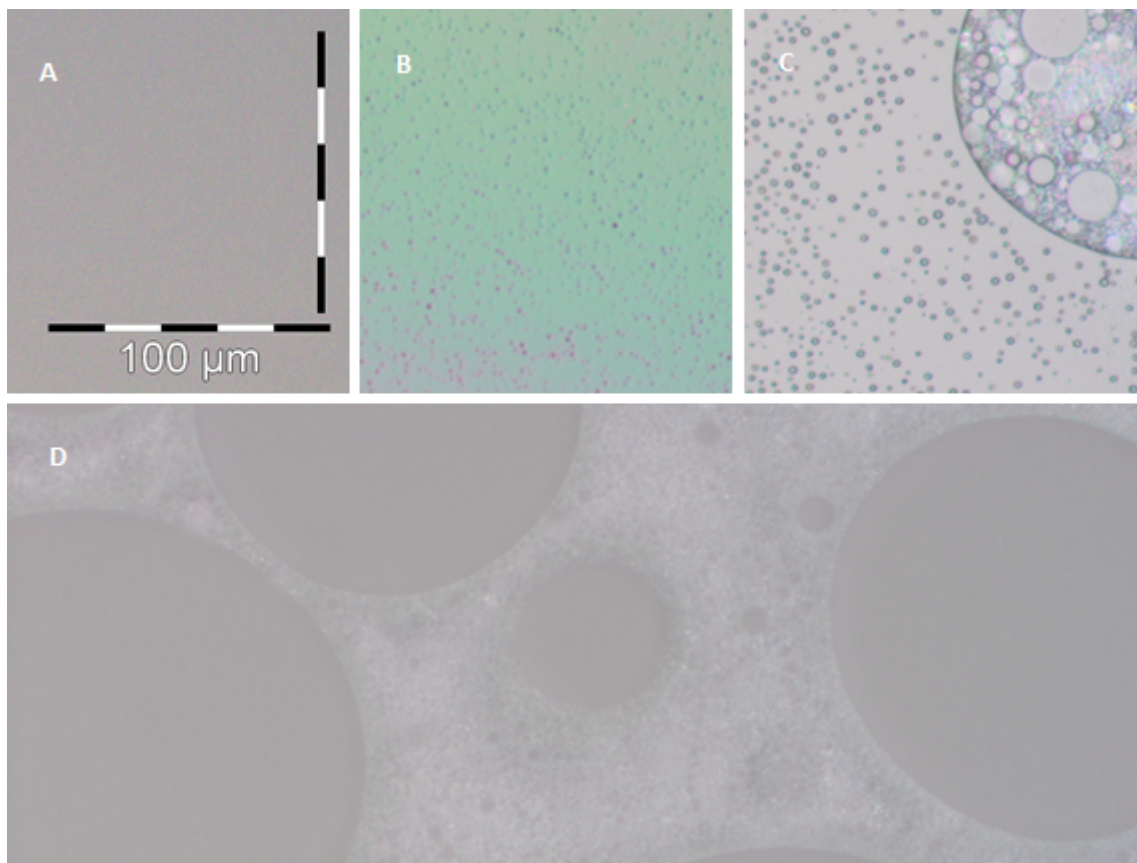


Figure 55: morphologies of BMI/DBA/PES¹ blends cured with the standard curing cycle.
A) neat resin ; B) 5 phr ; C) 10 phr ; D) 15 phr. Common scale 100 μm .

In the blend with 15 phr PES¹ (Figure 56), sulphur atoms are localised mainly in the continuous phase, which means that this composition leads to a phase-inverted morphology with big BMI-rich particles.

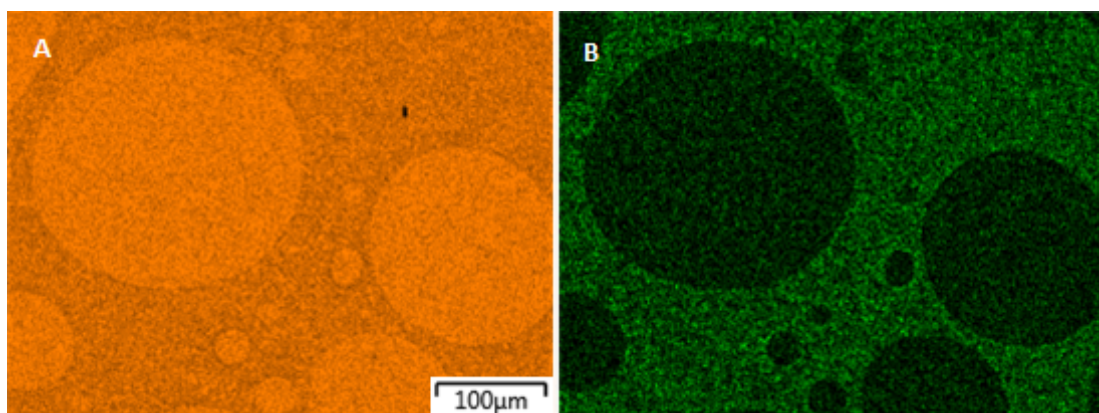


Figure 56: EDX images of a BMI/DBA/PES¹ 15 phr blend. A) carbon K $\alpha_{1,2}$; B) sulphur K α_1 . Common scale 100 μm .

Figure 57 shows the morphologies for solid samples corresponding to the previous blends with PES^h. The blend with 1 phr (Figure 57B) exhibits small particles between 1 and 2 μm . As expected, the particles in the blend with 5 phr (Figure 57C) are a little bigger: from 2 to 5 μm . The case of the blend with 10 phr (Figure 57D) is more complicated.

Two main phases are clearly identified. The continuous one seems to contain particles of various sizes while the other, big globules of a few hundreds micrometres, contains particles around 7 µm. All these observations are in agreement with the morphologies identified by *in situ* curing microscopy.

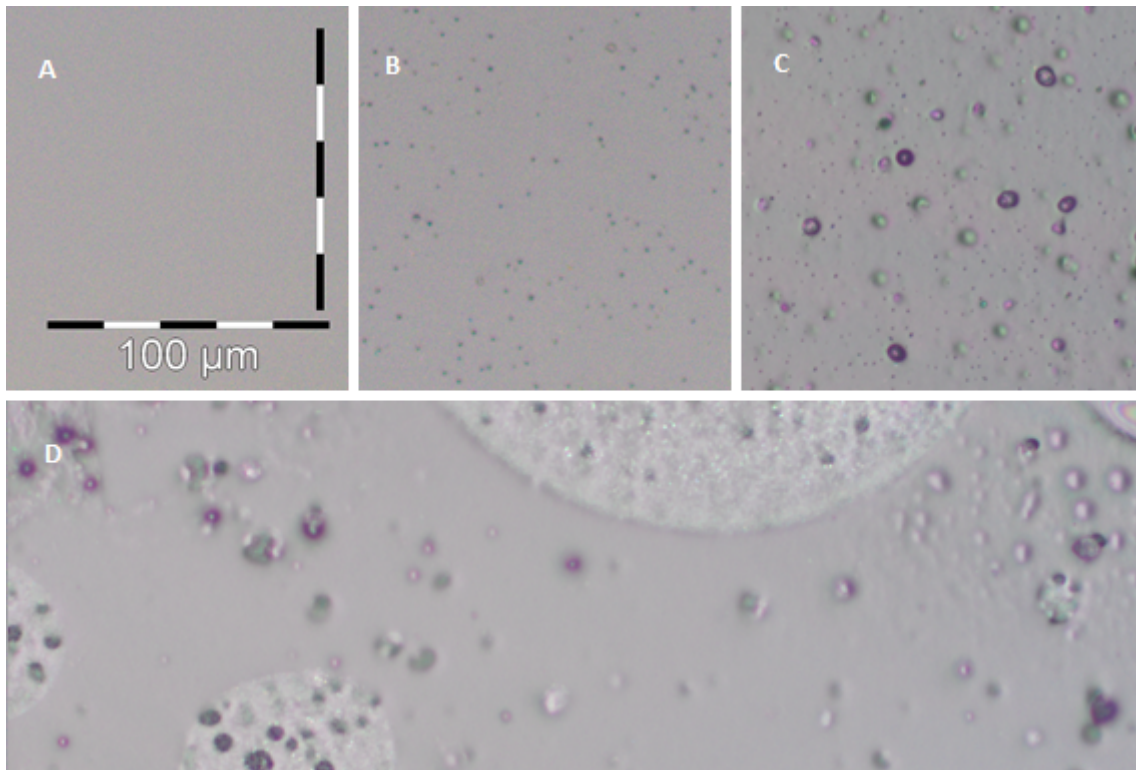


Figure 57: morphologies of BMI/DBA/PES^h blends cured with the standard curing cycle. A) neat resin ; B) 1 phr ; C) 5 phr ; D) 10 phr. Common scale 100 µm.

All three thermoplastics lead to similar morphologies. At low TP content, small particles are observed. Increasing the TP concentration makes particles bigger. For the higher contents investigated, a macro phase-inversion occurs, with a final morphology containing objects with several interlocked levels of phase separation. A noticeable difference is observed for PES^l. The concentration scale for this thermoplastic is shifted to higher contents.

2.4.2.3 Deeper look on morphologies

SEM observations with secondary electron and EDX imaging bring information on substructures. Images of the blend with 10 phr PES^l are shown on Figure 58. It can be seen that sulphur atoms are localised preferentially inside the particles, confirming a classical direct phase morphology. The sulphur repartition does not seem to be homogeneous in particles, but the resolution is limiting conclusions on a finer structure.

SEM images from fractured samples (see chapter 4) confirm a biphasic structure for all PES particles (Figure 59A to C). The same conclusion is reached with atomic force microscopy (AFM) on polished samples (Figure 60A). In this last image, the particle is stretched because located in front of the tip of a propagating crack (see chapters 3 and 4 for more information). Thermoset-rich nodules are formed in thermoplastic-rich particles, indicating a multi-step phase separation process.

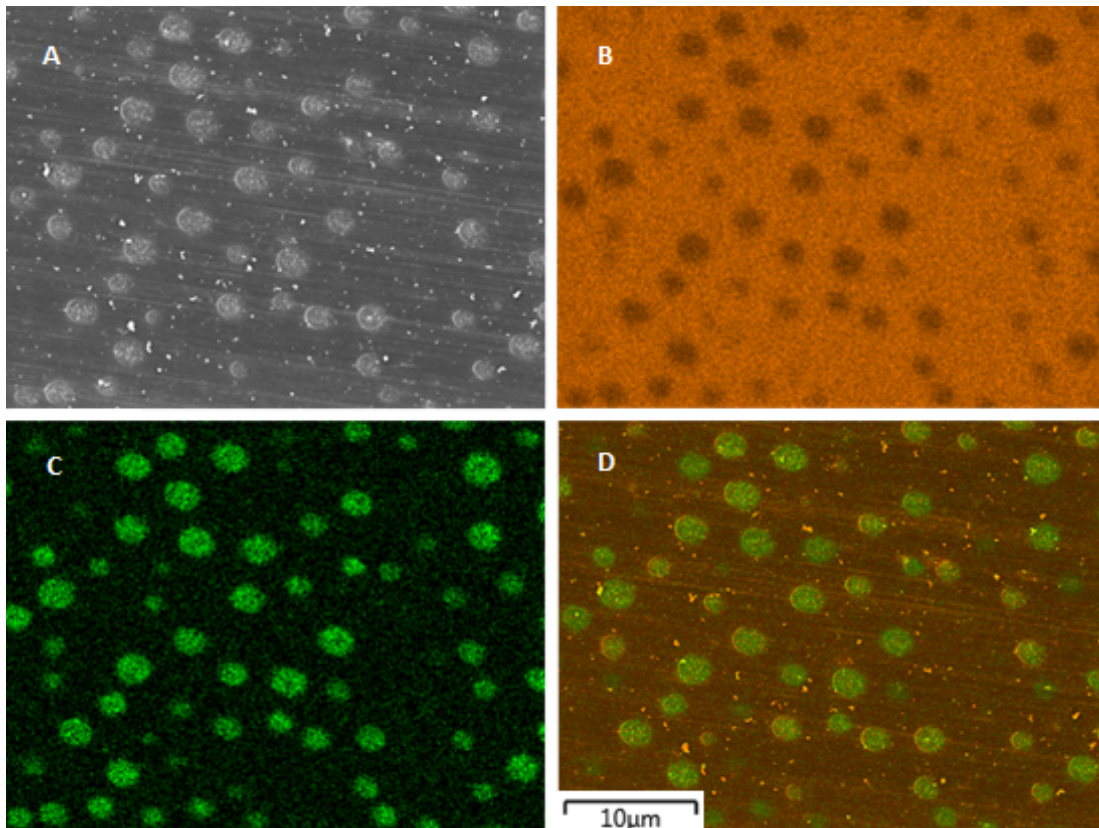


Figure 58: SEM images of a BMI/DBA/PES^l 10 phr blend. A) secondary electron image ; B) EDX for carbon K_{α1,2} ; C) EDX for sulphur K_{α1} ; D) superposition. Common scale 10 μ m.

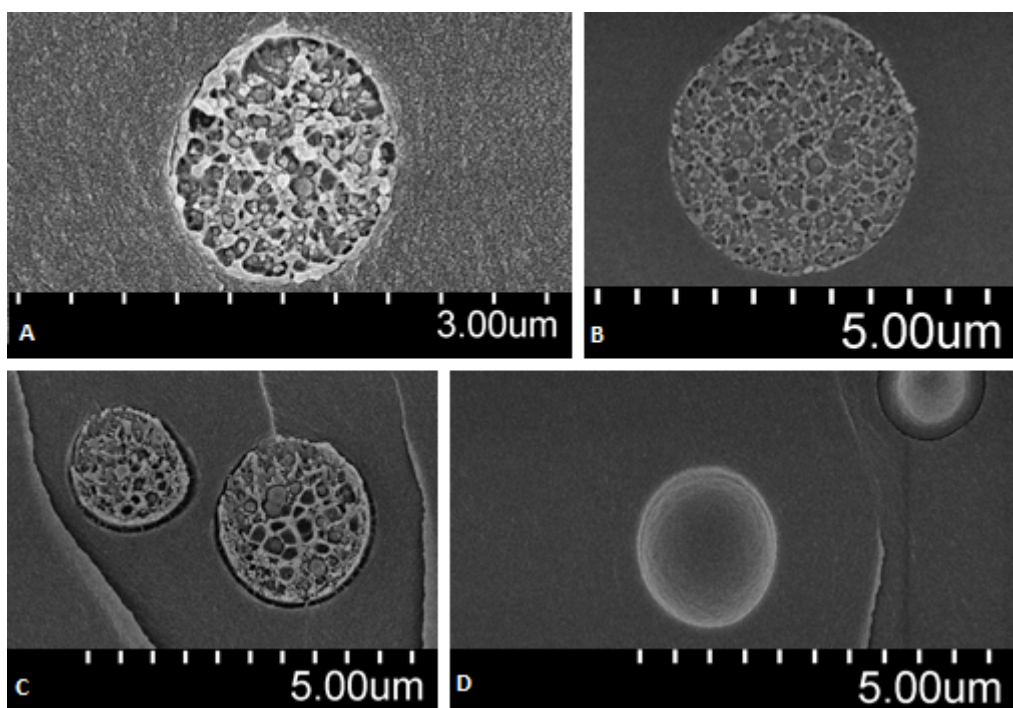


Figure 59: SEM images of broken thermoplastic particles embedded in a BMI/DBA matrix. A) PES^l 5 phr ; B) PES^l 10 phr ; C) PES^h 5 phr ; D) PEI 5 phr.

Observations on small PEI particles (Figure 59D) did not reveal obvious fine structure. AFM images (Figure 60B) suggest the presence of some nodules in particles up to 2 μ m,

but with a concentration (or a phase contrast) much lower than for similar PES particles. The inverted-phase fine structure appears clearly in bigger PEI objects (Figure 60C).

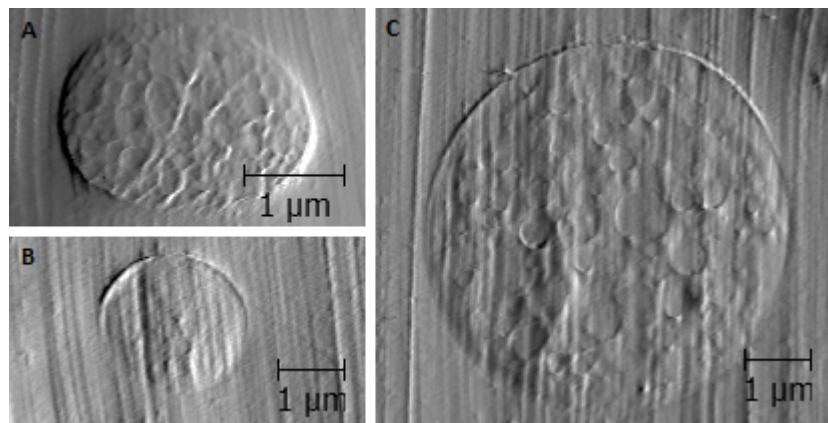


Figure 60: AFM images (deflection error) of thermoplastic particles embedded in a BMI/DBA matrix. A) PES^l 10 phr ; B) PEI 5 phr ; C) PEI 5 phr.

Some isolated inverted-phases big objects are also visible in PES^h blends (Figure 61) and might be due to local composition heterogeneities.

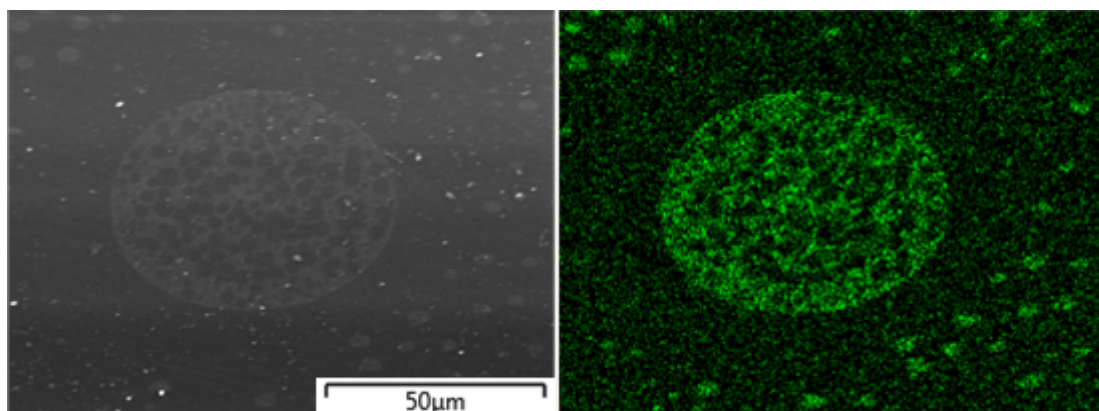


Figure 61: SEM images of an inverted-phase object in a BMI/DBA/PES^h 5 phr blend. A) secondary electron image ; B) sulphur K_{α1}. Common scale 50 μm.

2.4.3 Thermomechanical analysis

Dynamic mechanical analysis reveals the presence of a new relaxation around 225°C when PEI is added (Figure 62). The corresponding peak is barely visible at 1 phr but becomes higher when the PEI content increases. This has been attributed to the α -relaxation of PEI domains. The α -relaxation of the BMI domains seems to remain unchanged up to 5 phr. At 10 phr, this α peak become broader, suggesting a more heterogeneous cross-linked network. These results are supported by the corresponding morphologies. At low PEI content, the main phase is rich in BMI resin, giving mechanical properties very close to those of a neat resin sample. At high thermoplastic content, several kinds of phases have been observed and should lead to several relaxations. The superposition of these should lead to a broad peak, which is indeed the case here.

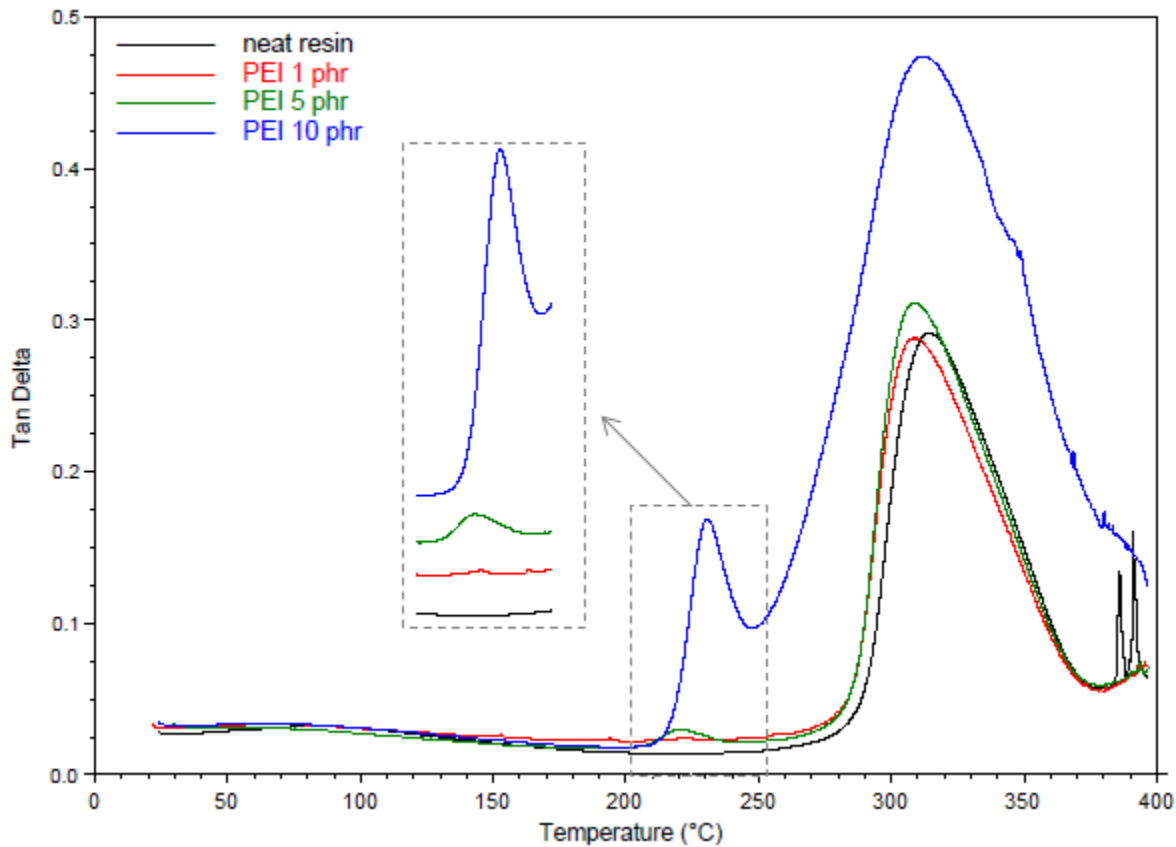


Figure 62: $\tan(\delta)$ profiles of BMI/DBA/PEI blends.

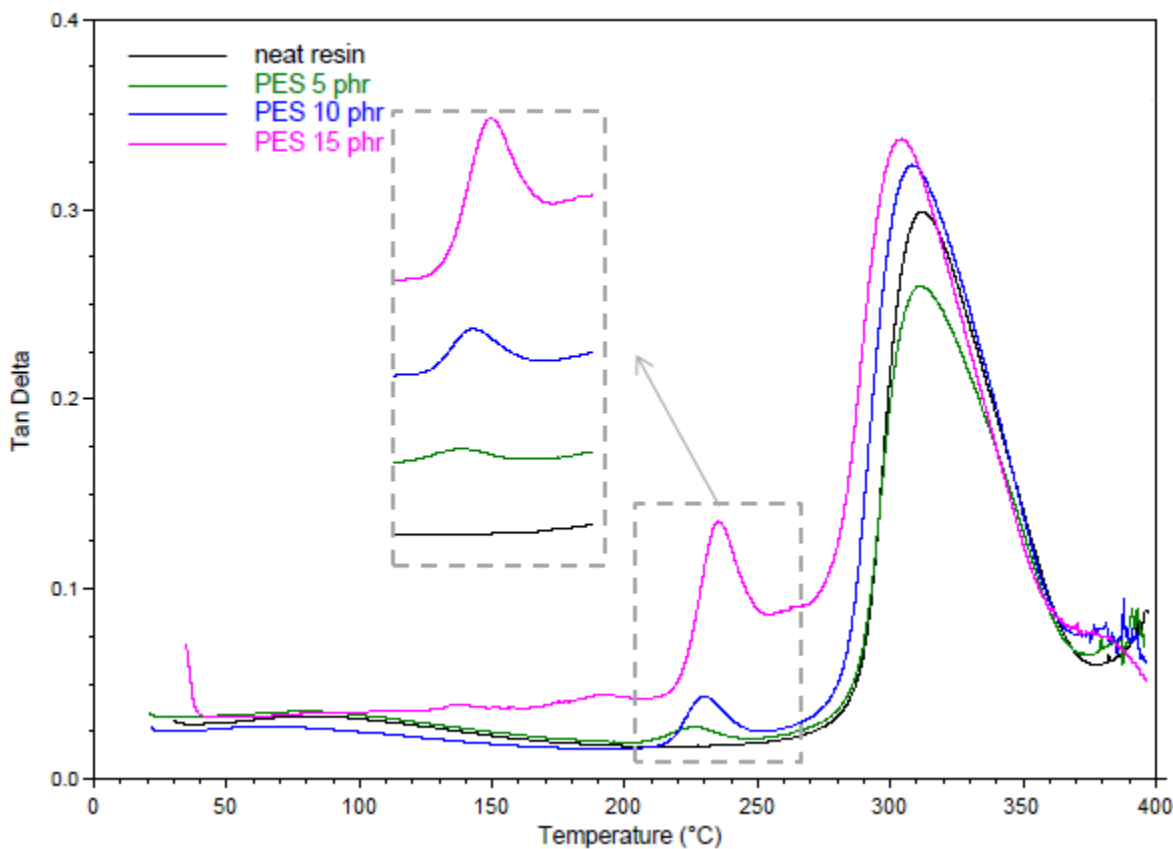


Figure 63: $\tan(\delta)$ profiles of BMI/DBA/PES^l blends.

With PES^l blends, the PES α -relaxation peak is once again visible around 230°C (Figure 63). The width of the α -relaxation peak of the BMI network remains constant whatever the PES content. This suggests again that the network formation is not hindered by the presence of thermoplastic.

Although the phase separation process is a little more complex than for the other thermoplastics, PES^h blends mechanical characterisation leads to similar behaviours as for PEI and PES^l (Figure 64). A relaxation around 230°C is clearly visible down to 5 phr of TP. It corresponds to the α relaxation of PES. The α -relaxation peak of the cross-linked bismaleimide network is not broadened by increasing the proportion of PES. This suggests that the cross-linking reaction remains unchanged through this range of PES content.

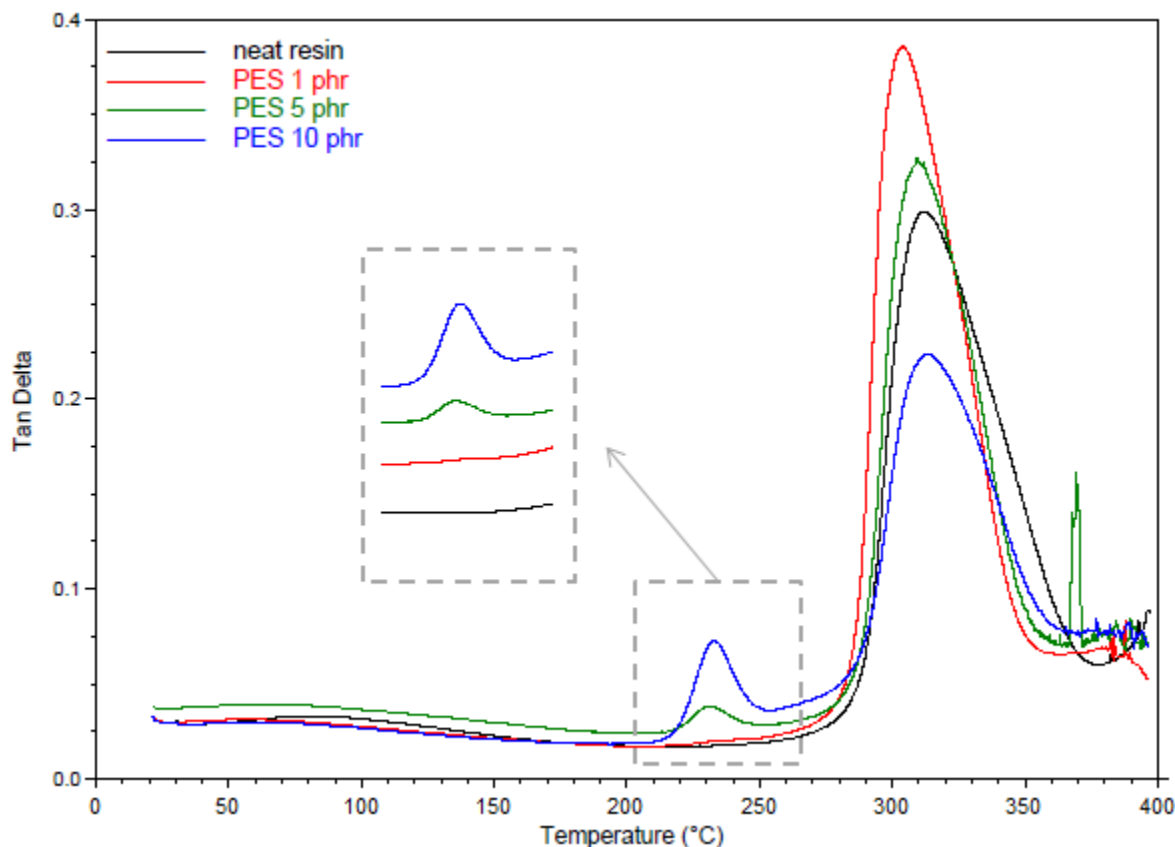


Figure 64: $\tan(\delta)$ profiles of BMI/DBA/PES^h blends.

The α -relaxation temperature of the thermoplastic depends on the thermoplastic content. Figure 65 displays these temperatures for BMI/DBA/TP blends and absolute values for neat thermoplastic samples, measured with the sample single cantilever test. In blends, T_α increases with the TP content, remains inferior to the neat TP value for PES^h and reaches it for PEI and PES^l.

There are several possible explanations for this evolution. The most immediate one is linked to phase separation. A decrease of T_α can be caused by the presence of smaller molecules which would be called here plasticizers^[118]. These small molecules could be low reacted thermoset pre-polymers or even unreacted monomers. It would mean that a higher degree of phase separation is obtained for higher TP content, or at least, more pure thermoplastic phases. Another effect to take into account is the residual stress that

may cause a glass transition temperature decrease [119]. There are two sources of residual stresses for the thermoplastic phase: contraction due to the matrix cross-linking and cooling after curing (due to the difference of thermal expansion coefficient compared to the cured thermoset). Bigger phases are expected to suffer less from these effects.

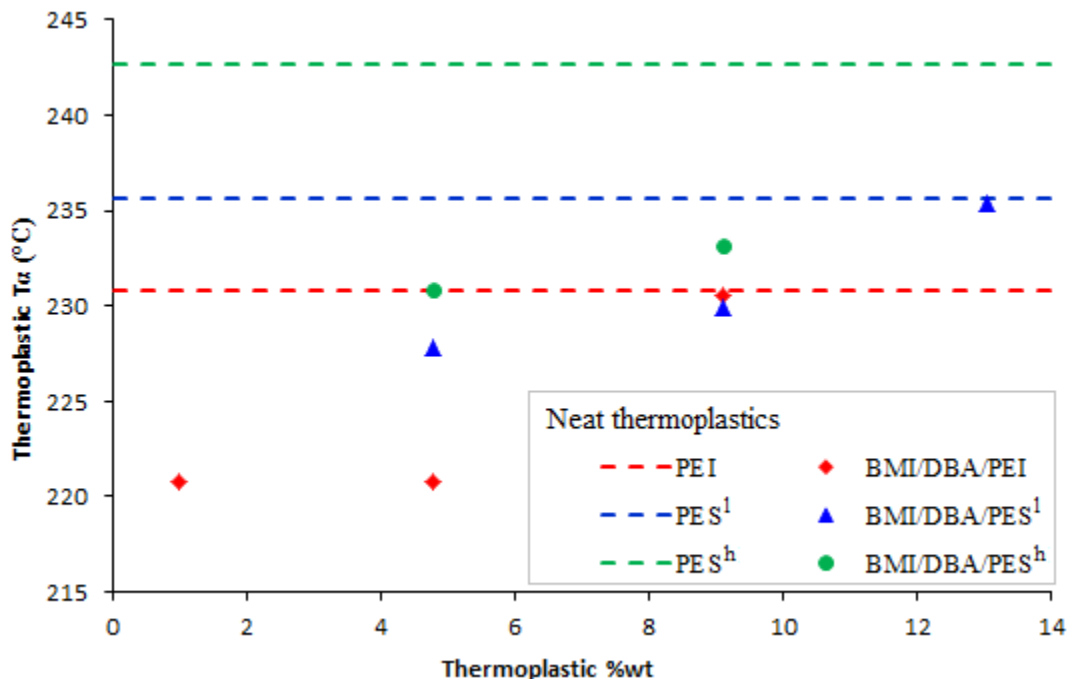


Figure 65: thermoplastic α -relaxation temperature for different blends.

2.4.4 First conclusions on solubilised thermoplastics

Among the three thermoplastics used, PEI and lower molecular mass PES exhibit a classical phase separation behaviour when blended with the bismaleimide resin. The higher molecular mass PES is no more completely soluble when the bismaleimide monomer is added to the blend, which adds a second phase separation process. However, the final morphologies are very similar and are little influenced by the thermal treatments investigated. The complexity of the observed structures increases with the thermoplastic content, from dispersed particles to multi-scale separated phases.

Comparison between the two kinds of PES reveals the effect of the weight average molecular mass on solubility. Considering the resulting morphologies with respect to the PES content, similar features are observed with a shift in thermoplastic content. Higher proportions of lower molecular mass PES are needed to keep up with the higher molecular mass PES phase separation extent. However, this parameter is less critical than the chemical structure of the thermoplastic. Indeed, the PEI used here has the highest weight average molecular mass and its solubility is comparable to the lower molecular weight PES one. This can be explained by a better affinity of imide units with the BMI monomer and network precursors that also contain imide groups. This affinity can also be the cause of the α -relaxation peak broadening of the bismaleimide network for high PEI content, where thermoplastic chains could remain longer in the BMI-rich phase and hinder the cross-linking reaction.

2.5 Bismaleimide/thermoplastic particles blends

Morphologies involving particles are often of great interest in thermoset toughening. It is usually admitted that co-continuous and phase-inverted morphologies lead to better improvement of toughness (K_C) and energy restitution rate (G_C). This never goes without a loss of mechanical (moduli values and variations) or thermal (T_g , stability) properties and also solvent and hygrothermal resistance. With a continuous phase made of a cross-linked network, particle morphologies enable solvent protection and better conservation of mechanical properties.

2.5.1 Soluble particles

2.5.1.1 Experimental considerations

A major parameter for composite in injection processing is the resin viscosity. The standard BMI/DBA resin exhibits an estimated minimum viscosity around 100 mPa.s, which progressively increases depending on the curing conditions. This viscosity is close to the limit value for the injection device (300 mPa.s). Adding thermoplastic dramatically increases the minimum viscosity up to 200 to 1000 mPa.s, depending on the thermoplastic nature and concentration. An alternative strategy for composite processing is to include thermoplastics in the preform and to inject a neat resin. This implies to study phase separation when thermoplastics are not pre-solubilised.

Considering the final application which in reinforcement of composite interleaves, particles should not be larger than 100 μm . Both PES^l and PES^h particles are suitable. To ensure that no solubilisation occurs before observation, temperature-controlled optical microscopy samples were prepared following a modified protocol. Particles were not mixed with the resin, which would lead to more homogeneous blends, but spread on microscope glass plates. A small piece of resin (for which BMI had been fully solubilised in DBA) was placed on the particles layer. The regular protocol then took over. Special attention was paid to the degassing step, for which the temperature was set to 80°C and never took longer than an hour. The PES content was set to 5 phr.

The temperature cycles were inspired from typical injection conditions with a first isothermal step at 120°C (see chapter 4). At the end of this stage, samples were heated at 3°C/min up to 180°C, which reproduces the beginning of a classical curing cycle for bismaleimide resins. Observations were stopped when no more evolution in morphologies was noticed.

2.5.1.2 Influence of the curing conditions

Samples were maintained at 120°C for 20 min, 1h or 3h without any change on the following part of the curing cycle. Figures 66 and 67 show the evolution of particle solubilisation for PES^l and PES^h respectively. General trends can be observed. After longer isothermal treatment at 120°C, particles shrink and a ring appears around them (Figures 66 and 67B, F and J). This ring is attributed to an intermediate phase of thermoplastic swollen by the resin components, which are believed to be mostly monomers and low molecular weight reaction products at this stage. Particles are progressively solubilised while heating. Mixing proceeds faster after a short isotherm at 120°C. The final morphology retains big areas of PES-rich phases, which comes from coalescence of swollen domains.

Both PES-rich and BMI-rich phases include smaller particles visible on Figure 66E and I and Figure 67E for instance. This is the trace of reaction induced phase separation after partial mixing of TP and TS.

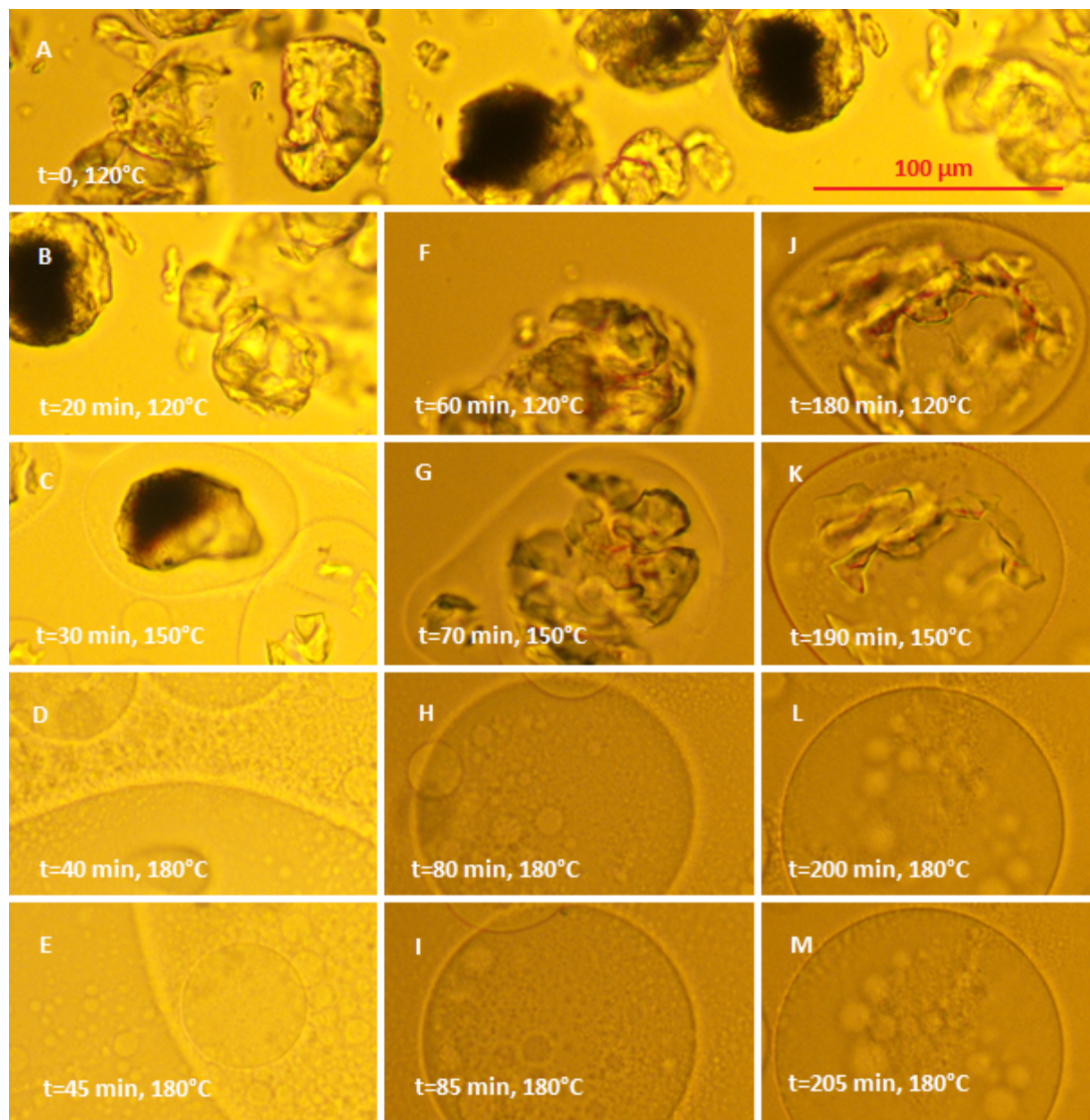


Figure 66: optical microscopy images of BMI/DBA blended with PES^l particles. Evolution of the morphology after isotherms at 120 °C: B) to E) 20 min ; F) to I) 1 h ; J) to M) 3h. Common scale 100 μm.

Less coalescence is observed after a long isotherm, but this effect is highly influenced by the initial dispersion of particles and flowing during the heating phase, it will not be discussed here. A greater extent of phase separation seems to be reached for short isotherms. This gives indication on the competition between PES solubilisation and polymerization reaction. In these experimental conditions, solubilisation proceeds quite slowly. Figures 66 and 67F show that even after 1h at 120°C PES particles are not dissolved. This process is mainly controlled by diffusion. On the contrary, the reaction between the resin monomers is still under kinetic control. No assumption could be made without knowledge about the characteristic time constants involved, but these observations tend

to demonstrate that the polymerization reaction proceeds more quickly at 120°C than PES dissolution under diffusion control.

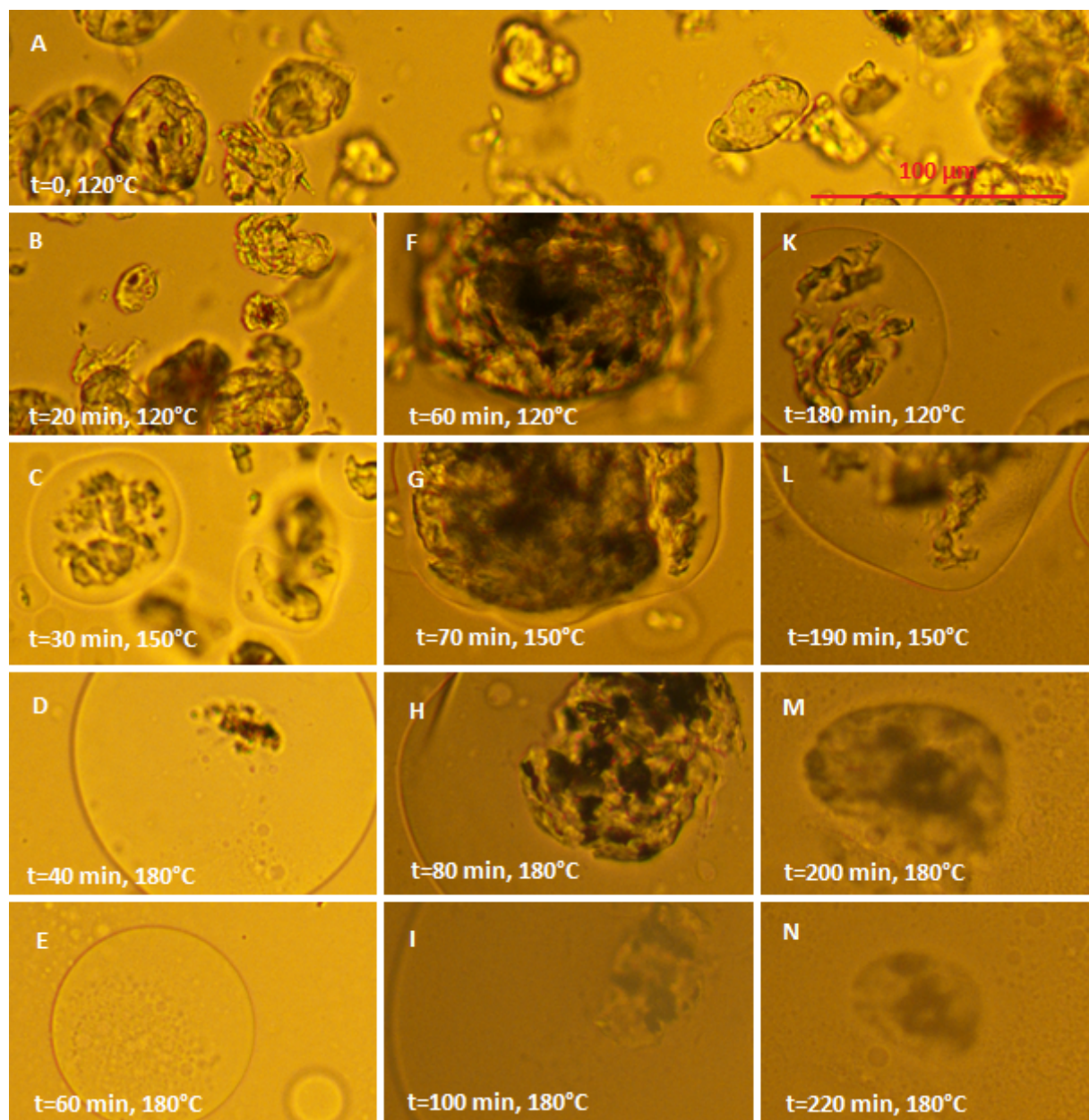


Figure 67: optical microscopy images of BMI/DBA blended with PES^h particles. Evolution of the morphology after isotherms at 120 °C: B) to E) 20 min ; F) to I) 1h ; J) to M) 3h. Common scale 100 μ m.

With PES^l, the last particles disappear earlier than with PES^h. It can be seen on Figure 67I and N that the core of bigger particles remains visible for quite a long time, even if they ultimately fade completely (not shown here). This is a consequence of the higher solubility of PES^l. Not only PES^h is swollen slower than PES^l but the resin molecules, whatever their reaction stage, inside the PES^h-rich phases are no good solvent. As explained before, with longer isotherms at 120°C, the polymerization reaction predominates on dissolution. This lead to PES-rich phases with lower solvent content for both thermoplastics but especially for PES^h, making particle core solubilisation more difficult.

2.5.1.3 Conclusion on morphological control

Including PES particles instead of dissolving the thermoplastic before curing leads to more heterogeneous morphologies. The tests were carried out for 5 phr blends for which pre-solubilisation result into small particles dispersions. Here PES-rich and bismaleimide-rich domains are formed from swelling thermoplastic particles, leading to locally phase-inverted morphology. Even if the final morphology is only little affected by thermal conditions, the composition of phases may depend on it.

2.5.2 Non-soluble particles

Polyamide-imide (PAI) and polyimide (PI) have stiff molecular chains and high glass transition temperatures. These two polymers are commercially available, by comparison polyimides described in paragraph 2.2.4 are home-made, probably with much lower molecular weight. Here neither PAI nor PI were soluble in DBA or in the BMI/DBA monomer blend. As a result, no morphological features were obtained. The particle dispersion was quite homogeneous through the thickness of cured samples. With a 7 phr thermoplastic content, no aggregates were observed.

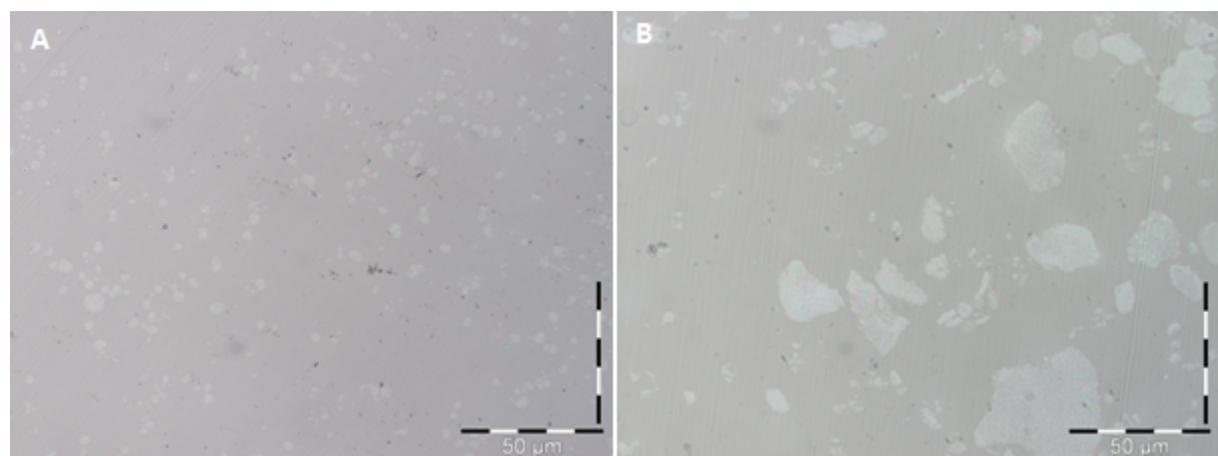


Figure 68: optical microscopy images of cured BMI/DBA blended with insoluble thermoplastics. A) PI 7 phr ; B) PAI 7 phr.

2.6 Conclusion

Polyethersulfone and polyetherimide blended with the standard bismaleimide resin lead to various morphologies. Even with a theoretical background slightly different from reaction-induced phase separation in epoxy/thermoplastic blends, similar behaviours are observed. Furthermore, the three thermoplastics used exhibit some differences, depending on their chemical structure and molecular weight, but the resulting morphologies are nearly the same. The investigated curing sequences showed little effect on final morphologies, the control key parameter is the thermoplastic content. Morphologies range from small particle dispersions to macrophase with a multi-scale phase separation. Even at low thermoplastic concentrations, fine structures are observed, especially with PES, with inverted-phase particles.

A good morphological control is achieved for cured resin samples. However, first investigations closer to composite processing suggest more heterogeneous thermoplastic

dispersion, with local phase-inverted structures, resulting from the competition between polymerization kinetics and solubilisation. In this case, the curing cycle is expected to have a greater influence on the final morphologies as well as on the phases composition.

Chapter 3

Fracture of bismaleimide resins

This chapter describes the fracture behaviour of the standard polymer network, in order to establish a comparison with other materials, especially glassy polymers. A specific observation method of sub-microscopic phenomena during crack propagation is introduced. The influence of the network inhomogeneous structure on crack propagation is also investigated.

3.1 Polymer fracture

3.1.1 Fracture mechanics

3.1.1.1 Linear elastic fracture mechanics

Inglis introduced the fundamental concept of stress concentration around a hole. It shows that at the edge of defects, the local stress can be many times higher than the remotely applied stress [120].

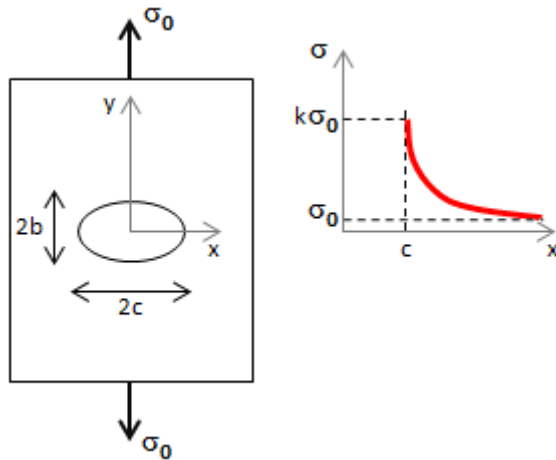


Figure 69: stress concentration at the edge of an elliptic hole.

For an applied stress σ_0 and an elliptic hole with $2b$ and $2c$ axes (see Figure 69), the maximum stress at the edge of hole is:

$$\sigma_m = k\sigma_0 \quad \text{Eq. 15}$$

with

$$k = \left(1 + 2\frac{c}{b}\right) = \left(1 + 2\sqrt{\frac{c}{R}}\right)$$

The stress concentration coefficient k depends on the local curvature radius R . A thinner defect with a smaller R leads to higher stress concentration. This calculation is based on

linear elasticity and known as a fundamental of linear elastic fracture mechanics (LEFM).

Further work was carried out by Irwin, introducing a stress intensity factor K as a coefficient for the first term of the limited development of the stress field at the tip of a sharp crack [121]:

$$\sigma(r, \theta) = \frac{K}{\sqrt{2\pi r}} f(\theta) \quad \text{Eq. 16}$$

with f an angular distribution function (the origin being at the crack-tip). K depends on the sample geometry and loading.

A fracture problem can also be interpreted with an energy approach. Griffith considered the energy needed to create the surface resulting from the crack [122]:

$$W^S = 2\gamma S \quad \text{Eq. 17}$$

with γ the surface energy and S the crack surface area. If the two created surfaces are separated from a distance a (typically an inter-atomic distance), the available elastic energy is:

$$W^E = \frac{1}{2E} \sigma^2 S a \quad \text{Eq. 18}$$

Combining equations 17 and 18 gives a theoretical fracture stress:

$$\sigma_{th} = \sqrt{\frac{\gamma E}{a}} \quad \text{Eq. 19}$$

E being the Young modulus of the material.

3.1.1.2 Crack propagation

Toughness is a characteristic property of a material that stands for the resistance to crack propagation. It is a critical value K_C for the stress intensity factor. Calculations based on purely elastic models lead to values much lower than experimentally measured ones. The reason lies in local reorganisation and material alteration around the crack-tip that consume energy.

U^S being the energy needed to create a surface and U^M the mechanical energy (potential and elastic), for a thermodynamically isolated system, the energy conservation law is:

$$U = U^M + U^S = cst$$

Consequently, if crack propagation leads to the creation of a surface, the equilibrium condition is:

$$\frac{dU}{dS} = \frac{dU^M}{dS} + \frac{dU^S}{dS} = 0$$

$\frac{dU^S}{dS}$ is the fracture energy G_C . Increasing the crack length consumes mechanical energy, the energy release rate is defined by:

$$G = -\frac{dU^M}{dS}$$

The energy criterion for crack propagation becomes $G \geq G_C$ (available mechanical energy superior to the separation energy).

A stability criterion can be defined with a first derivative of G . For $G = G_C$, instability is reached if increasing the crack surface increases the energy release rate: $\frac{dG}{dS} > 0$. The crack starts to propagate indefinitely.

Toughness K_C and critical release rate G_C are characteristics of a material. They are linked with the following relationship:

$$G_C = \frac{K_C^2}{E^*} \quad \text{Eq. 20}$$

with E^* the effective modulus depending on the loading conditions.

3.1.1.3 Fracture modes

Three fracture modes can be defined with three orthogonal characteristic displacements (see Figure 70). Mode I is called opening, mode II sliding and mode III tearing. Stress in mode I is tensile, whereas shear accounts for modes II and III.

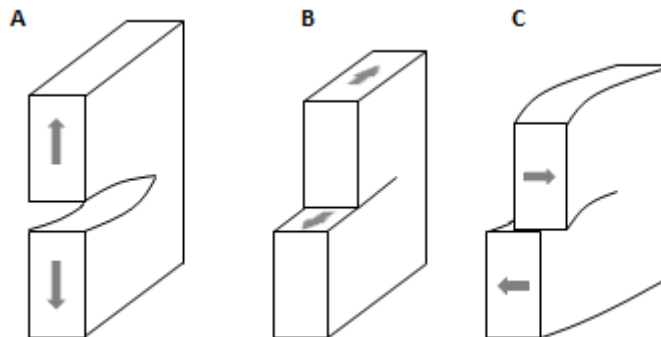


Figure 70: fracture modes: A) mode I ; B) mode II ; C) mode III.

The stress intensity factor K , introduced in the previous paragraph, also depends on the mode. In pure modes subscripts are used: K_I , K_{II} and K_{III} . Real applications are usually a combination of these modes. In this chapter, the only mode under consideration will be mode I.

3.1.1.4 Stress limitation at a crack-tip

Elliptic crack-tip are theoretical objects. From a macroscopic perspective, real cracks can be considered as elliptic holes with a curvature radius R close to 0. In that case, Inglis' theory predicts an infinite stress at the crack-tip (equation 15). This being physically meaningless, corrections have to account for a stress limitation. In the elasto-plastic

correction, the stress is capped and set equal to the yield stress σ_y in a plastic zone, which size is called R_z (Figure 71). For $x > R_z$, the behaviour can be predicted by elasticity laws. The result is a crack-tip blunting by plasticity.

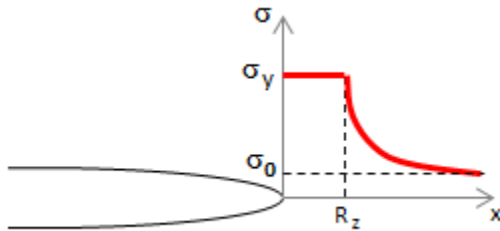


Figure 71: stress distribution with a crack-tip plastic zone.

Barenblatt considered the cohesion forces at the crack-tip to achieve a similarly capped stress [123]. These forces apply locally if the crack opening displacement $2u_y$ is small enough. The resulting crack opening is shaped as a beak (Figure 72).

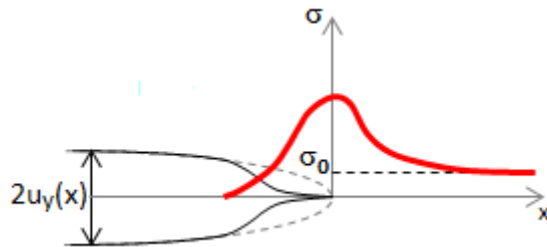


Figure 72: stress distribution in the Barenblatt theory.

In both kinds of theories, a zone at the crack-tip is responsible for stress limitation.

3.1.2 Failure of thermosets

Glassy polymers exhibit very different behaviours. Figure 73 displays stress-strain curves for which failure occurs in different domains. When it comes to thermosetting materials in uniaxial tension, they usually break before reaching the yield stress with a very low elongation at break (a few percents). In many polymers, crazing at the crack-tip is observed: local cavitation occurs and nanometric fibres are stretched between the crack edges. These fibrils are made of flowing material. This phenomenon is not observed in thermosets because of limitations to plastic flow due to cross-links.

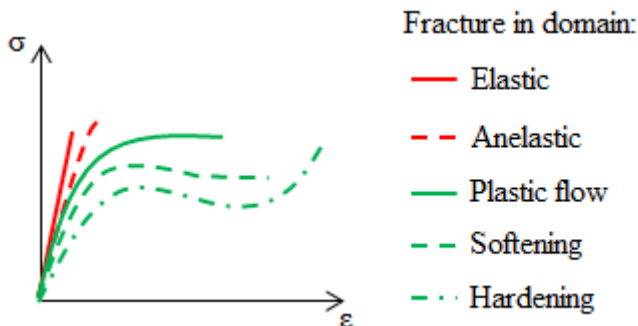


Figure 73: possible behaviour for polymeric materials under tensile tests.

A short elongation at break, failure in the elastic domain and smooth rupture surfaces rank thermosets as macroscopically brittle materials.

3.1.3 Crack propagation in glassy polymers

Once a crack is initiated, the propagation scenario varies depending on the test geometry and conditions, the material properties and the loading displacement rate. Two typical behaviours were evidenced, continuous cracking with a constant load (Figure 74A) and intermittent cracking called stick-slip (Figure 74B).

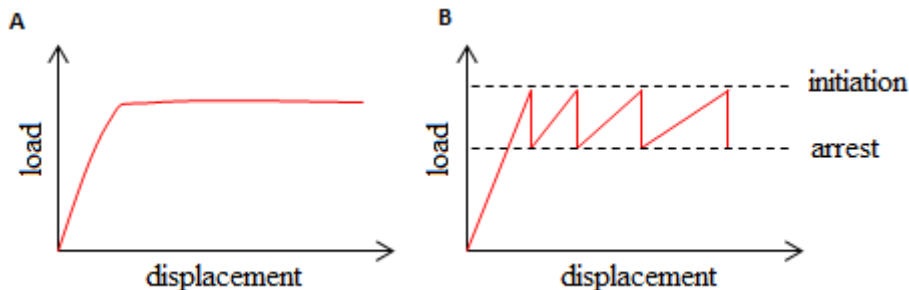


Figure 74: load-displacement curves for different crack behaviours. A) continuous cracking ; B) stick-slip.

The jolting propagation behaviour can be described in terms of a non-monotonic relationship between the stress intensity factor K or the release rate G with the crack velocity (Figure 75) [124]. The same approach is commonly used in the adhesion field [125]. A stick-slip cycle is displayed on Figure 75. The slip phase is a jump of velocity at constant K or G . The stick phase occurs after the decrease of K or G .

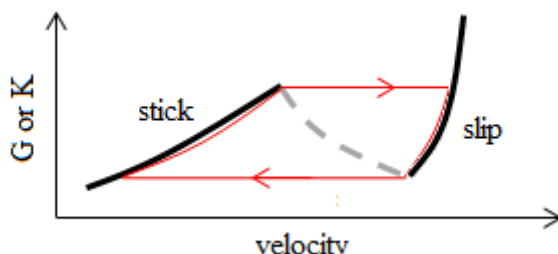


Figure 75: empirical curve for dynamic fracture mechanics.

Effort have been paid to model K or G variations with the velocity [126]. The theoretical interpretations about rate dependency, involve plasticity and sometimes visco-elasticity.

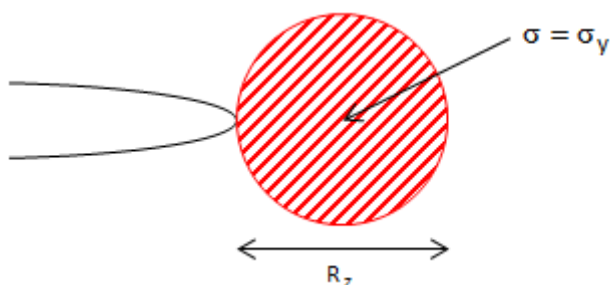


Figure 76: process zone with an uniform stress at a crack-tip.

The starting point of many plasticity treatments for polymer crack propagation is a process zone at the crack-tip, which comes from the Dugdale analysis on steels [127]. In this process zone, stresses are assumed uniform and equal to the yield stress σ_y (Figure 76).

The size of this zone can be estimated by:

$$R_Z \simeq \frac{\pi}{8} \left(\frac{K_{IC}}{\sigma_y} \right)^2 \quad \text{Eq. 21}$$

A first interpretation of equation 21 is brittleness quantification. A small process zone means a proportionally small energy used for plastic deformation. Table 6 gives a few examples of the process zone size at failure, for different kinds of materials.

Material	K_C (MPa.m $^{\frac{1}{2}}$)	σ_y (MPa)	R_Z
Steel	80	600	10 mm
PMMA	0.7	90	30 μm
Epoxy	0.7	100	10 μm
Glass	0.5	3000	15 nm

Table 6: process zone size estimations for different materials.

Often represented as a circular area, the process zone can be considered with much more complicated shapes (Figure 77) [128, 129], depending on the angular functions f in equation 16, the yield criterion (for instance, von Mises criterion [130] applied to the calculated stress field) and the stress triaxility.

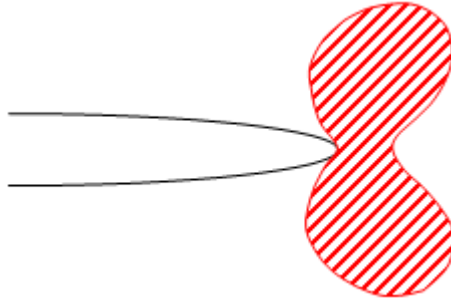


Figure 77: cohesive zone shape with plastic deformation at a crack-tip in mode I.

Schapery introduced visco-elasticity by considering a creep compliance (inverse of a modulus) C_v [131, 132], Marshall and Williams with a relaxation modulus $E(t)$ [133]. In both cases, time dependency is obtained by replacing the elastic modulus by one of these quantities [126]. The crack propagation condition $G \geq G_C$ can be expressed as:

$$G = C_v K_I^2 = \frac{K_I^2}{E(t)} \geq G_C$$

The shape of the $K(v)$ curve (v being the crack-tip velocity) is calculated using a characteristic time for visco-elastic displacement over the process zone:

$$\tilde{t} \propto \frac{R_Z}{v}$$

With a power law dependency $C_v \propto \tilde{t}^n$ or $E \propto \tilde{t}^{-n}$, both approaches lead to:

$$v \propto K^{\alpha(n)}$$

where $\alpha(n)$ is a function of n depending on the model. This predicts the first part of the $K(v)$ curve on Figure 75, corresponding to low velocities, but cannot account for the stick-slip phenomenon without further hypotheses (such as rate dependency of the separation energy or non-isothermal phenomena). These models assume a linear viscoelastic treatment of the material outside of the process zone. The non-linear behaviour is taken into account through the uniform stress σ_y in the process zone.

Gledhill and Kinloch observed both continuous propagation and stick-slip in epoxy networks, depending on their composition and curing cycle [134, 135]. They suggested failure criteria in the continuous regime such as a critical crack opening δ_c [134] or a critical process zone size [135].

A major theory on the amplitude of stick-slip in thermosetting resins was developed by Kinloch and Williams [136]. It involves blunting of the crack-tip, due to plastic deformation. In this model, the yield stress σ_y is the control parameter for the fracture behaviour. As long as the material remains brittle, a lower σ_y enable more blunting through plastic deformation, promoting stick-slip. Once again, the non-linear behaviour of the materials is described through σ_y , but the stress field on which their calculation is based (equation 3 in [136]), is a limited development of the linear elastic stress field near a thin and long elliptic hole.

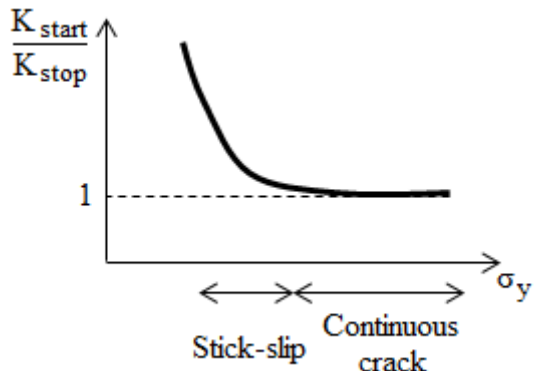


Figure 78: crack growth mode from Kinloch and Williams model [136].

At the beginning of a slip phase, the stress intensity factor reaches a value K_{start} . At the end of the slip phase, the value has decreased to K_{stop} . When the ratio between these two parameters falls to 1, no stick-slip is observed, the crack growth is macroscopically continuous (Figure 78). Investigations on epoxy resins gave a transition value for σ_y close to 100 MPa.

These predictions for glassy polymers fracture behaviour are based on alteration of the material near the crack-tip. Schapery considered the displacement of the process zone in a visco-elastic material. Kinloch and Williams defined a small length ahead of the crack-tip (close to 1 μm for epoxy/amine networks) at which a critical stress is attained. In all these models, the material behaviour at very tip of the crack is either considered as pure yielding or not considered at all. The following parts will introduce a method to observe and investigate the local displacements at a crack-tip at a sub-micrometric scale. A model taking into account deep transformations of the material will be suggested.

3.2 Experimental details

3.2.1 Materials

The main investigation was carried out on the standard BMI/DBA resin described in chapter 1. Additional observations were performed on a network modified with 0.25 equivalent of hydroquinone by BMI monomer, and with a pre-curing step of 3h at 140°C.

3.2.2 Methods

3.2.2.1 Mechanical characterisation

Both uniaxial tension and compression experiments were carried out on a Zwick testing machine.

Tension samples were designed according to the IGC04.26.253 standard [137] (Figure 79). The procedure followed the standard recommendations, with a cross-head speed of 2 mm/min, replacing self-tightening clamps by air-pressured clamps.

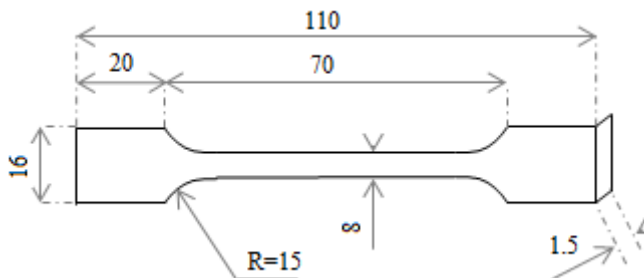


Figure 79: tensile test specimen.

Compression samples were designed as cylinders (5 mm diameter, 6 mm height). Contact between clamps and sample edges was made with grease containing molybdenum disulfide particles. The modulus of MoS₂ being over 0.2 TPa [138], its contribution is neglected. This kind of lubricating grease strongly limits the heterogeneity of stresses usually leading to a cask-deformation of samples. The plate displacement rate was set for the strain rate to range between 10⁻³ s⁻¹ to 10 s⁻¹. Test procedures were recorded with an optical camera to follow the evolution of the sample shape.

3.2.2.2 Compact tension

Tensile tests with a compact tension (CT) geometry were performed on an Instron testing machine to measure fracture toughness. Sample preparation and test procedure are described in IGC04.26.680 standard [139]. Samples were notched by placing a sharp razor blade in the hollow part (see Figure 80) and impacting the top of this blade with a falling weight.

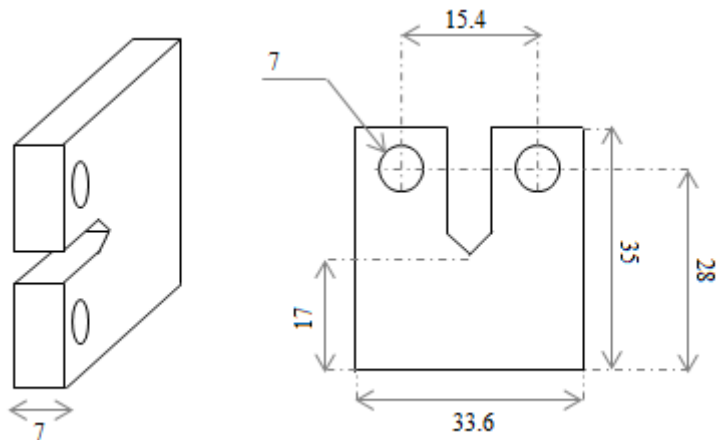


Figure 80: compact tension sample. Dimensions in mm.

The cross-head speed was set to 0.1 mm/min. After each crack propagation, samples were unloaded before starting a new loading cycle up to cracking. Figure 81 shows load-displacement cycles. A critical force F_C was measured at the onset of each crack propagation. Tests were carried out until the critical force fell under 1% of the maximum admissible force of the loading cell.

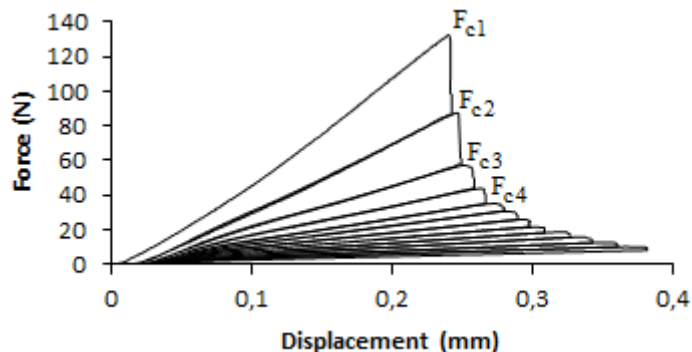


Figure 81: load-displacement curves for a compact tension test.

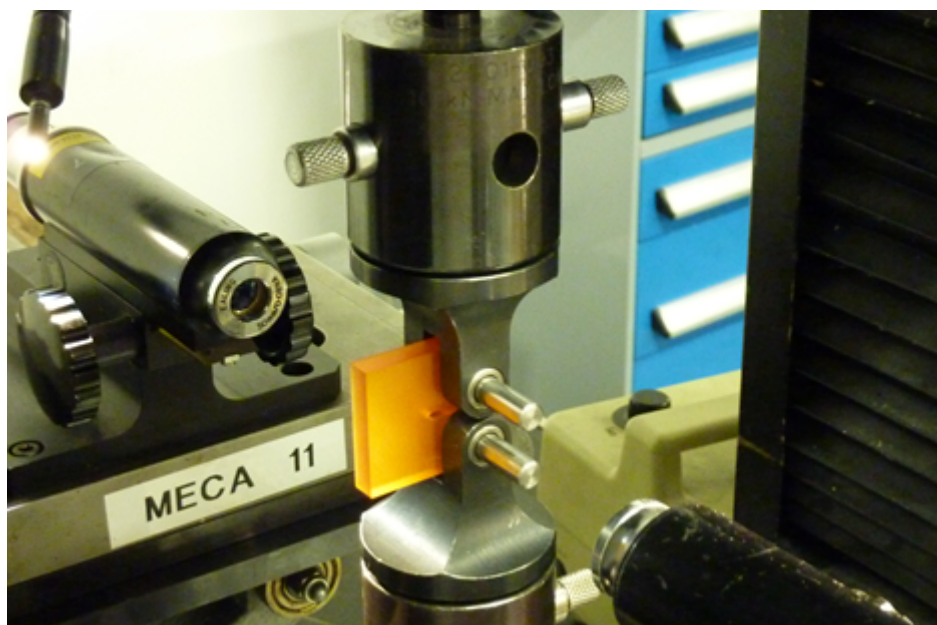


Figure 82: experimental device for compact tension tests.

In the meantime, the crack length is measured on both sides, using optical scopes (Figure 82). A mean crack length was calculated for each cycle.

Fracture toughness in mode I (K_{IC}) was calculated for each cycle with the following formula [139]:

$$K_{IC} = \frac{F_C}{B\sqrt{W}} \left(29.6 \left(\frac{c}{W} \right)^{0.5} - 185.5 \left(\frac{c}{W} \right)^{1.5} + 655.7 \left(\frac{c}{W} \right)^{2.5} - 1017 \left(\frac{c}{W} \right)^{3.5} + 638.9 \left(\frac{c}{W} \right)^{4.5} \right) \sqrt{10^{-3}}$$

with B the sample thickness (7 mm), W the effective sample width (28 mm) and c the crack length before each cycle. With lengths in mm and F_C in N, K_{IC} is expressed in MPa.m $^{\frac{1}{2}}$. Fracture toughness of a sample is a plateau value of K_{IC} for c/W values between 0.45 and 0.8 (avoiding initiation and edge effects). For each material, a minimum of 5 samples were tested.

3.2.2.3 Double Cantilever Drilled Compression

Double Cantilever Drilled Compression (DCDC) was first used to study the crack behaviour in very brittle materials such as glass [140–142]. By compressing a beam in which a hole has been drilled, the stress concentration generates a local transverse tension [120]. If conditions are met for a crack to nucleate from best defects and to propagate, this tension opens the crack. A perfectly centred hole would result into a mid-plane crack in a perfect mode I. Furthermore, this geometry allows to propagate cracks under highly stable conditions [141].

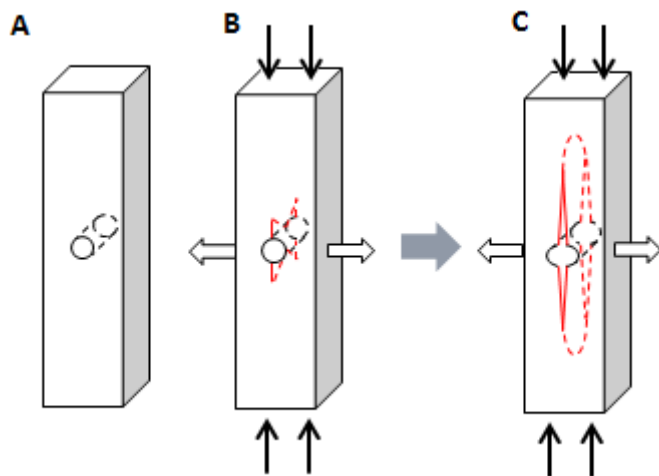


Figure 83: DCDC sample configurations. A) drilled sample ; B) notched sample under compression ; C) cracked sample.

DCDC specimens ($40(\pm 0.5) \times 8(\pm 0.2) \times 4(\pm 0.1)$ mm 3) were cut in cured plates. A 2 mm diameter hole was then drilled in their centre through the thickness. The upper side was finally polished with silicon carbide papers and diamond particle dispersions down to 1 μm . The last polishing step was chosen in order to obtain polishing lines oriented along

the main axis. Samples were notched on each face by slow indentation of a triangular razor blade along the diameter of the hole, in the mid-plane axis. This defines pre-cracks from which cracks will propagate along the main axis of the specimen. Figure 83 displays the sample configurations during a DCDC experiment.

DCDC tests proceeded following the method used by Nziakou and co-workers on PMMA and epoxy networks [143–145]. A notched specimen was placed, polished side up, in a precision Deben loading cell (Figure 84). Compression was applied with a controlled displacement speed of 0.01 mm/min. When the two cracks propagated from the notched edges of the hole, the loading was stopped and the compression displacement maintained constant for the whole remaining procedure.

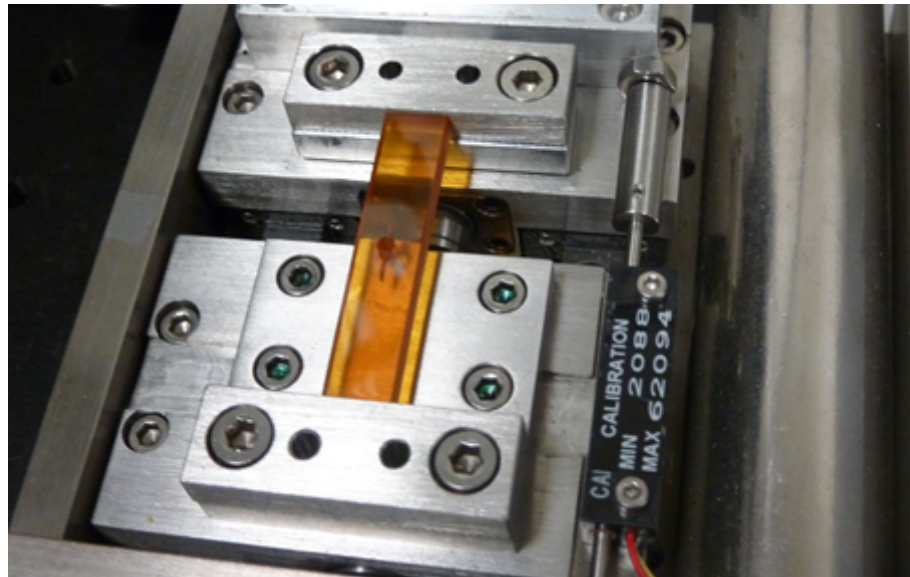


Figure 84: cracked DCDC sample in the loading cell.

3.2.2.4 Optical Imaging

DCDC cracked samples were observed under an optical 8-bit camera equipped with two objectives. The available widths for the observation field were roughly 1 mm and 4 mm. The loading cell was mounted on an horizontal plate with lateral mobility in both directions. The camera was mounted on an arm with a possible vertical displacement, enabling focus corrections. Remote control of the camera offered an acquisition frame rate between 0.01 Hz and 20 Hz with a full size field. Illumination was provided by a double-necked LED lamp. The whole set-up was placed on a compensating table that reduced the effects of vibrations (Figure 85).

A fracture opening profile can be extracted from the images to provide data for models. This requires an edge detection procedure to ensure reliability and reproducibility of measurements. Considering opened crack images, edges are strongly oriented (Figure 86). A very simple detection can be performed, looking for the two maxima of the gradient in the y direction. Details on edge detection tools are provided in appendix G.

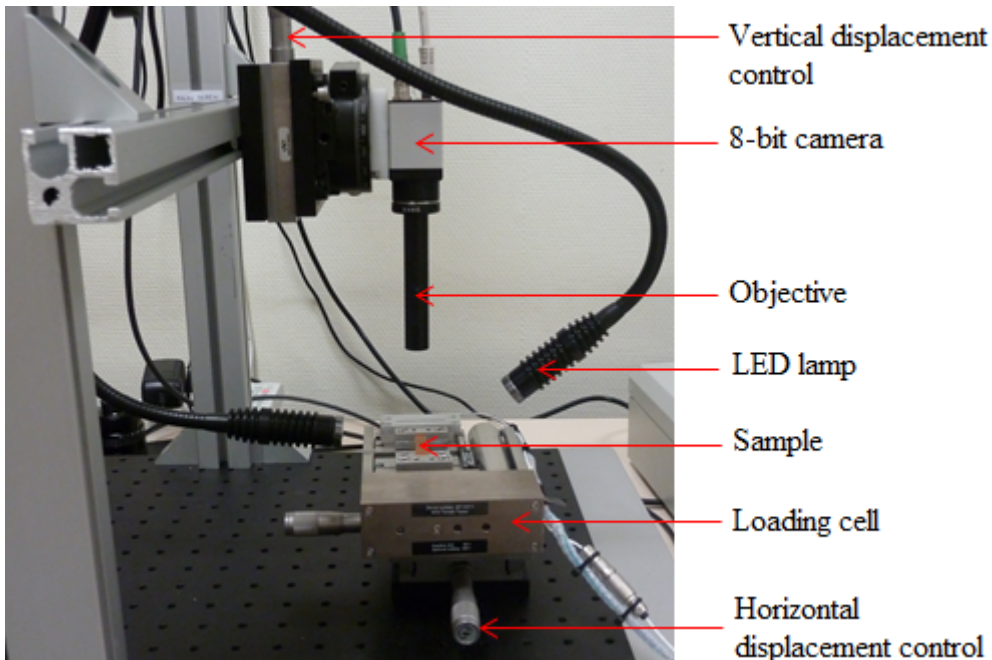


Figure 85: experimental device for optical images acquisition.

Edge detection was performed with ImageJ software program. Noise reduction and derivation along the y direction are obtained with a function recreating the following mask:

$$\begin{matrix} -1 & -2 & -1 \\ 0 & 0 & 0 \\ 1 & 2 & 1 \end{matrix}$$

The image is smoothed with a mean on three vertical lines, giving more weight to the current line. A function was preferred to the mask to keep a 8-bit derivative image with the same 0 to 255 grey scale. With a mask, negative values are not handled, whereas the function considers absolute values. Edges are localised on the two derivative maxima. This procedure is a simplified Canny edge detection, assuming a constant direction of the maximum gradient magnitude.

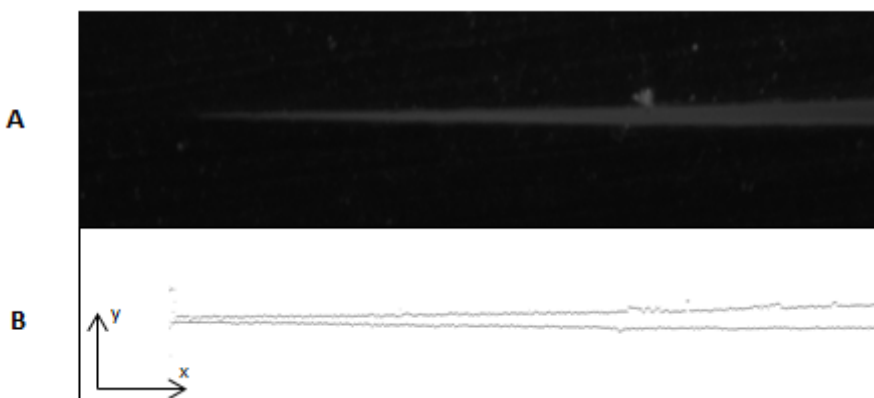


Figure 86: opened crack. A) optical camera image ; B) extracted profile.

Around the crack-tip, the procedure leads to a local aberration, where two edges are found (see Figure 86B). It can also be seen that dust alters the detected profile. The corresponding points are rejected. The crack-tip can be localised either manually on the original image or through a local edge detection along the crack axis, both methods giving

similar results.

Using a simple derivation in the y direction requires a perfectly oriented crack. Local deviations are sometimes observed. Considering a deviation angle of 10° , which is much higher than what was observed, the detected crack opening would be increased by a factor $1 - \cos(10)$, roughly 2%. Consequently, local deviations have little effect compared to other limiting factors, especially the camera resolution (leading to a 10% error on a 5 μm wide crack opening).

3.2.2.5 Interferometry

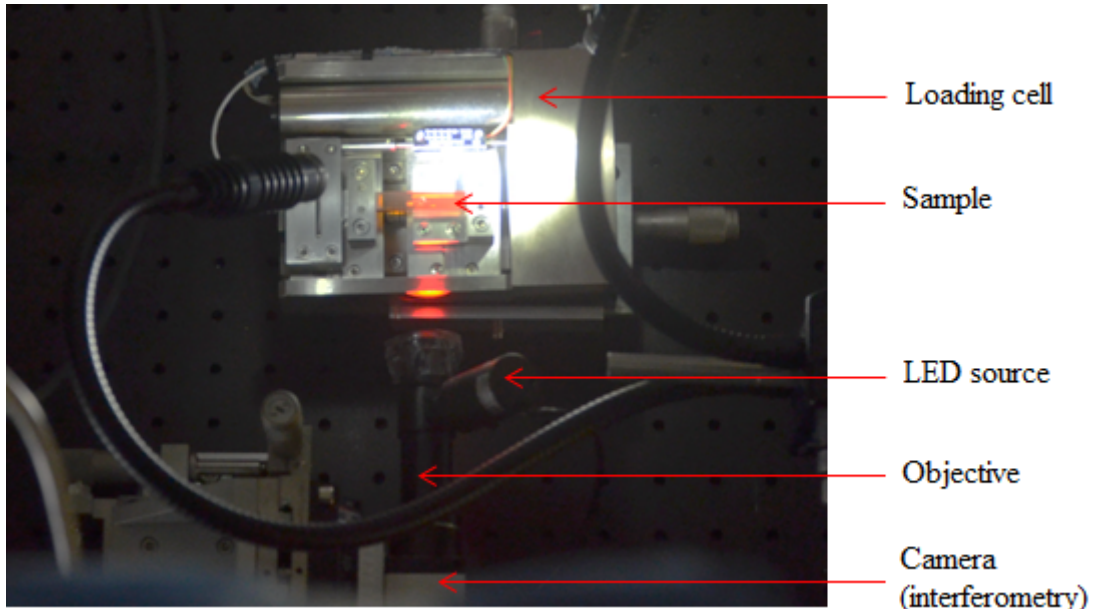


Figure 87: experimental device for interferometry on DCDC specimens.

A second camera could be placed next to the loading cell, to perform interferometric measurements of the crack opening profile in the bulk of loaded samples (Figure 87). In this case, the upper and the lateral sides of the sample, both exposed to light, were polished. The objective was designed to guide the light from a monochromatic source (LED at $\lambda = 630 \text{ nm}$) in the camera axis. In this configuration the phase shift between a primary and a secondary reflected beams (see Figure 88) is:

$$\psi = \pi + \frac{2\pi n}{\lambda} 4u_y(x)$$

with $2u_y$ the crack opening and n the air refractive index. For two monochromatic beams, satisfying the coherence criterion (originated from a single source here), a classic result is that the measured intensity is proportional to: $\cos^2(\frac{\psi}{2})$.

Here $n \approx 1$, the modulation coefficient of the light intensity is then:

$$\sin^2 \left(\frac{4\pi u_y(x)}{\lambda} \right)$$

The resulting interference pattern is a set of fringes, where the crack opening is constant along a line of constant intensity. The bright fringes are located at positions x_k satisfying the following condition:

$$2u_y(x_k) = \left(k + \frac{1}{2}\right) \frac{\lambda}{2} \quad \text{Eq. 22}$$

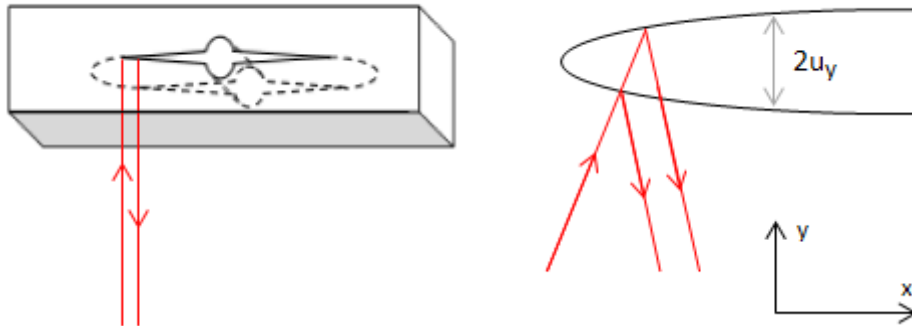


Figure 88: principle of interferometry on a cracked DCDC specimen.

3.2.2.6 Atomic force microscopy

AFM experiments were carried out on a Bruker Dimension Icon apparatus. A vibrating cantilever bearing a tip (Figure 89C) gives information on samples scanned surface. Displacements are controlled through piezo-electric ceramics. A laser beam reflecting on the cantilever tip is detected by photo-diodes. Deflection of the cantilever is measured by the displacement of the laser spot on the photo-diodes (Figure 89B). Two imaging modes were used. In the first one, the tip remains in the attractive domain (Figure 89A). In the second one, the tip moves through the repulsive to attractive domain (tapping).

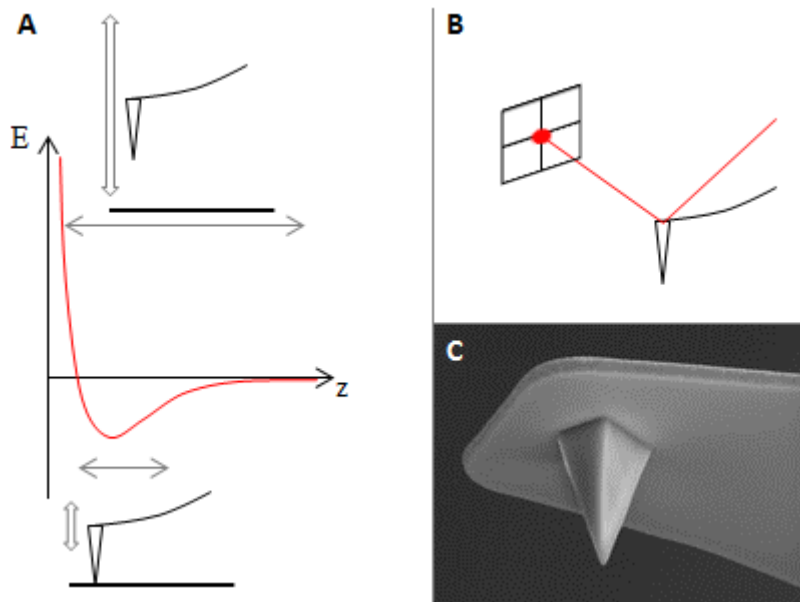


Figure 89: A) AFM modes ; B) deflection measurement ; C) cantilever tip.

The apparatus enabled simultaneous recording of several signals. Height provides main information on topography. Deflection error, which is the difference between the oscillation amplitude and the setpoint, usually gives a better contrast for fine structures.

Peak force error is a similar signal in the used tapping mode. These last two signals are feedback control parameters.

Many parameters, such as frequency, gains, lines number, scan angle, scan size and scan rate determine the resolution and acquisition quality. Effects of these parameters will not be extensively discussed here. The scan size ranged from 2 μm to 50 μm , the scan rate was set around 0.7 Hz. The scan angle was usually set as much as possible perpendicular to the crack propagation direction. Following relatively fast events required a compromise between space and time resolution, increasing the image aspect ratio enabled to keep a satisfying space resolution with acquisition times as short as 4 minutes.

When the characteristic time of evolution cannot be neglected compared to the acquisition time, images are altered depending on the scan direction. Considering the crack-tip as a constant shape in translation, an image for which the scan proceeds in the direction opposite to the propagation will seem compacted. On the contrary, if the scan direction is along the propagation direction, the resulting image will seem stretched. In an extreme case in which crack velocity and scan speed were equal, the image would show a constant crack opening. In addition, drifts of the scanning head can amplify or compensate this effect.

Compared to SEM, AFM requires no surface metallisation, allowing observations of the material failure at the sub-micrometre scale without questioning the effect of an additional metallic layer.

3.2.2.7 SEM Fractography

After failure, crack surfaces were prepared with a platinum deposition. They were then observed with scanning electron microscopy, secondary electron signals being used.

3.3 Neat bismaleimide network fracture

3.3.1 Mechanical properties

3.3.1.1 Uniaxial tension

Macroscopic mechanical properties of the material were determined with a simple tension test. Figure 90 shows the behaviour law of the standard resin, expressed with true stress (σ_v) and true strain (ϵ_v):

$$\sigma_v = \sigma_n(1 + \epsilon_n)$$

$$\epsilon_v = \ln(1 + \epsilon_n)$$

with σ_n and ϵ_n the nominal values for stress and strain, that are effectively calculated from the measured force and displacement. Here the difference between nominal and true quantities is extremely low because the range strain remains very low.

Remark: the Poisson ratio ν is expected to be close to 0.33 and the relationship between the true and nominal stresses for a cylindrical sample calculated from Poisson equation is $\sigma_v = \sigma_n(1 + 2\nu\epsilon_n)$ at first order. However, this relationship is only valid in the elastic

domain, in the present case, the behaviour above the yield stress is investigated. Consequently the isochoric approximation ($\nu = 0.5$) is preferred.

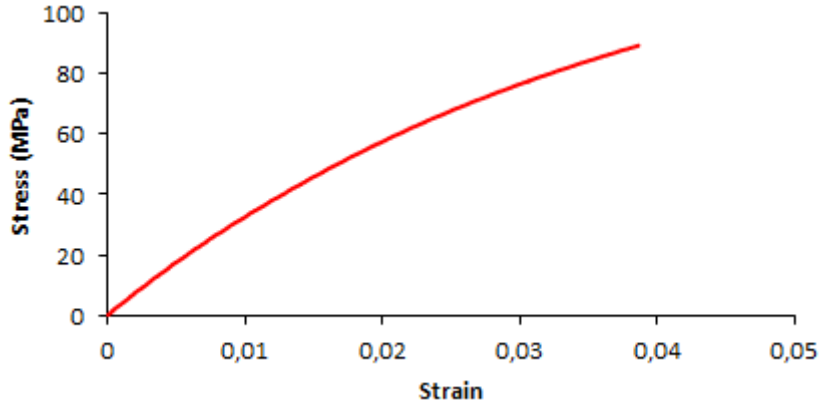


Figure 90: standard BMI/DBA network stress/strain curve for uniaxial tension.

The initial slope of the stress/strain curve gives the Young modulus of the material, here calculated at $3.45(\pm 0.05)$ GPa. The stress and strain at break can also be determined: $\sigma_R = 88 \pm 10$ MPa and $\epsilon_R = 0.038 \pm 0.005$. The presence of defects is responsible for failure and these properties are more dependent on the sample preparation and machining than on the material itself.

Remark: the storage modulus measured by DMA (see chapter 1) was close to 4 GPa at 40°C, which is a fair approximation.

3.3.1.2 Uniaxial compression

From a practical point of view, the full behaviour law in tension is not accessible at a macroscopic level because of early failure of macroscopic samples. Compression testing usually enables higher strains on thermosets because defects are closed on the contrary to tension testing. Because of that higher differences between nominal and true stress/strain are obtained.

The difference between true and nominal values is visible on Figure 91. The elastic domains overlap and the curves split up around the yield area. After yielding a hardening is visible, followed by what seems to be softening. The latter could be due to heterogeneities of the stress field under high loads, experimental artefact or partial damaging of samples. The optical control did not reveal any heterogeneous lateral strain in this particular domain, but unloaded samples displayed small cracks near the upper and lower surfaces. This part of the curve will therefore be discarded. The maximum load of the testing machine was usually reached before failure of samples.

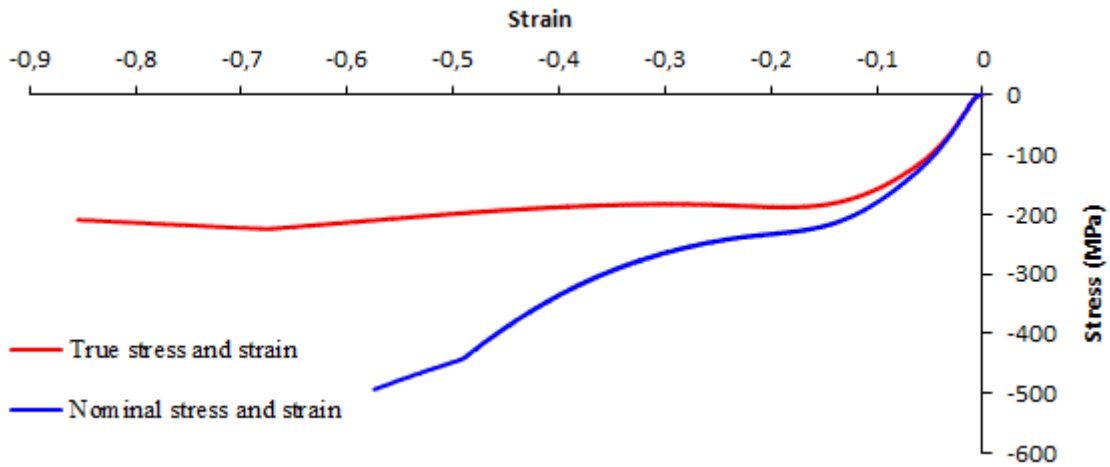


Figure 91: standard BMI/DBA resin stress/strain curves for uniaxial compression (strain rate: $10^{-3}s^{-1}$).

3.3.1.3 Extrapolated microscopic behaviour

At the crack-tip, during mode I failure, the material locally experiences tension. The behaviour law in tension is usually not easy to measure for brittle systems as thermosets. Here samples break in tension even before reaching the yield stress. As a result, no information arises on the plastic behaviour, which is a major property involved in most fracture mechanics theories for elasto-plastic materials. As a first approximation, compression tests can be used to predict the inaccessible data. Because of the strain rate ($\dot{\epsilon}_n$ applied by the testing machine) dependency, the nominal strain will be considered. Figure 92 displays a tension curve and an inverted compression curve. Both curves overlap on the elastic domain.

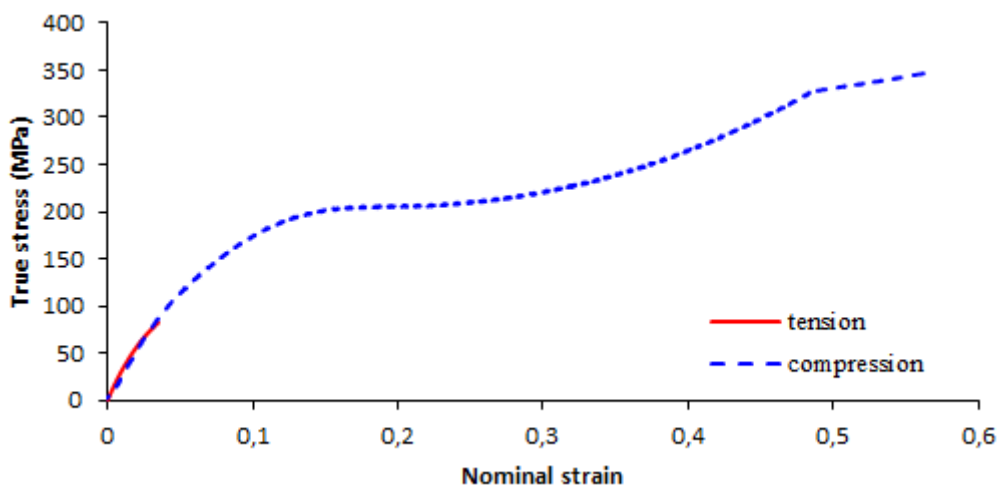


Figure 92: absolute stress/strain curves for uniaxial testing on the standard BMI/DBA network.

Increasing the strain rate increases the yield stress. The curves sequence displayed on Figure 93 follow a classic evolution with quite a low strain rate dependency, similarly to epoxies^[146,147]. Once in the hardening domain, no consistent strain rate dependency can be determined.

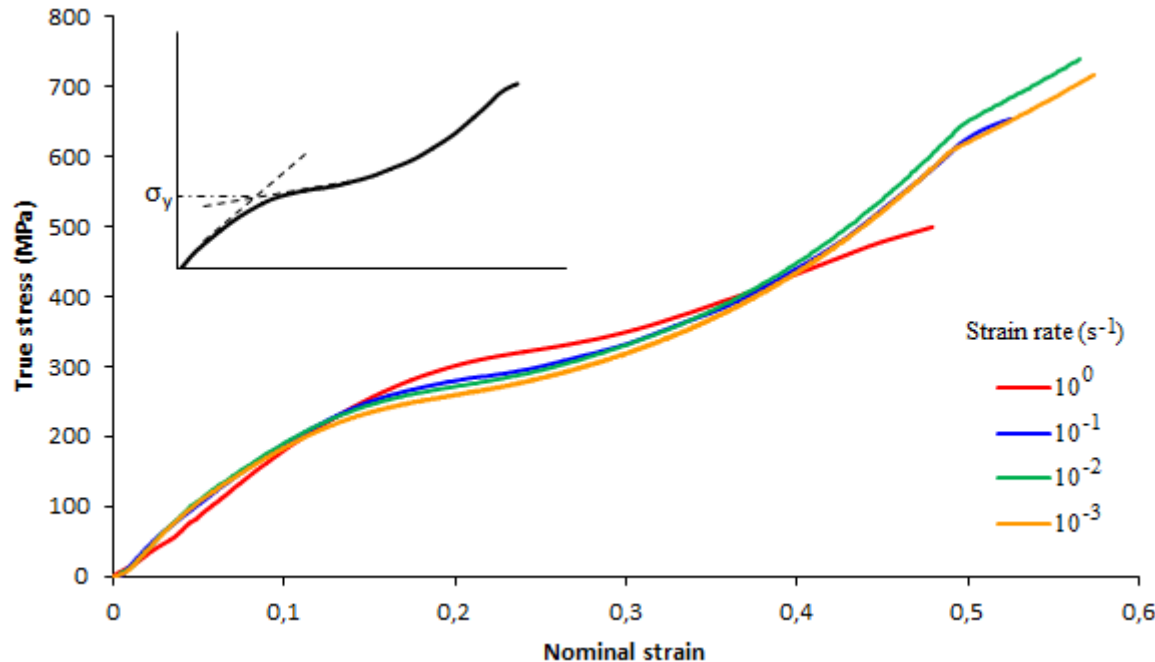


Figure 93: standard BMI/DBA behaviour in compressive mode at different strain rates.

The yield stress σ_y can be determined from these curves by the intersection of tangents in the elastic and yielding domains^[134] (see insert on Figure 93). The corresponding values are given in Table 7.

$\dot{\epsilon}$ (s $^{-1}$)	σ_y (MPa)
1	286
10^{-1}	253
10^{-2}	235
10^{-3}	218

Table 7: yield stress for the standard BMI/DBA network at different strain rates.

These yield stress values are far above the 100 MPa boundary value defined in the Kinloch-Williams theory and higher than yield stress for epoxy networks^[134, 147, 148], predicting quite a brittle behaviour.

Differences in the behaviour of polymeric materials in compression and tension can be pointed out^[149]. A correction is suggested by using a scaling factor between compression and tension stress values. This approach is inspired from modified von Mises criteria for the yield stress determination, the scaling factor being chosen at 0.75, owing to studies on various polymers^[149, 150] and especially epoxy networks^[151, 152]. This lowering of stress values will only be employed as a possible correction in the final evaluation of considered models.

3.3.1.4 Molecular behaviour

Information on the material behaviour at the molecular scale can be investigated from macroscopic mechanical characterisations. Ree and Eyring developed a theory establishing a relationship between mechanical stresses and molecular transitions^[153]. Considering a chain segment undergoing a transition between two sites, if $\Delta_t G$ is the energy associated to the transition without stress, the Ree-Eyring theory predicts equation 23 for an applied stress σ .

$$\frac{\sigma}{T} = \frac{\Delta_t G}{V_{act} T} + \frac{2.3k_B}{V_{act}} \log\left(\frac{\dot{\epsilon}}{\dot{\epsilon}_0}\right) \quad \text{Eq. 23}$$

with T the temperature (in K), V_{act} an activation volume, k_B the Boltzmann constant, $\dot{\epsilon}$ the strain rate and $\dot{\epsilon}_0$ a normalising constant (chosen at 1 s^{-1}). This model applied to the previously measured yield stress is displayed on Figure 94.

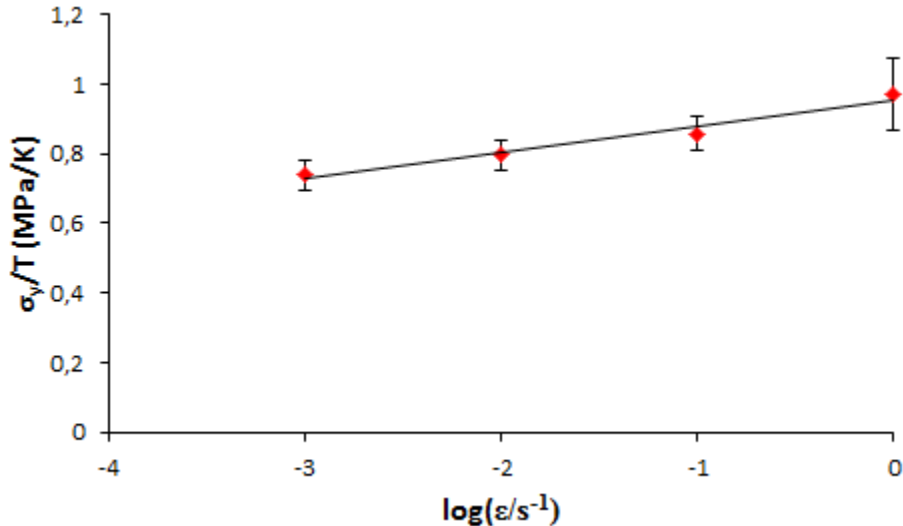


Figure 94: Ree-Eyring theory applied to yield stress under compression at 22°C (295 K).

A single linear regime is observed at room temperature over the whole strain rate range, which means that a single type of molecular transition is involved in the yielding process. With no data on the evolution of this curve by varying temperature, it is not possible to determine if this regime is associated to β or α -relaxations. However, measures were carried out 280°C below T_g , in the range of the β -relaxation peak (see Figure 15 in chapter 1), suggesting that β molecular transitions should be involved. V_{act} reflects the strain rate dependency, a high value being associated with a low rate dependency. The calculated value from equation 23 at room temperature is 0.42 nm^3 , which is lower than epoxy networks^[146, 147] but higher than other glassy polymers such as PMMA^[154].

3.3.2 Failure at the macroscopic scale

During fracture toughness measurements, the standard BMI/DBA cured resin behaved as a brittle material, being very sensitive to the notching procedure. Fractured surfaces appeared to be very smooth (mirror-like), SEM observation did not reveal any features even at a micrometric scale. Figure 95 shows images from an area between two crack-front prints, thus corresponding to the fast crack occurring for each testing cycle. Figure 96 focuses on a crack-stop area where a crack-front mark is barely visible (between red arrows). In both cases, no relief was observed.

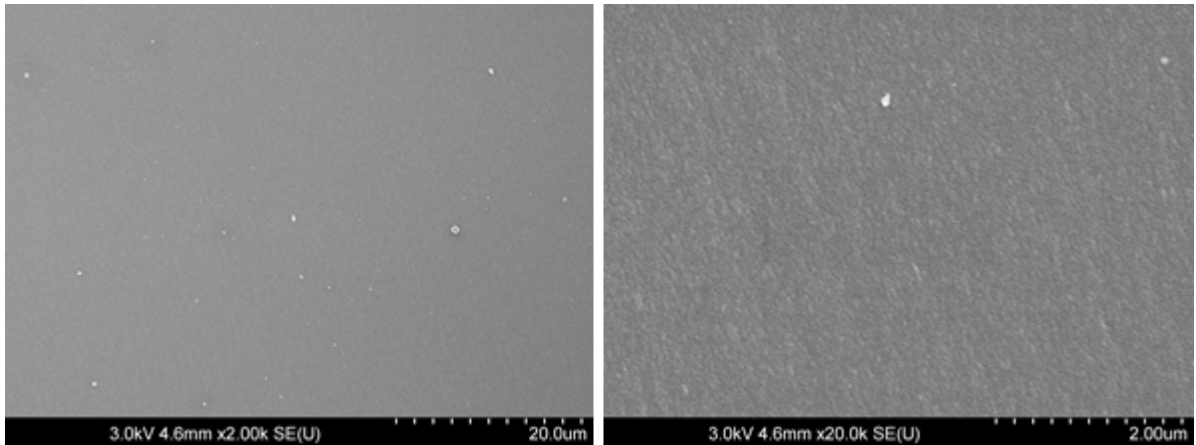


Figure 95: SEM fractography from a neat BMI/DBA compact tension sample.

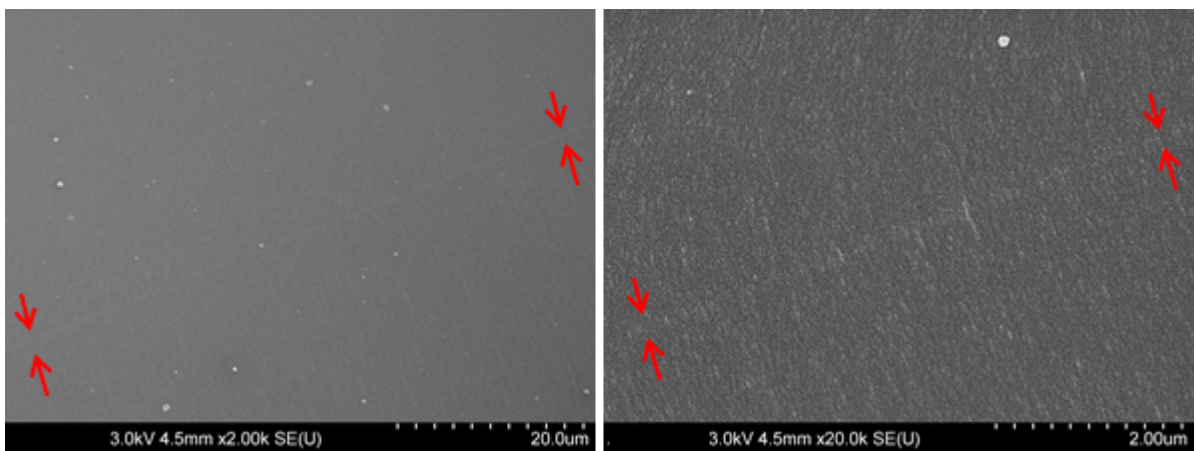


Figure 96: SEM fractography from a neat BMI/DBA compact tension sample: crack-stop area.

The fracture toughness in mode I was measured at $K_{IC} = 0.68 \pm 0.04 \text{ MPa.m}^{\frac{1}{2}}$, a value consistent with highly cross-linked epoxy networks (slightly higher) and silica inorganic glasses (a little lower).

3.3.3 Crack propagation kinetics

3.3.3.1 Evaluation of the stress intensity factor

As explained in paragraph 3.2.2.4, a crack-opening profile can be extracted from optical images in a DCDC experiment, or from interferometry. Pallares and co-workers used the crack-opening profile from DCDC on glass to evaluate the stress intensity factor in mode I: K_I ^[142]. Calculation is derived from Irwin fracture theory.

The extracted crack profile can be defined as a set of coordinates (x, y_1) and (x, y_2) . The crack-opening profile is defined as:

$$u_y(x) = \frac{y_2 - y_1}{2}$$

The crack-opening stands for half of the distance between the two edges. The selected fit equation is a Williams' expansion series:

$$u_y(x) = \frac{K_I}{E^*} \sqrt{\frac{\pi}{8}} (x^{0.5} + \alpha_3 x^{1.5} + \alpha_5 x^{2.5}) \quad \text{Eq. 24}$$

with, for plane strain conditions:

$$E^* = \frac{E}{1 - \nu^2}$$

Even if, as explained previously, edge detection is inaccurate near the crack-tip, AFM imaging provides complementary data. Figure 97 shows the superposition of two sets of points. No adjustment was made on the tip positions, determined independently, and the reconnection is extremely satisfying. However, this method can only be applied on static fractures with no evolution between optical and AFM imaging. Nevertheless, using the fit equation 24 with a fixed origin gave satisfying results, even without data exclusion near the crack-tip.

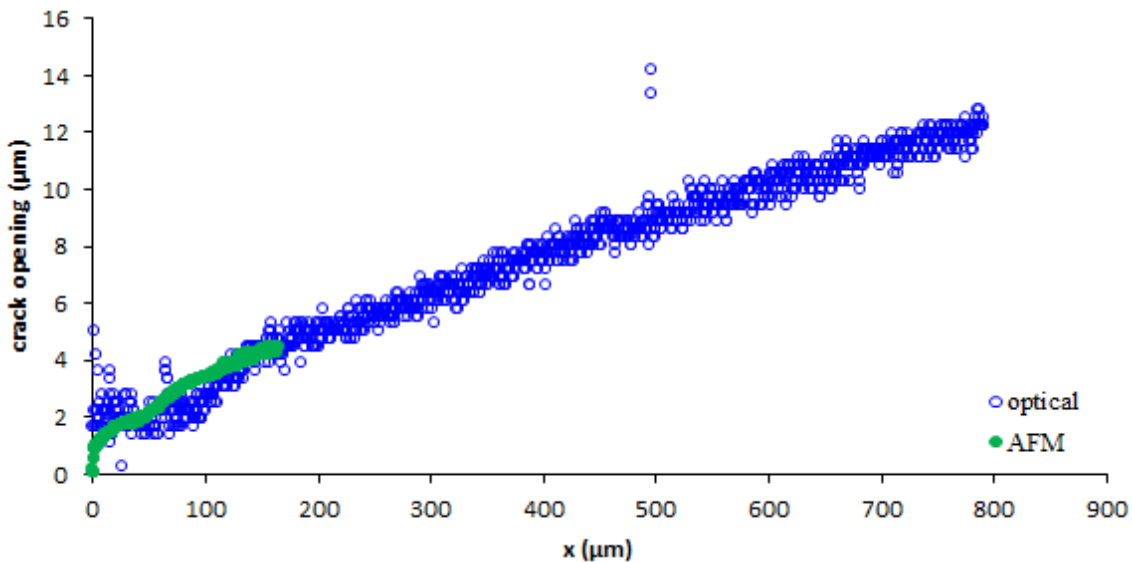


Figure 97: extracted crack-opening profile determined from optical and AFM imaging.

Equation 24 relies on an elasticity framework, consequently the assumption is made that the crack opening profile is not altered by plasticity. Considering the areas under yielding during a DCDC experiment (Figure 98), this requirement is partially fulfilled with a crack length avoiding edge effects. The plasticity at the crack tip is confined in a domain, which size can be estimated with equation 21. In the present case, the plastic zone size is close to a few micrometres (barely the optical camera resolution), and expected not to influence the crack opening profile at a millimetre scale.

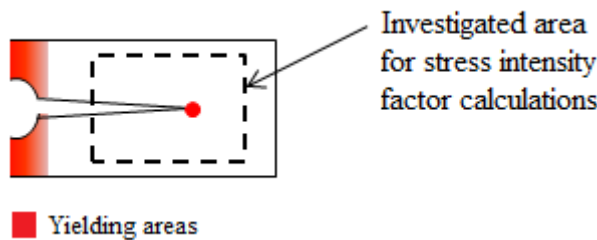


Figure 98: main locations of plasticity on DCDC samples.

Janssen used a calculation based on the crack length c to obtain the K_I values [140]:

$$\frac{\sigma\sqrt{R}}{K_I} = B_0 + B_1 \frac{c}{R} \quad \text{Eq. 25}$$

with R the DCDC specimen hole radius. Using finite element simulation, Janssen determined the B_0 and B_1 coefficients, allowing to calculate K_I knowing σ and c , independently from the material modulus E . Applied to bismaleimide networks DCDC samples, this method lead to K_I values higher than these resulting from equation 24 by 20 to 30%. As it will be displayed in the following paragraphs, stress intensity factors calculated with equation 24 are more consistent with the K_{IC} value measured by compact tension. Using the method from Pallares and co-workers on the images from the beginning of each experiment (right after the fast crack propagation) gives values from 0.63 to 0.67 MPa.m $^{\frac{1}{2}}$ that have to be compared to $K_{IC} = 0.68$ MPa.m $^{\frac{1}{2}}$, that stands for the initial value of K_I . Consequently stress intensity factors will be determined using equation 24.

3.3.3.2 Considerations on the crack opening measurement

The reliability of the stress intensity factor estimation will be addressed in this paragraph. Experiments provide crack opening profile measurements, for which accuracy has to be as much understood as possible. Different crack openings were obtained by loading cracked DCDC specimens, that were totally discharged right after crack propagation. Simultaneous measurements with interferometry and optical imaging were carried out on an compression range that did not allow the crack to propagate (progressive loading at 0.01 mm/min). Here the stress intensity factor K_I is used as a quantifier of the crack opening (equation 24 with $E = 3.45$ MPa).

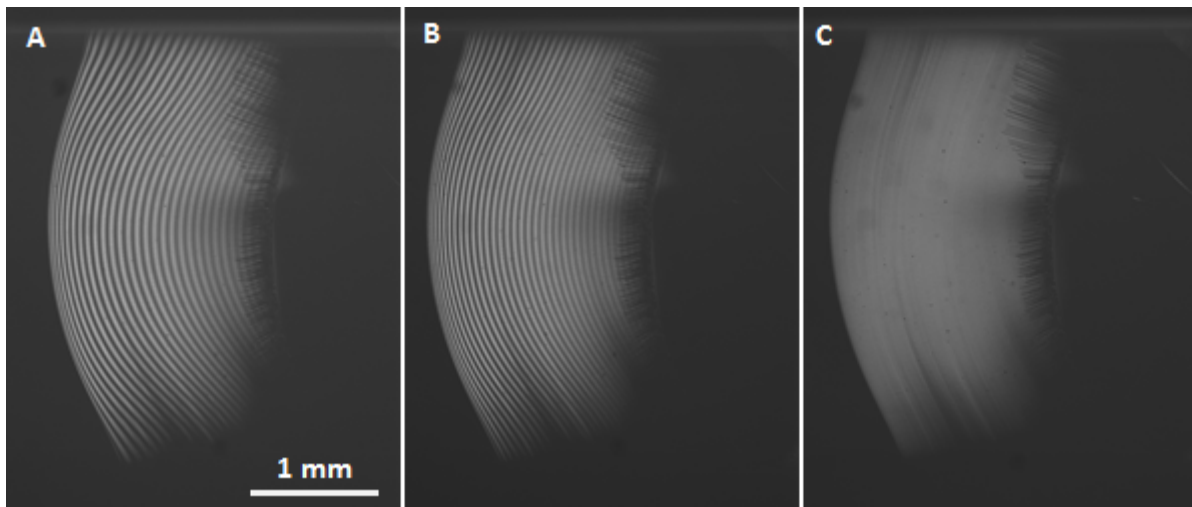


Figure 99: interference pattern of a crack in a DCDC sample at different applied forces.
A) $F = 100$ N ; B) $F = 300$ N ; C) $F = 1000$ N. Common scale: 1 mm.

The procedure to calculate K_I with optical imaging is described in the previous paragraph. Interferometric imaging provides fringe patterns as shown on Figure 99. From these, the crack opening profile $u_y(x)$ is obtained with equation 22 and an estimation K_{op} of K_I is determined with equation 24. The comparison between the two methods is given by Figure 100. Interferometric profiles were here measured near the sample upper external surface which correspond to the location of optical measurements for the opening.

The first noticeable result from interferometric observations is that under low loading levels, a significant difference is observed between the pattern in the middle specimen and near the surface. This difference progressively disappears by increasing the compression force (Figure 99A to C).

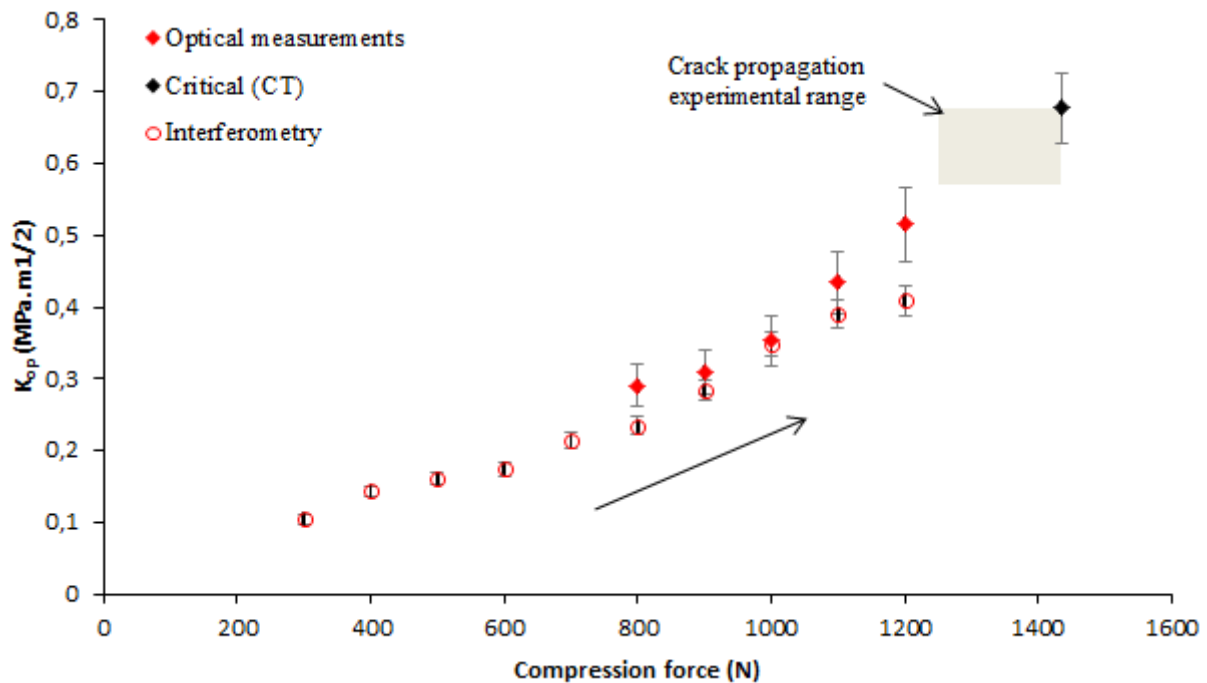


Figure 100: stress intensity factor calculated with optical and interferometric data for different applied forces while progressively loading.

Both optical and interferometric imaging appeared to be limited to different but complementary force ranges. Because of the camera resolution, optical imaging is not suitable to detect fine openings. Usually, data obtained under 600 N lead to inconsistent fits. On the contrary, a very good fringe resolution is achieved at these force levels, but for large opening profiles, the fringe spatial density is too high to be detected accurately. Both methods gave similar results in the 900-1100 N range.

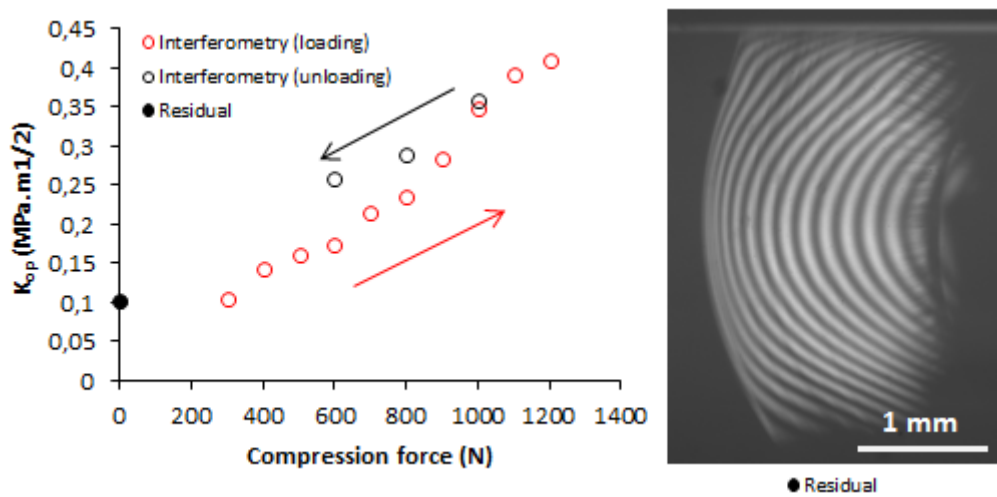


Figure 101: stress intensity factor calculated from interferometric data during loading up to 1200 N and unloading of a fresh fractured sample. Residual fringe pattern after complete unloading.

The opening profile is larger during the unloading phase and after complete unloading, a residual pattern is still visible (Figure 101). This points out the consequent plastic deformation occurring around the hole, where the lateral bending reaches its maximum.

3.3.3.3 Velocity measurements and $K(v)$ curves

Crack-tip velocity was measured during DCDC experiments, with optical imaging in a first step, then, when crack advances fall below the camera resolution, with AFM imaging [145]. The crack propagation is illustrated on Figure 102. Position measurements require a reference spot that is here dust or a local surface defect. Thanks to the compensating table, high image stability was achieved.

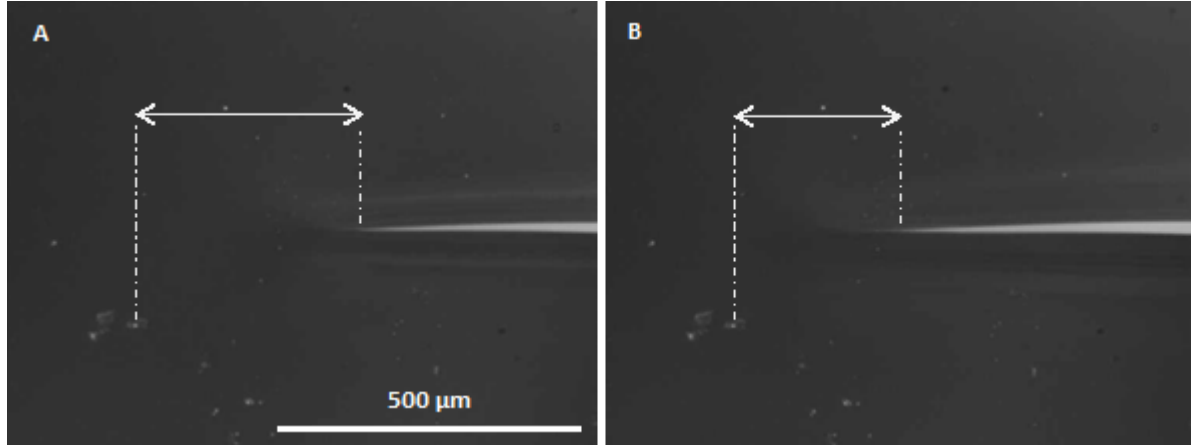


Figure 102: optical images of a crack-tip with enhanced contrast. A) t_0 ; B) $t_0 + 6$ min.
Common scale: 500 μm .

Figure 103 displays an example of crack-tip position measurements from four image acquisition sequences. Images were regularly sampled from series, for which the frame rate was chosen between 10 Hz and 0.2 Hz (decreasing as the crack-tip slowed down). Velocity was averaged over each set of images and corresponding time located at mid-sequence.

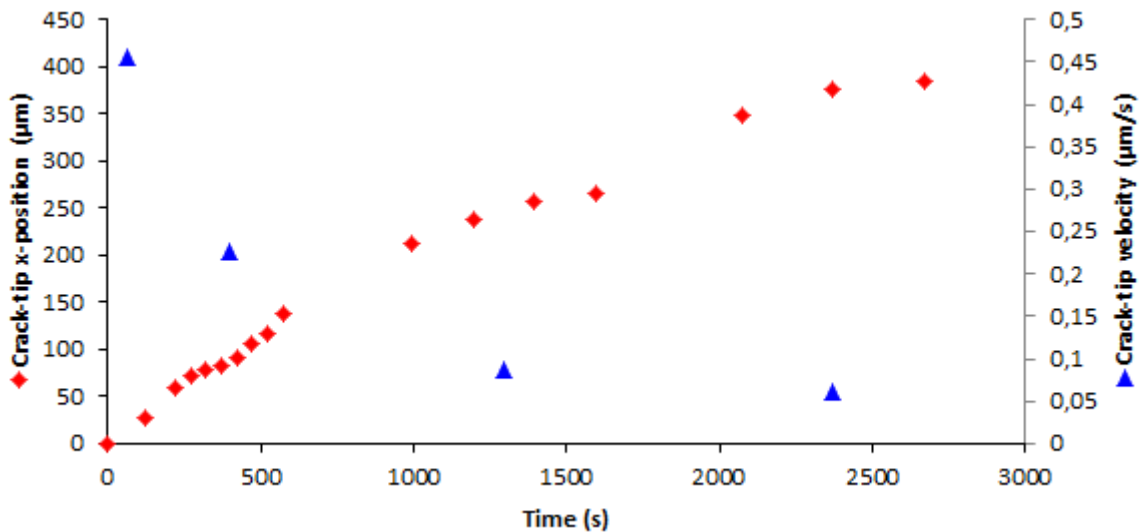


Figure 103: crack-tip position and velocity with optical measurements.

AFM observations usually started in the hour following the fast crack propagation and went on over a few days. As for optical imaging, crack propagation could still be observed (Figures 104 and 105). The polishing procedure provided excellent conditions for imaging. Comparison was made with samples cured on glass plates with no surface preparation and polished samples exhibited smoother surfaces. Moreover, orienting polishing lines along the propagation direction results into a good visualisation of local deformation.

Position measurements also require references, which constitutes a first complication for AFM imaging. With for the BMI/DBA standard resin $K_{IC} = 0.68 \pm 0.04 \text{ MPa.m}^{\frac{1}{2}}$ and σ_y values from Table 7, the process zone size is estimated with equation 21: $R_z \simeq 4 \pm 1 \mu\text{m}$. Considering that a perfectly valuable reference spot should be chosen outside the strained area (the process zone), a compromise with sufficient resolution, either time or space, has to be found. For high crack-tip velocity, small images and high acquisition rate are required to keep up with crack advances. For low velocities, high resolution, which implies a size limitation, is needed to detect small evolutions. The compromise was to select defects as far as possible from the crack-tip, considering that, locally, displacements are along the lateral axis while the crack moves through the main axis.

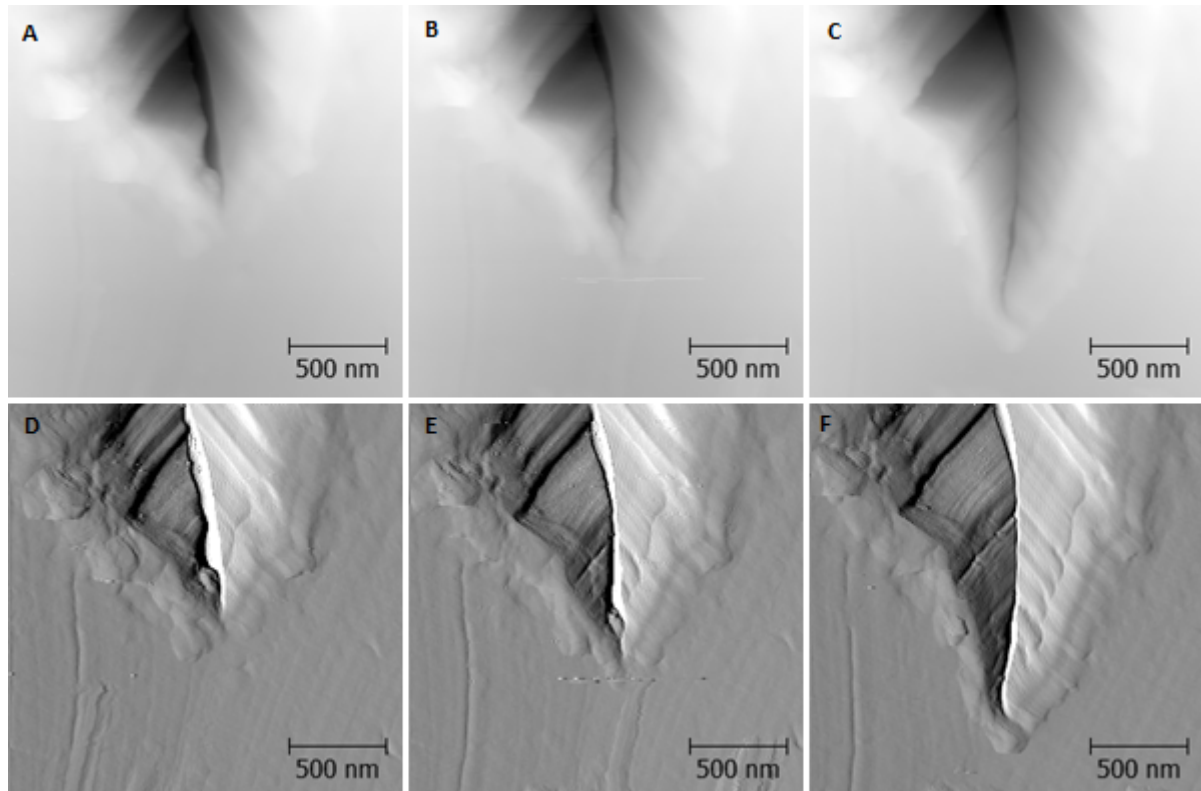


Figure 104: AFM images of a crack-tip: A),B),C) height ; D),E),F) peak force error.
A),D) t_0 ; B),E) $t_0 + 9 \text{ min}$; C),F) $t_0 + 22.5 \text{ min}$.

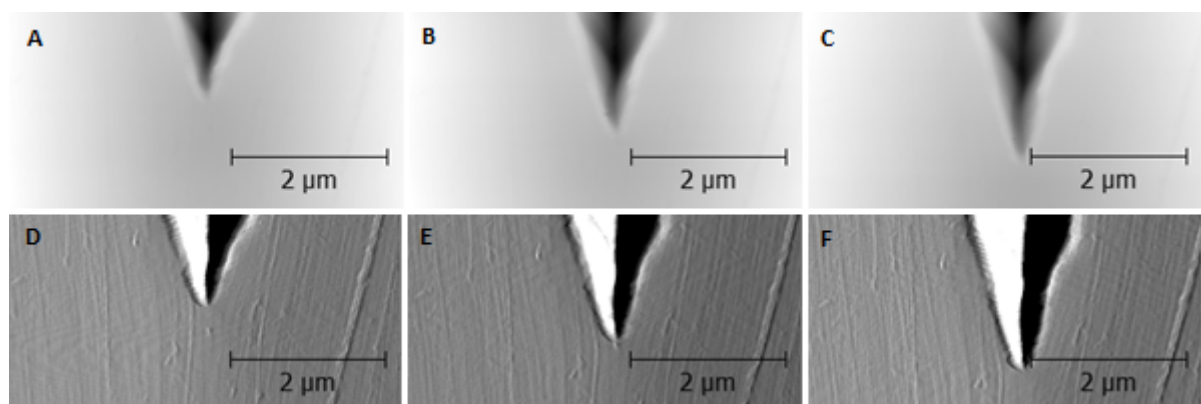


Figure 105: AFM images of a crack-tip: A),B),C) height ; D),E),F) deflection error.
A),D) t_0 ; B),E) $t_0 + 8.5 \text{ min}$; C),F) $t_0 + 13 \text{ min}$.

AFM velocity measurements were performed on images with a size included between 4 μm and 10 μm . For highest velocities, the aspect ratio was increased up to 4, Figure 105

being an example of an aspect ratio of 2. The slow scan direction was always opposite to the propagation direction in order to minimize bias due to crack propagation.

Very low velocities could be calculated from an image to the following one. If position was measured for each image, velocity, as a local derivative of position, was calculated with various time intervals. A criterion was to consider that a calculated speed had to cover a minimum distance (arbitrarily fixed to 10 times the spatial resolution) on the time interval used for calculation. This ensured that evaluated velocities would correspond to an actual propagation and possess a comparable accuracy.

The stress intensity factor measurement procedure described in paragraph 3.3.3.1 can only be applied on optical images. Moreover, the determination of K_I by that means is not expected to be accurate to more than 5-10%. Consequently, small variations of K_I would not be detected. On the other hand, the applied force F is measured continuously by the loading cell. Considering equation 25, the second member only depends on the crack length c for fixed geometrical parameters [140, 142, 155]. Thus, considering a low variation of the crack length during the experiment (less than 5%) and introducing the force F and the lateral sample surface S , equation 25 is simplified to:

$$F \propto \frac{S}{\sqrt{\pi R}} K_I \quad \text{Eq. 26}$$

From here, the hypothesis is drawn that K_I and F are simply proportional. Figure 106 shows the measured evolution of the applied force (the displayed displacement is a control parameter, not a measured value). During the loading phase, the force increases with a linear behaviour according to elasticity laws. Sample relaxation is observed immediately after crack fast propagation. After a few hours, the force can be considered as quasi-constant on quite long periods.

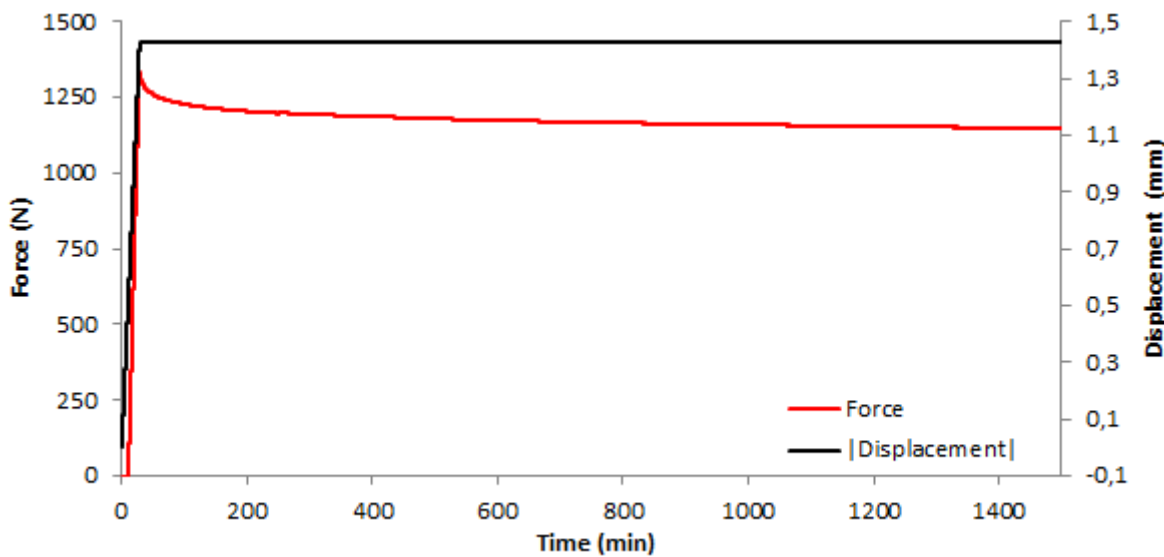


Figure 106: force evolution during a DCDC experiment.

A proportionality factor between K_I and F was determined for each experiment from the initial acquisition optical images, using edge detection and fit by Williams equation (equation 24). To each calculated crack-tip velocity, a measured force can be attributed (the corresponding parameter being the acquisition time) and therefore, a stress intensity factor value. The resulting $K_I(v)$ curves for three samples are plotted on Figure 107.

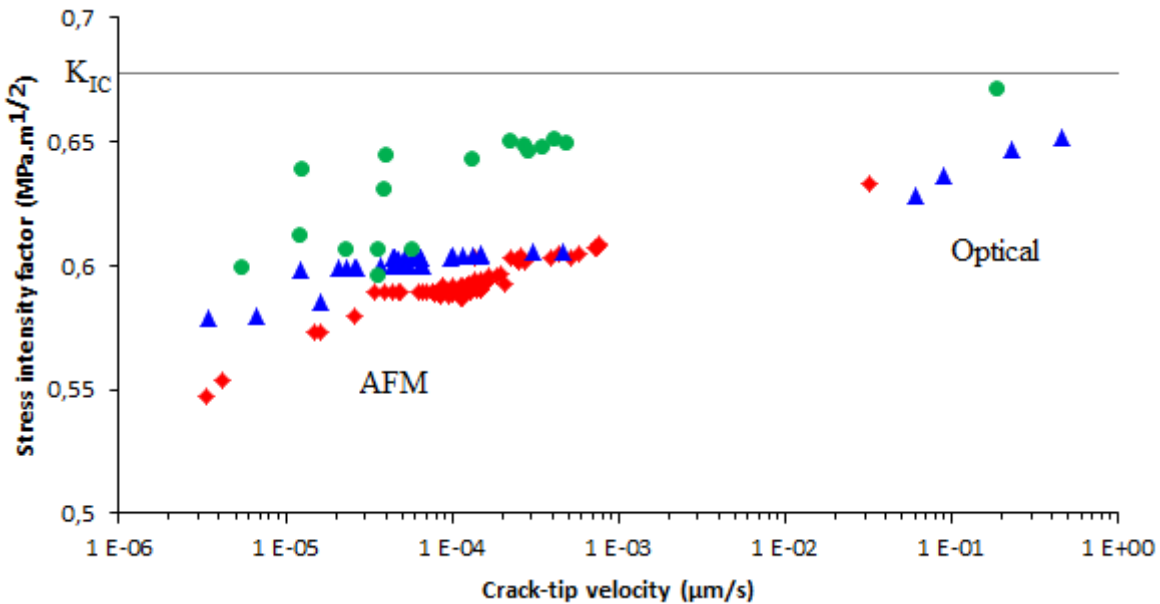


Figure 107: $K_I(v)$ curves for three standard BMI/DBA DCDC samples.

Optical imaging is suitable for velocities between 1 $\mu\text{m/s}$ and 10 nm/s (this last speed corresponding to roughly 1 pixel/min with the best resolution objective). AFM imaging is applied in the 1 nm/s –10 pm/s range. The gap between the two methods on Figure 107 corresponds to the transfer of the loading cell between the optical camera device and AFM. In addition, first AFM images cannot be used to properly measure velocities that are still too high. The highest values for K_I are noticeably close to the critical value: $K_{IC} = 0.68 \text{ MPa.m}^{\frac{1}{2}}$, a non-obvious fact considering the method precision.

Vertical scattering between samples is still under the 10% estimated accuracy. The stress intensity factor variation is quite small: 10 to 15% on nearly six decades for velocity, however a $K(v)$ curve can be obtained. Scattering within each curve will be discussed in the next part.

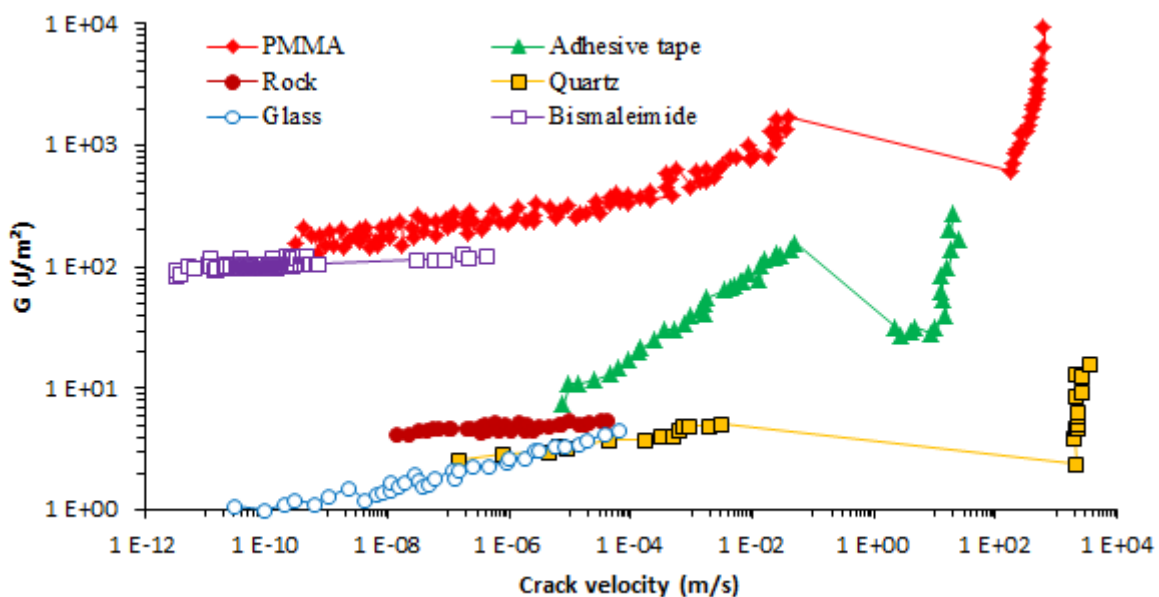


Figure 108: $G(v)$ curves for different kinds of materials. From: \blacklozenge [156, 157], \blacktriangle [158], \bullet [159], \blacksquare [160] and \circ [161].

These three $K(v)$ curves are transformed into $G(v)$ curves using equation 20 and reported with similar curves from various materials (Figure 108). It can be seen that this bismaleimide network ranges in the same region as PMMA, another glassy polymer, with a slightly smaller slope. As a result, these investigations on low velocity propagating cracks can be related to similar studies on very different materials, suggesting a wide frame to compare fracture behaviours.

3.4 Influence of the network architecture

3.4.1 Non-monotonic crack propagation

Scattering within $K(v)$ curves was mentioned in the previous part. Moving from an average analysis to an image to image analysis provides more information on local behaviours.

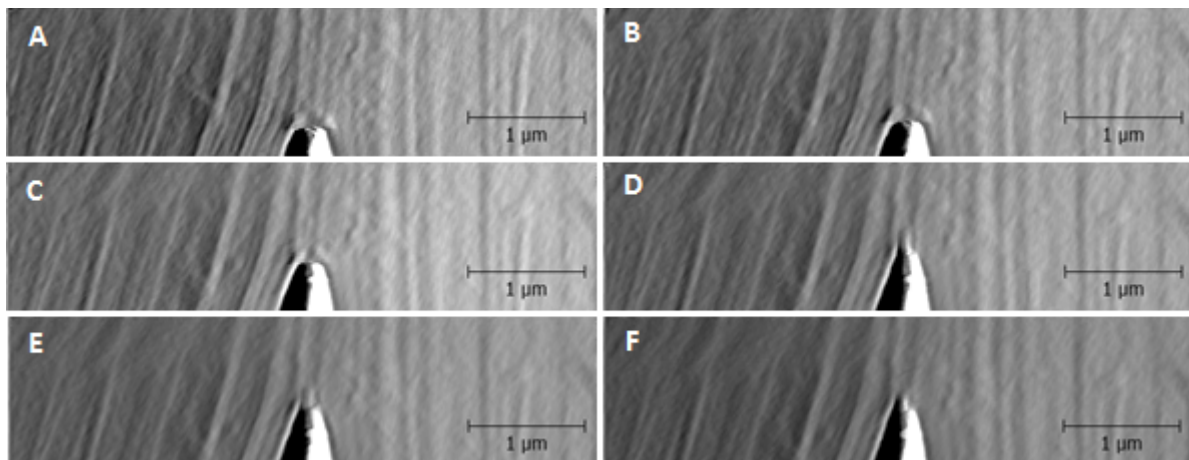


Figure 109: AFM images (deflection error) of crack-tip shape evolution during a slow propagation for the BMI/DBA network. A) t_0 ; B) $t_0 + 9.5$ min ; C) $t_0 + 20$ min ; D) $t_0 + 24$ min ; E) $t_0 + 28$ min ; F) $t_0 + 32$ min.

Figure 109 displays an image sequence showing the evolution of the crack tip when the average velocity is inferior to 0.1 nm/s, which was usually reached during the second day of observation. Trying to estimate the velocity with the propagation from an image to the following one gives two kinds of results. In most cases the crack-tip advance is barely measurable, consequently leading to speeds much lower than the average velocity (Figure 109A to C). A brutal propagation is observed on over 250 nm resulting into a very high velocity (Figure 109D). This last speed is only estimated by a lower value, due to the image acquisition time. The resulting velocity profile is plotted on Figure 110.

These local changes in the crack-tip velocity are correlated with changes in the tip-shape. During the slow phase, the tip is very rounded (Figure 109A to C). The brutal propagation is accompanied with a shape modification toward a fine and sharp tip (Figure 109D). The crack-tip then begins to be rounded again before the following fast propagation (Figure 109E and F).

This looks like a stick-slip phenomenon, but at very small scale. The rounded shape is consistent with Kinloch definition of crack blunting and the whole sequence is similar to the process suggested by Phillips and co-workers for epoxy networks at a larger scale [162]. This is not observed before the average velocity fell down under a critical value (roughly

0.1 nm/s), suggesting either a superposition of two processes or a variation of the characteristic time. The latter would involve a continuous decrease of the fast propagation frequency, which was not observed.

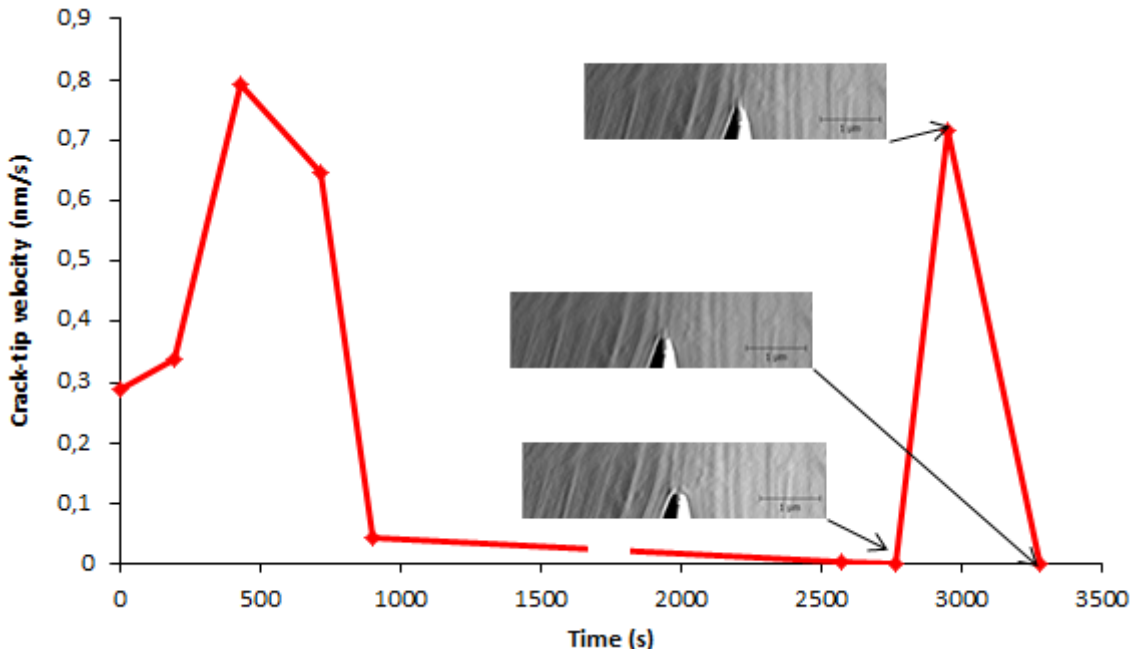


Figure 110: crack-tip image to image velocity for the standard BMI/DBA network. Line broken where images were omitted.

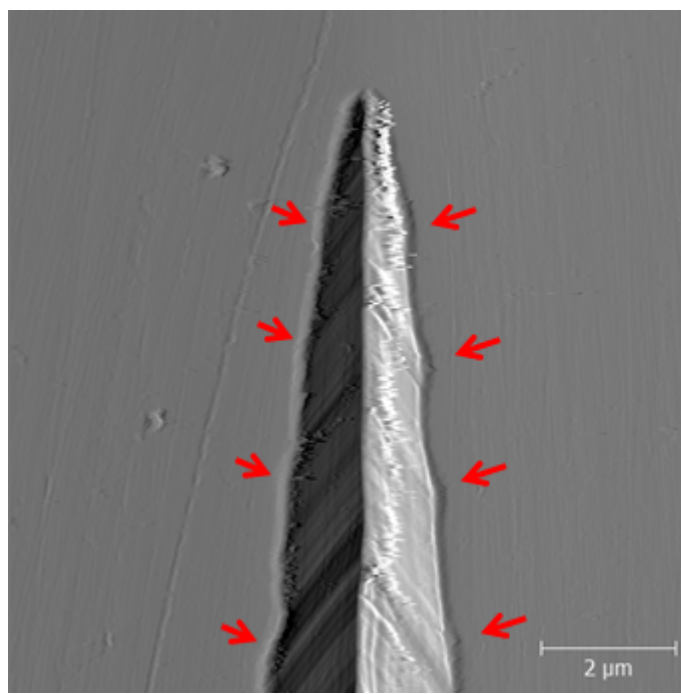


Figure 111: AFM image (deflection error) of a crack profile of the standard BMI/DBA network during a DCDC experiment.

Examination of the crack edges revealed a specific outline with irregularities. Already visible on Figure 104, “oscillations” of the edges can be seen up to a micrometric scale (red arrows on Figure 111). Small points are spaced out away from the crack-tip, resulting into a pine-tree shape. This shape can be associated with the marks of the alternating crack-tip shape changes. The spacing between these marks increases after cracking, possibly because of plastic yielding in the wake of the process zone.

3.4.2 Network modification

The chemical and physico-chemical investigations detailed in chapter 1 pointed out a complex reactivity of the thermoset, involving free radical polymerization. It was also shown how the network inhomogeneities could be reduced, using a radical inhibitor with an adapted curing cycle. The typical size of these inhomogeneities was not investigated directly but it is expected to be lower than a few hundred nanometres, an estimation comforted by the clear transparency of the cured material, indicating no light diffusion. The characteristic size of inhomogeneities and the typical leap-length during slow crack propagation, described in the previous paragraph, are on the same scale.

A more homogeneous network of hydroquinone-modified BMI/DBA resin was then similarly analysed under AFM during slow crack propagation. Special attention was paid to local changes in crack-tip velocity. Successive images are displayed on Figure 112. A shape evolution is still visible, from a rounded tip (Figure 112A to C) to a sharper one (Figure 112D and E), before starting to be rounded up again (Figure 112F). On the contrary to the standard resin, there is no brutal propagation, the shape modification occurs smoothly. Moreover, the sharp state is not as fine and sharp for this modified resin.

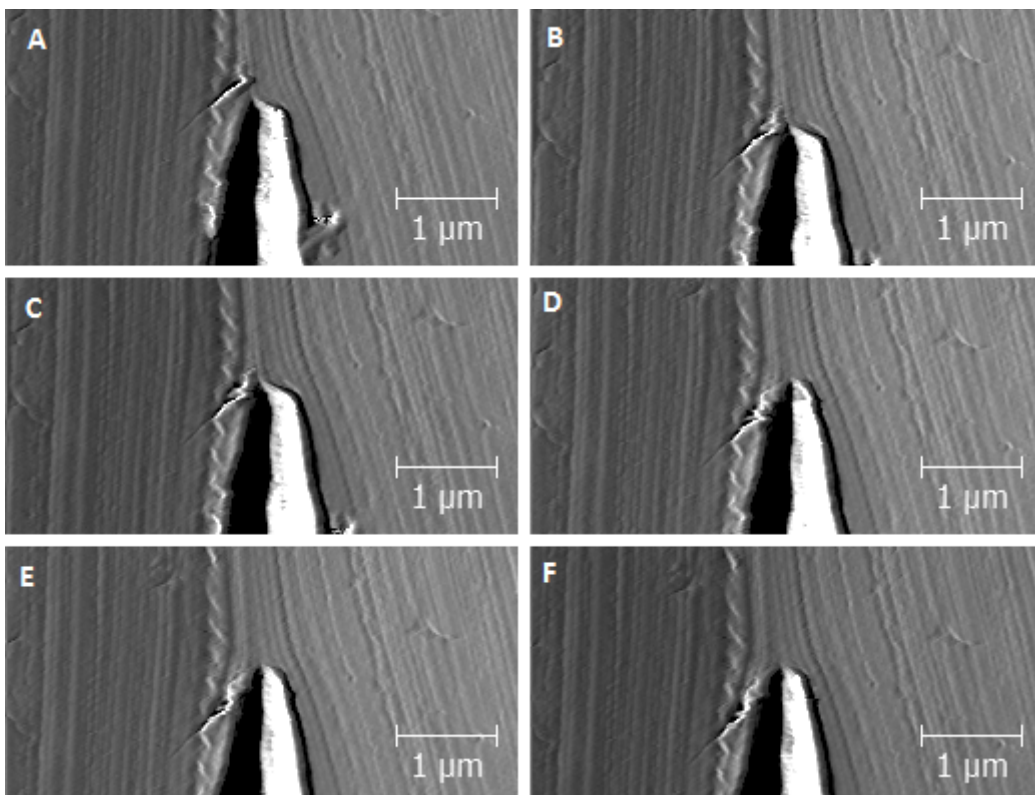


Figure 112: AFM images (deflection error) of crack-tip shape evolution during a slow propagation for the hydroquinone-modified BMI/DBA network. A) t_0 ; B) $t_0 + 6 \text{ min}$; C) $t_0 + 9.5 \text{ min}$; D) $t_0 + 13 \text{ min}$; E) $t_0 + 16.5 \text{ min}$; F) $t_0 + 20 \text{ min}$.

The image to image crack-tip velocity measurements revealed a consistent disappearance of sharp peaks along with brutal propagation. They are replaced by broader peaks with acceleration and deceleration phases (Figure 113). From a practical point of view, velocity measurements were much easier with a smoother evolution. The highest crack advance between two successive images are around 130 nm, compared to an average of 250 nm for the unmodified resin.

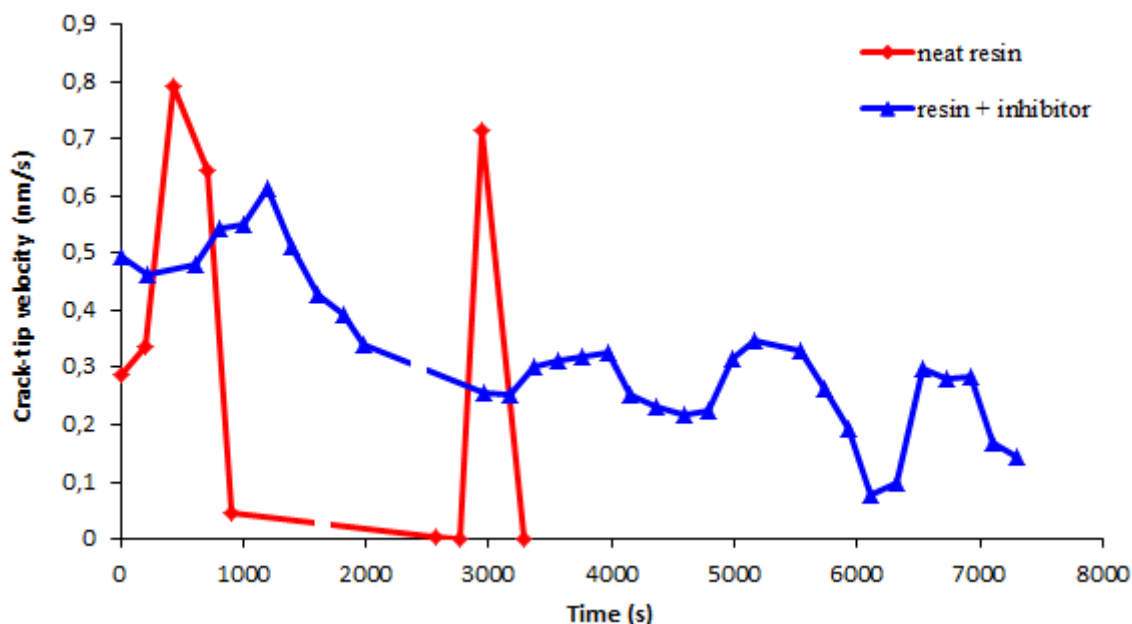


Figure 113: crack-tip velocity for the standard and hydroquinone-modified BMI/DBA networks. Lines broken where images were omitted.

A standard BMI/DBA resin sample could lead to 2 to 4 brutal propagations before the velocity was too low to carry on observations, whereas hydroquinone-modified resin samples usually exhibit over 6 acceleration/deceleration alternated phases. These are also less erratic and nearly appear as a modulation around a global decrease of the average crack-tip velocity.

Even the crack-profile is modified with the substantial disappearance of the “pine-tree” shape (Figure 114).

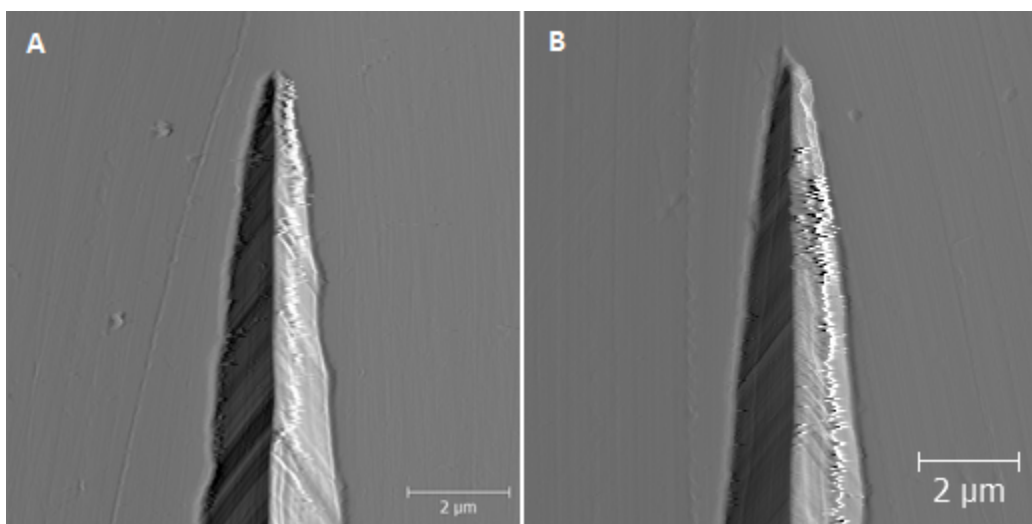


Figure 114: AFM images (deflection error) of crack-tip profiles: A) standard network ; B) hydroquinone-modified network.

Arising from these observations, the irregular crack-propagation appears to be related to the thermoset network structure. Inhomogeneities seem to promote brutal and erratic crack propagation. On the other hand, if the use of a more homogeneous network did not suppress completely the non-monotonic variations of the crack-tip velocity, it made

it smoother. Consequently, either these speed variations are only due to the network structure, suggesting that the homogenised material still contains inhomogeneities, which is plausible as long as free radical polymerization occurs, or there exist an underlying mechanical process that could be called “micro stick-slip”.

3.5 Modelling toughness

3.5.1 Steady state toughness

Steady state is a prerequisite to establish a $K(v)$ curve. In the case of DCDC experiments, the steady state hypothesis can be expressed as a crack propagation over at least the size of a process zone to make the corresponding measured velocity valid. High velocities are easily in agreement, whereas low velocities would require extremely long acquisition times (over 100h at 10 $\mu\text{m/s}$). Nevertheless, even low velocities provided results consistent with both the general aspect of a $K(v)$ curve and the critical value of K . In addition, as described in the previous part, other phenomena are visible in the low velocity range, leading to a scattering covering a possible effect of deviation from the steady state conditions.

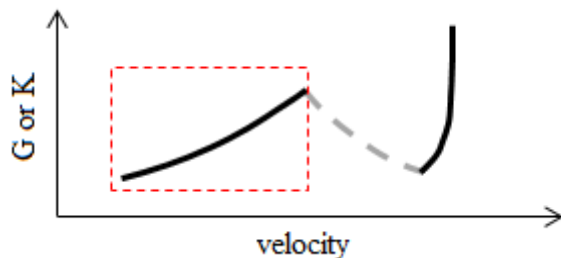


Figure 115: Steady state curve.

The rate dependent toughness of a material can be described by the $K(v)$ curve. The steady state corresponds to the low velocity part of the curve (Figure 115). The existence of such a range of low velocities is well established for glassy polymers such as PMMA [156] (see Figure 108) but not for thermosets. Using the same AFM imaging procedure as the present work, Nziakou observed similar low velocities in epoxy networks [143–145, 163]. As displayed previously, slow crack propagation was here evidenced for bismaleimide networks.

The following discussion suggests a theoretical approach to link the behaviour law of the material with the steady state curve. This is a part of general approach of fracture mechanics in polymers developed by Ciccotti and co-workers [145, 163, 164].

3.5.2 Material behaviour at the crack-tip

AFM imaging provided visual information on the crack-tip strain field. Using the polishing lines as markers, strain at the crack-tip can be estimated (Figure 116). Far from the crack-tip polishing lines are straight. They can be considered as parallel or with a small angle. Depending on the image and the chosen lines, extensional strains near the crack-tip are manually estimated between 20% and 40%.

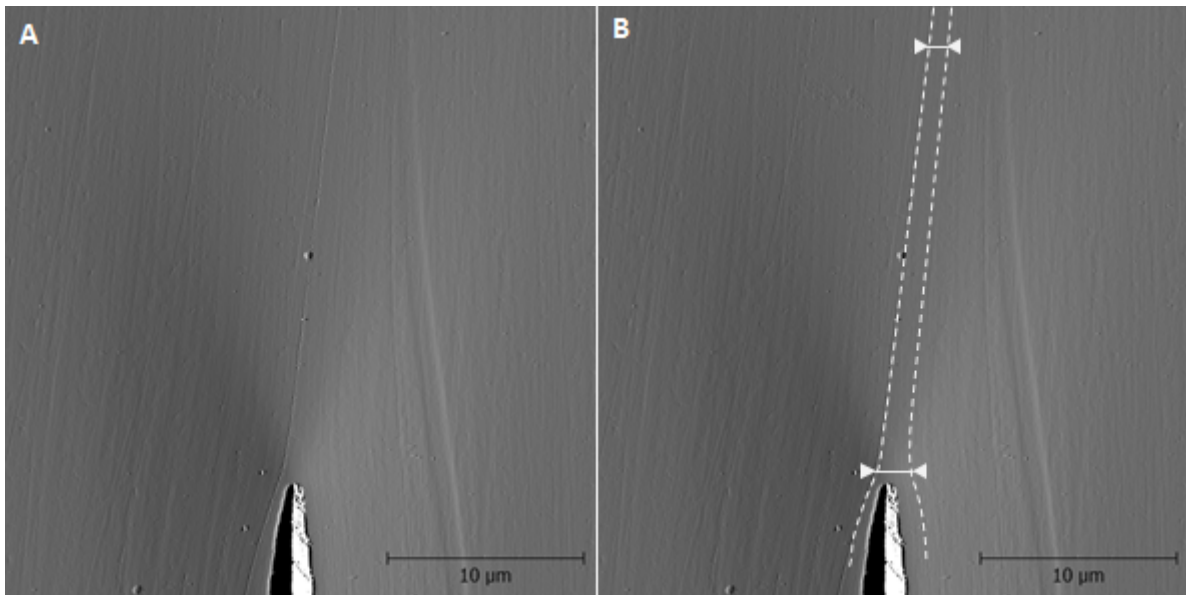


Figure 116: AFM image (deflection error) of a crack-tip. A) reference image ; B) image with markers for local strain estimation.

Even if these estimations are not very accurate, at 15% strain, a plastic behaviour is expected. Higher strain should lead to hardening (see Figure 93). At this scale, the material immediately in front of the crack-tip would experience a high level of alteration. A process zone with a size R_z is developed at the crack-tip. For a scaling approach, the exact shape of the process zone is not considered and it will be represented by a circular area.

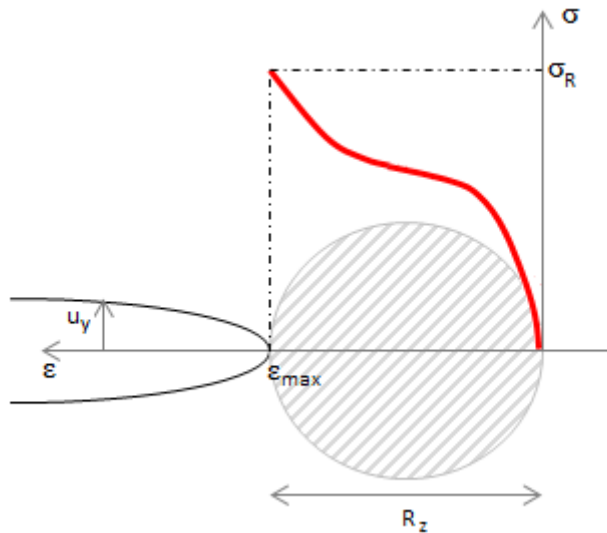


Figure 117: process zone at a crack-tip with complex material alteration.

The suggested relation between the material behaviour law and the alteration in the process zone is schematically displayed on Figure 117. The maximum strain ϵ_{max} is reached at the crack-tip before local material failure for a maximum stress σ_R . These absolute characteristic are not measurable with macroscopic samples because failure in tension is dictated by defects. At the process zone scale, critical defects have a very low presence probability, which makes the material experiencing its behaviour law on a deeper level.

3.5.3 Steady state crack propagation

Considering a steady state case, the crack-tip velocity v is constant. The strain rate in the process zone is determined by the propagating crack speed. In this case, the process zone size is constant and it propagates at the same velocity v . As a first approximation, a linear dependency of the strain ϵ with position along the crack direction (as assumed on Figure 117), gives for the mean strain rate at the crack-tip:

$$\dot{\epsilon}_f = \frac{\epsilon_{max} - \epsilon_{min}}{R_Z/v} \simeq \frac{v}{R_z} \epsilon_{max} \quad \text{Eq. 27}$$

Here the strain outside the process zone is considered negligible. This strain rate $\dot{\epsilon}_f$ determines the material behaviour in the process zone, leading to the stress profile sketched on Figure 117.

For the standard BMI/DBA network, $R_Z \simeq 4 \mu\text{m}$, v varies between $10^{-6} \mu\text{m/s}$ and $1 \mu\text{m/s}$, estimating ϵ_{max} close to 0.5 in tension at this scale (see paragraph 3.5.2), the resulting interval for $\dot{\epsilon}_f$ is estimated to 10^{-7} – 10^{-1}s^{-1} . Experiments in compression were performed between 10^{-3}s^{-1} and 10^1s^{-1} , but a low rate dependency was observed on this range (Figure 93).

The volume density of energy W dissipated by the local material alteration is expressed by:

$$W(\epsilon_{max}, \dot{\epsilon}) = \int_0^{\epsilon_{max}} \sigma(\dot{\epsilon}, \epsilon) d\epsilon \quad \text{Eq. 28}$$

Here the characteristic volume element is approximately $R_Z^2 h$ with h the sample thickness. When the crack propagates through a process zone size, the created area is $R_Z h$. Using equation 28, the dissipated energy per unit crack surface Γ is:

$$\Gamma \simeq \frac{R_Z^2 h}{R_Z h} W(\epsilon_{max}, \dot{\epsilon}) = R_Z \int_0^{\epsilon_{max}} \sigma(\dot{\epsilon}, \epsilon) d\epsilon \quad \text{Eq. 29}$$

The link between the dissipated energy at the crack-tip Γ is made with the rate dependent behaviour law of the material $\sigma(\dot{\epsilon}, \epsilon)$. The calculation involves the area under the appropriate stress/strain curve, selected with $\dot{\epsilon} = \dot{\epsilon}_f$, up to the maximum encountered strain ϵ_{max} . Not taking into account the deep material alteration (hardening) and considering only the plastic yielding dissipation leads to $\Gamma \simeq R_Z \sigma_y \epsilon_{max}$, a classical numerical application to justify the huge difference between the bonding energy in the material (1 J/m^2) and the observed dissipated energy (265 J/m^2 for $R_Z = 4 \mu\text{m}$, $\sigma_y = 220 \text{ MPa}$ and $\epsilon_{max} = 0.3$).

The steady state curve is calculated with $G(v) = \Gamma(\dot{\epsilon}(v))$ and $K = \sqrt{GE^*}$, E^* being the effective modulus depending on the loading conditions:

$$K(v) = \sqrt{\Gamma(\dot{\epsilon}(v)) E^*} \quad \text{Eq. 30}$$

Equations 29 and 30 express the fact that a low strain dependency of the material behaviour law should lead to a low variation of K with the crack-tip velocity, which is

consistent with the experimental data collected on the standard BMI/DBA network.

From a practical point of view, calculation of the $K(v)$ curve with these equations requires stress/strain curves of the material for different strain rates and an accurate measurement of the maximum strain at the crack-tip (ϵ_{max}), for instance through digital image correlation. With all the data available on the studied bismaleimide resin, only a rough numerical application is possible, ϵ_{max} being only estimated without any potential strain rate dependency. Using $\epsilon_{max} = 0.3$ and plane strain modulus, brings results summarized in Table 8 for the extreme values of the strain rate.

$\dot{\epsilon}$ (s ⁻¹)	v (μm/s) ^a	K_{th} (MPa.m ^{1/2}) ^b	K_{exp} (MPa.m ^{1/2}) ^c
10^{-1}	7.2×10^{-1}	1	0.655
10^{-2}	7.2×10^{-2}	0.995	0.635
10^{-3}	7.2×10^{-3}	0.977	0.62

Table 8: rate dependent stress intensity factor calculations.

a: calculated with equation 27 ; b: calculated with equations 29 and 30; c: estimated from Figure 107.

So far, the calculation leads to K values higher by 50% than measured ones, which is to be expected from a scaling approach. This can be compared to the plastic zone approximation taking into account the strain rate dependency of σ_y :

$$\Gamma \simeq R_Z \sigma_y(\dot{\epsilon}) \epsilon_{max} \quad \text{Eq. 31}$$

Comparison between predictions deriving from equations 29 and 31 are displayed on Figure 118A. Both overestimate the K value, the integral model being slightly closer to those given by experiments. One of the reason for this overestimation may lie in the use of compression data while the material locally experiences tension. The 0.75 scaling factor from uniaxial compression to uniaxial tension stresses can also be applied as introduced in paragraph 3.3.1.3 . The corrected data are plotted on Figure 118B, the overestimation is lowered to 30%.

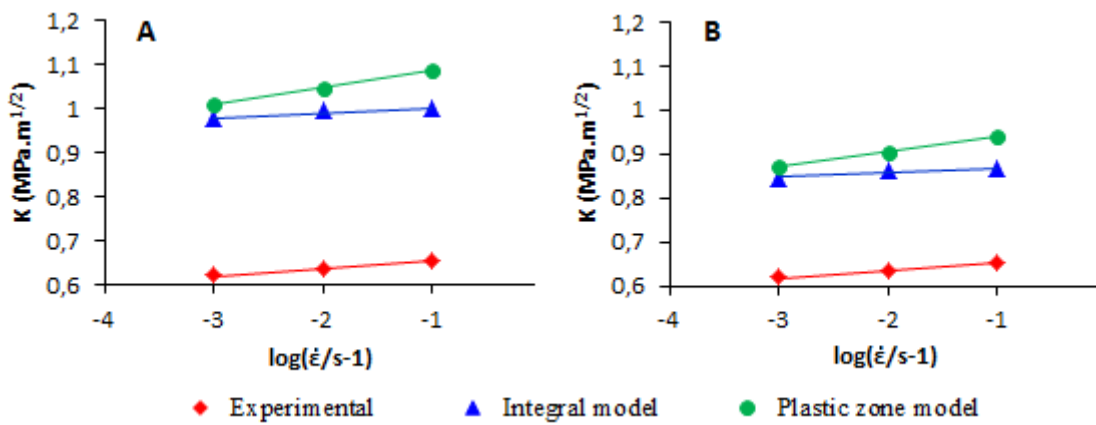


Figure 118: experimental and calculated values of K . \blacklozenge estimated from Figure 107.
 A) \blacktriangle calculated with equations 29 and 30, \bullet calculated with equations 31 and 30.
 B) \blacktriangle and \bullet including von Mises stress correction.

The remarkable fact is that despite the rough approximation on ϵ_{max} , the low variation of K with the crack-tip velocity is found by a correct order of magnitude. Comparison

between the slopes resulting from experimental $K(v)$ curves (Figure 107 and equation 27) and those of both models are given in Table 9. It can be seen that the integral gives a better prediction than the plastic zone model.

Model	Basic models	Corrected models
Integral ^a	11.5	10
Plastic zone ^b	38.9	33.7
Experimental		17.5

Table 9: slopes of $K(\dot{\epsilon})$ curves in $\text{Pa} \cdot \text{m}^{\frac{1}{2}}/\text{decade}$ from Figure 118.

a: calculated with equations 29 and 30; b: calculated with equations 31 and 30.

Equations 23, 27, 31 and 30 establish a prediction of the $K(v)$ curve from the Re-Eyring theory, with the correct range of K but a slope too high by a factor 2 on the investigated range of velocities/strain rates. This provides a tool to investigate the polymer chain movements involved during the slow crack propagation. Equation 29, adding deeper non-linear contributions, achieves a better prediction of the slope.

Considering the lack of determination of the crucial parameter ϵ_{max} , the limited data available and the experimental scattering, no further conclusion will be drawn.

3.6 Conclusion

Crack propagation phenomena were investigated for the standard BMI/DBA network at the sub-microscopic scale. With the DCDC geometry, slow crack propagation was observed with crack-tip velocities ranging from $10^{-6} \mu\text{m/s}$ to $1 \mu\text{m/s}$. A relationship between the crack-tip velocity and the stress intensity factor was suggested, resulting to $K(v)$ curves. This can be compared to other glassy polymers such as PMMA, but also to very different materials such as glass, rocks or adhesives. AFM observations of the crack-tip provided valuable information on strain fields at a local scale, allowing investigations inside the process zone. A model to predict the shape of the $K(v)$ curve, taking the material local high level of alteration into account, was suggested. It provided an estimation of the stress intensity factor with a correct order of magnitude and a satisfying prediction of velocity dependency.

A non-monotonic crack propagation was observed for the lowest crack-tip velocities, with evidence of blunting. This phenomenon that resemble a “micro stick-slip” appeared to be linked to the network structure. However, owing to the lack of complementary data on these networks, an explanation through a mechanical process can also be considered.

Chapter 4

Fracture in heterogeneous materials

Modified bismaleimide resins exhibit various morphological features, the second chapter gathers information about these morphologies and the means to obtain them. The third chapter focuses on the neat bismaleimide network fracture, using a specific testing geometry. This experimental device was adapted to study thermoplastic-modified matrices. After general considerations on thermoset toughening and composite failure, crack propagation in multi-phase materials will be investigated. The last part will address failure mechanisms of complex composite laminates and compare them to the previous study.

4.1 Material toughness

4.1.1 Toughening of thermosetting polymers

4.1.1.1 Modifiers for thermosets

Because of their large use in aeronautic applications, most efforts were paid on improvement of epoxy-based composites. In the 1970s, toughness enhancement started with the use of various elastomers derived from polybutadiene-*co*-acrylonitrile (CTBN: carboxy-terminated, ETBN: epoxy-terminated) [165, 166]. These elastomers, initially soluble in epoxy monomers, lead to biphasic matrices by RIPS [167]. An increase of toughness was evidenced through different mechanisms [168–170] (crack-blunting, crack-bridging, yielding and cavitation, see next paragraph for more details). Unfortunately, the remaining elastomer fraction in the thermoset phase caused a dramatic loss of mechanical properties and a consequent drop of the glass transition temperature.

Elastomers were also used as preformed particles [78, 171]. In parallel, research on core-shell went on until the late 1990s, with investigations on the influence of the matrix composition, nature of the particles, modifier content, particle size and functionalisation [78, 172, 173]. From the late 1980s to the late 1990s, studies were carried out to evaluate optimized parameters for core-shell and elastomeric toughening of composites, with enhanced toughness and resistance to impact [78].

Because of the dramatic reduction of mechanical and thermal properties and the fact that the toughening efficiency was found to be less effective with highly cross-linked thermosets, another type of modification was investigated. Modification of epoxies with thermoplastics finds its origin in adjustment of viscosity for better processing. The resulting increase in toughness and impact resistance was originally a side-effect, but with a better retention of mechanical and thermal properties (solvent sensitivity sometimes remains a problem). Epoxies modification was expensively studied using high- T_g thermoplastics, such as PES and PEI, that are initially soluble in the thermosetting monomers [77]. As for CTBN/ETBN modifications, thermoplastic particles generated by that means result from RIPS (see chapter 2 for more details). The influence of many parameters (thermoplastic molecular weight [174], curing time [175], curing temperature [176], heating rate [177] or even

mixing temperature [178]) on the toughness and damage tolerance properties was studied. A parallel between morphological structure and performance upon failure was drawn [179]. For an optimal and effective toughening, the following principles are generally admitted in the literature [77]:

- The thermoplastic has to be soluble in the initial resin but the mixture undergoes a phase separation while curing (RIPS).
- Co-continuous and phase-inverted morphologies are the most effective with high- T_g thermoplastics.
- High- T_g thermoplastics are more effective on highly cross-linked systems (on the contrary to elastomers), without dramatic consequences on thermomechanical properties (as their T_g is close to the network's one).
- High thermoplastic molecular masses favour toughness improvement.

The literature is more ambivalent about the role of reactive end of chains, for which contradictory effects seem to be obtained [77].

The third and last generation of composite materials involves even more complex matrices, with the reinforcement of the interlaminar space between fibre layers. This space, called interleaf, originally filled with the thermoset is reinforced with thermoplastic particles or films [93].

4.1.1.2 Toughening mechanisms

Co-continuous and phase-inverted morphologies are extremely efficient to increase toughness, especially because of the high thermoplastic volume fraction [77, 98–100, 113, 115, 116]. In these cases, the desirable mechanical and thermal properties of the thermosetting matrix are lost to those of the thermoplastic. In addition, solvent sensitivity dramatically increases. For these reasons, only particle-based morphologies with a thermoset as the continuous phase will be considered.

Particles lead to stress concentration with an intensity and a space distribution that depend on their stiffness, size, shape and concentration. The stress triaxiality can also be locally modified. The strength of the interphase is also involved in every toughening mechanism, some of them are described hereafter.

If the interface between thermoset and particles is relatively weak, a decohesion can occur. The crack path is then distorted, which leads to a higher surface creation (Figure 119), increasing the required energy for fracture.

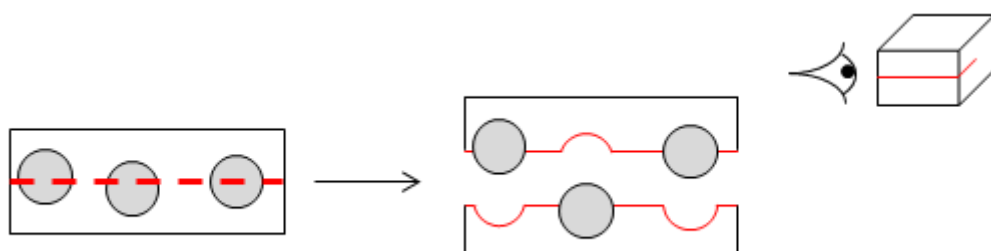


Figure 119: increased fractured surface by matrix/particle decohesion.

Different models qualitatively describe the surface increase effect through an increase of the global fracture surface energy. Considering steps created at the particle/matrix interface, with a height h , the fracture energy becomes [3]:

$$\gamma = \gamma_m(1 - \Phi_v) + k \frac{h}{d} \quad \text{Eq. 32}$$

with γ_m the fracture surface energy of the matrix, Φ_v the volume fraction of particles, d the particle spacing and k a constant. A simple mixing law, considering an average equatorial position of particles in the fracture plan leads to a similar expression:

$$\gamma = \gamma_m(1 - \Phi_v) + 2\gamma_{mp}\Phi_v \quad \text{Eq. 33}$$

with γ_{mp} the particle/matrix surface energy. Here the surface is increased by half a sphere per particle. In both cases, the particle surface density is set equal to the volume fraction.

The local curvature of a crack path generates a transition from failure in mode I to a mixed mode I and II (Figure 120). In many cases, G_{IIC} is higher than G_{IC} , which increases the total energy dissipation [3].

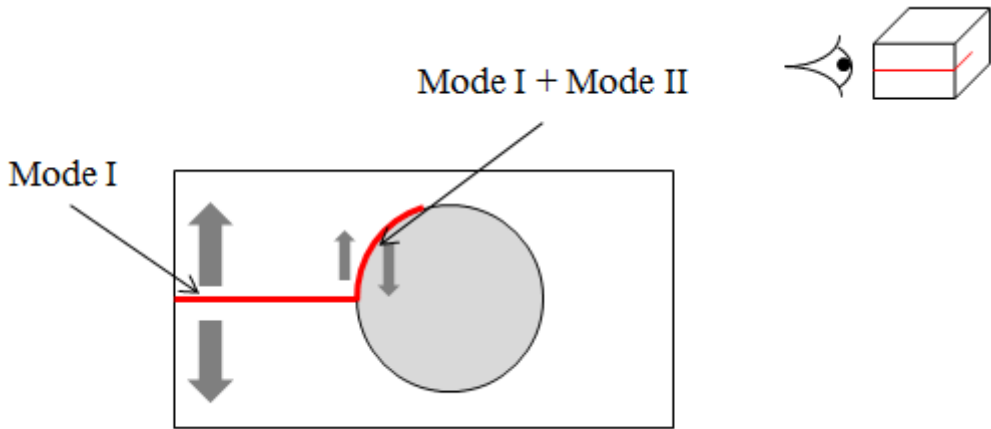


Figure 120: crack deviation.

Faber and Evans solved the modified energy release rate, introducing local stress intensity factors with a dependency on the crack tilt angle. Possible angles are given by the geometry of particles (in this case through an aspect ratio). Integrating on all angles for a sphere, the authors calculated the following toughening increment [180, 181]:

$$\Gamma = \Gamma_0(1 + 0.87\Phi_v) \quad \text{Eq. 34}$$

where Γ and Γ_0 are fracture energies of the toughened and neat matrices, respectively, and can be associated to critical energy release rates (G_C).

If the interface is strong enough and the particles quite soft, they can undergo high strain, dissipating energy by plastic flow. If the strain is high enough for the crack to propagate before the particle failure, local-bridging can be observed (Figure 121).

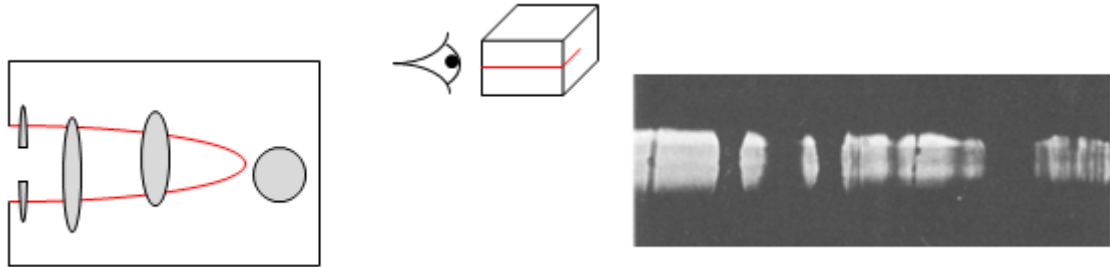


Figure 121: crack-bridging. Image from [182].

This phenomenon was observed and analytically described by Kunz-Douglass and co-workers for epoxy/rubber blends. They identified the toughening mechanism to be an elastic deformation of rubber particles, limited by tearing of the elastomer phase. For a high tearing extension ratio λ_t , they expressed the resulting toughening as [182]:

$$\Gamma = \Gamma_0(1 - \Phi_v) + 4\Gamma_t\Phi_v \quad \text{Eq. 35}$$

with Γ_t the surface tearing energy of the elastomeric phase. Because of the low modulus of rubbers, low efficiency is expected [3]. Cardwell and Yee developed a model for toughness in the case of thermoplastic particles crack-bridging [183]:

$$K_C = AK_{C,m} + \frac{E_m^* \Phi_v W_p}{2AK_{C,m}} \quad \text{Eq. 36}$$

with $K_{C,m}$ the matrix toughness, E_m^* the effective modulus (depending on the loading conditions) and A a coefficient accounting for crack-bowing (described hereafter). The bridging potential W_p is associated to the particle plastic work of failure.

A plastic particle with a strong interface can also virtually and locally increase the plastic zone size. As a result, the crack tip can undergo blunting (Figure 122).

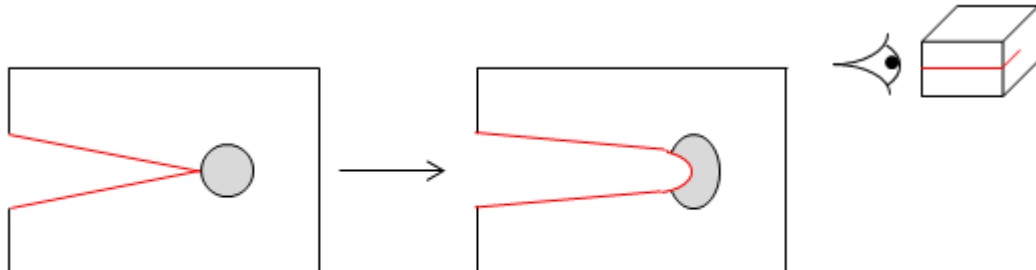


Figure 122: crack-blunting.

Finally, if particles are close enough to each other, the crack front can be locally altered (crack bowing) and delayed (crack-pinning: Figure 123).

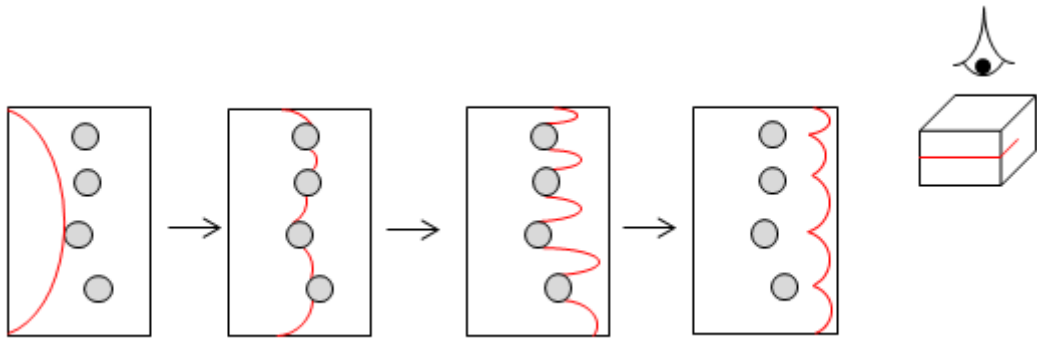


Figure 123: crack-pinning.

This mechanism, which is common in metallic alloys, is expected to be more efficient in polymers filled with rigid particles (having a higher modulus than the matrix), such as thermoplastics, than soft rubber particles. Lange gave an interpretation borrowing the concept of tension-line from dislocation in metals^[184]:

$$\Gamma = \Gamma_0 + \frac{T_l}{2d} \quad \text{Eq. 37}$$

The tension-line T_l stands for an energy density per unit of crack front length. d is the particle spacing. For a regular semi-circular arc with a curvature radius R_c , the tension-line can be approximated by^[185]:

$$T_l = \frac{2}{3}\Gamma_0 R_c \quad \text{Eq. 38}$$

Combining equations 37 and 38:

$$\Gamma = \Gamma_0 \left(1 + \frac{R_c}{3d} \right) \quad \text{Eq. 39}$$

Qualitative analysis of equation 39 establishes the effect of the filler volume fraction. A higher content of filler decreases the particle spacing d , increasing the effectiveness of crack-pinning. Evans introduced different calculations for T_l , considering an elliptical shape of the bowing cracks and possible coupling of neighbouring curved cracks during propagation. From these refined models, arises a T_l dependency on the particles size, and consequently the particles volume fraction^[186].

Equations 32, 33, 34, 35 and 37 take the general form: $\Gamma = \Gamma_0 + \Gamma_{tough}$. Equation 36 can also be rewritten (assuming $K = \sqrt{E^* \Gamma}$) to reach a similar form. In most cases, the toughening mechanism is described with a first order dependency on the particle volume fraction Φ_v . These quite simple models have to be adapted to account for deviation at high filler content.

4.1.2 Toughness in composite laminates

Composite materials can be considered here as made of three main components: fibres, polymer matrix and fibre/matrix interface. Consequently, three kinds of failure can be observed. For laminates with a mode I delamination, most of the fractured surface is

developed either at the interface (adhesive fracture) or in the matrix (cohesive fracture).

The interlaminar thickness is typically between 20 µm and 100 µm for unidirectional fibre layers [1]. The thickness is not uniform with woven fibres layers that exhibit local undulations. For unidirectional fibres that are not tightened up, migration and displacement of fibres during the processing phase can lead to bridging between plies, contributing to the delamination energy.

Confinement in thin interlaminar spaces may also modify the crack-tip behaviour and the local phenomena reported in the previous paragraph. Increasing the process zone size encounters limitations due to the lateral fibres boundaries, (Figure 124), for which inter-fibre spacing is at most a few microns, consequently, energy dissipation by plastic yielding is also limited. Moreover, the crack path is confined and the crack is forced to propagate through a particle distribution. The proximity to fibres may also lead the crack to change its path from the toughened matrix to a weaker fibre/matrix interface.

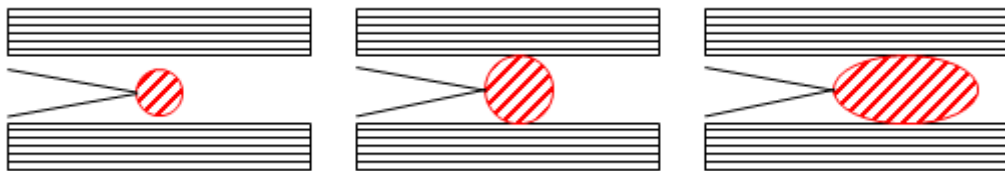


Figure 124: effect of interlaminar confinement for different process zone sizes.

The damage geometry is extremely dependent on the testing configuration and stacking sequence. Laminates are strongly oriented and designed in accordance with targeted functions. Fibres are usually aligned in directions under strain to use their full mechanical potential. Stacking sequences with alternated orientations allows mechanical performance in every directions within the laminate plane. The weak axis is usually through the thickness (leaving aside complex shapes and three-dimensional weaving). Consequently, two classic testing geometries are applied stress in the laminate main direction (or plane) and impact on the surface. These involve two different aspects, damage tolerance (evolution of properties and damaging when stress is applied) and damage resistance (damage creation at impact). Both can be enhanced by thermoplastic modification [187–189].

Considering a model laminate, two kinds of damage are observed: transverse cracking and delamination (Figure 125). Multiple cracks appear in composites, which makes damage mechanics a more relevant theoretical background than for thermosets, where fracture mechanics is usually used. This is a consequence of constrained cracks that do not lead to a dramatic failure but contribute to a wide range damaging process, until critical damaging is reached.

In a conventional tensile test, transverse cracks usually appear first (opening mode). Delamination is initiated by transverse cracks-tips reaching the interlaminar area. The whole damage process leading to failure depends on the stacking sequence, the matrix nature, toughening and even temperature [187, 190, 191]. Impact can lead to both transverse cracking and delamination.

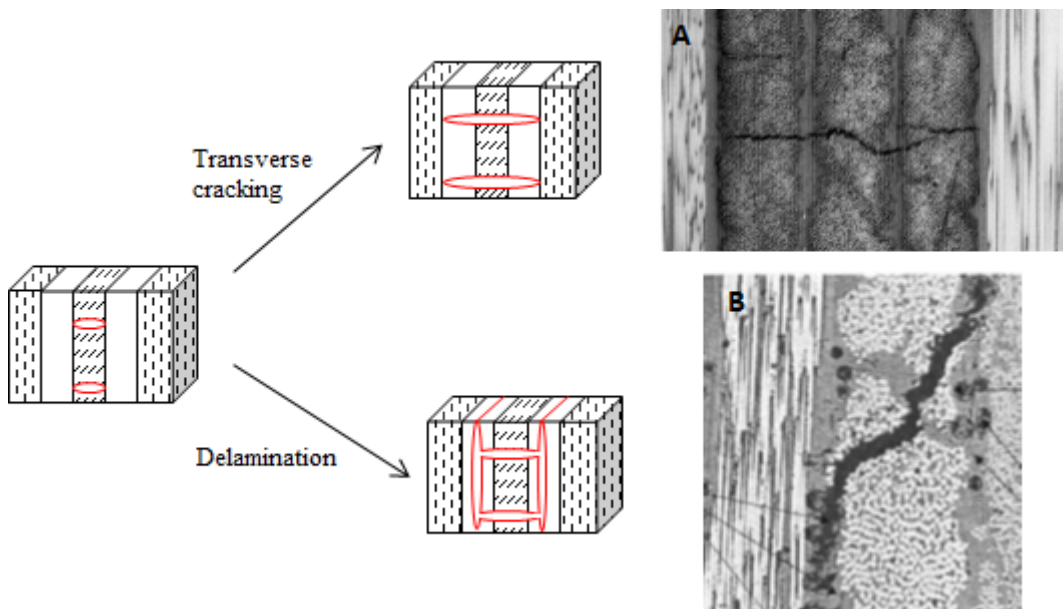


Figure 125: damage in a composite laminate. A) from [190] ; B) from [188].

4.2 Experimental details

4.2.1 Materials

4.2.1.1 Modified resins

Samples were cut in resin slabs, cured according to the standard cycle (see chapter 1). The matrices were modified using thermoplastics and methods described in chapter 2. As explained in the previous part, only particle morphologies were selected, to maintain high thermomechanical properties. Table 10 gathers all studied morphologies, more details about obtaining such structured materials are also developed in chapter 2.

Thermoplastic	Solubility	Content (phr)	Particle size (μm)
PES ^l	soluble	5	1-2
PES ^l	soluble	10	2-5
PES ^h	soluble	5	2-5
PEI	soluble	5	2-10
PAI	insoluble	7	1-25
PI	insoluble	7	5

Table 10: main formulations for thermoplastic-modified bismaleimide matrices.

4.2.1.2 Composites

Composite plates were built from 10-ply preforms by injection process. The plies were made of G986 carbon fabric, which is twill fabric made of 6K carbon fibres with an epoxy sizing.

As introduced in paragraph 2.5.1.1, thermoplastic-modified BMI/DBA resins are not suitable for injection processes with the available tooling, because of their high viscosity. Thermoplastic-modified composites were obtained by inserting thermoplastics directly inside the preform. Each ply was sprayed manually with a sieve to lay the appropriate

amount of thermoplastic powder, that was further spread with a PTFE squeegee. In the case of PES, the preform was heated at 250°C and pressed for 15 minutes with a controlled thickness of 3 mm.

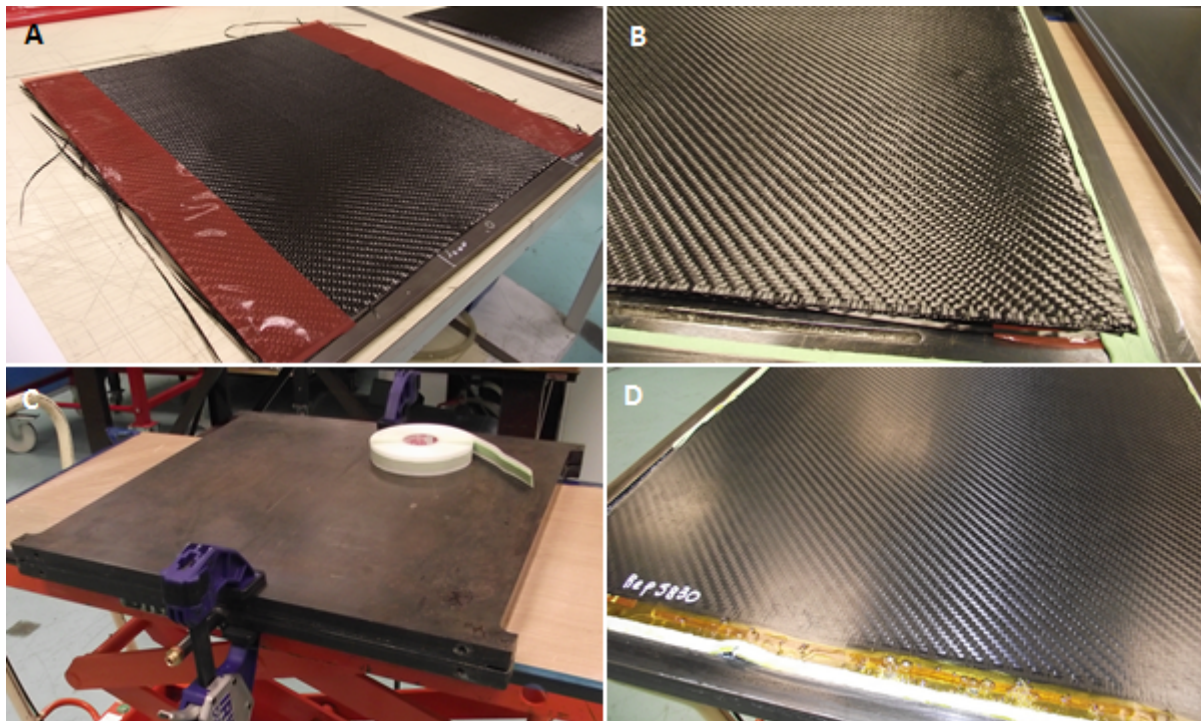


Figure 126: composite fabrication at different steps. A) ply-stacking ; B) open mould ; C) mould sealing ; D) de-moulding after curing.

While stacking up the plies, an anti-adhesive ribbon was placed on two sides of the plates between the central plies (Figure 126A). This would form a pre-crack for delamination tests. Preforms were placed into a mould for injection with a 3 mm thickness (Figure 126B and C). In these conditions, the carbon fibre volume fraction was calculated to be close to 55%. The neat standard BMI/DBA resin was degassed and injected inside the sealed mould until a zero flow at 5 bars was reached. During this phase, the resin and the whole tooling were heated around 125°C. The standard curing cycle was then applied: 3°C/min up to 180°C, isotherm for 1h ; 1°C/min up to 200°C, isotherm for 2h ; 1°C/min up to 250°C, isotherm for 6h. The cooling rate was set to 1°C/min.

Remark: to obtain a symmetric plate through the thickness, plies were turned around after the fifth one.

4.2.2 Methods

4.2.2.1 Tension

The same procedure as described in chapter 3 was applied, following the requirements of the IGC04.26.253 standard^[137], with a cross-head speed of 2 mm/min.

4.2.2.2 Compact tension

The same procedure as described in chapter 3 was applied, following the requirements of the IGC04.26.680 standard^[139].

4.2.2.3 Double Cantilever Drilled Compression

The complete description of the testing device can be found in chapter 3. This specific procedure was used so far on relatively homogeneous samples, considering that polymer network inhomogeneities scale lies between one and two order of magnitude below the characteristic size of morphologies resulting from thermoplastic modification. The application of the DCDC procedure to heterogeneous samples was used only with the purpose to follow the phenomena occurring when a crack, propagating through the thermosetting matrix, meets a thermoplastic-rich particle. No attention was paid to stress and strain heterogeneity, neither to the crack-tip velocity.

A limiting factor for AFM observations was the random presence of a particle on the crack path. Because fine mechanical analysis was not a purpose here, samples were reloaded until a new crack propagation occurred, to maximize the number of observations per sample. The crack-tip had to remain more than 5 mm away from the sample end, to avoid local edge effects.

4.2.2.4 Composite delamination

Delamination tests were performed on an Instron testing machine to measure fracture toughness energy. Sample preparation and test procedure are described in AITM1.0005 standard [192]. The pre-delaminated area was initially located on the edge of the composite plate where an anti-adhesive ribbon had been placed. Aluminium tabs were stuck on each side of the specimens (see Figure 127) with strong epoxy glue.

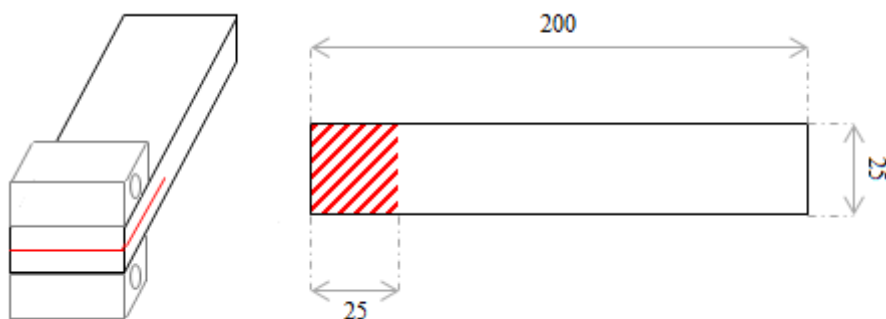


Figure 127: composite delamination sample. Dimensions in mm.

A pre-crack is generated by initiating the delamination on 10 mm. The cross-head speed was set to 10 mm/min. The load-displacement curves were registered during the whole procedure. Tests were carried out until the delaminated length reached 100 mm. Initial (after pre-cracking) and final delaminated length are measured on both sides of specimens (Figure 128).

The area between the loading and unloading curves (Figure 129) corresponds to the dissipated energy U_f . Measuring the delaminated area A_d , the critical release rate is calculated by:

$$G_{IC} = \frac{U_f}{A_d}$$

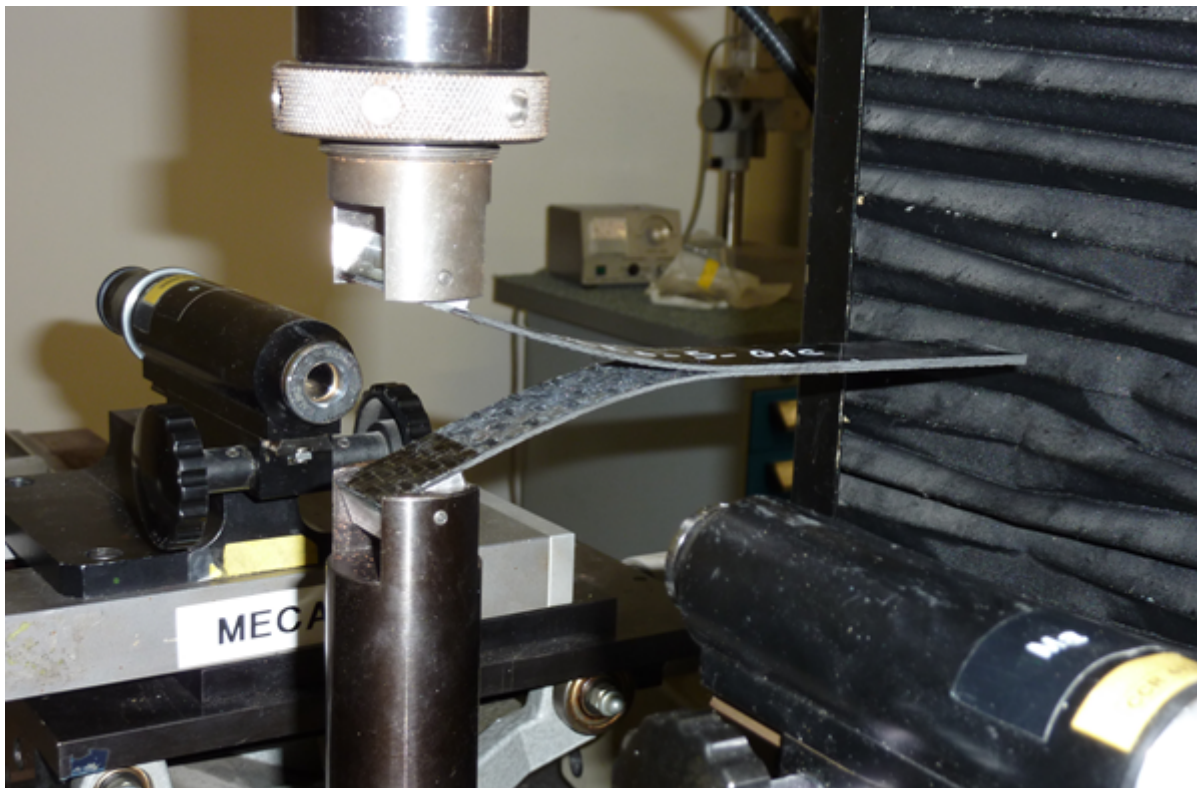


Figure 128: experimental device for composite delamination tests.

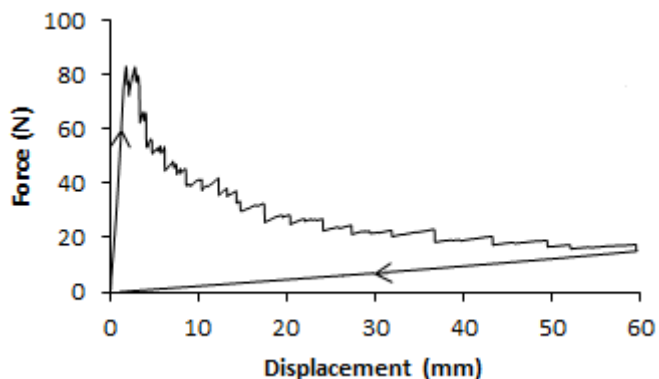


Figure 129: load-displacement curves for a delamination test.

4.2.2.5 Atomic force microscopy

Similarly to DCDC experiments described in chapter 3, atomic force microscopy was used to investigate the local crack-tip mechanisms in heterogeneous samples. Because the aim was not to measure precisely the crack-tip velocity, greater spatial resolution or bigger images could be obtained. The propagation direction (usually from down to up) will be indicated on images by a white or black arrow.

4.2.2.6 Fractography

After failure of DCDC, CT and delaminated samples, crack surfaces were prepared with a platinum deposition. Then they were observed with scanning electron microscopy, secondary electron signals being used. The propagation direction (usually from down to up) will be indicated on images by a white or black arrow.

4.3 Fracture behaviour in matrices

4.3.1 Mechanical properties

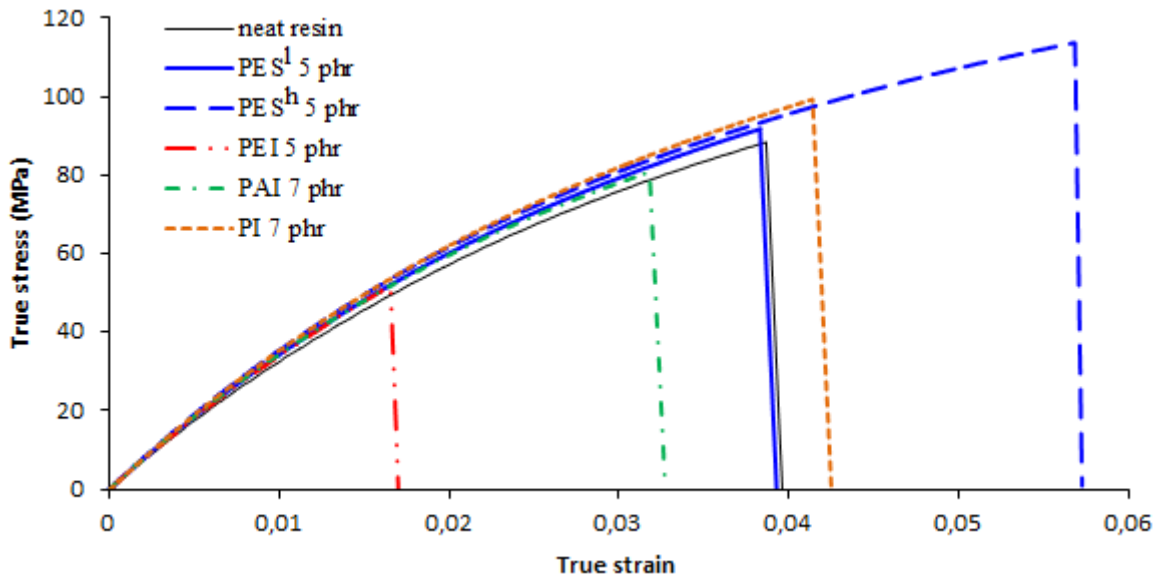


Figure 130: strain-stress curves for uniaxial tensile tests of different thermoplastic-modified BMI/DBA networks.

Tensile tests on the different formulations were performed to further investigate the effect of modification on mechanical properties (see chapter 2 for thermomechanical analysis). Stress/strain curves are displayed on Figure 130. With a constant initial slope, the Young modulus remains unchanged in the selected range of modification. Differences in stress and strain at break are visible, Figure 131 shows the corresponding measurements for failure stresses (σ_R). PES^h modification leads to a significant increase, whereas PEI brings a decrease of σ_R . Other blends exhibit the same strength level.

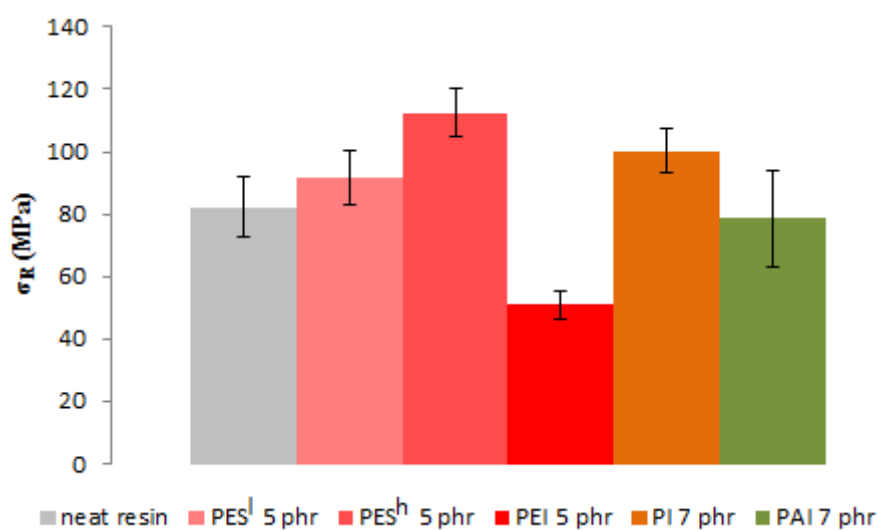


Figure 131: failure stress in uniaxial tension for different thermoplastic-modified BMI/DBA networks.

Failure in tension is strongly dependent on the quality of sample preparation and machining. The presence of defects leads to a decrease of tensile strength, especially for

brittle materials. Here, curing conditions and machining are expected to be the same, and the relatively low statistic scattering seems to indicate a trend. However, σ_R remains more an indicator than a criterion for matrices selection.

4.3.2 Toughening

Toughness for mode I failure of thermoplastic-modified BMI/DBA networks was measured (Figure 132). For PES and PEI-based materials, only particle morphologies were considered. All soluble thermoplastic-modified matrices remain within the same range of toughness close to $0.85 \text{ MPa.m}^{1/2}$ (18-28% improvement compared to the neat matrix). The highest improvement is reached for PES^l (5 phr) with $0.87 \text{ MPa.m}^{1/2}$. Polyimide modification leads to the lowest improvement with only $0.7 \text{ MPa.m}^{1/2}$. On the other hand, PAI leads to an enhancement similar to insoluble thermoplastics with $0.85 \text{ MPa.m}^{1/2}$ (25%).

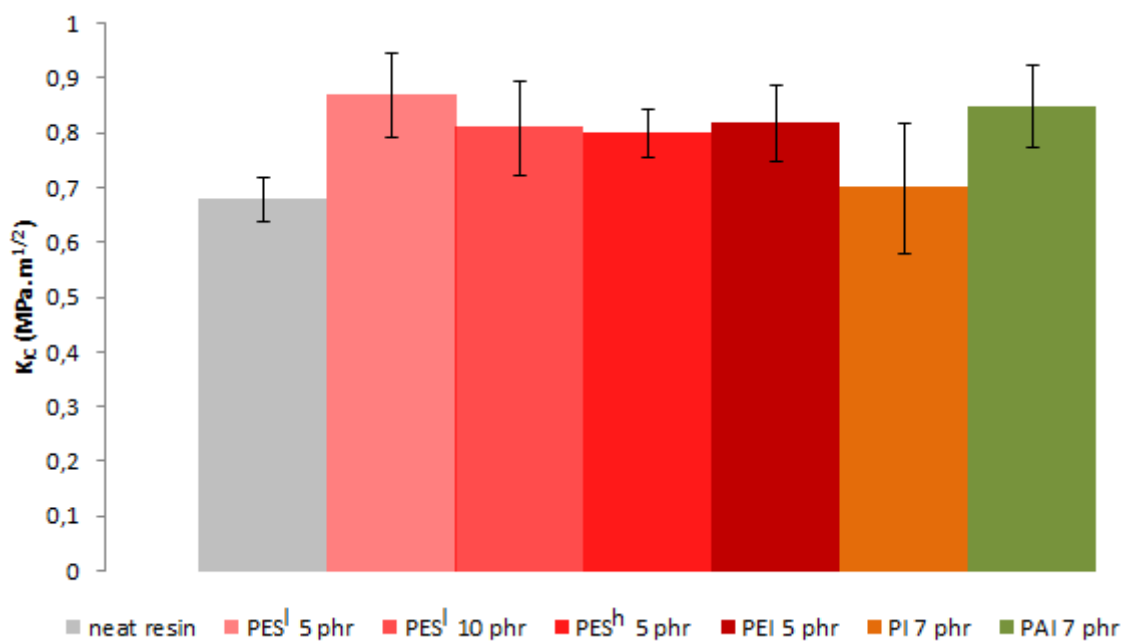


Figure 132: toughness in mode I for neat and thermoplastic-modified BMI/DBA resin.

Considering the procedure accuracy, toughness improvements are not highly significant, but best thermoplastics candidates for different kinds of toughening can be selected. The choice criteria also have to take into account composite processing. Because the thermoplastic has to be included directly in the preform interlaminar space, PEI is rejected due to its high particle size. For the soluble thermoplastics, similar matrix performances are achieved with PES^l and PES^h. PES^l will be selected because of its higher solubility in the resin monomers, a major property considering that during composite processing, solubilisation is limited by the simultaneous thermoset polymerization. PES^l also seems to be slightly more efficient. Concerning insoluble particles, PAI is the most promising.

4.3.3 Crack path in modified matrices

In this part, comparison will be made between AFM observations and fractography. Comparing AFM images with fractured surface analysis of the bulk DCDC sample can discriminate surface effects. Comparing DCDC with CT fractography will confirm that encountered phenomena are not purely dependent on the testing geometry.

4.3.3.1 Particles from phase separation

AFM investigations on mechanisms occurring when a crack-tip meets a thermoplastic-rich particle were mainly carried out on BMI/DBA/PES¹ 10 phr samples. This formulation lead to the highest particle content, maximising the probability of finding a particle on the crack path in the observation field.

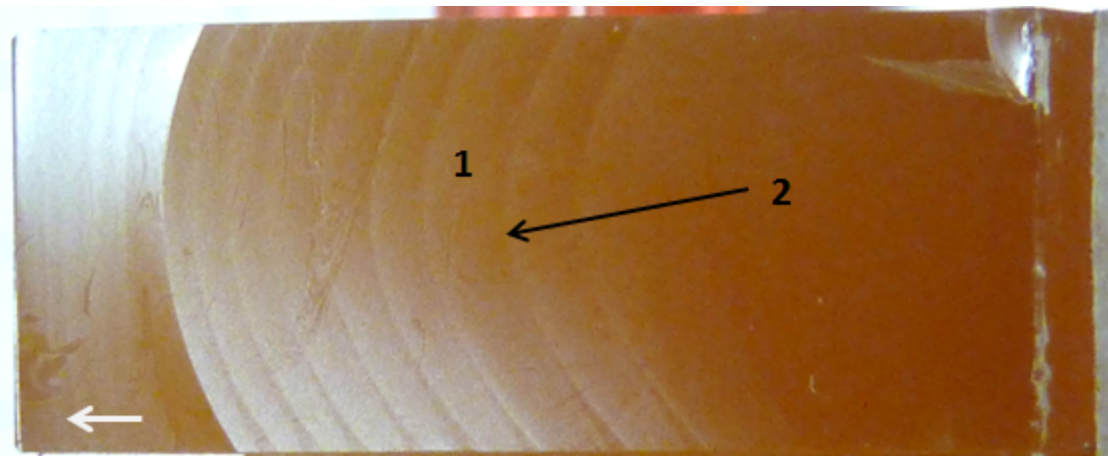


Figure 133: fractured surface of a CT sample. 1: fast crack area ; 2: crack stop area.

Compact tension samples containing PES particles exhibit two kinds of fractured surfaces. The propagation area is very smooth with particles neatly cut (Figure 134A and B). It corresponds to the fast crack propagation at the end of a loading phase and is found between two crack front lines (Figure 133). This propagation mode is not representative of DCDC experiments because of the low velocities involved in the latter geometry. The crack stop area exhibits much more features that can be compared to AFM observations during DCDC experiments (Figure 134C and D).

Each event observed with AFM was compared to some aspect of fractured surfaces for CT and DCDC samples.

A striking difference between fast crack and crack stop areas is the decohesion between particles and matrix in the latter. This decohesion is found for every blend containing PES (Figure 134C and D, Figure 135). Moreover, this local separation of particles with the matrix is oriented in the propagation direction. Even fully separated particles exhibit a larger gap in this direction (lower right corner of Figure 134C).

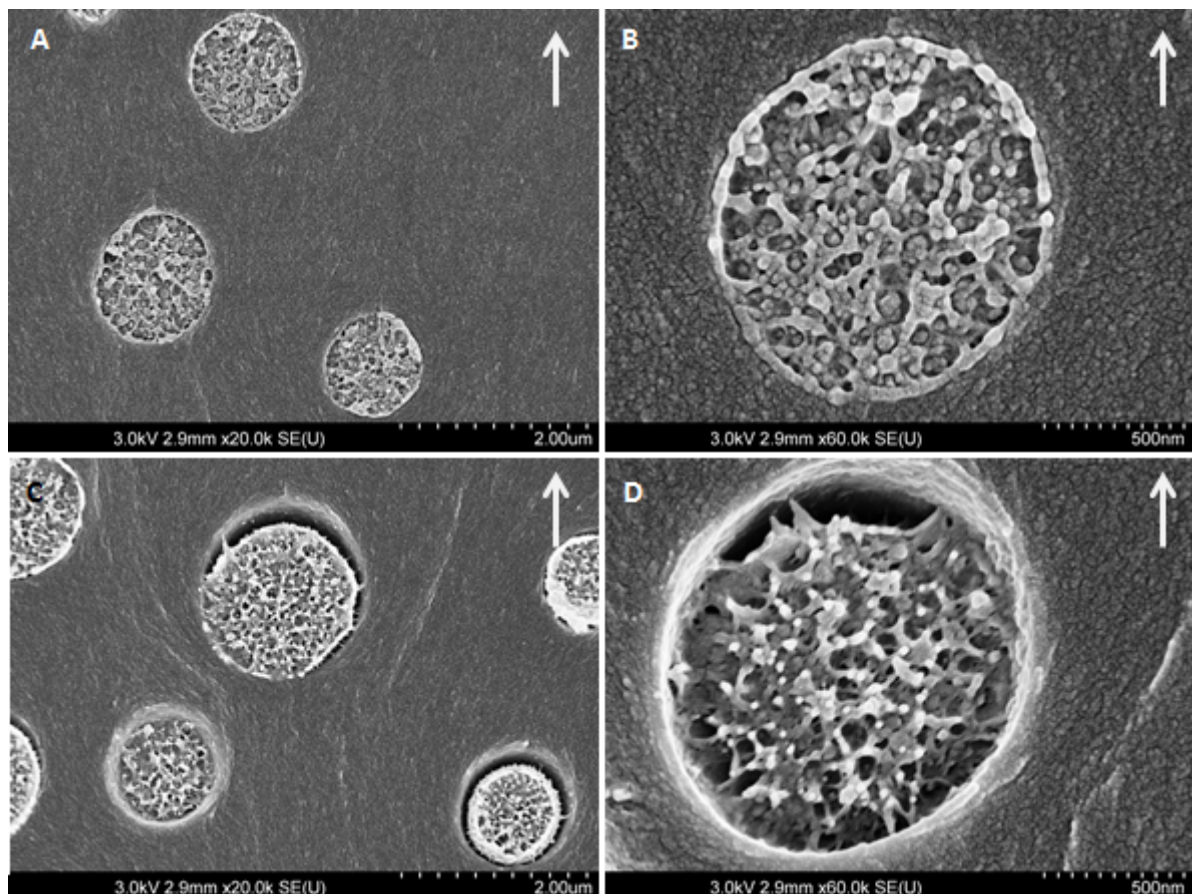


Figure 134: SEM fractography of a BMI/DBA/PES^l 5 phr CT sample. A) and B) fast crack area ; C) and D) slow crack area. Propagation direction: up.

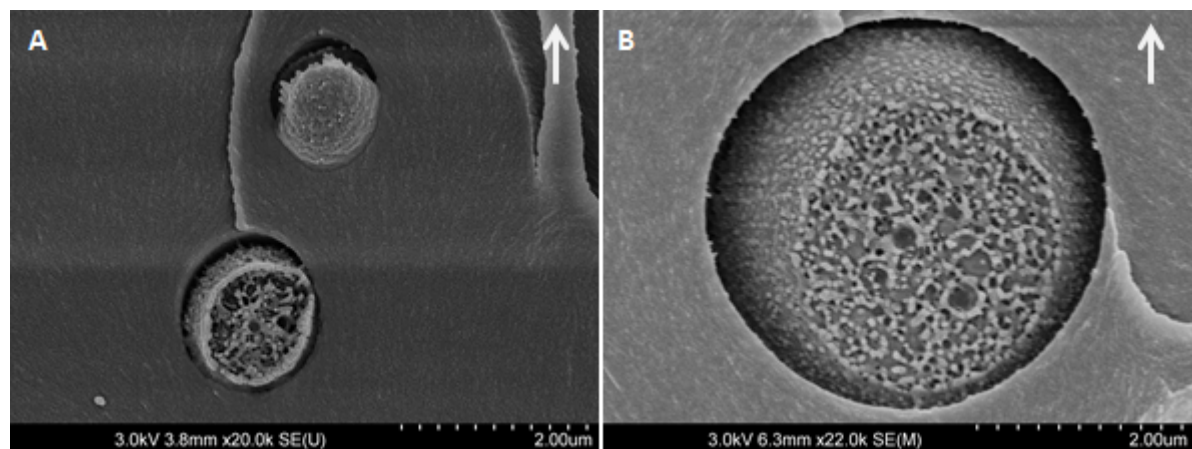


Figure 135: SEM fractography BMI/DBA/PES blends CT samples. A) PES^h 5 phr ; B) PES^l 10 phr. Propagation direction: up.

Figure 136 shows a crack cutting through a particle, the red arrow pointing at the particle part being cut away. At first sight, the crack seems to be deviated along the particle-matrix boundary (Figure 136A). Letting propagation going on a little further leads to a double-headed crack (Figure 136B). The second crack tip appears along the natural prolongation of the crack path before meeting the particle, revealing an unchanged propagation direction.

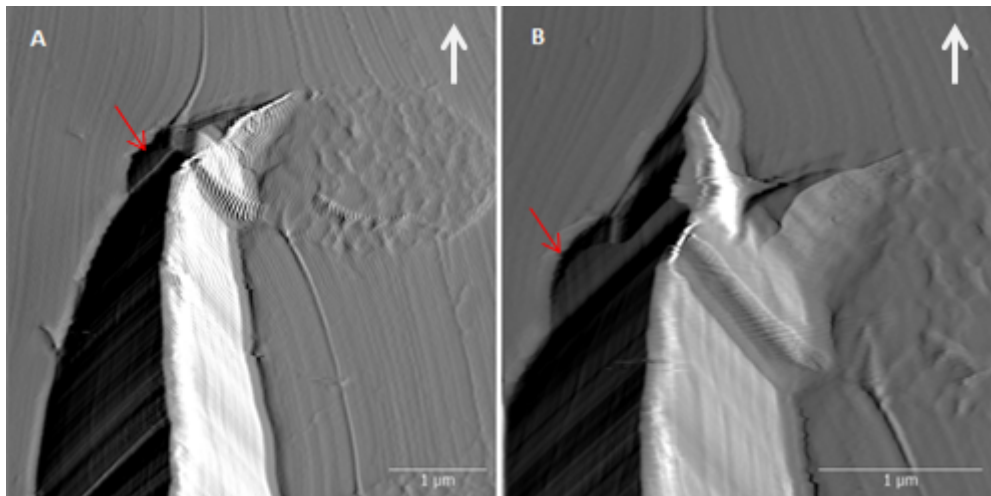


Figure 136: AFM images (deflection error) of a BMI/DBA/PES^l 10 phr blend. A) t_0 ; B) $t_0 + 29$ min. Propagation direction: up.

This apparent local and partial crack deviation results to the failure of the particle-matrix interface on the “out” side of the propagation direction. Correlation can be made with the oriented decohesion observed on CT fractured surfaces. Fractography of DCDC samples confirmed similar structures in the bulk material (Figure 137).

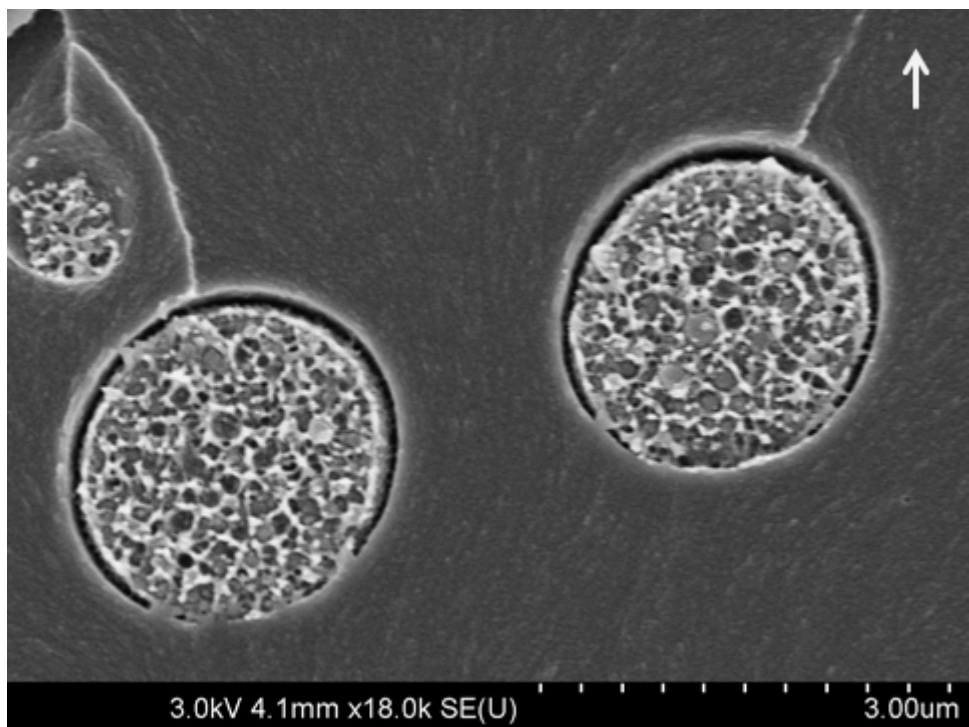


Figure 137: SEM fractography of a BMI/DBA/PES^l 10 phr blend DCDC sample. Propagation direction: up.

Figure 138 shows a particle being cut by the crack at several stages. In this case, the crack is crossing the particle roughly through its mid-plane. Very little crack deviation is observed here but the shape of the tip is strongly altered when inside the particle, suggesting quite heavy local heterogeneity. Figure 139 is the three-dimension reconstruction corresponding to Figure 138C. Some kind of plateau is visible under the surface level, localised under the particle. The precise nature of this signal, coming from a height sensor, is difficult to establish. AFM height images are here visible as the convolution of the real

surface and the shape of the AFM scanning-tip. Consequently, it can clearly be seen on Figure 139 that the walls of the crack are sloping to join a few micrometres under the surface. The resulting angle is characteristic from the scanning tip, the crack edges being, in fact, much more parallel. This shows how topological information can be altered with AFM when sharp height changes are encountered. Here a height drop between 500 nm and 1 μm under the surface mean plane is visible. Previous observations on neat networks and of crack tips out of particles did not reveal such topological features. It can be at least suggested that some underlying material is located beneath the thermoplastic particle, further suggesting a particle stretching. It was not possible to observe this phenomenon more accurately even with a better resolution or by changing the scanning angle.

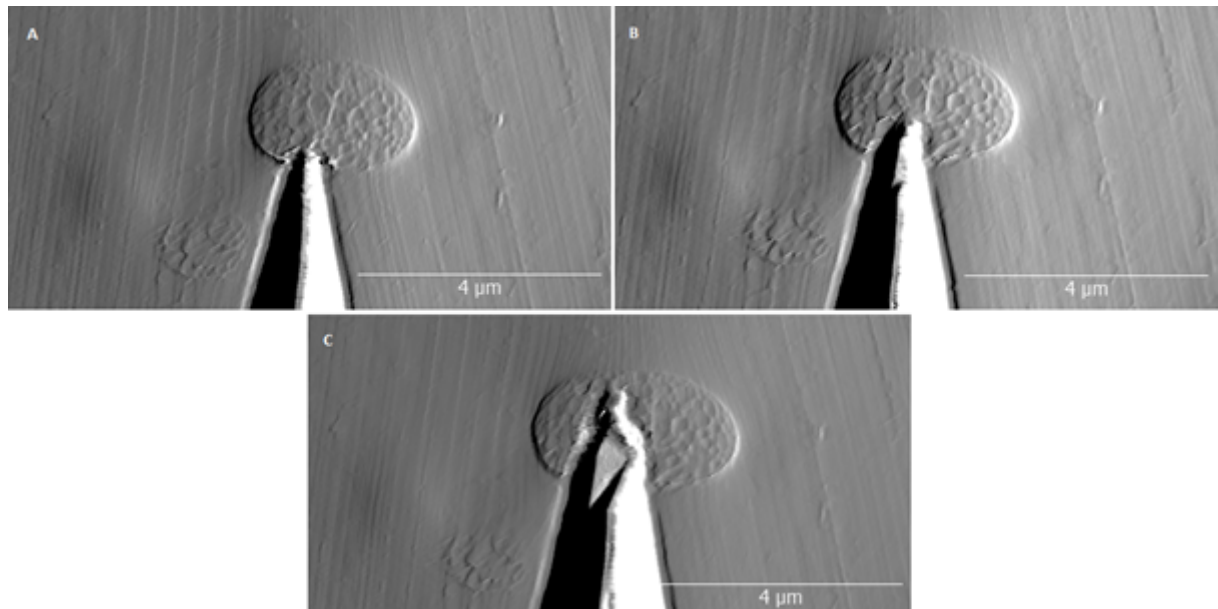


Figure 138: AFM images (deflection error) of a BMI/DBA/PES^l 10 phr blend. A) t_0 ; B) $t_0 + 413 \text{ min}$; C) $t_0 + 1102 \text{ min}$. Propagation direction: up.

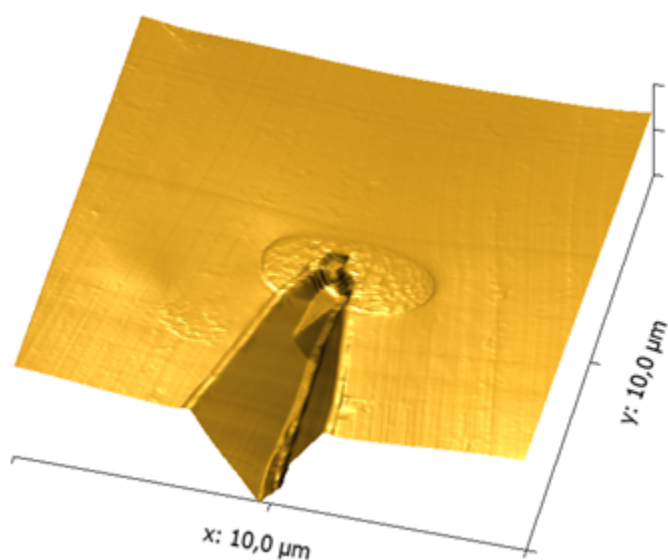
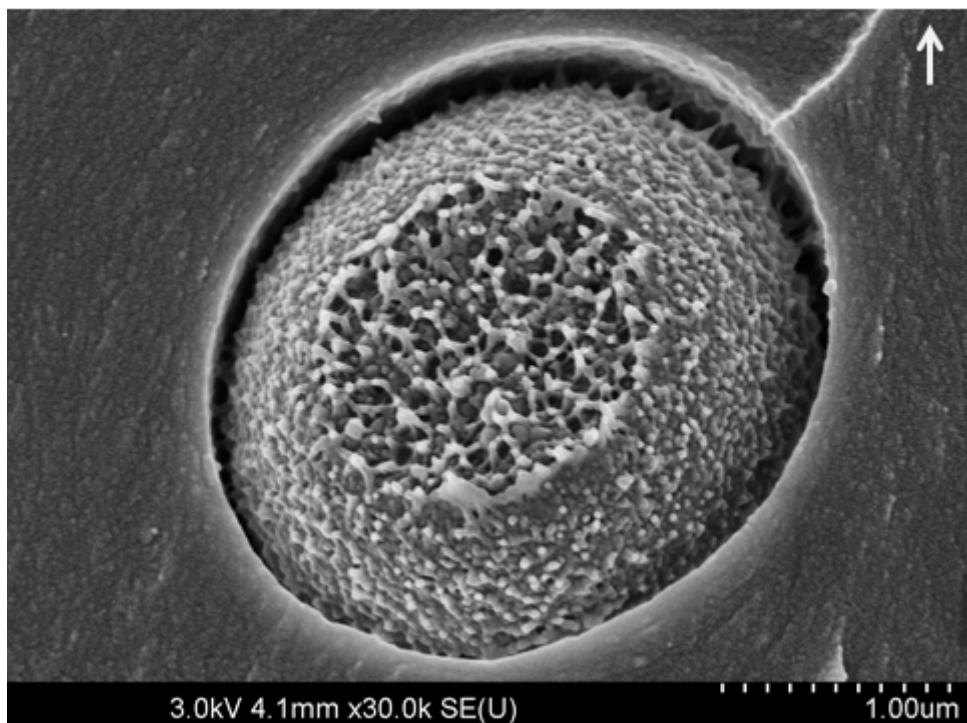


Figure 139: AFM 3D reconstruction (height signal) of a BMI/DBA/PES^l 10 phr blend DCDC sample.

Stretching of particles is confirmed by fractography of various samples, where an out of plane deformation of can be identified (Figure 134D, Figures 137 and 140). The fractured

surfaces of broken particles are very distorted with out of plane tubular objects and apparent porosity. By comparison, surfaces corresponding to the fast crack propagation are smooth without porosity (Figure 134B). This suggests that in CT samples crack stop areas and DCDC samples, the apparent porosity is not due to pre-existing voids but to cavitation during stretching. The biphasic nature of particles can also be incriminated, with a higher compliance of the thermoplastic phase (tubular network) and a probable low deformation of thermoset-rich embedded sub-particles, leading to a decohesion and a removal of thermoset nodules.



*Figure 140: SEM fractography of a BMI/DBA/PES^l 10 phr blend DCDC sample.
Propagation direction: up.*

Close observation revealed the presence of small fibrils with a 20 nm thickness in the particle/matrix decohesion gap (Figure 141). It was not possible to obtain similar observations with AFM, because of the spatial resolution and the fact that the corresponding zone on the surface of a DCDC sample is very small.

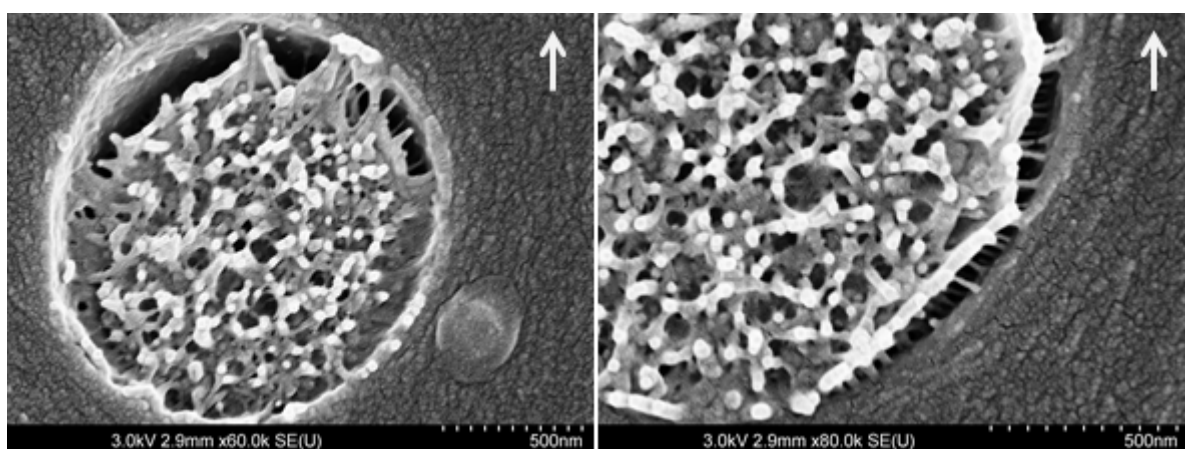


Figure 141: particle details on SEM fractography of a BMI/DBA/PES^l 5 phr CT sample. Propagation direction: up.

A full investigation on crack behaviour in PEI toughened blends was not carried out by AFM observation of DCDC specimens. However, fractography of CT samples provided comparative information. A relatively wide field seems to display particles and holes (Figure 142A) but higher magnification reveals two kinds of altered particles. Those which first appeared to be holes are neatly cut with a smooth surface and are still fully attached to the matrix (Figure 142D). The others have encountered decohesion with the matrix (Figure 142C). Both kinds of alteration are met on the whole fractured surface, but oriented decohesion seems to be mainly located in the crack stop areas (red arrows on Figure 142A and B), suggesting similarities with PES blends.

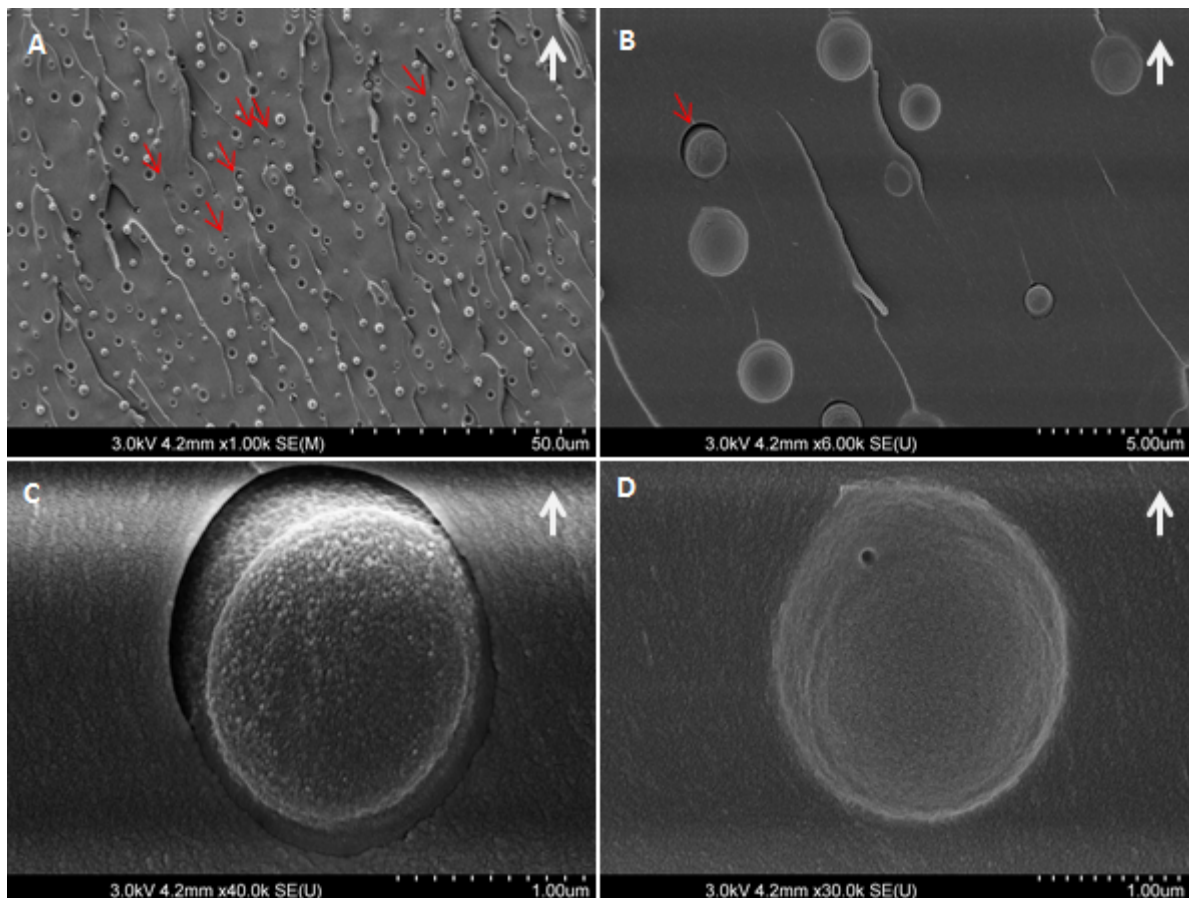


Figure 142: SEM fractography of a BMI/DBA/PEI 5 phr blend CT sample. Propagation direction: up.

4.3.3.2 Initially insoluble particles

The difference of toughening effectiveness between PI and PAI is also visible with fractography of CT fractured samples. For the PI particles blend, fractured surface are extremely smooth with thermoplastic particles quite neatly cut (Figure 143). With PAI, the fractured surface are much more rough, with holes and un-cut particles (Figure 144). There are several possible reasons for these different behaviours upon crack propagation: mechanical properties, adhesion at the surface of the particles and shape of the particles. The main conclusion here is that PI particle splitting is not as effective as PAI particle bypassing.

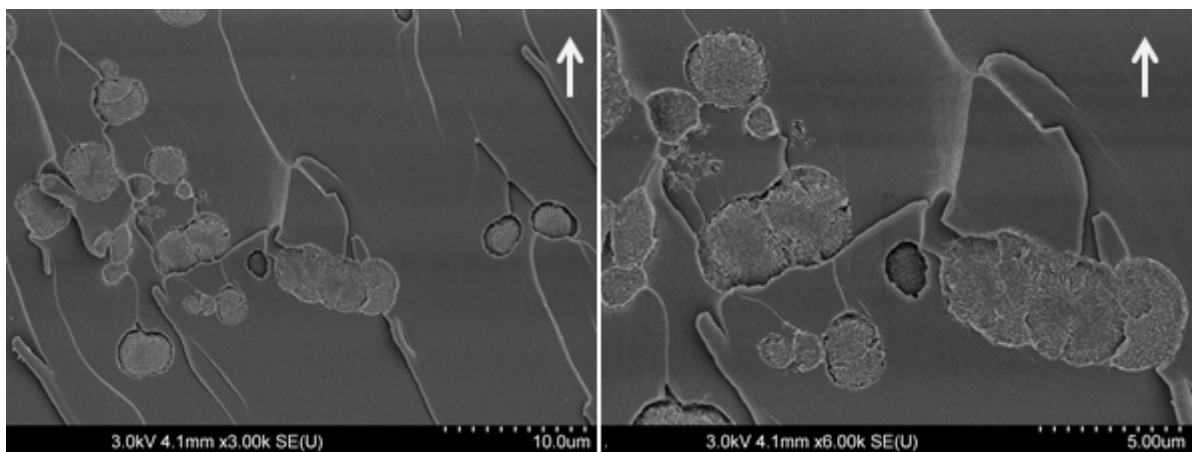


Figure 143: SEM fractography of a BMI/DBA/PI 7 phr blend CT sample. Propagation direction: up.

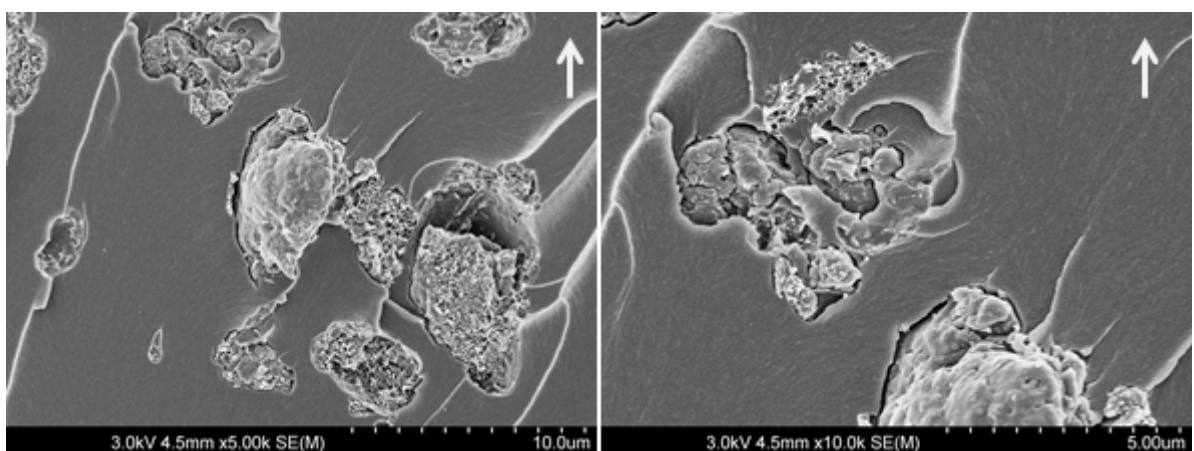


Figure 144: SEM fractography of a BMI/DBA/PAI 7 phr blend CT sample. Propagation direction: up.

DCDC experiments were carried out on BMI/DBA/PAI 7 phr samples. Several events were observed when a crack-tip met a particle. Fractography of DCDC and CT samples was done in parallel.

The most visible effect is the modification of the crack path (Figure 145A). In most cases, the crack bypasses particles, generating kinks and curvature. Once the crack circles half of a particle, no propagation is observed at first (Figure 145A and B). In this “stationary” state, the crack-tip direction is nearly perpendicular to the global propagation direction. This phase ends with the crack starting over along the main propagation direction (Figure 145C and D), which means a nearly 90° angle within the crack path.

These strong deviations of the crack path are consistent with the distorted fracture surfaces observed by SEM fractography for both CT (Figure 144) and DCDC (Figure 146) samples.

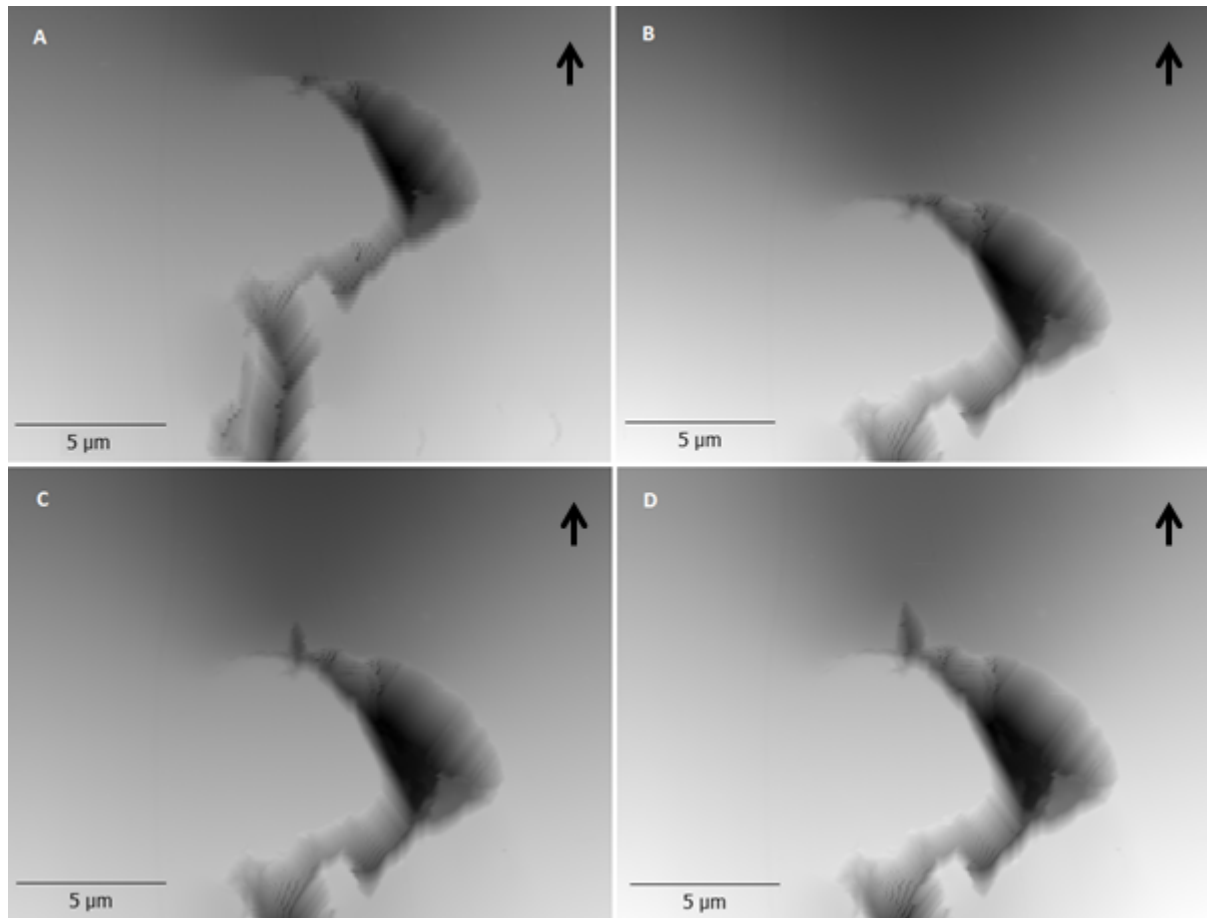


Figure 145: AFM images (height signal) of a crack bypassing a PAI particle in a BMI/DBA/PAI 7 phr. A) t_0 ; B) $t_0 + 30\text{ min}$; C) $t_0 + 42\text{ min}$; D) $t_0 + 55\text{ min}$. Propagation direction: up.

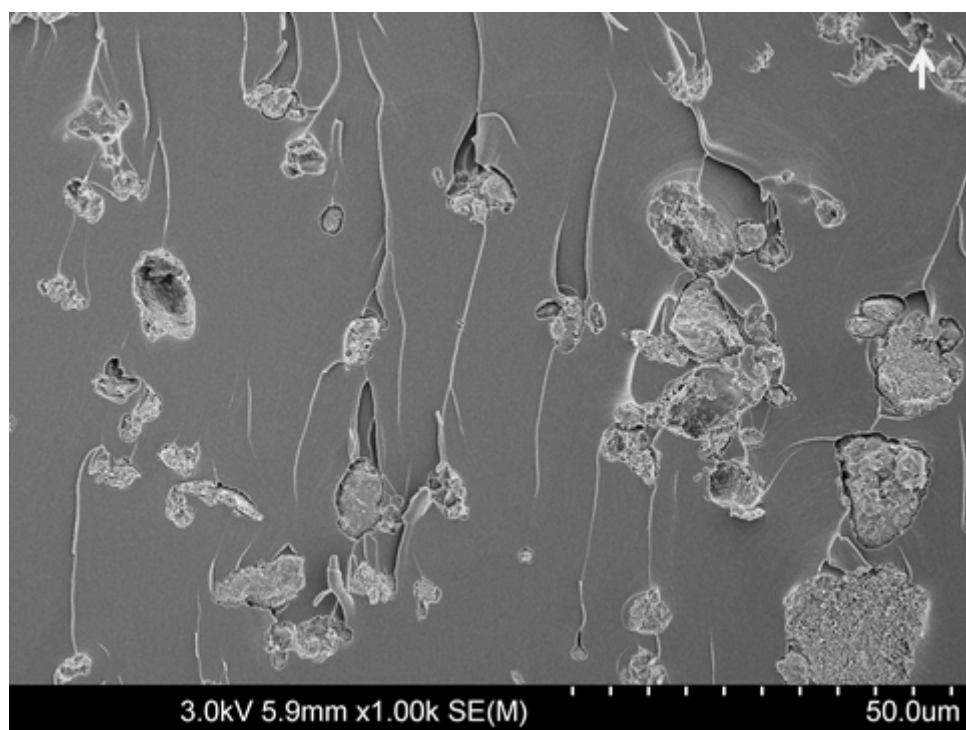


Figure 146: SEM fractography of a BMI/DBA/PAI 7 phr blend DCDC sample. Propagation direction: up.

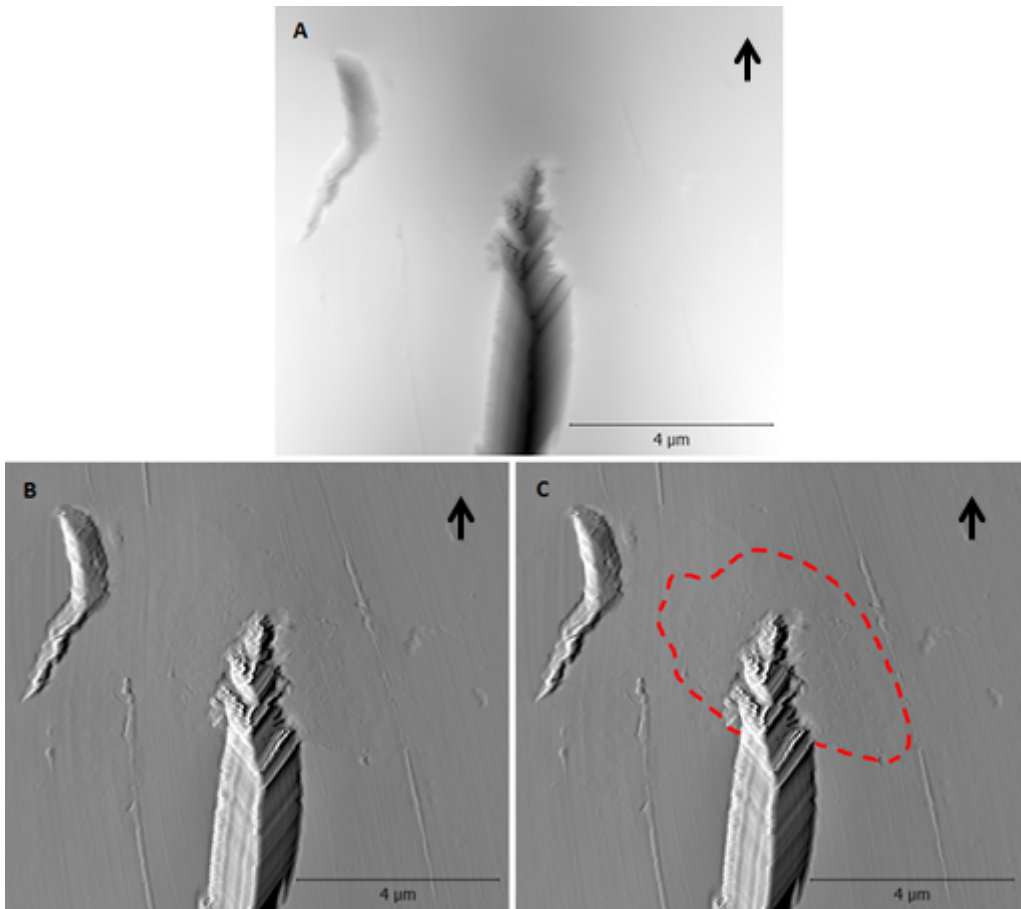


Figure 147: AFM images of a crack tip passing through a PAI particle. A) height signal ; B) deflection error signal ; C) deflection error signal with an estimation of the particle boundaries. Propagation direction: up.

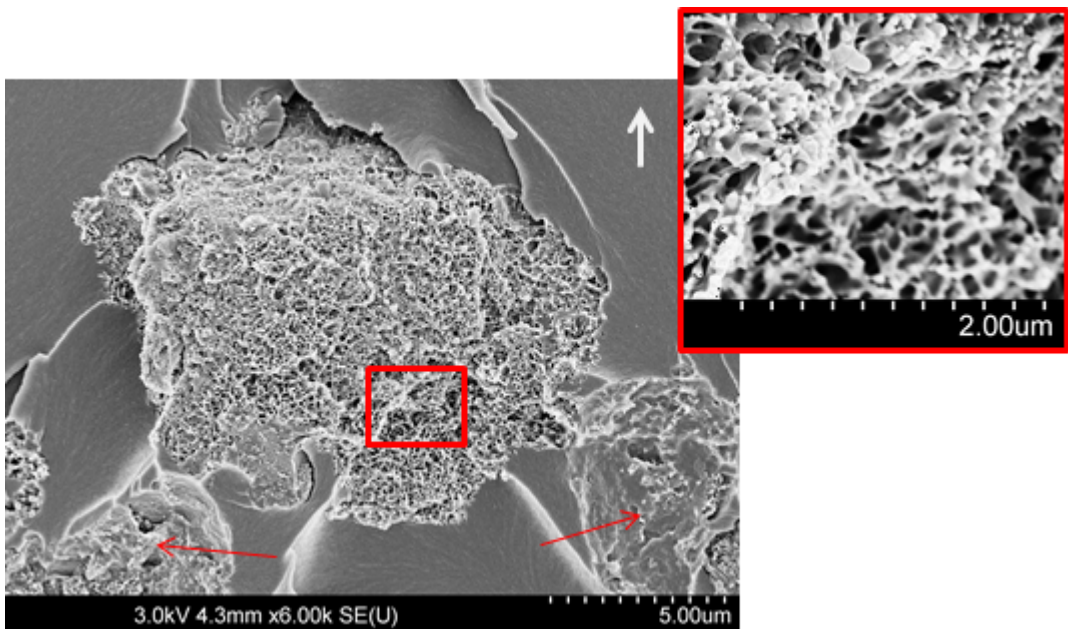


Figure 148: SEM fractography of a BMI/DBA/PAI 7 phr blend CT sample. Propagation direction: up.

It was also possible to observe a crack splitting a particle (Figure 147). The contrast between the particle and the matrix is low, probably because of similar hardness for both materials. By close observation of discontinuities in polishing lines, the particle

boundaries can be guessed (Figure 147C). The crack tip changes from smooth edges to a strongly distorted shape as it cuts through the particle.

Fractography revealed consistent split particles that are recognized with a porous aspect compared to bypassed particles. Figure 148 shows such a cut particle. On the lower corners two uncut particles are visible (red arrows). The surface aspect is smoother, without any porosity.

Closer analysis of crack-stop areas in DCDC samples reveals very specific fractographic features. Figure 149 displays a crack stop line drawing an arc between two PAI particles (red arrows). This suggests a very well-known phenomenon: crack bowing, which is a step in a crack-pinning process. In this scenario, the crack front is locally delayed around particles, whereas it propagates in the particle-free areas. This has to be compared to the crack-tip being “trapped” with a high deviation angle after bypassing a particle (Figure 145A and B), the characteristic of crack-pinning, being delaying the crack on particles.

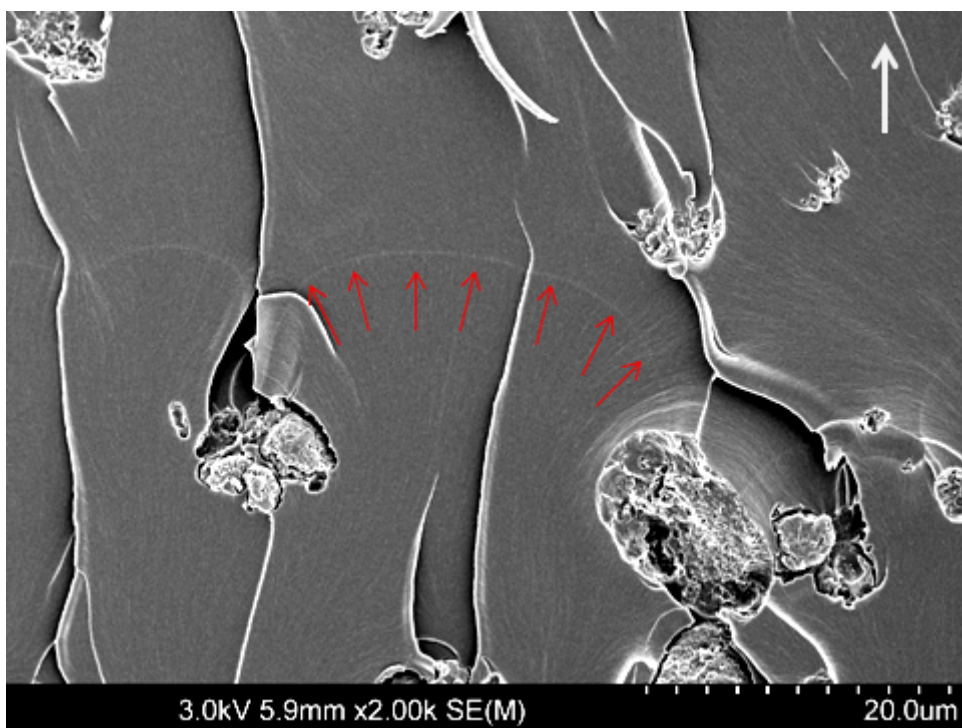


Figure 149: SEM fractography of a BMI/DBA/PAI 7 phr blend DCDC sample. Enhanced contrast. Propagation direction: up.

Compared to PES particles, no clear difference was observed between fast crack and crack stop areas. Fractography first suggests that the crack behaviour of PAI toughened resin is less sensitive to the crack velocity. Nevertheless, no statistical analysis was carried out, for instance to determine a ratio between split and un-split particles from an area to another.

4.3.4 Conclusions

Thermoplastic modification of the standard BMI/DBA network has little influence on the tensile modulus. An increase in toughness (K_{IC}) was observed with a limited extent (less than 30%). Soluble thermoplastics (PES and PEI) have similar performances. PAI is the

most effective of insoluble modifiers, PI having nearly no positive effect. PAI and PES¹ were selected for further study.

Using DCDC and AFM investigations, different phenomena were observed for different kinds of toughening. Each phenomenon was compared to a characteristic feature of fractured surfaces in both DCDC and CT samples. Insoluble PAI particles lead to crack deflection, particles being mainly un-split by the propagating crack. On the contrary, PES particles resulting from reaction-induced phase separation are always cut, with differences depending on the crack velocity. Low velocity phenomena, in the range of AFM observations, lead to particle stretching. Consequently, energy dissipation mechanisms are very different, with deflection, surface creation and crack-pinning for PAI and plastic deformation for PES.

4.4 Composite materials properties

4.4.1 Selected formulations

From the previous study on fracture properties and morphological control, considering the processability restrictions, thermoplastic-modified composite samples were designed. Formulations and preparation conditions are given in Table 11.

Matrix	Thermoplastic content (phr)	Preform preparation
Standard BMI/DBA	-	none
BMI/DBA/PES ¹	5	powdered and hot compression
BMI/DBA/PAI	7	powdered
BMI/DBA/PES ¹ /PAI	5 + 7	powdered and hot compression

Table 11: selected formulations for thermoplastic-modified composites.



Figure 150: non-destructive testing of a composite plate. A) single transmission attenuation (dB) ; B) single transmission time of flight (mm) ; C) double transmission attenuation (dB).

Composite plates were controlled by a non-destructive acoustic method to localise defects and porosity. Figure 150 shows control map for a whole plate. Attenuation gives the position of potential defects (Figure 150A). Double transmission attenuation (Figure 150C) is the loss of signal getting two-way through, because the plate is crossed twice, the loss is amplified and contrast on defects is enhanced. The time of flight evaluation

is useful to localise defects in the thickness (Figure 150A). The anti-adhesive ribbon can clearly be seen on Figure 150.

These maps were used to cut samples in healthy areas and to adjust the length of the pre-crack on fracture specimens.

4.4.2 Morphologies

Various testing specimens were cut from composite plates. To ensure that no experimental disparity would be due to a faulty thermoplastic powder dispersion in the preform, samples were cut in the same areas as testing specimens and were observed by optical microscopy. In all cases, samples were polished, and were then etched with dichloromethane if containing PES.

4.4.2.1 Neat bismaleimide-based composite

Composite plates were designed using a carbon fabric, two orthogonal fibre directions are observed within each ply, fibres being gathered in bundles of roughly 7 mm wide. Interlaminar spacing cannot be defined here as a regular resin layer because of the wavering weft (Figure 151A). Fibres from adjacent plies often comes in contact, however resin areas can be found between bundles with a 50-150 μm thickness (Figure 151A and B).

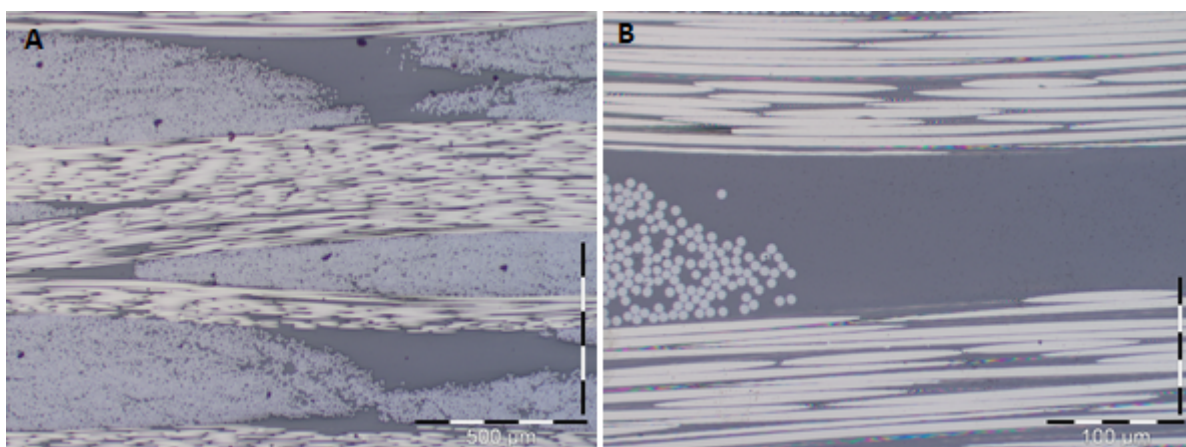
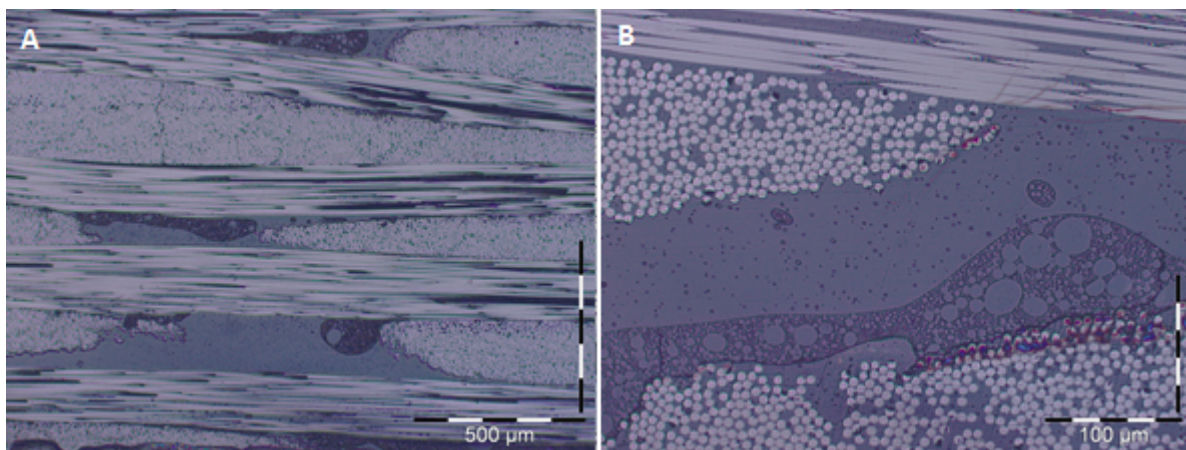


Figure 151: optical microscopy from standard BMI/DBA composite.
Scales: A) 500 μm ; B) 100 μm .

Even with different polymerization kinetics from epoxies and a higher viscosity, composite manufacturing has been successfully carried out with standard tooling.

4.4.2.2 Polyethersulfone-modified composite

PES with a low molecular weight was selected because of its higher solubility in the BMI/DBA resin and its adequate particle size (75 μm). Morphologies resulting from a configuration where PES particles are not pre-solubilised in the monomers were studied in paragraph 2.5.1.1. However, differences are expected for a hand-dispersed thermoplastic in a hot-pressed preform with a carbon fibre network limiting the resin flow. Microscopy control showed that PES is regularly dispersed in the composite plate, over the testing specimens area.



*Figure 152: optical microscopy from BMI/DBA/PES^l 5 phr composite.
Scales: A) 500 μm ; B) 100 μm .*

Close analysis of microscopy observations revealed the coexistence of two distinct morphologies. Dark areas on Figure 152 correspond to PES-rich phases. Etched particles are visible in the resin-rich main phase, even within fibre bundles. Inverted-phase morphologies are also found, mainly layered on carbon fibres. A scenario can be suggested from the previous morphological investigations. Softened PES was flattened and stuck to the carbon fabric while the preform was pressed. During the injection at 125°C, the resin diffuses in the bulk of PES particles, leading to a partial solubilisation. From the solubilised PES, reaction-induced phase separation generates particles in the resin-rich phase. Whether the swollen PES-rich phase remains partially solubilised or ultimately is fully solubilised, the result is in both cases, a local persistent high PES concentration. Consequently, when phase separation finally occurs, an inverted-phase morphology is formed.

Varley and Hodgkin studied the effect of the presence of fibres during phase separation of polysulfones in an epoxy/amine matrix [193]. They observed that, independently from the fibre nature (carbon, glass or aramid), the thermoplastic is attracted to the surface of fibres as soon as phase separation begins. Consequently, very different morphologies are obtained near fibres, where the polysulfone concentration is locally increased. The authors explained this effect by the attraction of the less polar thermoplastic to fibre surfaces. The major difference with the present case, leaving aside the chemical nature of the matrix, is that their thermoplastic was initially fully solubilised in the thermoset monomers. However, their observations are consistent with the preferential distribution of PES near carbon fibres.

Bonnaud and co-workers' study on PEI-modified epoxy/amine resins in the presence of glass and carbon fibres, also tend to confirm the change of morphology from a neat matrix to a composite [194]. They suggested that fibres act as a barrier inhibiting the flow of the more viscous thermoplastic-rich phase. Consequently, a higher thermoplastic concentration is generated near fibres, with consequences on the resulting local morphology.

4.4.2.3 Polyamide-imide-modified composite

With unsoluble PAI particles, the only potential problem would come from the initial dispersion in the preform. Microscopy control over the composite plate showed a satisfying dispersion.

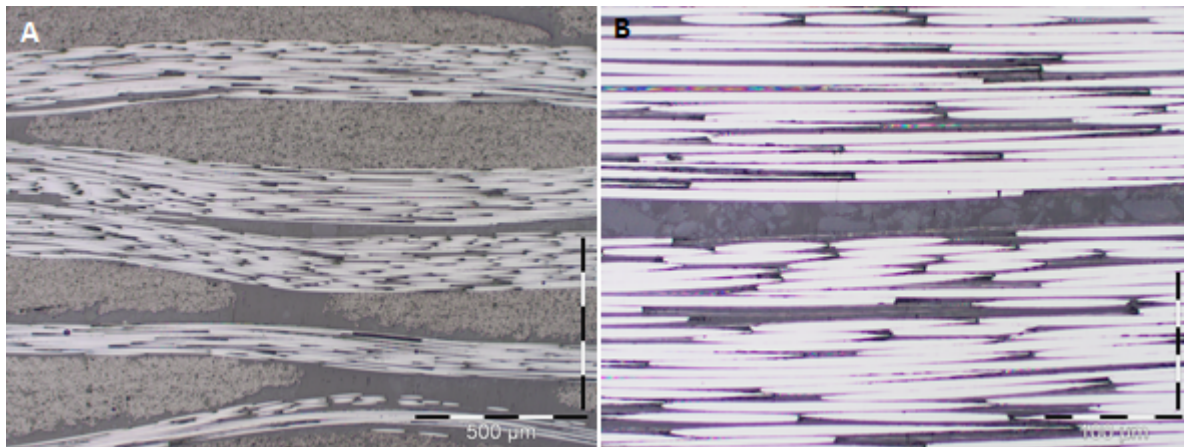


Figure 153: optical microscopy from BMI/DBA/PAI 7 phr composite.
Scales: A) 500 μm ; B) 100 μm .

If the composite structure is similar to the neat matrix one, the presence of rigid particles between plies leads to the development of thin matrix layers with a 20-50 μm thickness (Figure 153B). These come in addition to the 50-150 μm matrix areas between bundles, already observed on the previous composite plates. PAI particles are found everywhere in the matrix but exhibit a higher concentration in narrow areas.

Because PAI cannot penetrate the fibre bundles, the thermoplastic content is virtually increased. Defining a volume occupied by the matrix inside fibre bundles (*intra*) and between plies (*inter*), the matrix volume V_m is then:

$$V_m = V^{inter} + V^{intra}$$

Expressing the volumes in terms of resin (V_r) and of thermoplastic (V_{TP}):

$$V_m = V_r^{inter} + V_{TP}^{inter} + V_r^{intra} + V_{TP}^{intra}$$

PAI particles are excluded from the fibre bundles: $V_{TP}^{intra} = 0$. As a result the thermoplastic volume fraction is calculated as:

$$\Phi_{TP}^{inter} = \frac{V_{TP}^{inter}}{V^{inter}} = \frac{V_{TP}}{V_m - V^{intra}}$$

with Φ_{TP} the thermoplastic volume fraction in a fibre-less matrix:

$$\Phi_{TP}^{inter} = \frac{V_{TP}}{V_m - V^{intra}} > \Phi_{TP} = \frac{V_{TP}}{V_m}$$

From this increase of the particle volume fraction, considering the various models for toughening (paragraph 4.1.1.2), a higher efficiency is expected.

4.4.2.4 PES/PAI-modified composite

The thermoplastic dispersion was also satisfying after microscopy control. The resulting matrix is basically a combination of both previous blends (Figure 154). PES leads to particles and inverted-phase morphologies, PAI is dispersed between the plies. The interlaninar spacing, when existing, seems to be slightly higher than for PES or PAI alone. Various configurations are observed. PAI and inverted-phase PES are found separated (Figure 154B) but also with PAI particles embedded in PES-rich phases (Figure 154C and D).

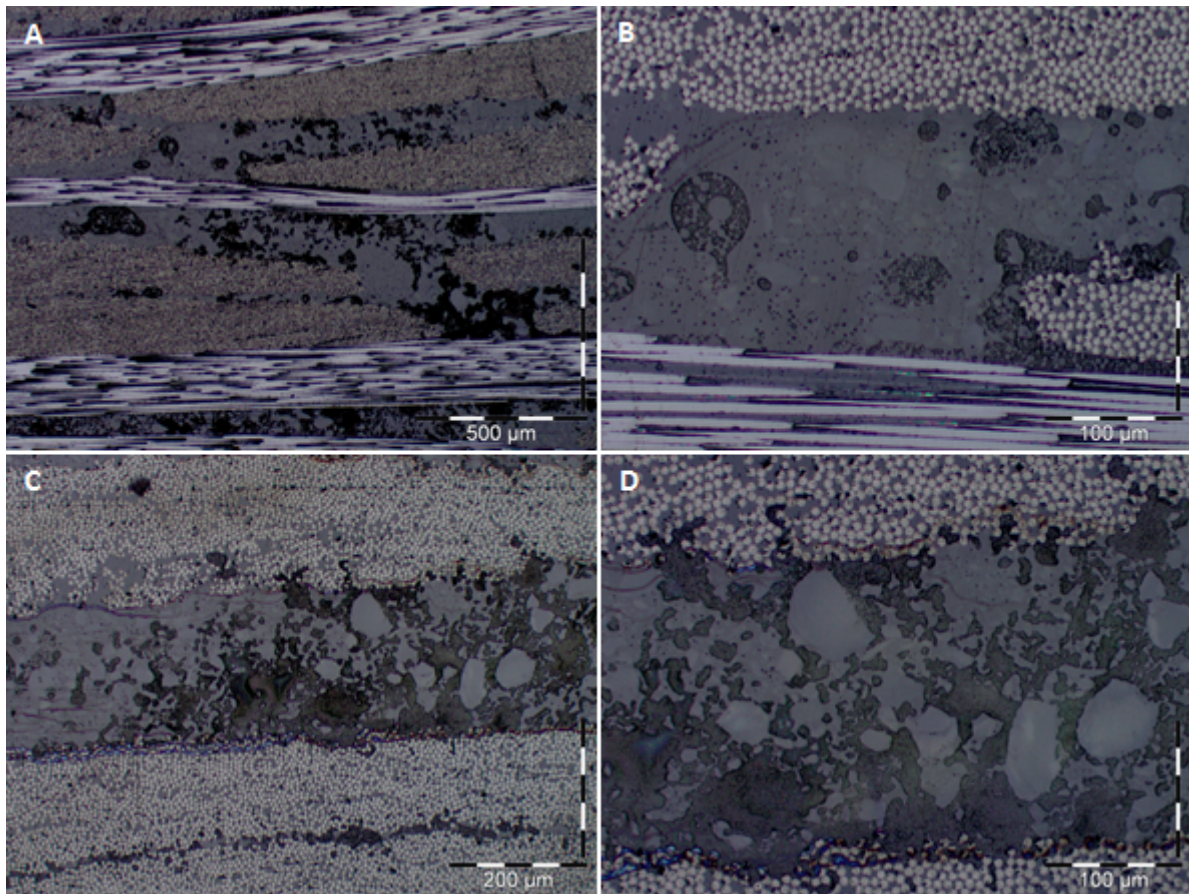


*Figure 154: optical microscopy from BMI/DBA/PES^l 5 phr, PAI 7 phr composite.
Scales: A) 500 μm ; B) 100 μm ; C) 200 μm ; D) 100 μm .*

4.4.2.5 Conclusions

Four different kinds of composite samples were designed following a simple procedure that brings a good macroscopic homogeneity over a single plate. The effect of toughening will be investigated in the following section. For the PES-modified matrix, the composite processing leads to a higher proportion of inverted-phase domains in the interleaves than for matrices. A potential effect on toughening is expected.

4.4.3 Toughening

Figure 155 displays the K_{IC} for the resin formulations corresponding to the composite plates. The toughness improvement is limited (under 30% for all cases) and no enhancement is observed by combining PES and PAI, compared to single PES and PAI.

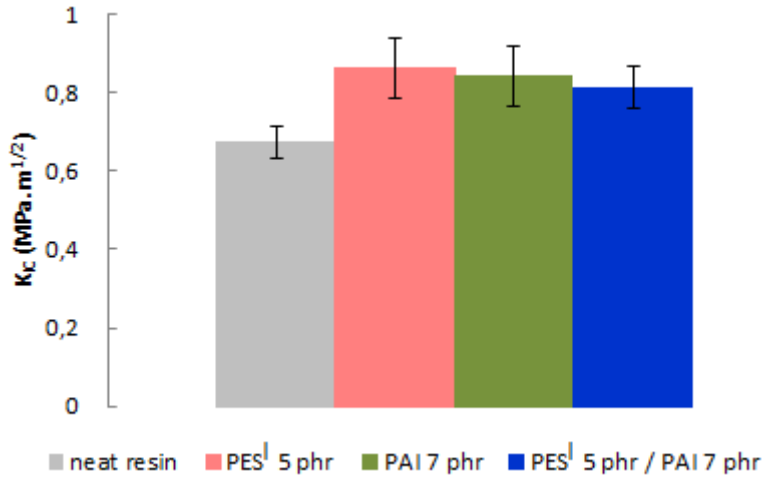


Figure 155: K_{IC} values from standard and thermoplastic-modified BMI/DBA matrices.

As explained in the first part of this chapter, transposition of properties from the matrix to the composite is subjected to several limitations, from a loss of efficiency to a change in encountered mechanisms. The fracture resistance in mode I was investigated through composite delamination tests.

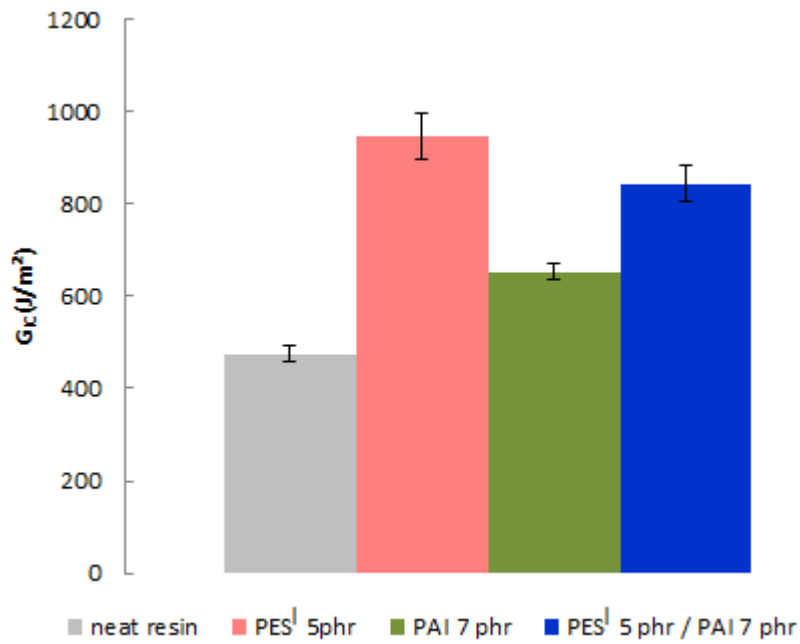


Figure 156: G_{IC} values from standard and thermoplastic-modified composites.

During testing, very few fibre bridging was observed, which is expected from woven composites. Consequently, the observed toughness improvement (Figure 156) is mainly due the matrix modification. The reference delamination energy for the standard BMI/DBA composite is consistent with analogous epoxy/carbon fabric laminates, though

476 J/m² is among the lowest values, reflecting the matrix brittleness. Each formulation lead to a significant enhancement of this property: 37% for PAI, 77% for PES/PAI and 99% for PES.

For matrices, PES is only slightly more effective than PAI, but much more for composite laminates. Two effects have to be taken into consideration, the first one being the already discussed intrinsic differences between toughness in composites and corresponding resins. More importantly, here a difference in morphology was observed for PES in laminates. The high proportion of inverted-phase domains is expected to lead to a better efficiency (see first part of this chapter). Attempts to reproduce a similar morphology in resin samples with the same PES content were inconclusive. Dispersing PES particles in the monomers without pre-solubilising the thermoplastic resulted into particle morphologies (slightly more heterogeneous) after curing, even with a pre-curing step at 125°C to mimic the composite processing cycle. As a matter of fact, after hot-pressing of the pre-form, PES is stuck to fibres and expected to form large clusters by particles coalescence, that would be more difficult to solubilise than dispersed particles. Here the effect of the whole composite processing has to be taken into account.

The combination of PES with PAI is more effective than PAI alone but not as much as single PES. The weakest link hypothesis can be suggested to explain this result, for instance with PAI particles inside PES-rich phases acting as weak points. Further investigation is needed to determine the exact nature of involved toughening mechanisms and to account for the role of fibre matrix interface.

4.4.4 Crack path

Fractured surface from delaminated composite samples were observed by SEM. More information about the crack path in composites and fracture mechanisms were gathered for each formulation.

4.4.4.1 Neat bismaleimide-based composite

Analysis of the standard BMI/DBA composite provided general information on crack propagation in this kind of laminates. Most of the fractured surface is made of bare fibres or fibre prints in resin blocks (Figure 157), indicating a cohesive fracture and a weak fibre/matrix interface. This suggests either a low reactivity between the resin and the epoxy sizing (where the phenol group of DBA is expected to be involved), or a partial degradation of the sizing during the curing step at 250°C. This seems to be a common observation on carbon fibre reinforced bismaleimide composites [195, 196].

The presence of fractured resin surfaces with an out of plane orientation (Figure 157B, C and D) is a sign of non-mode I failure. For such a composite, the test geometry applies a macroscopic mode I but the presence of woven fibres implies local distortion of the crack path, resulting to a multi-mode propagation. As a result direct correlation between the matrix mode I failure and the composite properties is difficult. However, the matrix properties remains an valuable indicator.

Resin fractured surfaces are relatively smooth (Figure 157B), a consistent point for a brittle failure. The presence of river line patterns (Figure 157D) suggests a mixed

mode I/III and failure by shear [197].

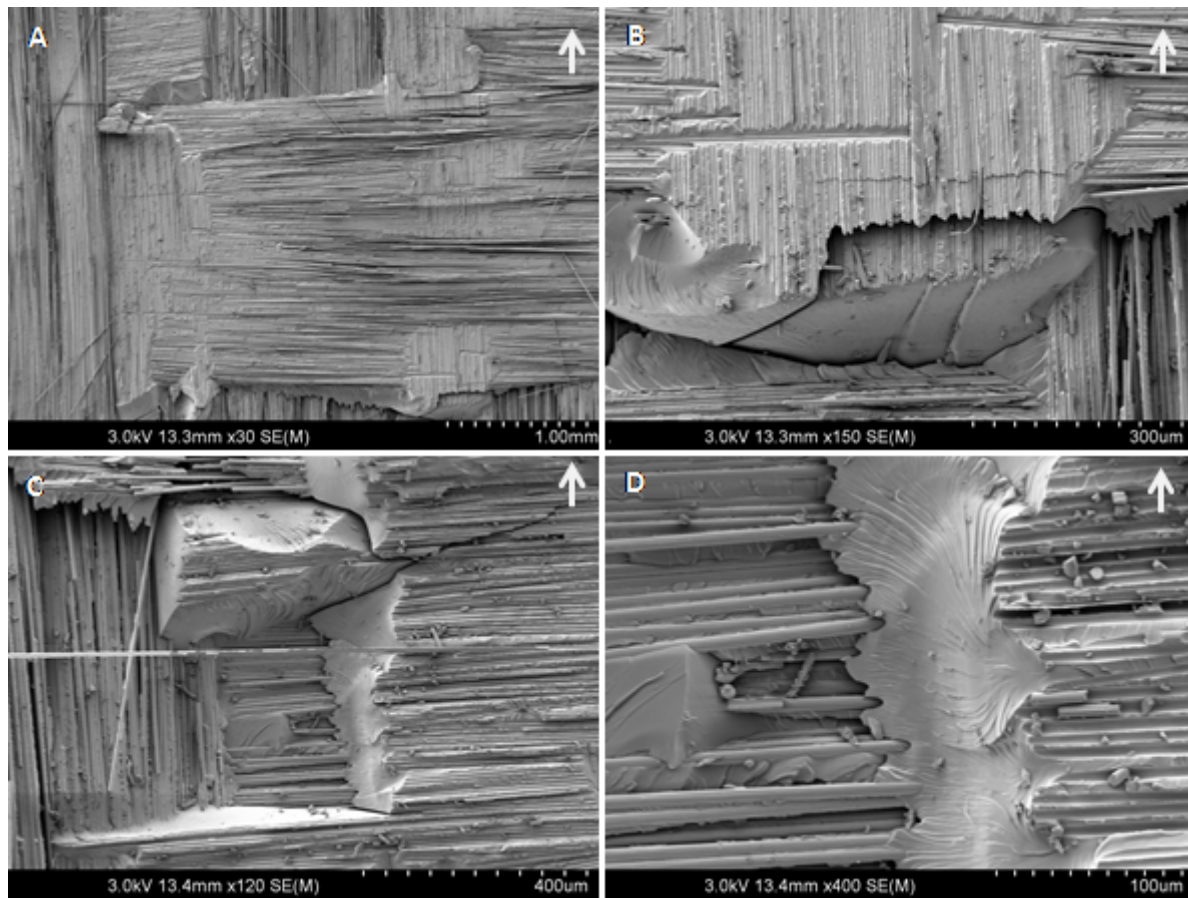


Figure 157: SEM fractography from a delaminated standard BMI/DBA composite specimen.

4.4.4.2 Polyethersulfone-modified composite

From a global point of view, the fractography of PES-toughened samples showed a similar behaviour as for the standard composite. The fracture remains cohesive, with a lot of fibre/matrix debonding (Figure 158A). Inclined surfaces and river line patterns (Figure 158B and C) are also indicators for mixed mode and shear.

The high increase in delamination energy (nearly 100%) does not find its origin in a drastic change of the failure process. Local modifications of the crack behaviour due to PES morphologies, especially inverted-phases, have to account for more energy dissipation.

Most of the matrix volume consists into a particle morphology. Fractured particles exhibit a rough surface compared to the thermoset phase (Figure 158C), reminding of the out of plane deformation observed in the modified matrices. Here again, the apparent porosity reflects the cavitation around thermoset-rich sub-particles inside PES particles.

The localisation of inverted-phases may also have a contribution. They are indeed located mainly on or close to carbon fibres, a configuration probably inherited from the preform processing, where PES particles are softened and pressed between woven carbon plies. Because the fracture of these composites mainly takes place at the fibre/matrix interface, changing the nature of the matrix near the interface, is expected to modify

the adhesion work and energy dissipated by plastic deformation. Figure 158D shows an area with a morphology gradient from a thermoset-rich phase on the left hand side to a thermoplastic-rich phase on the right hand side. The change in morphology is accompanied by a rise of roughness when the PES concentration increases. Ultimately (extreme right side) a high level of deformation is observed with nearly no marking of the fibre print.

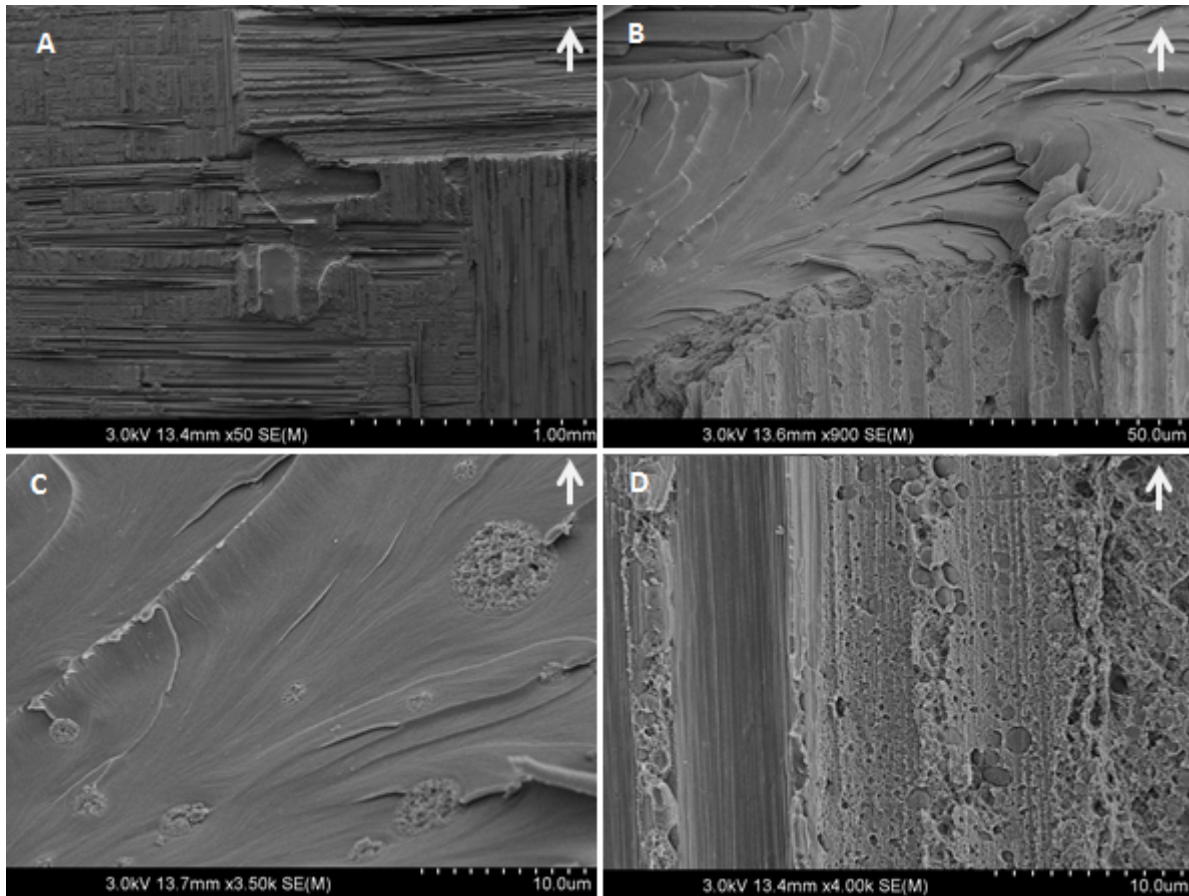


Figure 158: SEM fractography from a delaminated BMI/DBA/PES^l 5 phr composite specimen.

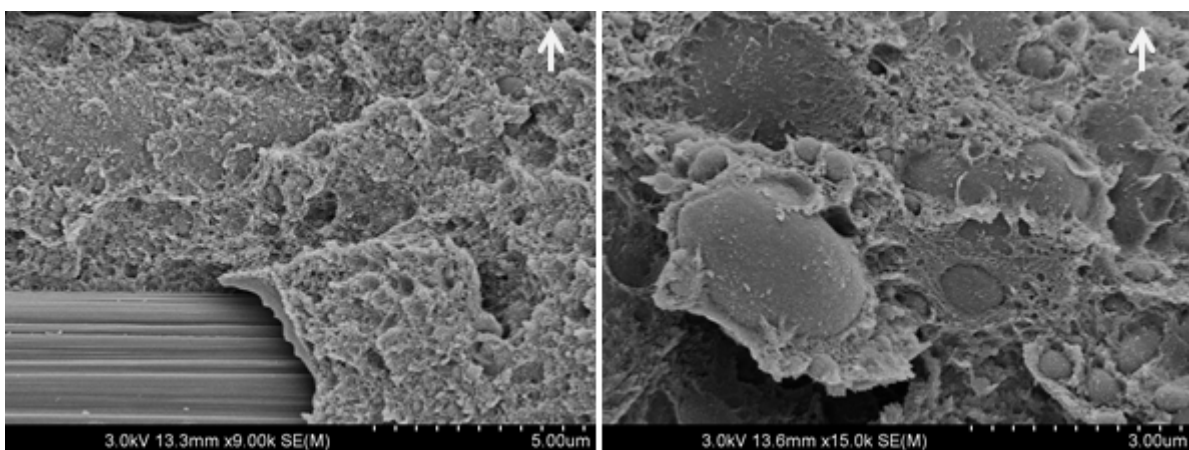


Figure 159: SEM fractography from a delaminated BMI/DBA/PES^l 5 phr composite specimen.

On the contrary to thermoset-rich phases, fractured surface of inverted-phases are not smooth at all. (Figure 159) shows rough surfaces with thermoset-rich inclusions. These

structures are somehow similar to dimples observed in metals with particle inclusions. They are developed by nucleation around particles and indicate a high level of plastic deformation [197]. This points out the coexistence of brittle and ductile failure processes due to the wide range of encountered morphologies.

Toughening of uni-dimensional laminates with PAEK, leading to inverted-phase morphologies showed very similar fractographic features with a substantial increase of G_{IC} [196].

4.4.4.3 Polyamide-imide-modified composite

As for the standard composite, the PAI-modified laminate exhibit mainly fibre/matrix decohesion (Figure 160A). The matrix failure also shows characteristic signs of brittleness with quite smooth surfaces (Figure 160B). Multi-mode and shear are once again suggested by out of plane orientation of fractured surfaces and river line patterns (Figure 160B, C and D).

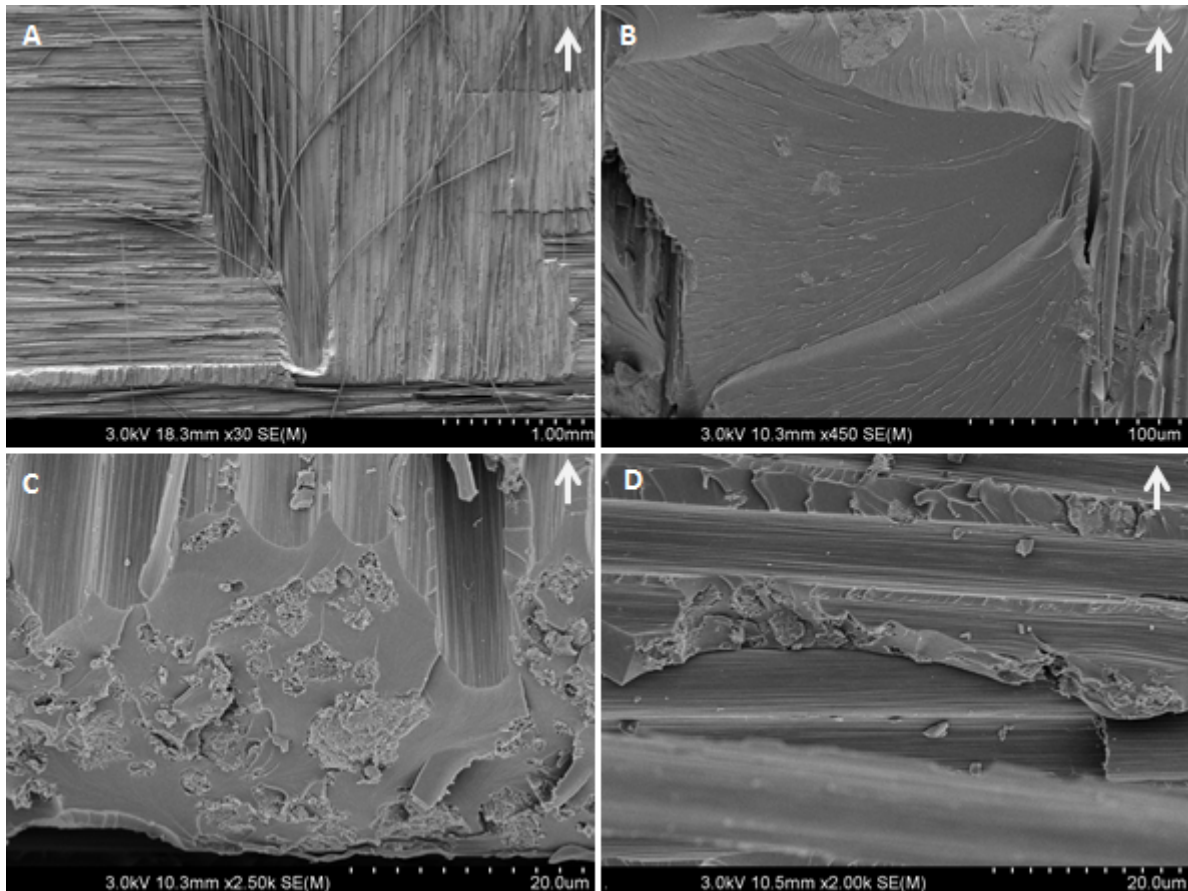


Figure 160: SEM fractography from a delaminated BMI/DBA/PAI 7 phr composite specimen.

The effect of PAI particles seems to be comparable to observations for crack propagation in the matrix. Local crack deviations, bypassing particles, are suggested by apparent un-split particles (Figure 160C and D). Broken particles are also observed, with a characteristic porous aspect.

4.4.4.4 PES/PAI-modified composite

Common features of cohesive fracture are met once again with both modifiers together (Figure 161A and B). Fractographic features simply reproduce the previous observations

for both toughening agents. PAI particles are met both un-split and broken (Figure 161C and D). PES inverted-phases lead to ductile failure process. Figure 161D displays two interesting features. First, the interruption of lines associated with a local deflection of the crack plane. These lines are located in the thermoset-rich phase and stop when meeting the inverted-phase domain, suggesting a brutal transition between brittle and ductile failure. Second, dimples-like structures in the PES-rich phase seems to be here quite equiaxed, which can be associated to a low shear level. Shear would tend to create parabolic dimples^[197].

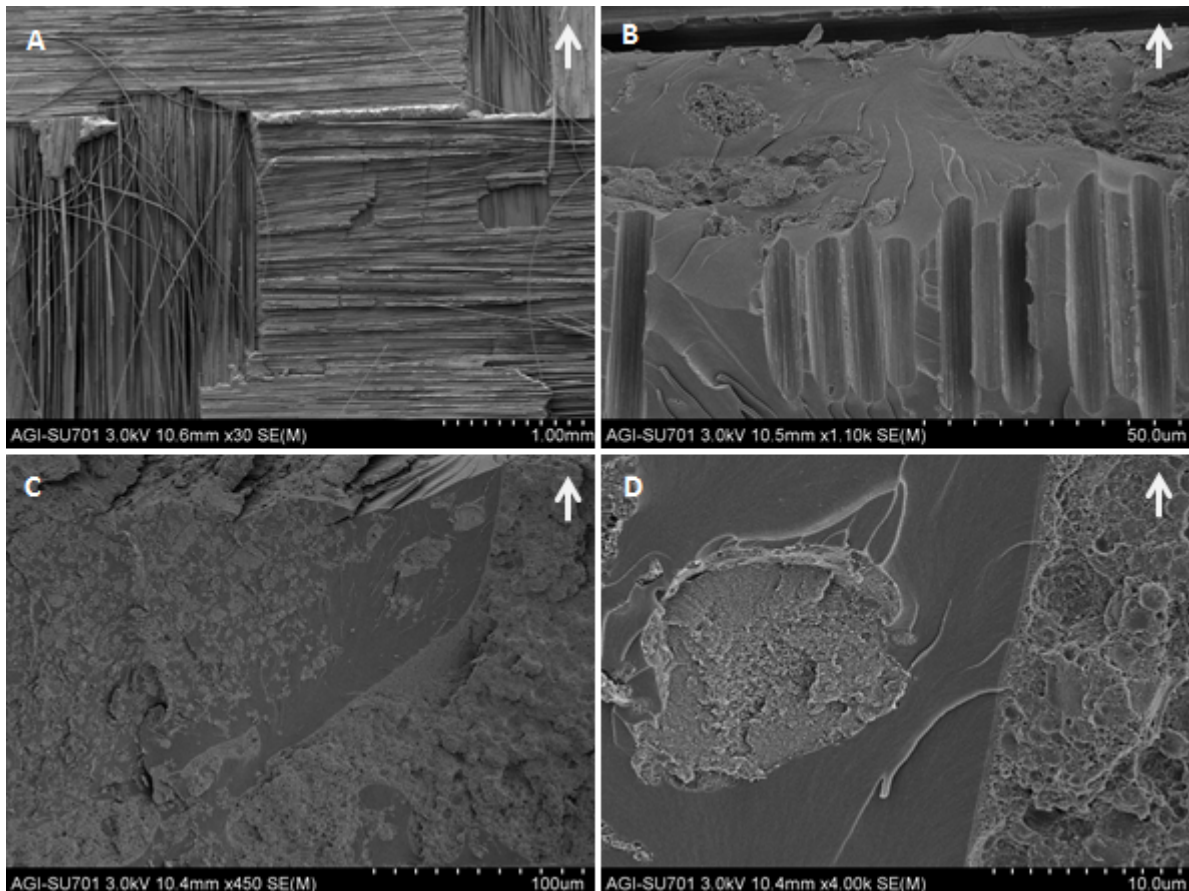


Figure 161: SEM fractography from a delaminated BMI/DBA/PES^l 5 phr, PAI 7 phr composite specimen.

4.4.4.5 Matrix-composite comparison

Fractography on composite samples revealed several aspects to keep in mind when investigating matrices properties. More than just fibres, composites introduce an interface than can become the weak point of the whole material. If this is clearly the case here, the matrix toughening did not prove to be pointless at all, with a significant improvement of composites properties. A macroscopic mode I failure process can be associated with local mixed-modes, especially with carbon fabrics where the interlaminar space has no constant thickness. Consequently, more complex phenomena than those observed in a pure mode I crack propagation are expected.

Some mechanisms are easily transposed from the matrix to the composite, as the crack path deviation by PAI particles or the stretching of PES particles. Others were not encountered as the oriented particle-matrix decohesion with PES. Occurrence of crack-pinning was not clearly identified, but this kind of observation is disturbed with such

irregular fractured surfaces. It was shown that the crack velocity had an influence on fractographic features, especially for PES particles. Composite delamination tests proceed with a constant cross-head speed, but propagations and apparent non-propagative steps alternate. Consequently, a wide range of velocities are expected to be encountered. However, once again, the material complexity makes difficult correlation between fractography and a potential rate dependency.

Finally, non negligible morphological differences were observed between the PES-modified model matrix and the corresponding PES-toughened composite. As a result investigation on the matrix can only be partially transposed to the composite.

4.5 Conclusions

4.5.1 On crack propagation in modified resins

In chapter 3, DCDC geometry, coupled with AFM observations, was used for fine mechanical analysis of failure in homogeneous samples. The whole experimental device was successfully transposed to multiphasic materials to investigate toughening mechanisms. Observations were consistent with classic SEM fractography and the major advantage compared to this method, is the introduction of time resolution.

PAI and PES¹ were selected for these investigations. Different phenomena were observed for the different kinds of toughening. Insoluble PAI particles lead to crack-deflection and crack-pinning. Particles resulting from PES RIPS encounter stretching, revealing different energy dissipation mechanisms.

4.5.2 On composite processing and toughening

Composite plate were successfully designed by an injection process, using standard tooling. Thermoplastic toughening with PAI and PES¹ was efficient (between nearly 40% and 100% in G_{IC}) and gave promising results for further optimisation (thermoplastic content, preform preparation, curing cycle...).

Because thermoplastics had to be included directly in the preform prior to the injection, the resulting morphology for PES¹ was evidenced to be sensitive to the composite processing. In addition to the expected particle dispersion, inverted-phases were obtained. As a consequence, the failure mechanism was changed, introducing a ductile contribution, that was actually the most effective toughening configuration.

Even if the whole toughening process, starting from the matrix up to the complex composite, achieved its objective, failure in the composite mainly occurs at the fibre/matrix interface. Thus optimisation should also be done on the carbon fibre sizing for this kind of thermoset.

Chapter 5

Suggestions for further work and general conclusion

This conclusion chapter gives suggestions on the different themes addressed in this study. When these are based on additional work, supplementary information is provided. The final part is dedicated to the general conclusion.

5.1 Reactivity of bismaleimides

5.1.1 Chemical characterisations

Studies from the literature employed various methods to analyse reaction products from maleimide/allyl reaction. Spectroscopy (solid state NMR, IR...) provided information on chemical functions consumption and creation, but structure resolution by these means is extremely complex and often requires complementary characterisation. Chromatography methods always encountered problems because of the low solubility of reaction products. Previous studies on high pressure liquid chromatography optimisation confirmed the high difficulty to find a suitable solvent [198]. On the other hand, the formation of quickly insoluble species was an indication for free radical polymerization, that was then confirmed by rheological analysis. Mass spectroscopy methods, such as MALDI-TOF (Matrix-Assisted Laser Desorption/Ionisation Time of Flight mass spectroscopy) might provide new information for chemical structure characterization. Nevertheless, considering the general aim of this work, with a limited time allocated to chemical investigations, the choice was made to move on to physico-chemical characterization, which highlighted the radical nature of the cross-linking process.

If the complete reaction path of bismaleimide/bisallyl resins was not solved, a hierarchy among possible mechanisms arose. Main reactions are Alder-ene chain extension and radical cross-linking, but Diels-Alder/Wagner-Jauregg reactions are not completely excluded. Even only considering the first two, a better understanding of the thermoset network was achieved. It also brought out fundamental differences between epoxy resins and bismaleimides, as much from a theoretical point of view (physico-chemistry, phase separation process) as from a practical one (weak gel, control with radical inhibitors). Nevertheless, this had no negative influence on composite processing that was successful using standard tooling.

5.1.2 Simulated network architecture

The program was easily adapted to multi-core processing for a higher efficiency, nevertheless the code still requires optimisation. In particular, the random generation of radicals and the Alder-ene reaction are time consuming because they scan the whole matrix. An improvement could be to gather as much as possible these steps to reduce the number of scans per cycle. The use of a radical table avoids this downside for radical reactions, but

introduces a counterproductive dynamic size allocation. A study to evaluate a suitable maximum size of this table, with a consequent adaptation of the code, would solve the problem.

The model itself is limited by the number of parameters. The choice has been made to set reaction probabilities, consequently reducing the number of reactions (no side reactions such as Diels-Alder were taken into account). On the other hand, simple models, such as Arrhenius law, can link reaction probabilities to a single parameter: temperature. Required constants, such as activation energies, can be determined from kinetics. Hopewell and co-workers determined radical concentration evolution with time at different temperatures [31]. This provides data for radical initiation activation energy, the initial reaction rates lead to a value of 136 kJ/mol. They only explored the 190°C-230°C temperature range but extrapolation to lower temperatures can be made. The scientific literature also provides kinetics data about the Alder-ene reaction, but never without occurrence of other reactions [41, 199, 200]. A massive use of radical inhibitor may get rid of the radical polymerization but not other potential addition reactions.

The mobility of chemical species was not implemented in the program. In the case of free radical polymerization, radical trapping is often observed and simulation is not accurate without mobility, but reference cases deal with a fixed initial radical content [74, 75]. In the present code, radicals are generated at each step, avoiding a premature end of reaction due to trapping of activated species. Considering the Fick law, diffusion coefficients arise, and a simple temperature dependency would allow to control the whole simulation (reactions kinetics and diffusion) with temperature as a single parameter. From a computational point of view, diffusion of reacted species introduces a high level of complexity compared to the current very simple model. Enabling diffusion only for monomers could be a first approximation.

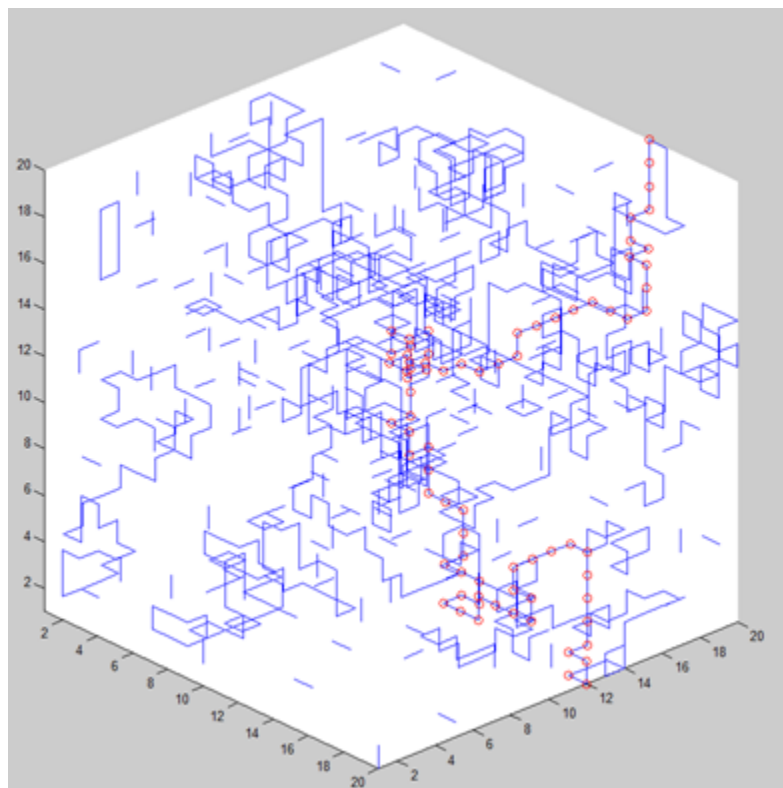


Figure 162: percolation path in a simulated network.

The program was used so far only for illustrative purposes. Nevertheless, quantitative analysis can easily be performed on simulated networks. Counters can be placed inside reaction loops, increasing for each consumed double bond, to calculate a conversion after each step. The gel state can also be determined using a percolation detection. Percolation is here defined as the existence of a continuous path of bonds between two opposite sides of the cubic matrix. A Djikstra algorithm was used to test networks upon this criterion, Figure 162 shows such a path in a percolated simulated sample.

Remark: the network on Figure 162 was obtained using only free radical polymerization with an initial distribution of radicals (no thermal initiation at each step).

Other analysis could be considered, such as prediction of inhomogeneity characteristic length but the model still need to be deeply refined.

5.2 Fracture mechanics of bismaleimides

Many efforts were devoted to adapt AFM observations with a DCDC geometry to bismaleimide resins. This enabled to explore the fracture behaviour of these materials on a crack velocity range that was not investigated so far. Non-monotonic variations of the crack-tip velocity were observed and seemed related to the polymer network inhomogeneity.

A scaling approach for the rate dependency of crack propagation was suggested in chapter 3. Quantitative analysis with experimental data lead to a fair prediction of the stress intensity factor, considering the required approximations. The strongest hypothesis was made on the maximum encountered strain at the crack-tip (ϵ_{max}). This parameter was only evaluated manually and is critical for the model accuracy. Because the bismaleimide material showed a low rate dependency, the effect of a mis-estimation is tempered. A possible method to measure ϵ_{max} is digital image correlation (DIC), for which AFM imaging of crack propagation shows a great potential. DIC relies on the comparison between two images to determine the adequate transformation from one to the other. The surface preparation of DCDC samples generates lines that are extremely useful for DIC. Imaging an area at different steps, from long before the crack propagation to the crack-tip arrival, would enable to observe the evolution of the strain field. More than simply the maximum strain at the crack-tip, the shape of the process zone and the stress distribution (knowing the stress/strain relationship) could also be determined. From this point, a more quantitative analysis, integrating the dissipated energy in the process zone (with the stress and strain at each point), can be suggested.

5.3 Failure of modified resins

Materials were selected among industrial grade products to design model yet realistic modified bismaleimide resins. Some formulations were selected owing to their promising properties, but optimisation still offers a lot of possibilities (curing cycle, thermoplastic blends, particle size and shape...). A fundamental aspect was not addressed: surface interaction between the thermosetting matrix and thermoplastic particles. Tuning the surface interactions, for instance by chemical functionalisation, is expected to modify the toughening mechanisms and the crack path. The present study tried to comply with both

material enhancement and development of an observation method. These two aspects appeared to be quite complementary and the same could be expected by applying this strategy to thermosets modified with tuned functionalised particles.

Two kinds of thermoplastics were used to toughen the selected bismaleimide resin. Soluble PES and PEI lead to particles, at low concentration, by RIPS. Insoluble and amorphous PAI and PI simply lead to particle dispersions. Semi-crystalline polymers were not investigated, yet they offer a new dimension for morphological control. Depending on the chemical nature of the thermoplastic, solubilisation in monomers may or may not be achieved in a molten or crystalline state. As a consequence, adapting the curing cycle taking into consideration the melting temperature (T_m), can generate different morphologies from a single formulation. If monomers cannot solubilise crystallites but are miscible with the free chains, polymerization before melting would result to a particle dispersion, whereas quickly increasing the temperature above T_m would lead to (partial) solubilisation with potential RIPS. Fine control over the curing cycle could provide intermediate states.

5.4 Composites properties

5.4.1 Fracture of composites

Investigations on toughening mechanisms in composite laminates were limited to fractography. This analysis provided valuable information on the morphology/toughness relationship. Considering the great potential of DCDC-AFM, first attempts were made to use this procedure to follow crack propagation in composites. A 6.8 mm-thick composite plate was made with G986 carbon fabric (24 plies). A 5 mm-wide separating ribbon was placed between the two middle plies to create the pre-cracks. DCDC specimens were machined from this laminate, the hole being drilled in the middle of the ribbon (delimited by white arrows on Figure 163).

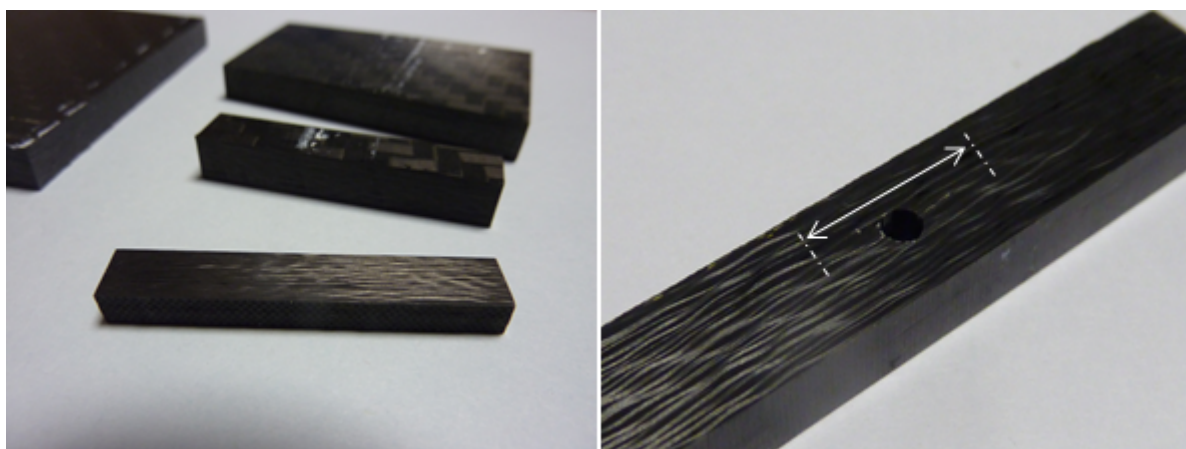


Figure 163: DCDC composite samples designed out of a thick plate.

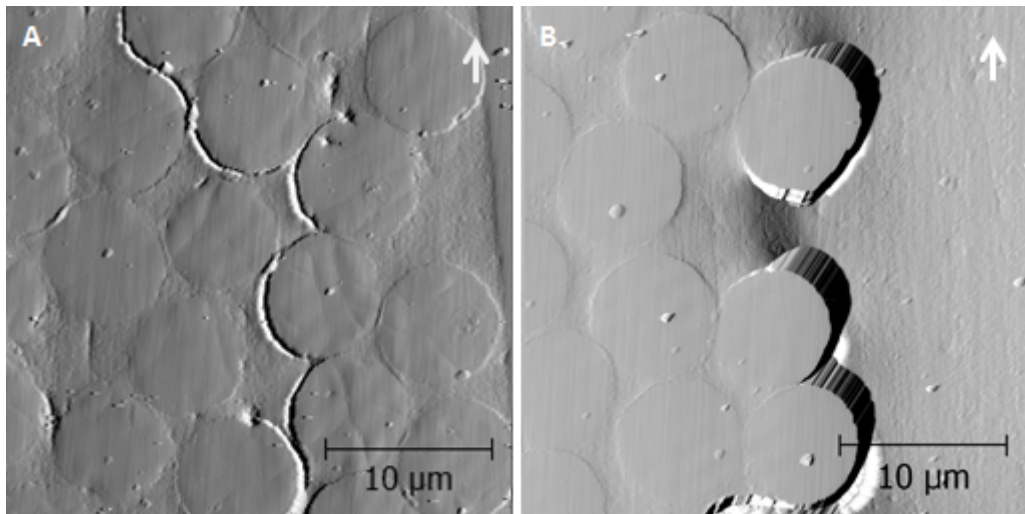


Figure 164: AFM images (deflection error) of a crack propagating in a DCDC composite specimen. A) intralaminar crack ; B) interlaminar crack.

First observations are consistent with fractography and other classic images, with cracks propagating along the fibre/matrix interface (Figure 164A). Several problems arose with this kind of propagation. First, composites are prone to multiple cracking. The DCDC geometry seemed to generate quite neat cracks but having several of them makes difficult the localisation of the propagating one. Samples undergo a damaging process in which material alteration is widely spread (for AFM scale) which makes fracture mechanisms investigation highly complex. Moreover, most of the cracks being localised at the fibre/matrix boundary, clearly identifying the crack-tip is also difficult, especially for propagation along interlaminar out of plane fibres (Figure 164B). In this case, the height difference between fibres and matrix becomes an obstacle for the scanning tip, creating nearly a blind area where the crack lies.

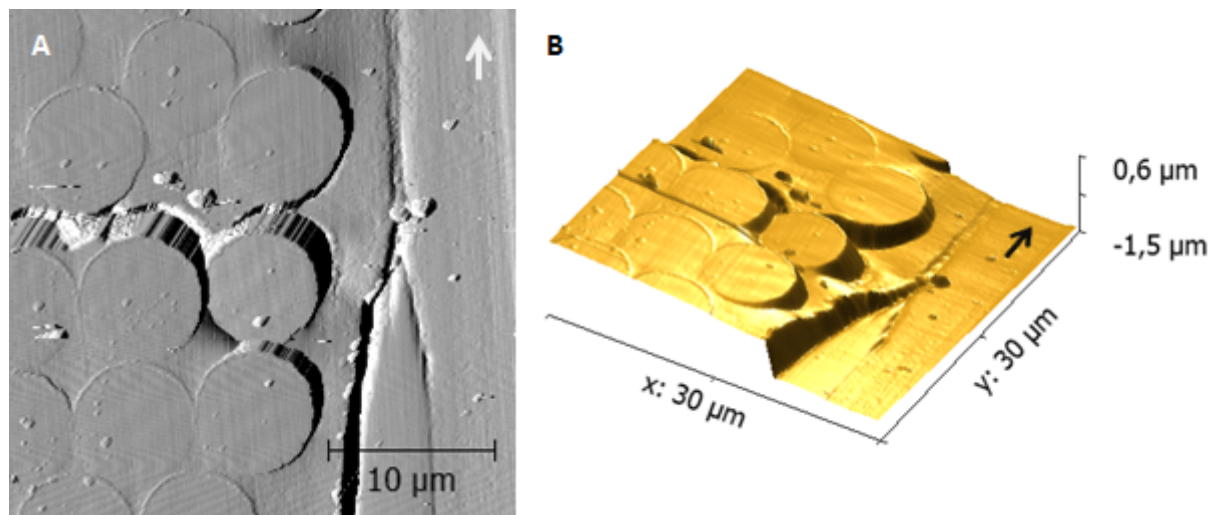


Figure 165: AFM images of a crack propagating in a DCDC composite specimen. A) deflection error ; B) height 3D reconstruction.

When the crack-tip was identified, complex local strains were evidenced. Figure 165 shows the creation of a step along the crack between plies where fibre orientations are different. Out of plane fibres nearly seem pulled out (AFM being not suitable to determine whether the interface broke or not), a discrepancy that decreases ahead of the crack-tip.

Real composite samples appeared to be too complex to be analysed with the DCDC-AFM method in the present state. To study the confinement effects on toughened resins, model composites should be designed. Unidirectional fibre orientation is suggested. The main conception difficulty is the control over the interlaminar thickness. Using unidirectional fibre bundles infused by resin inside a mould, simplified composite DCDC samples were designed. Figure 166 shows the suggested sample, with a 200 µm-thick interlaminar space and a pre-crack at the edge of the hole (formed with anti-adhesive ribbon).

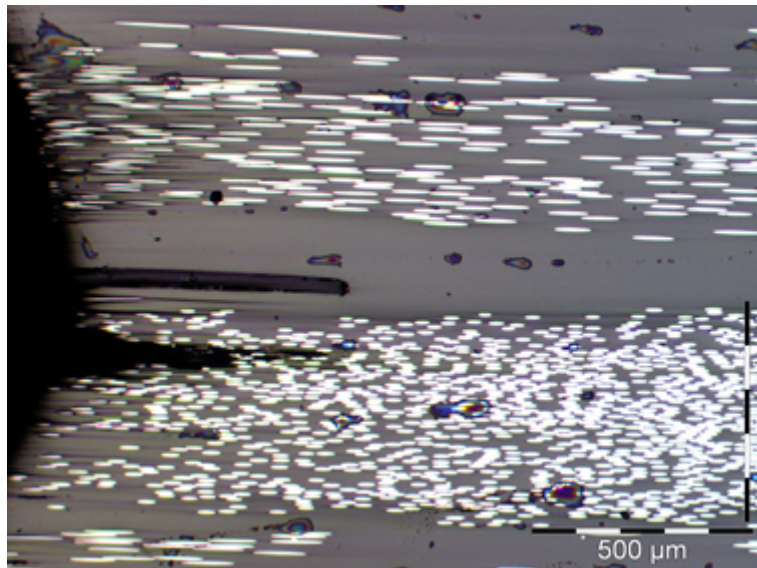


Figure 166: optical microscopy at the surface of a model composite DCDC sample.

5.4.2 Compression after impact

A very common test for composite laminates relies on the combined study of impact damaging and properties retentions of damaged materials. Impact consists into a falling weight for which the mass and initial height determine the energy. The size of the damaged area and the nature of damage is usually investigated. Compression after impact (CAI) sets the damaged laminate in lateral compression to evaluate the residual strength of the composite (Figure 167). This configuration with an initial damaged laminate put under compression is close to the principle of the DCDC geometry. DCDC on composite samples could be a new method to better understand mechanisms involved during CAI experiments.

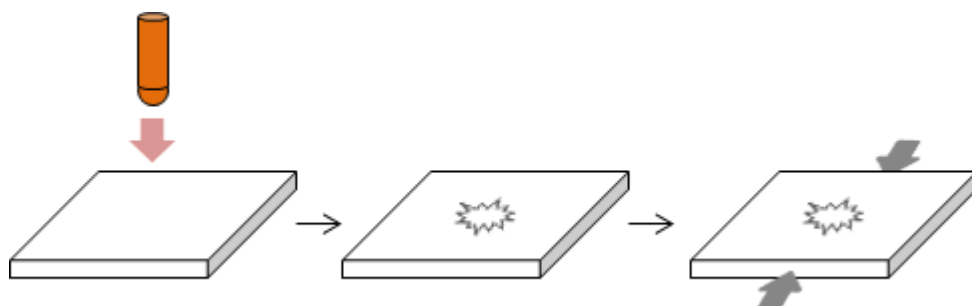


Figure 167: impact and compression after impact procedure.

5.4.3 Other types of alteration

Because the aeronautic field requires an extreme reliability, materials have to follow a very demanding path of certifications, where properties are evaluated in various conditions. For the targeted structural high temperature applications, ageing tests still have to be carried out. The material has to sustain excellent properties after thermal ageing and in wet conditions. Some studies have investigated the water uptake of bismaleimide composites [201–204], others focused on thermal degradation and oxidation [10–12, 52, 205, 206]. Micro-cracks develop during ageing (usually above 200°C) in non-modified resins. Water uptake is associated with plasticizing of the matrix, leading to a loss of T_g , and also promote micro-cracking above 60°C. Cycling ageing was also investigated, with similar degradation observed, under combined effects of temperature, moisture and/or stress [13, 207]. Thermoplastic modifiers are expected to change this behaviour. If water uptake may reach a higher extent in the presence of PES or PEI (that are known to absorb small amounts of water), micro-cracking might also be limited.

5.5 Conclusions

This work was dedicated to bismaleimide-based composite materials fracture properties enhancement, for high temperature (up to 200°C) aeronautic applications. The investigations went into very different aspects of this subject, from the chemistry of bismaleimide thermosets to the failure of toughened composites.

As mentioned all through the different parts of this study, bismaleimide resins exhibit a lot of differences compared to epoxy resins, the reference for aeronautic grade composite materials. The origin lies in their completely different thermosetting reaction path. The complex chemical reactions involved in the bismaleimide resins polymerization process and especially a radical-based cross-linking mechanism lead to inhomogeneous network architectures.

Among the consequences, the fracture behaviour of these materials, investigated at a sub-microscopic scale, seems to depend on the network structure. More efforts have also been paid to better understand the relationship between the strain rate dependency of the polymer (linked to the structure through thermomechanical properties) and the crack propagation.

Despite being deeply different from epoxy networks, the toughening strategy for bismaleimide materials was to apply thermoplastic modification, already in use with epoxy-based composites. This modification offers a wide range of morphologies for matrices. Toughening mechanisms have been identified with a time resolved observation method, allowing to follow the crack propagation at a microscopic scale. Composite laminates deriving from these promising matrices have achieved enhanced performances such as nearly 100% higher delamination energy in mode I, compared to non-modified bismaleimide-based composites.

The successful transposition of the thermoplastic modification strategy between two thermosets, strongly different in their polymerization processes and network architectures, is promising for widening to other thermosetting materials. Bismaleimides have been selected for this study because of their availability at an industrial scale and their long use

in aeronautics. Other thermosets such as cyanate esters or benzoxazines are suitable for high temperature applications, providing a potential wider range of complex, structured and tough high temperature polymer matrix composite materials.

Abbreviations

- AP: 1-allylphenol
BMI: bismaleimide or 1,1'-(methyldi-4,1-phenyl)bismaleimide
CAI: Compression After Impact
CE: cyanate ester
CTBN: carboxy-terminated polybutadiene-*co*-acrylonitrile
CT: Compact Tension
DBA: 2,2'-diallylbisphenol A
DCDC: Double Cantilever Drilled Compression
DDS: 4,4'-diaminodiphenylsulfone
DGEBF: diglycidylether bisphenol F
DMA: Dynamic Mechanical Analysis
DSC: Differential Scanning Calorimetry
EDX: Electron Dispersive X-ray spectrometry
EPR: Electron Paramagnetic Resonance
FT-IR: Fourier Transformed Infrared Spectroscopy
ETBN: epoxy-terminated polybutadiene-*co*-acrylonitrile
HQ: hydroquinone
i.e.: *id est*
IPN: Interpenetrated Polymer Network
IR: infrared
LCST: Lower Critical Solution Temperature
LFEM: Linear Elastic fracture Mechanics
LIPN: Linked Interpenetrated Polymer Network
MALDI-TOF: Matrix-Assisted Laser Desorption/Ionisation Time of Flight mass spectroscopy
MI: N-phenylmaleimide
 M_w : weight average molecular mass
NIR: Near Infrared
NMR: Nuclear Magnetic Resonance
OOP: Oriented Object Programming
PAEK: poly(aryl ether ketone)
phr: parts per hundred parts of resin
PEEK: poly(ether ether ketone)
PEI: polyetherimide
PEKK: poly(ether ketone ketone)
PES: polyethersulfone
PI: polyimide
PMMA: polymethylmethacrylate
PP: 1-propenylphenol
PPEK: poly(phtalazinone ether ketone)
PTFE: polytetrafluoroethylene
RIPS: Reaction Induced Phase Separation
SEM: Scanning Electron Microscopy
SiC: Silicon Carbide
TS: thermosetting polymer
 T_g : glass transition temperature

Abbreviations

TGA: Thermogravimetry Analysis
TGMDA: tetraglycidylaminodiphenylmethane
 T_m : melting temperature
TP: thermoplastic
TRLS: Time Resolved Light Scattering
TTT: Time-Temperature-Transformation (diagram)
UCST: Upper Critical Solution Temperature
UD: uni-directional
UV: ultraviolet

Bibliography

- [1] K. CHAWLA, Composite materials. Springer, 1998.
- [2] L. PILATO and M. MICHNO, Advanced composite materials. Springer-Verlag, 1994.
- [3] J.-P. PASCAULT, H. SAUTEREAU, J. VERDU, and R. WILLIAMS, Thermosetting Polymers. Marcel Dekker, 2002.
- [4] S. TSAI and H. HAHN, Introduction to composite materials. Technomic Publishing, 1980.
- [5] A. BRATUKHIN, V. BOGOLYUBOV, V. RAZUMOVSKI, A. SAVIN, V. MISHIN, and V. SADKOV, Composite manufacturing technology. Springer Science, 1995, ch. 7, pp. 284–341.
- [6] J. CINQUIN, Les composites en aéronautique, Techniques de l'ingénieur, 2002, vol. 5645, pp. 1–14.
- [7] S. PAYAN, Comportement à la corrosion galvanique de matériaux composites à matrice d'alliage d'aluminium renforcée par des fibres de carbone haut-module, Ph.D. thesis, Université Bordeaux I, 2001.
- [8] J. BOYD, Bismaleimide resins. ASM Handbook, 2001, ch. Constituent Materials, pp. 97–104.
- [9] FEDERAL AVIATION ADMINISTRATION, Aviation maintenance technician Handbook - Airframe, Volume 1. Flight Standards Service, 2012.
- [10] L. BURCHAM, R. EDULJEE, and J. GILLEPSIE Jr, Investigation of the Microcracking Behavior of Bismaleimide Composites During Thermal Aging, *Polym. Compos.*, 1995, vol. 16, no. 6, pp. 507–517.
- [11] I. SALIN and J. SEFERIS, Anisotropic Degradation of Polymeric Composites: From Neat Resin to Composite, *Polym. Compos.*, 1996, vol. 17, no. 3, pp. 430–442.
- [12] N. HANCOX, Thermal effects on polymer matrix composites: Part 2. Thermal degradation, *Materials and Design*, 1998, vol. 19, pp. 93–97.
- [13] J. JU and R. MORGAN, Characterization of Microcrack Development in BMI-Carbon Fiber Composite under Stress and Thermal Cycling, *Journal of Composite Materials*, 2004, vol. 38, no. 22, pp. 2007–2023.
- [14] I. VARMA and S. SHARMA, Curing of bismaleimides : 3. Effect of structure on thermal behaviour of bis(amide-maleimide), *Polymer*, 1985, vol. 26, pp. 1561–1565.
- [15] S. EVSYUKOV, T. POHLMANN, and H. STENZENBERGER, m-Xylylene bismaleimide: a versatile building block for high-performance thermosets, *Polym. Adv. Technol.*, 2015, vol. 26, pp. 574–580.

- [16] A. SERIS-ROUSSEL, Etude cinétique et thermodynamique des mélanges constitués de bismaléimides et de polysiloxanes., Ph.D. thesis, INSA de Lyon, Matériaux macromoléculaires, 1990.
- [17] J. HOPEWELL, G. GEORGE, and D. HILL, Analysis of the kinetics and mechanism of the cure of a bismaleimide-diamine thermoset, *Polymer*, 2000, vol. 41, pp. 8231–8239.
- [18] J. HOPEWELL, G. GEORGE, and D. HILL, Quantitative analysis of bismaleimide-diamine thermosets using near infrared spectroscopy, *Polymer*, 2000, vol. 41, pp. 8221–8229.
- [19] H. CHUAH and P. WANG, High Temperature Thermosets Based on the Cocuring of a Novel Spirodilactam Bisallylether and Bismaleimide, *Polym. Eng. Sci.*, 1994, vol. 34, no. 1, pp. 12–16.
- [20] G. LIANG and A. GU, New Bismaleimide Resin with Improved Tack and Drape Properties for Advanced Composites, *J. Appl. Polym. Sci.*, 1997, vol. 64, pp. 273–279.
- [21] Y. YU, M. WANG, X. LIU, L. ZHAO, X. TANG, and S. LI, Synthesis and Cure of Liquid Crystalline Diallyl Modifiers for Bismaleimide Resin, *J. Appl. Polym. Sci.*, 2006, vol. 101, pp. 4366–4371.
- [22] A. GU, Novel high performance RTM bismaleimide resin with low cure temperature for advanced composites, *Polym. Adv. Technol.*, 2005, vol. 16, pp. 563–566.
- [23] L. DIX, J. EBDON, and P. HODGES, Chain extension and crosslinking of telechelic oligomers - II. Michael additions of bisthiols to bismaleimides, bismaleates and bis(acetylene ketone)s to give linear and crosslinked polymers, *Eur. Polym. J.*, 1995, vol. 31, no. 7, pp. 653–658.
- [24] M. XIAOYAN, Y. HONGXIA, and N. RONGCHANG, Modification of Bismaleimide With Allyl Compound and N-Phenylmaleimide, *J. Appl. Polym. Sci.*, 2001, vol. 80, pp. 2518–2522.
- [25] K.-F. LIN, J.-S. LIN, and C.-H. CHENG, High temperature resins based on allylamine/bismaleimides, *Polymer*, 1996, vol. 37, pp. 4729–4737.
- [26] K.-F. LIN, J.-S. LIN, and C.-H. CHENG, Synthesis, Curing, and Decomposition of Allylamine- Adducted 3,3'-Bismaleimidodiphenylsulphone Resins, *J. Polym. Sci., Part A: Polym. Chem.*, 1997, vol. 35, pp. 2469–3478.
- [27] J. HAO, L. JIANG, and X. CAI, Investigation on bismaleimide bearing polysiloxane (BPS) toughening of 4,4'-bismaleimido diphenylmethane (BMI) matrix synthesis, characterization and toughness, *Polymer*, 1996, vol. 37, no. 16, pp. 3721–3727.
- [28] H. TANG, N. SONG, Z. GAO, X. CHEN, X. FAN, Q. XIANG, and Q. ZHOU, Preparation and properties of high performance bismaleimide resins based on 1,3,4-oxadiazole-containing monomers, *Eur. Polym. J.*, 2007, vol. 43, pp. 1313–1321.
- [29] M.-F. GRENIER-LOUSTALOT and L. Da CUNHA, Sterically hindered bismaleimide monomer: molten state reactivity and kinetics of polymerization, *Eur. Polym. J.*, 1998, vol. 34, no. 1, pp. 95–102.

- [30] M.-F. GRENIER-LOUSTALOT and L. Da CUNHA, Study of molten-state polymerization of bismaleimide monomers by solid-state ^{13}C n.m.r, and FTIR., *Polymer*, 1998, vol. 39, no. 10, pp. 1833–1843.
- [31] J. HOPEWELL and D. H. P. POMERY, Electron spin resonance study of the homopolymerization of aromatic bismaleimides, *Polymer*, 1998, vol. 39, no. 23, pp. 5601–5607.
- [32] M.-F. GRENIER-LOUSTALOT and L. Da CUNHA, Eutectic mixture of two bismaleimide monomers: thermal and mechanistic study in the molten state, *Polymer*, 1997, vol. 38, no. 26, pp. 6303–6315.
- [33] M.-F. GRENIER-LOUSTALOT and N. AYCAGUER, Monofunctional maleimide or acetylene terminated model compounds-I. Molten state homopolymerization reactivity and kinetics, *Eur. Polym. J.*, 1998, vol. 34, no. 11, pp. 1705–1714.
- [34] V. TRIPATHI, D. LAL, S. AGGARWAL, and A. SEN, Kinetic Studies on Bismaleimide Polymerization Using Inverse Gas Chromatography, *J. Appl. Polym. Sci.*, 1997, vol. 66, pp. 1613–1619.
- [35] Z. SHEN and J. SCHLUP, Mid- and Near-Infrared Spectroscopic Investigations of N-Phenylmaleimide (NPM)/Amine Reactions, *J. Appl. Polym. Sci.*, 1998, vol. 67, pp. 267–276.
- [36] M.-F. GRENIER-LOUSTALOT and L. Da CUNHA, Influence of steric hindrance on the reactivity and kinetics of molten-state radical polymerization of binary bismaleimide-diamine systems, *Polymer*, 1998, vol. 39, no. 10, pp. 1799–1814.
- [37] F. BOEY, X. SONG, C. YUE, and Q. ZHAO, Modeling the Curing Kinetics for a Modified Bismaleimide Resin, *J. Polym. Sci., Part A: Polym. Chem.*, 2000, vol. 38, pp. 907–913.
- [38] W. WU, D. WANG, and C. YE, Preparation and Characterization of Bismaleimide-Diamine Prepolymers and Their Thermal-Curing Behavior, *J. Appl. Polym. Sci.*, 1998, vol. 70, pp. 2471–2477.
- [39] S. ZAHIR, M. CHAUDHARI, and J. KING, Novel high temperature resins based on bis(4-maleimido-phenyl)methane, *Makromol. Chem. Macromol. Symp.*, 1989, vol. 25, pp. 141–154.
- [40] D. REYX, I. CAMPISTRON, C. CAILLAUD, M. VILLATE, and A. CAVEDON, Thermal reaction between N-phenylmaleimide and 2-allylphenol as a model for the crosslinking reaction in bismaleimide polymerization with diallylbisphenol A, *Macromol. Chem. Phys.*, 1995, vol. 196, pp. 775–789.
- [41] J. MIJOVIĆ and S. ANDJELIĆ, Study of the Mechanism and Rate of Bismaleimide Cure by Remote in-Situ Real Time Fiber Optic Near-Infrared Spectroscopy, *Macromolecules*, 1996, vol. 29, pp. 239–246.
- [42] I. CUNNINGHAM, A. BROWNHILL, I. HAMERTON, and B. HOWLING, The Ene Reaction between Maleimides and Allyl-substituted Aromatics, *Tetrahedron*, 1997, vol. 53, pp. 13 473–13 494.

- [43] R. MORGAN, E. SHIN, B. ROZENBERG, and A. JUREK, Characterization of the cure reactions of bismaleimide composite matrices, *Polymer*, 1997, vol. 38, no. 3, pp. 639–646.
- [44] J. PHELAN and C. SUNG, Fluorescence Characteristics of Cure Products in Bis(maleimide)/Diallylbisphenol A Resin, *Macromolecules*, 1997, vol. 30, pp. 6837–6844.
- [45] J. PHELAN and C. SUNG, Cure Characterization in Bis(maleimide)/Diallylbisphenol A Resin by Fluorescence, FT-IR, and UV-Reflection Spectroscopy, *Macromolecules*, 1997, vol. 30, pp. 6845–6851.
- [46] A. TENTERIS-NOEBE, Structure-property relationships of bismaleimides, Ph.D. thesis, University of Akron, 1997.
- [47] B. ROZENBERG, E. DZHAVADYAN, R. MORGAN, and E. SHIN, The Polyaddition, Chain, and Polycondensation Mechanisms of Formation of Networks Based on Bismaleimides, *Macromol. Symp.*, 2001, vol. 171, pp. 87–96.
- [48] Б.А. РОЗЕНБЕРГ, З.А. ДЖАВАДЯН, R. MORGAN, and E. SHIN, Калориметрическое исследование системы 4,4'-(N,N'-бисмалеимид)дифенилметан-2,2'-диаллилбисфенол А, Высокомолекулярные соединения, 2001, vol. 43, no. 4, pp. 630–645.
- [49] Б.А. РОЗЕНБЕРГ, Г.Н. БОЙКО, R. MORGAN, and E. SHIN, Механизм отверждения системы 4,4'-(N,N'-бисмалеимид)дифенилметан-2,2'-диаллилбисфенол А, Высокомолекулярные соединения, 2001, vol. 43, no. 4, pp. 646–654.
- [50] C. GOURI, C. REGHUNADHAN NAIR, and R. RAMASWAMY, Reactive Alderene blend of diallyl bisphenol A novolac and bisphenol A bismaleimide: synthesis, cure and adhesion studies, *Polym. Int.*, 2001, vol. 50, pp. 403–413.
- [51] B. ROZENBERG, E. DZHAVADYAN, R. MORGAN, and E. SHIN, High-performance Bismaleimides matrices: Cure kinetics and mechanism, *Polym. Adv. Technol.*, 2002, vol. 13, pp. 837–844.
- [52] I. SALIN and J. SEFERIS, Mass Transfer Effects in Degradation of Bismaleimide Matrix Composite, *J. Appl. Polym. Sci.*, 1996, vol. 62, pp. 1023–1027.
- [53] J.-F. GERARD, J. GALY, J.-P. PASCAULT, S. CUKIERMAN, and J.-L. HALARY, Viscoelastic Response of Model Epoxy Networks in the Glass Transition Region, *Polym. Eng. Sci.*, 1991, vol. 31, pp. 615–621.
- [54] A. RENNER, I. FORGO, W. HOFMANN, and K. RAMSTEINER, Über die Reaktion von Phenolen mit N-substituierten Maleimidien, *Helv. Chim. Acta*, 1978, vol. 61, pp. 1443–1453.
- [55] Z. YERLIKAYA, Z. ÖKTEM, and E. BAYRAMLI, Chain-Extended Bismaleimides. I. Preparation and Characterization of Maleimide-Terminated Resins, *J. Appl. Polym. Sci.*, 1996, vol. 59, pp. 165–171.
- [56] M. SAVA, Bismaleimide Monomers with Amide Units: Synthesis and Properties, *J. Appl. Polym. Sci.*, 2006, vol. 101, pp. 567–572.

- [57] S. HAN, S. IM, J. WON, J. LEE, K.-Y. CHOI, and Y. KIM, Synthesis and characterization of new polyimides containing ethynylene linkages, *Eur. Polym. J.*, 2007, vol. 43, pp. 1541–1548.
- [58] F. YILMAZ, L. CIANGA, Y. GUNER, L. TOPPARE, and Y. YAGCI, Synthesis and characterization of alternating copolymers of thiophene-containing N-phenyl maleimide and styrene by photoinduced radical polymerization and their use in electropolymerization, *Polymer*, 2004, vol. 45, pp. 5765–5774.
- [59] P. FLORY, Molecular Size Distribution in Three Dimensional Polymers. I. Gelation, *J. Am. Chem. Soc.*, 1941, vol. 11, pp. 3083–3090.
- [60] W. STOCKMAYER, Theory of Molecular Size Distribution and Gel Formation in Branched Polymers II. General Cross Linking, *J. Chem. Phys.*, 1944, vol. 12, pp. 125–131.
- [61] C. MACOSKO and D. MILLER, A new derivation of average molecular weight of nonlinear polymers, *Macromolecules*, 1976, vol. 19, pp. 199–206.
- [62] H. WINTER, Can the gel point of cross-linking polymer be detected by the $G' - G''$ crossover?, *Polym. Eng. Sci.*, 1987, vol. 27, no. 22, pp. 1698–1702.
- [63] H. WINTER and F. CHAMBON, Analysis of linear viscoelastic of a crosslinking polymer at the gel point, *J. Rheol.*, 1986, vol. 30, pp. 367–382.
- [64] C. HSU and L. LEE, Structure formation during the copolymerization of styrene and unsaturated polyester resin, *Polymer*, 1991, vol. 32, pp. 2263–2271.
- [65] C. HSU and L. LEE, Free-radical crosslinking copolymerization of styrene/unsaturated polyester resins: 1. Phase separation and microgel formation, *Polymer*, 1993, vol. 34, pp. 4496–4505.
- [66] C. HSU and L. LEE, Free-radical crosslinking copolymerization of styrene/unsaturated polyester resins: 2. Electron spin resonance study, *Polymer*, 1993, vol. 34, pp. 4506–4515.
- [67] C. HSU and L. LEE, Free-radical crosslinking copolymerization of styrene/unsaturated polyester resins: 3. Kinetics-gelation mechanism, *Polymer*, 1993, vol. 34, pp. 4516–4523.
- [68] J. GILLHAM, Developments in Polymer Characterisation. Applied Science Publishers, 1982, vol. 3, ch. 5, pp. 159–227.
- [69] G. Van ASSCHE, A. Van HEMELRIJCK, H. RAHIER, and B. Van MELE, Modulated differential scanning calorimetry: isothermal cure and vitrification of thermosetting systems, *Thermochim. Acta*, 1995, vol. 268, pp. 121–142.
- [70] G. Van ASSCHE, A. Van HEMELRIJCK, H. RAHIER, and B. Van MELE, Modulated temperature differential scanning calorimetry: Cure, vitrification, and de-vitrification of thermosetting systems, *Thermochim. Acta*, 1997, vol. 304/305, pp. 317–334.

- [71] G. Van ASSCHE, E. VERDONCK, and B. Van MELE, Interrelations between mechanism, kinetics, and rheology in an isothermal cross-linking chain-growth copolymerisation, *Polymer*, 2001, vol. 42, pp. 2959–2968.
- [72] J. SCHAWE, A comparison of different evaluation methods in modulated temperature DSC, *Thermochim. Acta*, 1995, vol. 260, pp. 1–16.
- [73] K. DUŠEK, Are cured thermoset resins inhomogeneous?, *Angew. Makromol. Chem.*, 1996, vol. 240, pp. 1–15.
- [74] R. BANSIL, H. HERRMANN, and D. STAUFFER, Computer Simulation of Kinetics of Gelation by Addition Polymerization in a Solvent, *Macromolecules*, 1984, vol. 17, pp. 998–1004.
- [75] R. BANSIL, H. HERRMANN, and D. STAUFFER, Kinetic percolation with mobile monomers and ssolvent as a model for gelation, *Journal of Polymer Science: Polymer Symposium*, 1985, vol. 73, pp. 175–180.
- [76] K. DUŠEK, L. MATĚJKA, P. ŠPACĚK, and H. WINTER, Network formation in the free-radical copolymerization of a bismaleimide and styrene, *Polymer*, 1996, vol. 37, no. 11, pp. 2233–2242.
- [77] J. HODGKIN, G. SIMON, and R. VARLEY, Thermoplastic Toughening of Epoxy Resins: a Critical Review, *Polym. Adv. Technol.*, 1998, vol. 9, pp. 3–10.
- [78] B. HAYES and J. SEFEREIS, Modification of Thermosetting Resins and Composites Through Preformed Polymer Particles: A Review, *Polym. Compos.*, 2001, vol. 22, no. 4, pp. 451–467.
- [79] M. HUGGINS, Theory solutions of high polymers, *J. Am. Chem. Soc.*, 1942, vol. 64, pp. 1712–1719.
- [80] J. HILDEBRAND and R. SCOTT, The solubility of Non-Electrolytes. Reinhold, 1949.
- [81] P. SMALL, Some factors affecting the solubility of polymers, *J. Appl. Chem.*, 1953, vol. 3, pp. 71–80.
- [82] K. HOY, New values of the solubility parameters from vapor pressure data, *J. Paint Technol.*, 1970, vol. 42, pp. 76–118.
- [83] P. van KREVELEN, Properties of Polymers. Elsevier, 1972, ch. IV, p. 135.
- [84] M. COLEMAN, C. SERMAN, D. BHAGWAGAR, and P. PAINTER, A practical guide to polymer miscibility, *Polymer*, 1990, vol. 31, pp. 1187–1203.
- [85] C. HANSEN, Hansen solubility parameters - second edition. Taylor and Francis, 2007.
- [86] S. KRAUSE, Polymer Compatibility, *J. Macromol. Sci., Part C: Polym. Rev.*, 1972, vol. 7, pp. 251–314.

- [87] W. SCHROEDER, M. ARANGUREN, G. E. ABE, and J. BORRAJO, Free-radical Polymerization induced macrophase separation in poly(methyl methacrylate)/dimethacrylate blends: Experiment and modeling, *Eur. Polym. J.*, 2013, vol. 49, pp. 3956–3965.
- [88] P. FLORY and J. REHNER, Statistical theory of chain configuration and physical properties of high polymers, *J. Chem. Phys.*, 1943, vol. 11, pp. 521–526.
- [89] K. DUŠEK and M. DUŠKOVÁ-SMRČKOVÁ, Network structure formation during crosslinking of organic coating systems, *Prog. Polym. Sci.*, 2000, vol. 25, pp. 1215–1260.
- [90] M. ABBATE, E. MARTUSCELLI, P. MUSTO, and G. RAGOSTA, Toughened thermosetting bismaleimides: Molecular structure, morphology and mechanical properties, *Angew. Makromol. Chem.*, 1997, vol. 246, no. 4274, pp. 23–48.
- [91] K. CHIAN, X. DU, H. GOY, J. FENG, S. YI, and C. YUE, Mechanical Properties and Morphology of Poly(ethylene glycol)-Side-Chain-Modified Bismaleimide Polymer, *J. Appl. Polym. Sci.*, 2002, vol. 86, pp. 715–724.
- [92] V. ALTSTÄDT, Effect of the polymer matrix on the properties of advanced composites, *Makromol. Chem. Macromol. Symp.*, 1991, vol. 50, pp. 137–145.
- [93] V. ALTSTÄDT, D. GERTH, M. STÄNGLE, and H. RECKER, Interlaminar crack growth in third-generation thermoset prepreg systems, *Polymer*, 1993, vol. 34, no. 4, pp. 907–909.
- [94] X. LIU, Y. YU, and S. LI, Viscoelastic phase separation in polyethersulfone modified bismaleimide resin, *Eur. Polym. J.*, 2006, vol. 42, pp. 835–842.
- [95] X. LIU, G. ZHAN, Z. HAN, S. LI, and Y. YU, Phase Morphology and Mechanical Properties of a Poly(ether sulfone)-Modified Bismaleimide Resin, *J. Appl. Polym. Sci.*, 2007, vol. 106, pp. 77–83.
- [96] J. KURDI and A. KUMAR, Synthesis and Characterization of Modified Bismaleimide/Polysulfone Semi-Interpenetrating Polymer Networks, *J. Appl. Polym. Sci.*, 2006, vol. 102, pp. 369–379.
- [97] J. JIN, J. CUI, X. TANG, Y. DING, S. LI, J. WANG, Q. ZHAO, X. HUA, and X. CAI, On polyetherimide modified bismaleimide resins, I. Effect of the chemical backbone of polyetherimide, *Macromol. Chem. Phys.*, 1999, vol. 200, pp. 1956–1960.
- [98] J. JIN, J. CUI, X. TANG, S. LI, J. WANG, Q. ZHAO, X. HUA, and X. CAI, Polyetherimide-Modified Bismaleimide Resins. II. Effect of Polyetherimide Content, *J. Appl. Polym. Sci.*, 2001, vol. 81, pp. 350–358.
- [99] T. IIJIMA, H. SHIONO, W. FUKUDA, and M. TOMOI, Toughening of Bismaleimide Resin by Modification with Poly(ethylene phthalate) and Poly(ethylene phthalate-co-ethylene isophthalate), *J. Appl. Polym. Sci.*, 1997, vol. 65, pp. 1349–1357.
- [100] T. IIJIMA, N. YUASA, and M. TOMOI, Modification of Three-Component Bismaleimide Resin by Poly(phthaloyl diphenyl ether) and Related Copolymers, *J. Appl. Polym. Sci.*, 2001, vol. 82, pp. 2991–3000.

- [101] T. IIJIMA, N. HAYASHI, T. OYAMA, and M. TOMOI, Modification of bismaleimide resin by soluble poly(ester imide) containing trimellitimide moieties, *Polym. Int.*, 2004, vol. 53, pp. 1417–1425.
- [102] A. GOPALA, H. WU, J. XU, and P. HEIDEN, Investigation of Readily Processable Thermoplastic-Toughened Thermosets: IV. BMIs Toughened with Hyperbranched Polyester, *J. Appl. Polym. Sci.*, 1999, vol. 71, pp. 1909–1817.
- [103] J. XU, H. WU, O. MILLS, and P. HEIDEN, A Morphological Investigation of Thermosets Toughened with Novel Thermoplastics. I. Bismaleimide Modified with Hyperbranched Polyester, *J. Appl. Polym. Sci.*, 1999, vol. 72, pp. 1065–1076.
- [104] T. PASCAL, R. MERCIER, and B. SILLION, New semi-interpenetrating polymeric networks from linear polyimides and thermosetting bismaleimides. 1: Synthesis and characterization of starting components, *Polymer*, 1989, vol. 30, pp. 739–744.
- [105] T. PASCAL, R. MERCIER, and B. SILLION, New semi-interpenetrating polymeric networks from linear polyimides and thermosetting bismaleimides: 2. Mechanical and thermal properties of the blends, *Polymer*, 1990, vol. 31, pp. 78–83.
- [106] H. QIN, P. MATHER, J.-B. BAEK, and L.-S. TAN, Modification of bisphenol-A based bismaleimide resin (BPA-BMI) with an allyl-terminated hyperbranched polyimide (AT-PAEKI), *Polymer*, 2006, vol. 47, pp. 2813–2821.
- [107] A. GOPALA, H. WU, F. HARRIS, and HEIDEN, Investigation of Readily Processable Thermoplastic-Toughened Thermosets. I. BMIs Toughened via a Reactive Solvent Approach, *J. Appl. Polym. Sci.*, 1998, vol. 69, pp. 469–477.
- [108] A. GOPALA, H. WU, and P. HEIDEN, Investigation of Readily Processable Thermoplastic-Toughened Thermosets. III. Toughening BMIs and Epoxy with a Comb-Shaped Imide Oligomer, *J. Appl. Polym. Sci.*, 1998, vol. 70, pp. 943–951.
- [109] T. IIJIMA, T. NISHINA, W. FUKUDA, and M. TOMOI, Modification of Bismaleimide Resin by Poly(phthaloyldiphenyl ether) and the Related Copolymers, *J. Appl. Polym. Sci.*, 1998, vol. 67, pp. 769–780.
- [110] T. IIJIMA, H. ONA, and M. TOMOI, Modification of Bismaleimide Resin by Poly(ethylene phthalate-co-ethylene terephthalate), Poly(ethylene phthalate-co-ethylene 4,4'-biphenyl dicarboxylate), and Poly(ethylene phthalate-co-ethylene 2,6-naphthalene dicarboxylate), *J. Appl. Polym. Sci.*, 2001, vol. 81, pp. 2352–2367.
- [111] Y. HAN, G. LIAO, Y. XU, G. YU, and X. JIAN, Cure Kinetics, Phase Behaviors, and Fracture Properties of Bismaleimide Resin Toughened by Poly(phthalazinone ether ketone), *Polym. Eng. Sci.*, 2009, vol. 49, pp. 2301–2308.
- [112] K. MAI, J. HUANG, and H. ZENG, Studies of the Stability of Thermoplastic-Modified Bismaleimide Resin, *J. Appl. Polym. Sci.*, 1997, vol. 66, pp. 1965–1970.
- [113] B. ZHANG, P. LI, and X. CHEN, Studies of modified bismaleimide resins Part I The influence of resin composition on thermal and impact properties, *J. Mater. Sci.*, 1998, vol. 33, pp. 5683–5687.

- [114] F. DING, Q. CHEN, S. LAI, and X. LIU, Bismaleimide (BMI) Resin Modified by PEEK Bearing Pendant Reactive Propenyl Groups, Advanced Materials Research, 2011, vol. 197-198, pp. 1299–1305.
- [115] T. IIJIMA, T. NISHINA, W. FUKUDA, and M. TOMOI, Effect of Matrix Compositions on Modification of Bismaleimide Resin by N-Phenylmaleimide-Styrene Copolymers, *J. Appl. Polym. Sci.*, 1996, vol. 60, pp. 37–45.
- [116] T. IIJIMA, K. OHNISHI, W. FUKUDA, and M. TOMOI, Modification of Bismaleimide Resin with N-Phenylmaleimide-Styrene-p-Hydroxystyrene and N-Phenylmaleimide-Styrene-p-Allyloxystyrene Terpolymers, *J. Appl. Polym. Sci.*, 1997, vol. 65, pp. 1451–1461.
- [117] W. COX and E. MERZ, Correlation of dynamic and steady flow viscosities, *Journal of Polymer Science*, 1958, vol. 28, pp. 619–622.
- [118] E. DIMARZIO and J. GIBBS, Molecular interpretation of glass temperature depression by plasticizers, *J. Polym. Sci., Part A: Polym. Chem.*, 1963, vol. 1, pp. 1417–1428.
- [119] K. PAE, C. TANG, and K. VIJAYAN, Effect of simple stress on the glass transition of polymers at high pressures, *J. Mater. Sci.*, 1986, vol. 21, pp. 2901–2907.
- [120] C. INGLIS, Stress in a plate due to the presence of crack and sharp corners, *Trans. Int. Nav. Archit.*, 1913, vol. 55, pp. 219–230.
- [121] G. IRWIN, Analysis of stress and strains near the end of a crack traversing in a plate, *J. Appl. Mech.*, 1957, vol. 24, pp. 361–364.
- [122] A. GRIFFITH, Phenomena of rupture and flow in solids, *Philos. Trans. R. Soc.*, 1920, vol. A221, pp. 163–198.
- [123] G. BARENBLATT, The mathematical theory of equilibrium crack in brittle fracture, *Adv. Appl. Mech.*, 1962, vol. 7, pp. 55–129.
- [124] D. MAUGIS and M. BARQUINS, Fracture mechanics and the adherence of viscoelastic bodies, *J. Phys. D: Appl. Phys.*, 1978, vol. 11, pp. 1989–2024.
- [125] M. CICCOTTI, B. GIORGINI, D. VALLET, and M. BARQUINS, Complex dynamics in the peeling of an adhesive tape, *Int. J. Adhes.*, 2004, vol. 24, pp. 143–151.
- [126] W. BRADLEY, W. CANTWELL, and H. KAUSCH, Viscoelastic creep crack growth: a review of fracture mechanical analyses, *Mechanics of Time-Dependent Materials*, 1998, vol. 1, pp. 241–268.
- [127] D. DUGDALE, Yielding of steel sheets containing slits, *Journal of the Mechanics and Physics of Solids*, 1960, vol. 8, pp. 100–104.
- [128] M. WILLIAMS, On the Stress Distribution at the Base of a Stationary Crack, *J. Appl. Mech.*, 1957, vol. 14, pp. 109–114.
- [129] C. LANDIS, T. PARDOEN, and J. HUTCHINSON, Crack velocity dependent toughness in rate dependent materials, *Mechanics of Materials*, 2000, vol. 32, pp. 663–678.

- [130] R. von MISES, Mechanik der festen Körper im plastisch deformablen Zustand, Nachr. Königl. Ges. Wis. Göttingen, Math.-Phys. K., 1913, vol. 4, pp. 582–592.
- [131] R. SCHAPERY, A theory of crack initiation and growth in viscoelastic media: I. Theoretical development, Int. J. Fract., 1975, vol. 11, pp. 141–159.
- [132] R. SCHAPERY, A theory of crack initiation and growth in viscoelastic media: II. Approximate methods of analysis, Int. J. Fract., 1975, vol. 11, pp. 369–388.
- [133] G. MARSHALL and J. WILLIAMS, The correlation of fracture data for PMMA, J. Mater. Sci., 1973, vol. 8, pp. 138–140.
- [134] R. GLEDHILL and A. KINLOCH, Failure criterion for the fracture of structural adhesive joints, Polymer, 1976, vol. 17, pp. 727–731.
- [135] R. GLEDHILL and A. KINLOCH, Relationship between mechanical properties of and crack propagation in epoxy resin adhesives, Polymer, 1978, vol. 19, pp. 574–582.
- [136] A. KINLOCH and J. WILLIAMS, Crack blunting properties in polymers, J. Mater. Sci., 1980, vol. 15, pp. 987–996.
- [137] AEROSPATIALE Std., Résines thermodurcissables essai de traction. IGC04.26.253, 1992.
- [138] A. CASTELLANOS-GOMEZ, M. POOT, G. STEELE, H. van der ZANT, N. AGRAÏT, and G. RUBIO-BOLLINGER, Elastic properties of freely suspended MoS₂ nanosheets, Advanced Materials, 2012, vol. 24, pp. 772–775.
- [139] AEROSPATIALE Std., Résines thermodurcissables essai de ténacité. IGC04.26.680, 1988.
- [140] C. JANSSEN, Specimen for fracture mechanics studies on glass, in 10th International Congress on Glass, 1974.
- [141] T. MICHALSKY, W. SMITH, and E. CHEN, Stress intensity calibration for the double cleavage drilled compression specimen, Engin. Fract. Mech., 1993, vol. 45, no. 5, pp. 637–642.
- [142] G. PALLARES, L. PONSON, A. GRIMALDI, M. GEORGE, G. PREVOT, and M. CICCOTTI, Crack opening profile in DCDC specimen, Int. J. Fract., 2009, vol. 156, pp. 11–20.
- [143] Y. NZIAKOU, AFM investigation of slow crack propagation in polymer glasses, in 17ème Forum des microscopies à sonde locale, 2014.
- [144] Y. NZIAKOU, Multiscale investigation of slow crack propagation in polymer glasses, in Matériaux 2014, 2014.
- [145] Y. NZIAKOU-DJOUGUELA, Analyse multi-échelle des mécanismes d'endommagement des matériaux composites à morphologie complexe destinés à l'aéronautique, Ph.D. thesis, Université Pierre et Marie Curie, ESPCI ParisTech, 2015.

- [146] A. MAYR, W. COOK, and G. EDWARD, Yielding behaviour in model epoxy thermosets-I. Effect of strain rate and composition, *Polymer*, 1998, vol. 39, pp. 3719–3724.
- [147] W. COOK, A. MAYR, and G. EDWARD, Yielding behaviour in model epoxy thermosets-II. Temperature dependence, *Polymer*, 1998, vol. 39, pp. 3725–3733.
- [148] O. SINDT, J. PEREZ, and J.-F. GERARD, Molecular architecture-mechanical behaviour relationships in epoxy networks, *Polymer*, 1996, vol. 37, pp. 2989–2997.
- [149] R. RAGHAVA, R. CADDELL, and G. YEH, The macroscopic yield behaviour of polymers, *J. Mater. Sci.*, 1973, vol. 8, pp. 225–232.
- [150] J. ROTTLER and M. ROBBINS, Yield conditions for deformation of amorphous polymer glasses, *Phys. Rev. E: Stat., Nonlinear, Soft Matter Phys.*, 2001, vol. 64, pp. 1–9.
- [151] R. KODY and A. LESSER, Deformation and yield of epoxy networks in constrained states of stress, *J. Mater. Sci.*, 1997, vol. 32, pp. 5637–5643.
- [152] A. LESSER and R. KODY, A Generalized Model for the Yield Behavior of Epoxy Networks in Multiaxial Stress States, *J. Polym. Sci. Part B: Polym. Phys.*, 1997, vol. 35, pp. 1611–1619.
- [153] T. REE and H. EYRING, Theory of Non-Newtonian Flow. I. Solid Plastic System, *J. Appl. Phys.*, 1955, vol. 26, pp. 793–799.
- [154] J.-L. HALARY, F. LAUPRETRE, and L. MONNERIE, *Polymer Materials: Macroscopic Properties and Molecular Interpretations*. Wiley, 2011, ch. 9, p. 175.
- [155] M. HE, M. TURNER, and A. EVANS, Analysis of the double cleavage drilled compression specimen for interface fracture energy measurements over a range of mode mixities, *Acta metall. mater.*, 1995, vol. 43, no. 9, pp. 3453–3458.
- [156] W. DÖLL, Advances in Polymer Science 53/54 (Crazing in Polymers). Springer-Verlag, 1983, ch. 3, pp. 105–168.
- [157] J. FINEBERG and M. MARDER, Instability in dynamic fracture, *Physics Reports*, 1999, vol. 313, pp. 1–108.
- [158] D. MAUGIS and M. BARQUINS, Adhesion 12. Springer, 1988, ch. 14, pp. 205–222.
- [159] M. CICCOTTI, N. NEGRI, L. SASSI, G. GONZATO, and F. MULARGIA, Elastic and fracture parameters of Etna, Stromboli, and Vulcano lava rocks, *J. Volcanol. Geotherm. Res.*, 2000, vol. 98, pp. 209–217.
- [160] B. ATKINSON and P. MEREDITH, *Fracture Mechanics of Rock*. Academic Press Inc, 1987.
- [161] S. WIEDERHORN, Influence of Water Vapor on Crack Propagation in Soda-Lime Glass, *J. Am. Ceram. Soc.*, 1967, vol. 50, pp. 407–414.
- [162] D. PHILLIPS, J. SCOTT, and M. JONES, Crack propagation in an amine-cured epoxide resin, *J. Mater. Sci.*, 1978, vol. 13, pp. 311–322.

- [163] M. CICCOTTI, Micromechanisms of fracture propagation in glassy polymers, in 16th International Conference on Deformation, Yield and Fracture of Polymers, 2015.
- [164] R. VILLEY, C. CRETON, P.-P. CORRET, B. SAINTYVES, T. JET, M.-J. DALBE, S. SANTUCCI, L. VANEL, D. YARUSSO, and M. CICCOTTI, Rate-dependent elastic hysteresis during the peeling of pressure sensitive adhesives, *Soft Matter*, 2015, vol. 11, pp. 3480–3491.
- [165] J. SCOTT and D. PHILLIPS, Carbon fibre composites with rubber toughened matrices, *J. Mater. Sci.*, 1975, vol. 10, pp. 551–562.
- [166] P. WEISS, *Toughened plastics*. Applied Science Publishers, 1978.
- [167] A. KINLOCH, S. SHAW, D. TOD, and D. HUNSTON, Deformation and fracture behaviour of a rubber-toughened epoxy: 1. Microstructure and fracture studies, *Polymer*, 1983, vol. 24, pp. 1341–1354.
- [168] C. BUCKNALL, The micromechanics of rubber toughening, *Makromol. Chem. Macromol. Symp.*, 1988, vol. 20/21, pp. 425–439.
- [169] C. BUCKNALL, Fracture resistance in rubber-toughened polymers, *Makro*, 1990, vol. 38, pp. 1–15.
- [170] C. BUCKNALL, Quantitative Approaches to Particle Cavitation, Shear Yielding, and Crazing in Rubber-Toughened Polymers, *J. Pol. Sci. B: Pol. Phys.*, 2007, vol. 45, pp. 1399–1409.
- [171] H.-J. SUE and A. YEE, Micromechanical Modeling of Crack-Tip Rubber Particle Cavitational Process in Polymer Toughening, *Polym. Eng. Sci.*, 1996, vol. 36, pp. 2320–2326.
- [172] L. BÉCU, H. SAUTEREAU, A. MAAZOUZ, J.-F. GÉRARD, M. PABON, and C. PICHEOT, Synthesis and Structure-Property Relationships of Acrylic Core-Shell Particle-toughened Epoxy Networks, *Polym. Adv. Technol.*, 1995, vol. 6, pp. 316–325.
- [173] L. BÉCU, H. SAUTEREAU, A. MAAZOUZ, and J.-F. GÉRARD, Fracture Behavior of Epoxy Polymers Modified with Core-Shell Rubber Particles, *J. Appl. Polym. Sci.*, 1997, vol. 65, pp. 2419–2431.
- [174] S. GRISHCHUK, O. GRYSHCHUK, M. WEBER, and J. KARGER-KOCSIS, Structure and Toughness of Polyethersulfone (PESU)-Modified Anhydride-Cured Tetrafunctional Epoxy Resin: Effect of PESU Molecular Mass, *J. Appl. Polym. Sci.*, 2012, vol. 123, pp. 1193–1200.
- [175] J. ZHANG, Q. GUO, and B. FOX, Structural and Material Properties of a Rapidly Cured Thermoplastic-Toughened Epoxy System, *J. Appl. Polym. Sci.*, 2009, vol. 113, pp. 485–491.
- [176] E. GIRARD-REYDET, V. VICARD, J.-P. PASCAULT, and H. SAUTEREAU, Polyetherimide-Modified Epoxy Networks: Influence of Cure Conditions on Morphology and Mechanical Properties, *J. Appl. Polym. Sci.*, 1997, vol. 65, pp. 2433–2445.

- [177] J. ZHANG, Q. GUO, and B. FOX, Study on thermoplastic-modified multifunctional epoxies: Influence of heating rate on cure behaviour and phase separation, *Compos. Sci. Technol.*, 2009, vol. 69, pp. 1172–1179.
- [178] S. KIM, J. KIM, S. LIM, W. JO, and C. CHOE, Effects of Mixing Temperatures on the Morphology and Toughness of Epoxy/Polyamide Blends, *J. Appl. Polym. Sci.*, 1999, vol. 72, pp. 1055–1063.
- [179] C. BUCKNALL and I. PARTRIDGE, Phase separation in epoxy resins containing polyethersulphone, *Polymer*, 1983, vol. 24, pp. 639–644.
- [180] K. FABER and A. EVANS, Crack deflection processes - I. Theory, *Acta Metall.*, 1983, vol. 31, pp. 565–576.
- [181] K. FABER and A. EVANS, Crack deflection processes - II. Experiment, *Acta Metall.*, 1983, vol. 31, pp. 565–576.
- [182] S. KUNZ-DOUGLASS, P. BEAUMONT, and M. ASHBY, A model for the toughness of epoxy-rubber particulate composites, *J. Mater. Sci.*, 1980, vol. 15, pp. 1109–1123.
- [183] B. CARDWELL and A. YEE, Toughening of epoxies through thermoplastic crack bridging, *J. Mater. Sci.*, 1998, vol. 33, pp. 5473–5484.
- [184] F. LANGE, The interaction of a crack front with a second-phase dispersion, *Philos. Mag.*, 1970, vol. 22, pp. 983–992.
- [185] R. RICE, Treatise on Materials Science and Technology - vol. 11: Properties and Microstructure. Academic Press Inc, 1977, ch. 4, p. 247.
- [186] A. EVANS, The strength of brittle materials containing second phase dispersions, *Philo*, 1972, vol. 26, pp. 1327–1344.
- [187] S. OGIHARA, N. TAKEDA, and A. KOBAYASHI, Experimental characterization of microscopic failre process under quasi-static tension in interleaved and toughness-improved CFRP cross-ply laminates, *Compos. Sci. Technol.*, 1997, vol. 57, pp. 267–275.
- [188] B. DERKOWSKI and H.-J. SUE, Morphology and Compression-After-Impact Strength Relationship in Interleaved Toughened Composites, *Polym. Compos.*, 2003, vol. 24, pp. 158–170.
- [189] C. QUNFENG, F.ZHENGPING, X. YAHONG, and Y. XIAO-SU, Morphological and Spatial Effects on Toughness and Impact Damage Resistance of PAEK-toughened BMI and Graphite Fiber Composite Laminates, *Chinese Journal of Aeronautics*, 2009, vol. 22, pp. 87–96.
- [190] S. KOBAYASHI and N. TAKEDA, Experimental and analytical characterization of transverse cracking behavior in carbon/bismaleimide cross-ply laminates under mechanical fatigue loading, *Composites : Part B*, 2002, vol. 33, pp. 471–478.
- [191] S. KOBAYASHI and N. TAKEDA, Experimental characterization of microscopic damage behavior in carbon/bismaleimide composite-effects of temperature and laminate configuration, *Composites: Part A*, 2002, vol. 33, pp. 1529–1538.

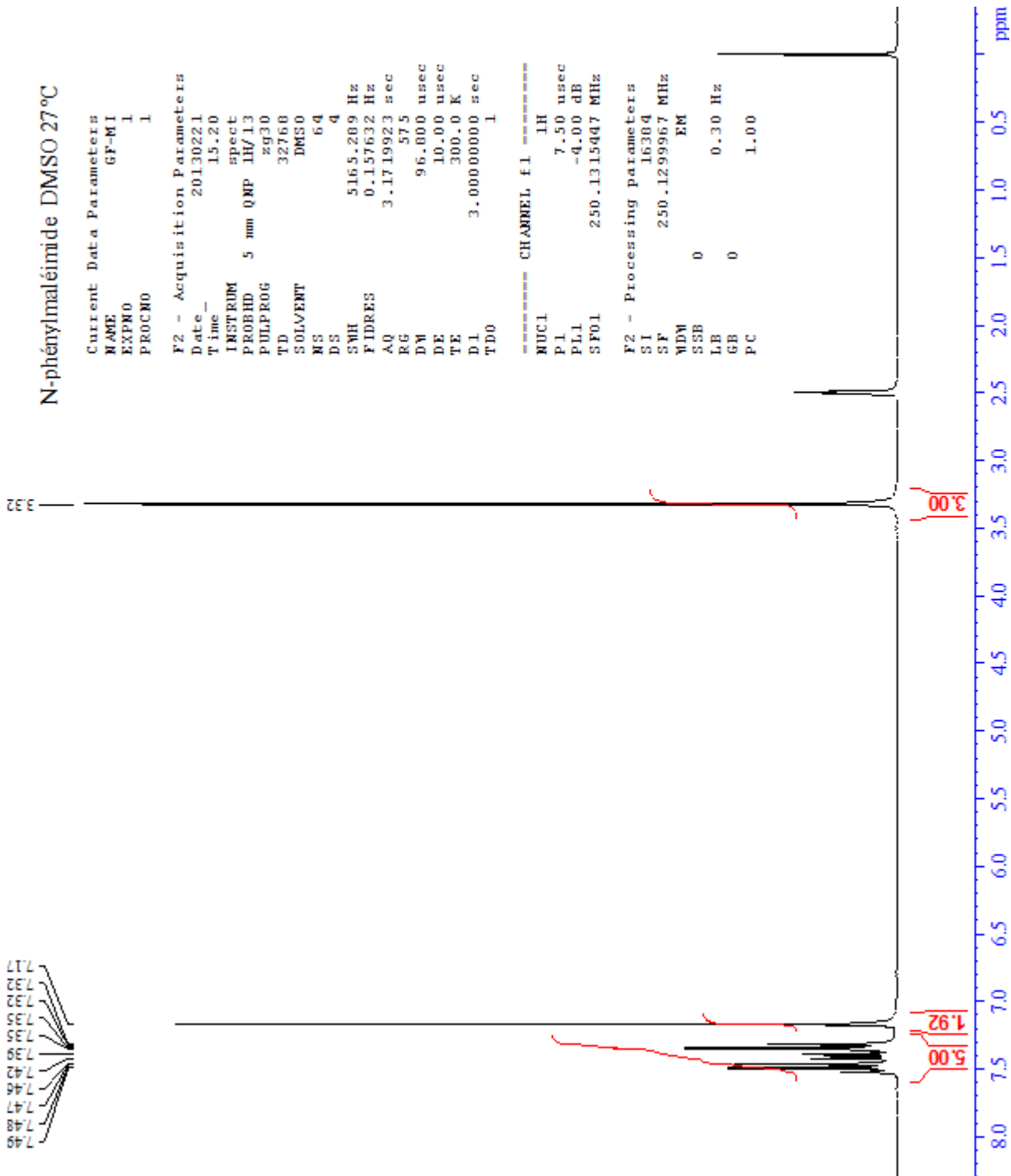
Bibliography

- [192] AIRBUS INDUSTRIE Std., Carbon fiber reinforced plastics - Determination of interlaminar fracture toughness energy. AITM1.0005, 1994.
- [193] R. VARLEY and J. HODGKIN, Effect of reinforcing fibres on the morphology of a toughened epoxy/amine system, *Polymer*, 1997, vol. 38, no. 5, pp. 1005–1009.
- [194] L. BONNAUD, J. PASCAULT, H. SAUTEREAU, J. ZHAO, and D. JIA, Effect of Reinforcing Glass Fibers on Morphology and Properties of Thermoplastic Modified Epoxy-Aromatic Diamine Matrix, *Polym. Compos.*, 2004, vol. 25, no. 4, pp. 368–374.
- [195] K. CAIN, G. GLINKA, and A. PLUMTREE, Damage evolution in an off-axis unidirectional graphite bismaleimide composite loaded in tension, *Composites: Part A*, 2003, vol. 34, pp. 987–993.
- [196] C. QUNFENG, F. ZHENGPING, Y. XIAO-SU, A. XUEFENG, T. BANGMING, and X. YAHONG, Ex-situ Concept for Toughening the RTMable BMI Matrix Composites, Part I: Improving the Interlaminar Fracture Toughness, *J. Appl. Polym. Sci.*, 2008, vol. 109, pp. 1625–1634.
- [197] D. HULL, *Fractography*. Cambridge University Press, 1999.
- [198] C. CAILLAUD, Étude de la formation du monoadduct et du diadduct du N-phénylmaléimide et de l'allylphénol, *Aerospatiale, Tech. Rep.*, 1992.
- [199] F. BOEY, Y. XIONG, and S. RATH, Glass-Transition Temperature in the Curing Process of Bismaleimide Modified with Diallylbisphenol A, *J. Appl. Polym. Sci.*, 2004, vol. 91, pp. 3244–3247.
- [200] J. MEISSONNIER and J. SEFERIS, Rheological characterization and analysis of a bismaleimide matrix, *Makromol. Chem. Macromol. Symp.*, 1989, vol. 25, pp. 125–140.
- [201] Y. LI, J. MIRANDA, and H.-J. SUE, Hygrothermal diffusion behaviour in bismaleimide resin, *Polymer*, 2001, vol. 42, pp. 7791–7799.
- [202] L.-R. BAO, A. YEE, and C.-C. LEE, Moisture absorption and hygrothermal aging in a bismaleimide resin, *Polymer*, 2001, vol. 42, pp. 7327–7333.
- [203] L.-R. BAO and A. YEE, Effect of temperature on moisture absorption in a bismaleimide resin and its carbon fiber composites, *Polymer*, 2002, vol. 43, pp. 3987–3997.
- [204] L.-R. BAO and A. YEE, Moisture diffusion and hygrothermal aging in bismaleimide matrix carbon fiber composites: part II-woven and hybrid composites, *Compos. Sci. Technol.*, 2002, vol. 62, pp. 2111–2119.
- [205] M. AKAY, G. SPRATT, and B. MEENAN, The effects of long-term exposure to high temperatures on the ILSS and impact performance of carbon fibre reinforced bismaleimide, *Compos. Sci. Technol.*, 2003, vol. 63, pp. 1053–1059.
- [206] E. DRUKKER, A. GREEN, and G. MAROM, Mechanical and chemical consequences of through thickness thermal gradients in polyimide matrix composite materials, *Composites: Part A*, 2003, vol. 34, pp. 125–133.

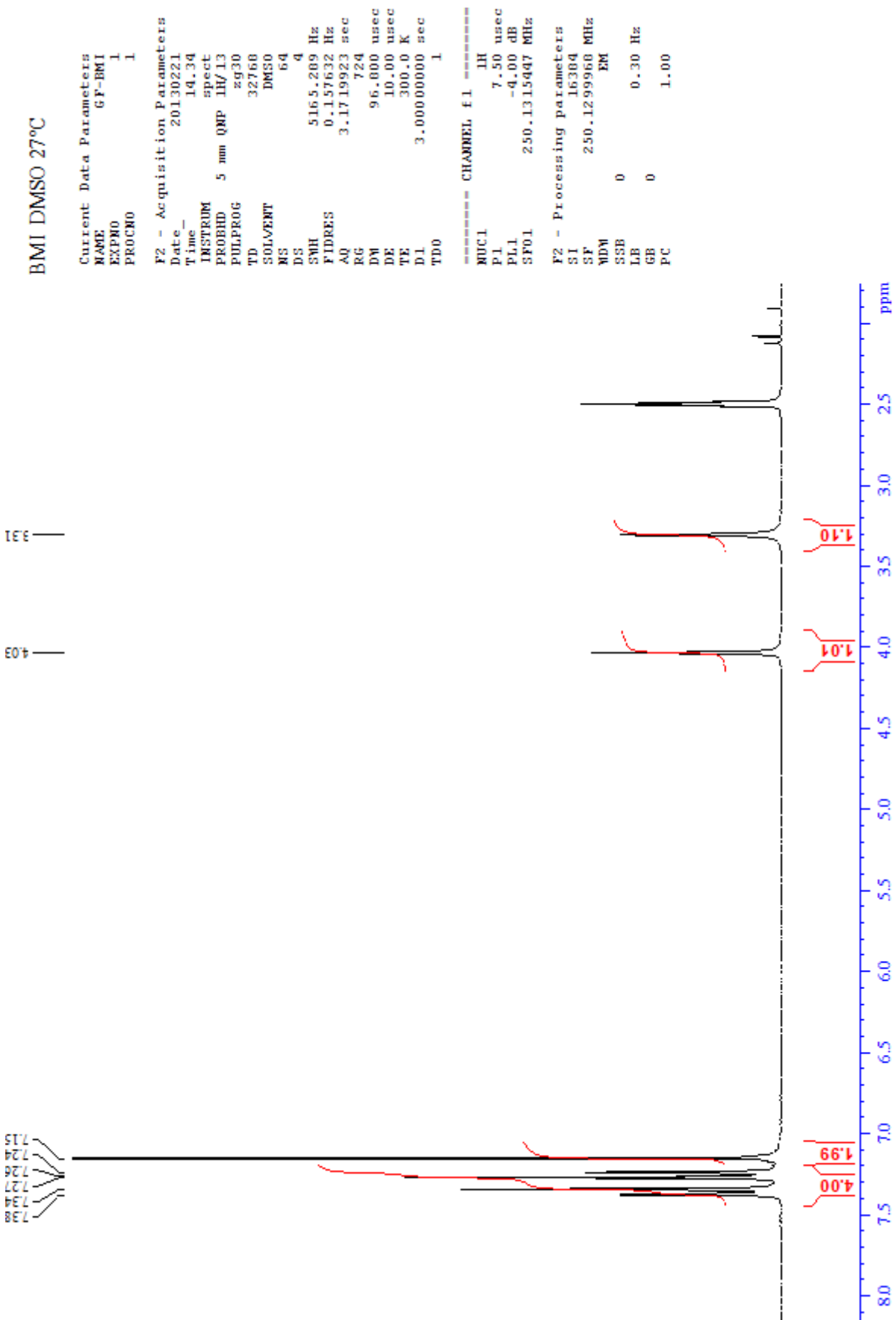
- [207] P. SUN, Y. ZHAO, Y. LUO, and L. SUN, Effect of temperature and cyclic hydrothermal aging on the interlaminar shear strength of carbon fiber/bismaleimide (BMI) composite, *Materials and Design*, 2011, vol. 32, pp. 4341–4347.

Appendix A: NMR spectra

N-phenylmaleimide (MI), DMSO-d6, 27°C.

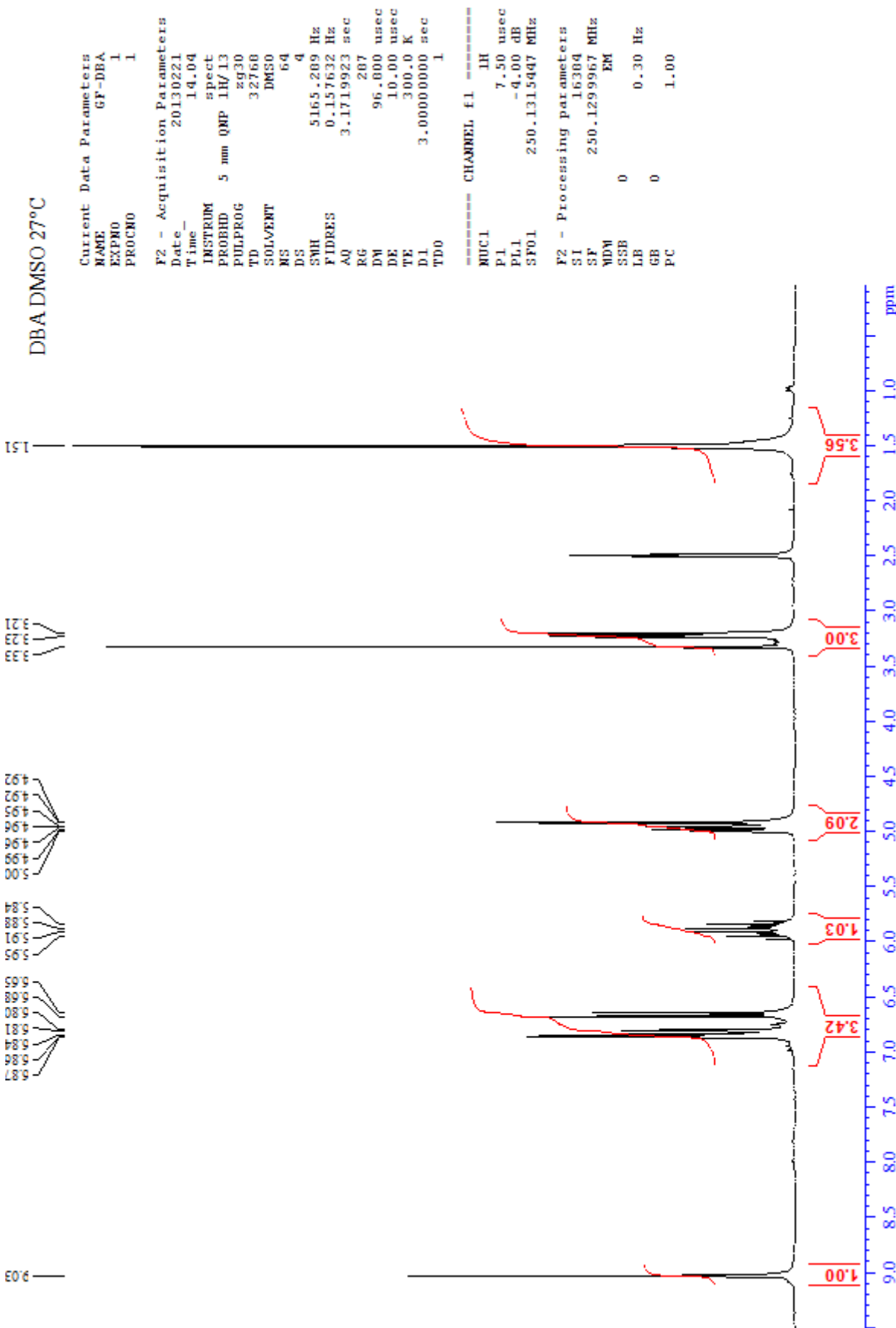


1,1'-(methyldi-4,1-phenyl)bismaleimide (BMI), DMSO-d6, 27°C.

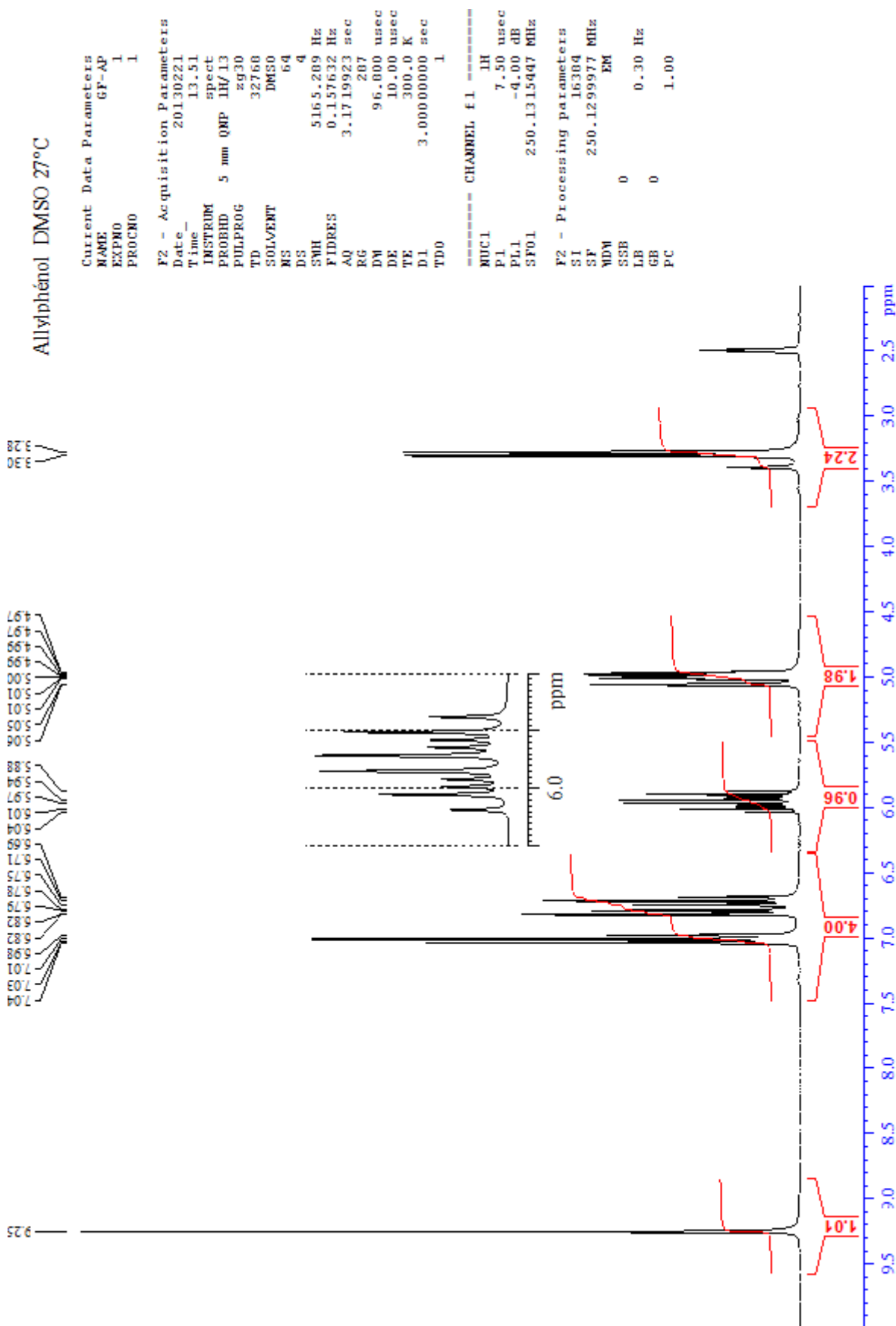


Appendix A: NMR spectra

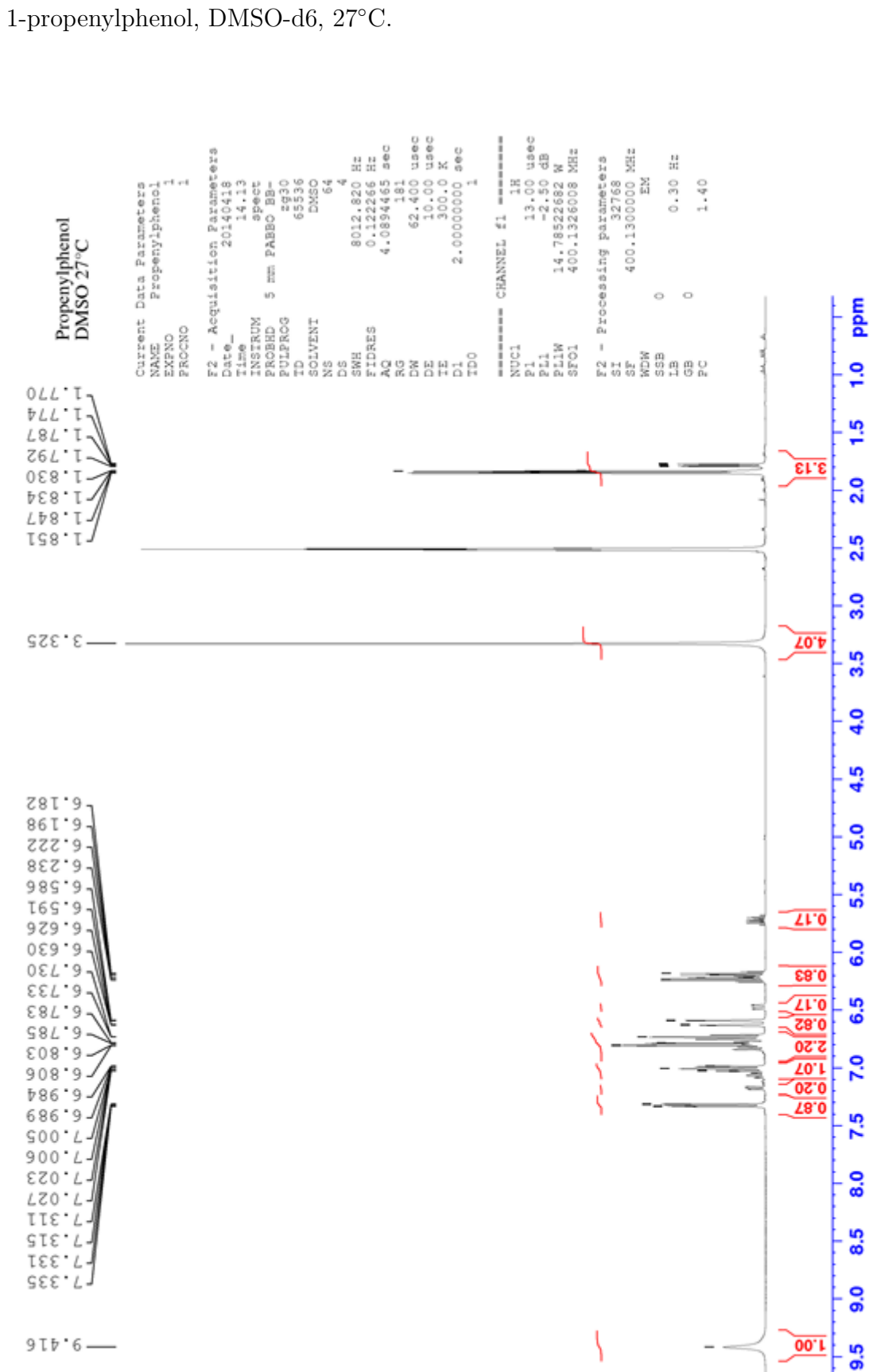
2,2'-diallylbisphenol A (DBA), DMSO-d6, 27°C.

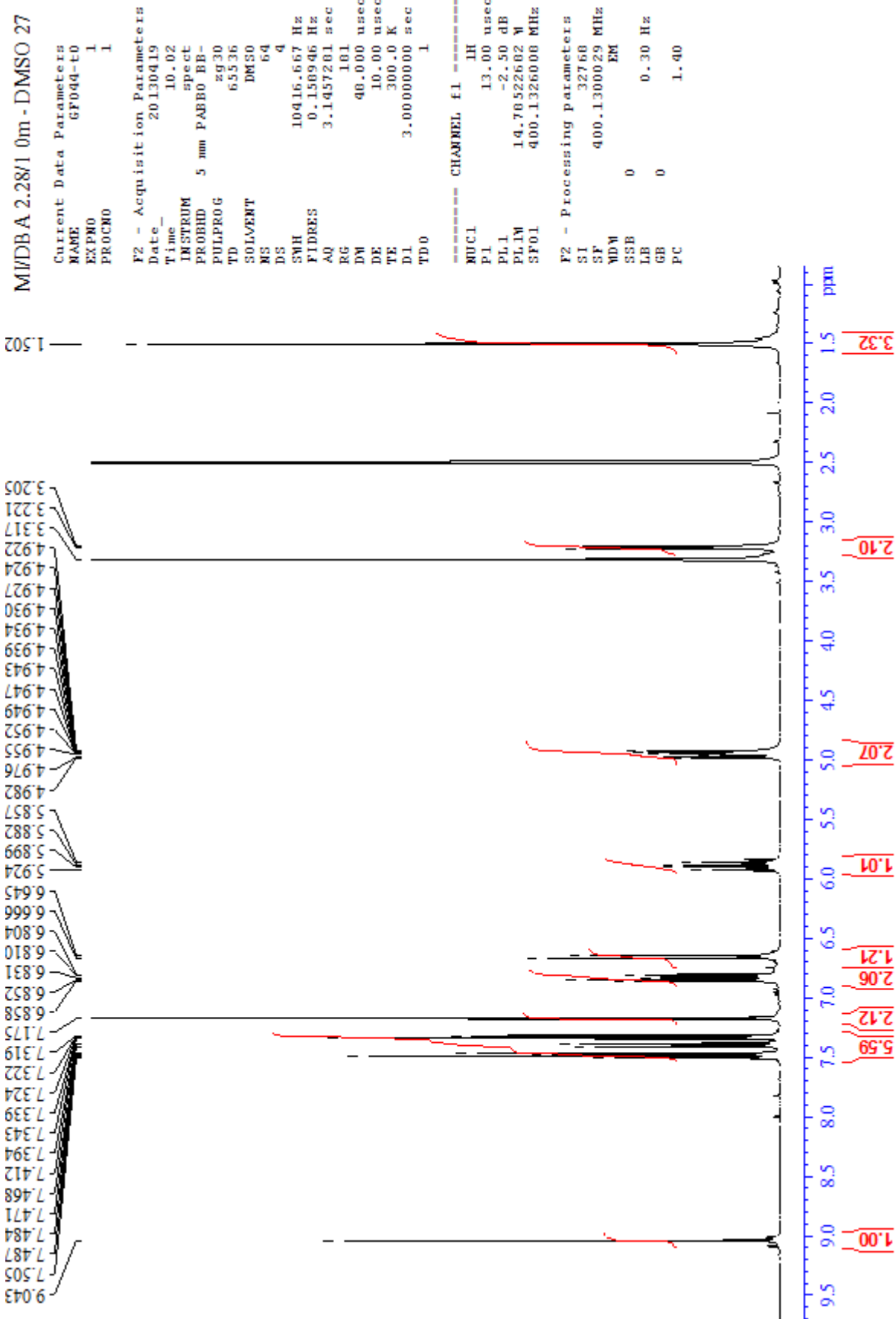


1-allylphenol (AP), DMSO-d6, 27°C.



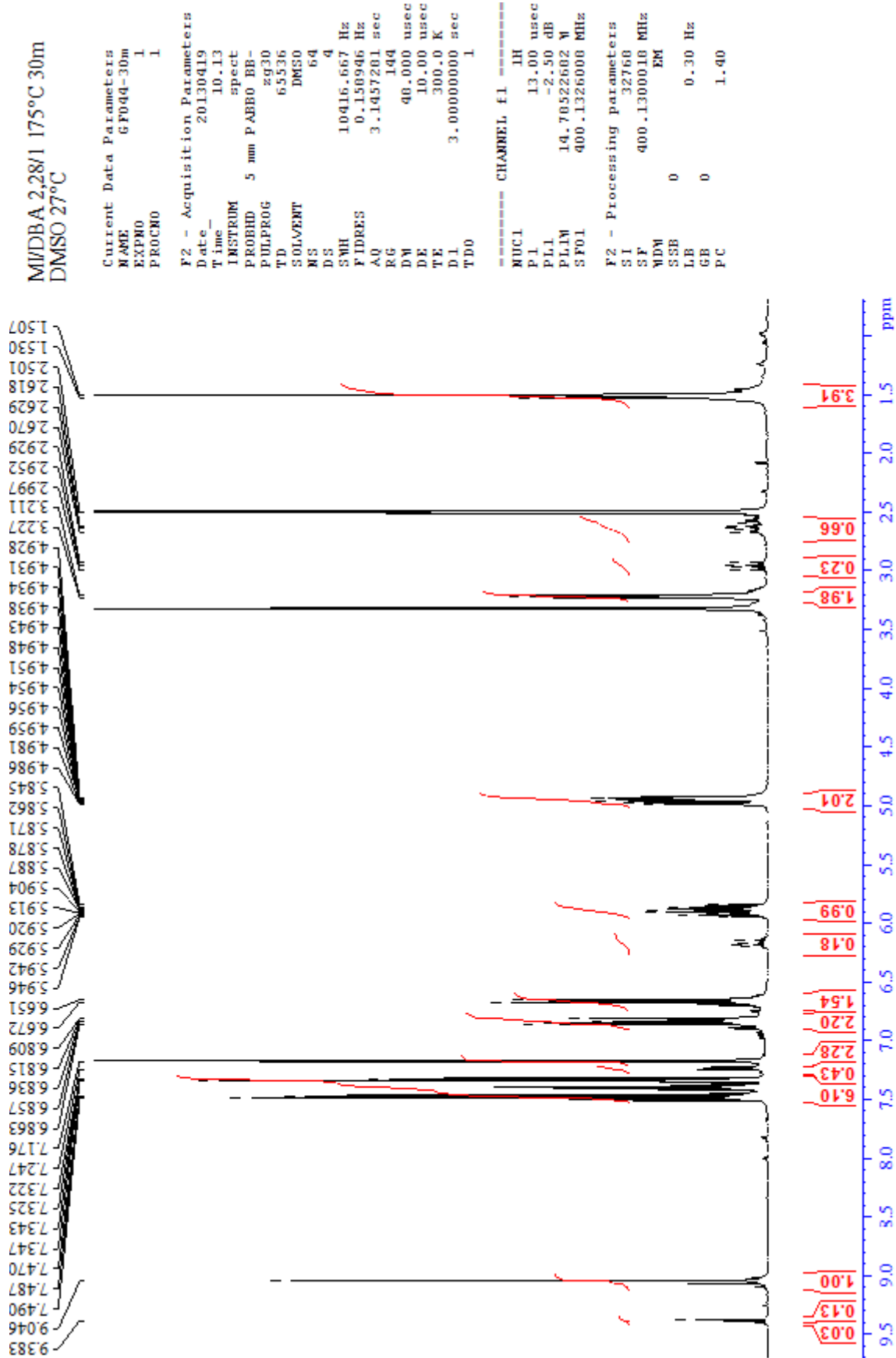
Appendix A: NMR spectra



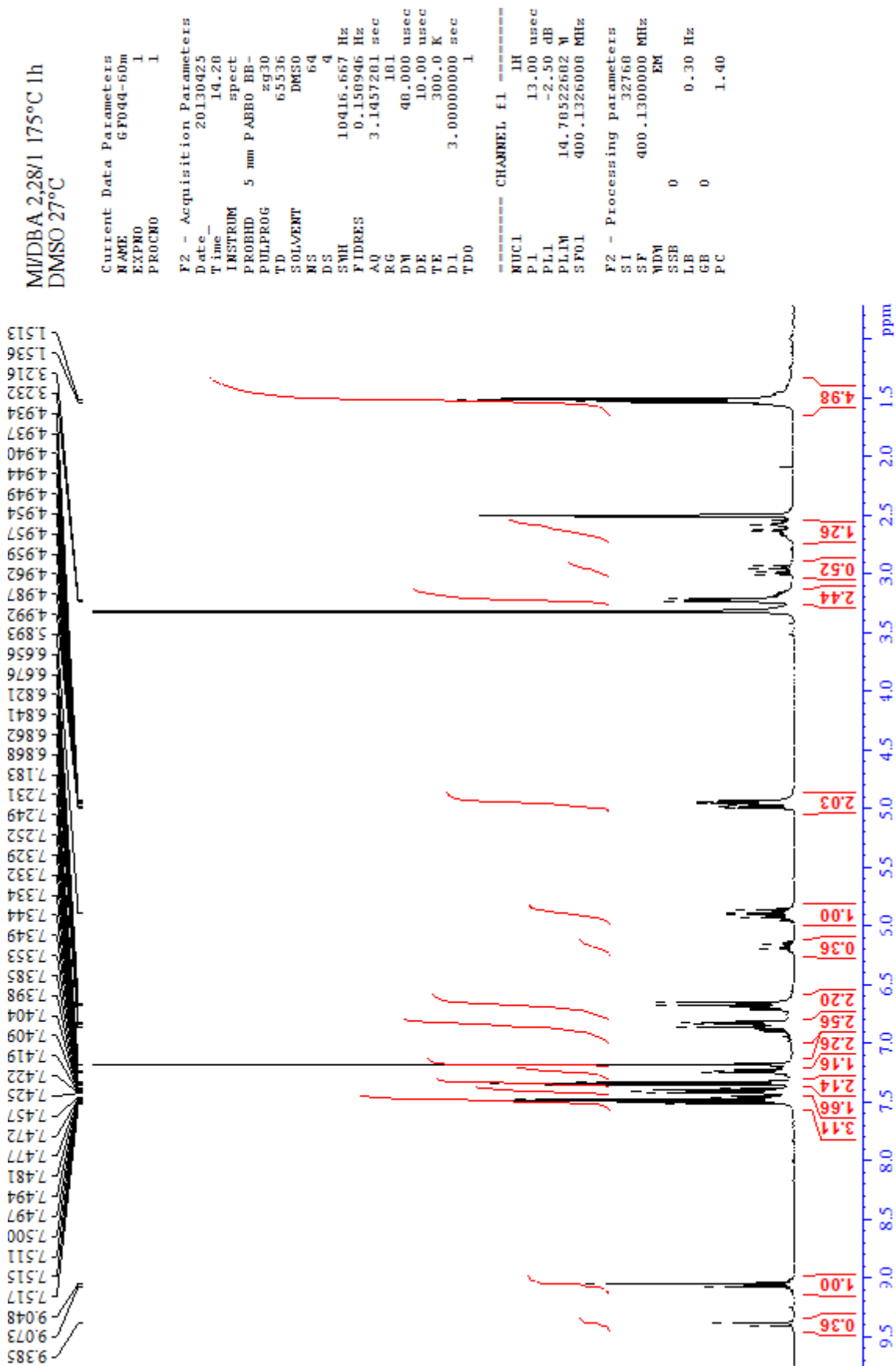
MI/DBA 2.28:1, DMSO-d₆, 27°C.

Appendix A: NMR spectra

MI/DBA 2.28:1 cured 30 min at 175°C, DMSO-d6, 27°C.

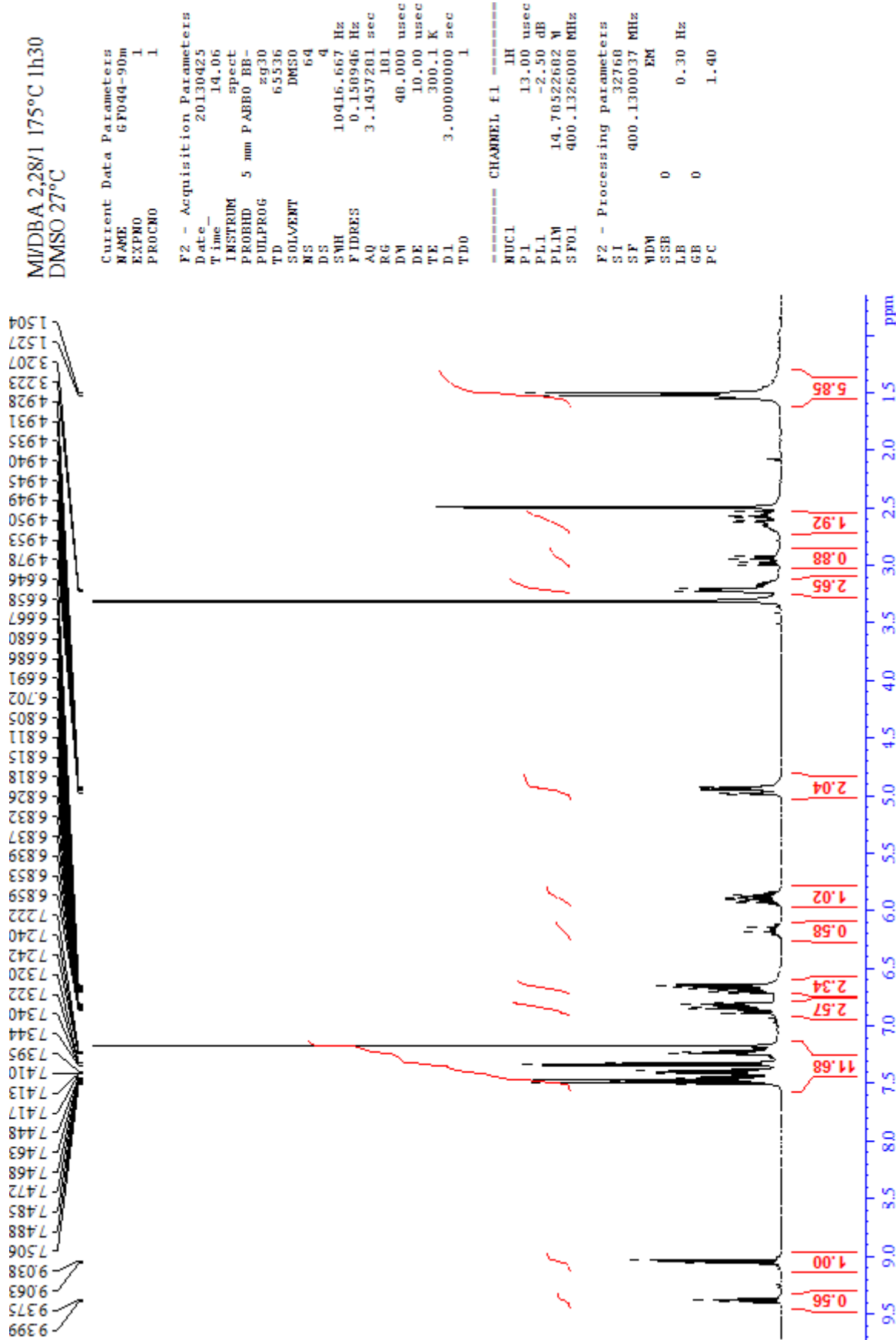


MI/DBA 2.28:1 cured 60 min at 175°C, DMSO-d6, 27°C.

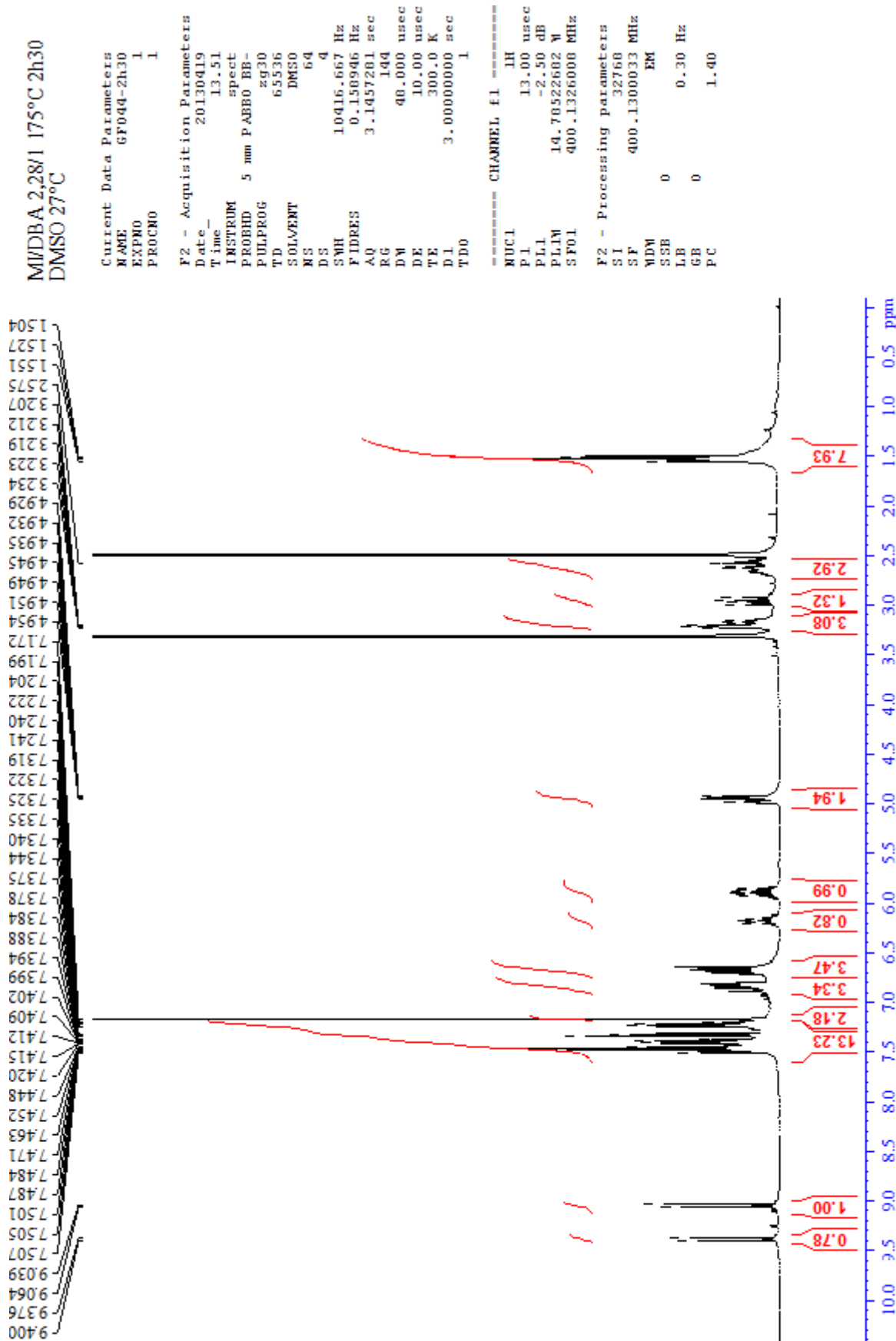


Appendix A: NMR spectra

MI/DBA 2.28:1 cured 90 min at 175°C, DMSO-d6, 27°C.

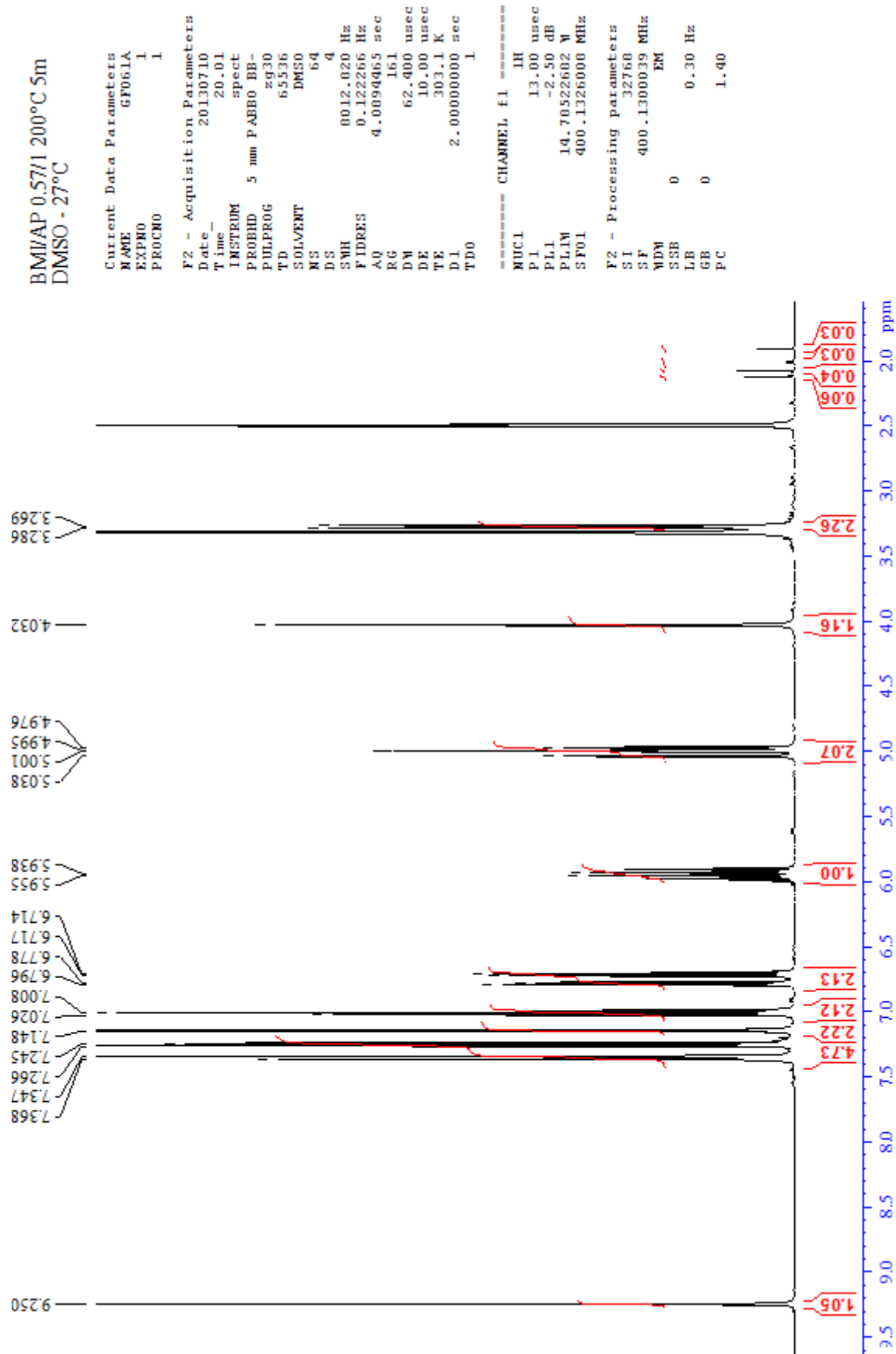


MI/DBA 2.28:1 cured 150 min at 175°C, DMSO-d6, 27°C.

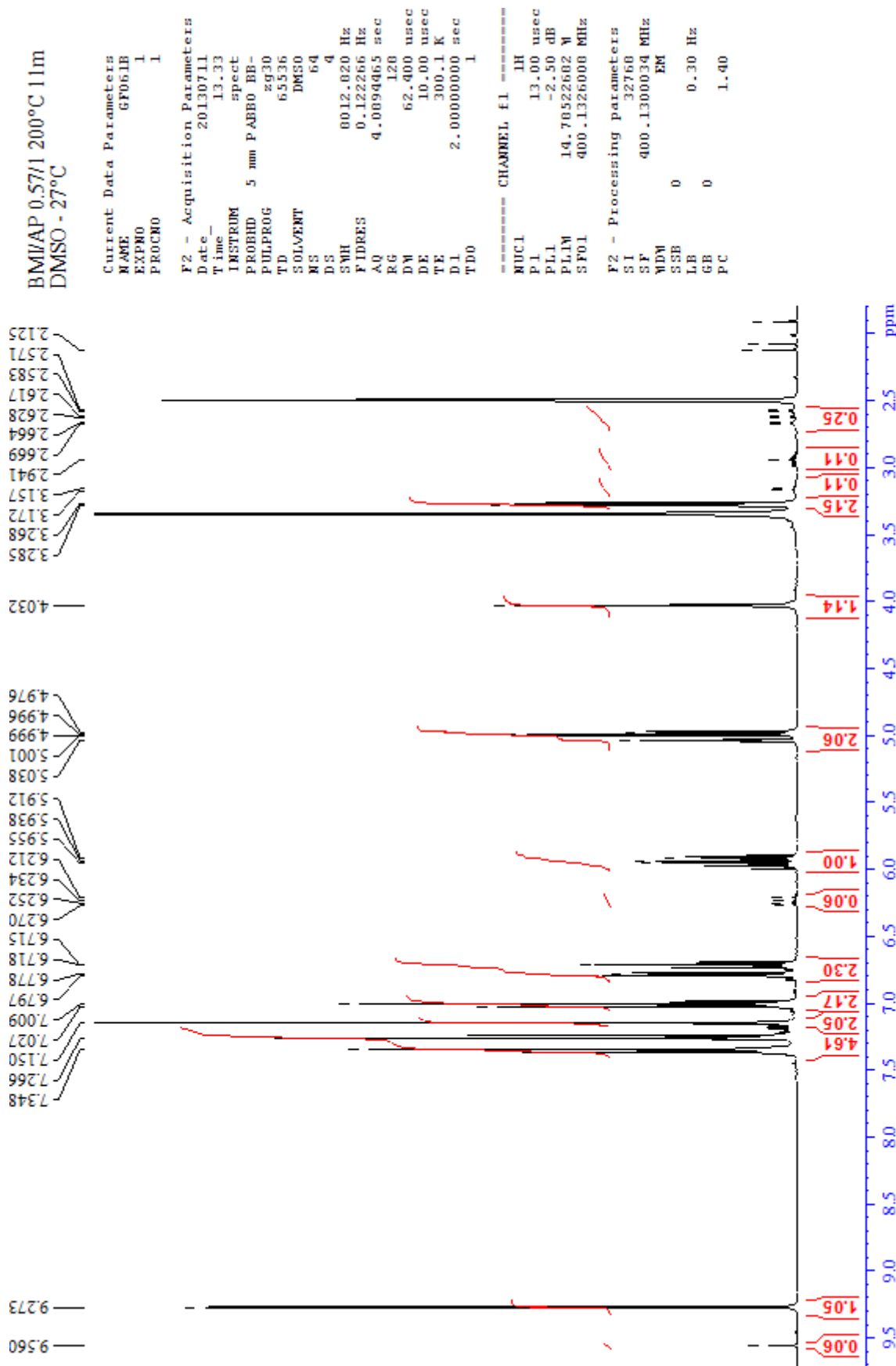


Appendix A: NMR spectra

BMI/AP 0.57:1 200°C 5m
DMSO - 27°C

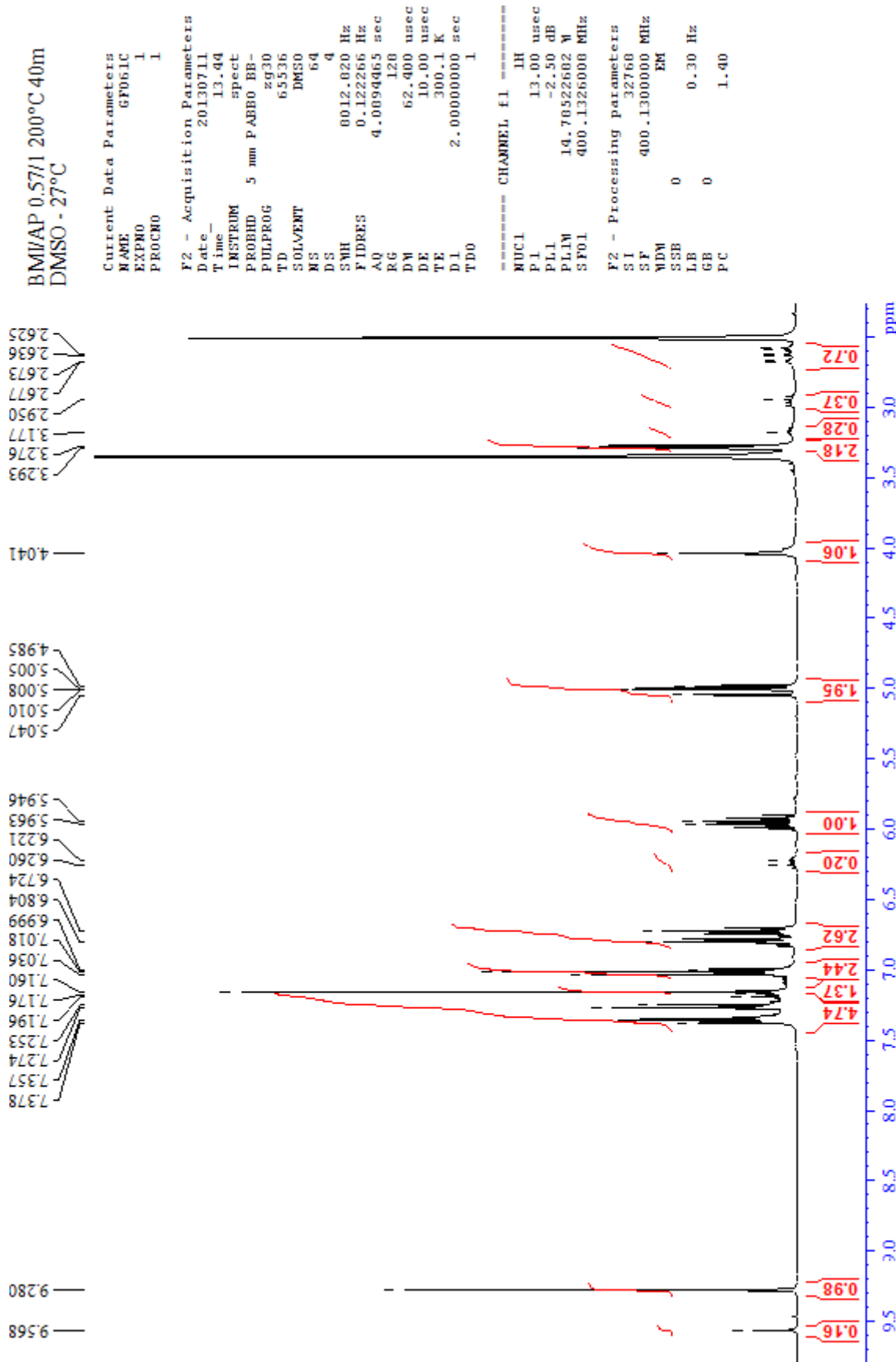


BMI/AP 0.57:1 cured 11 min at 200°C, DMSO-d6, 27°C.

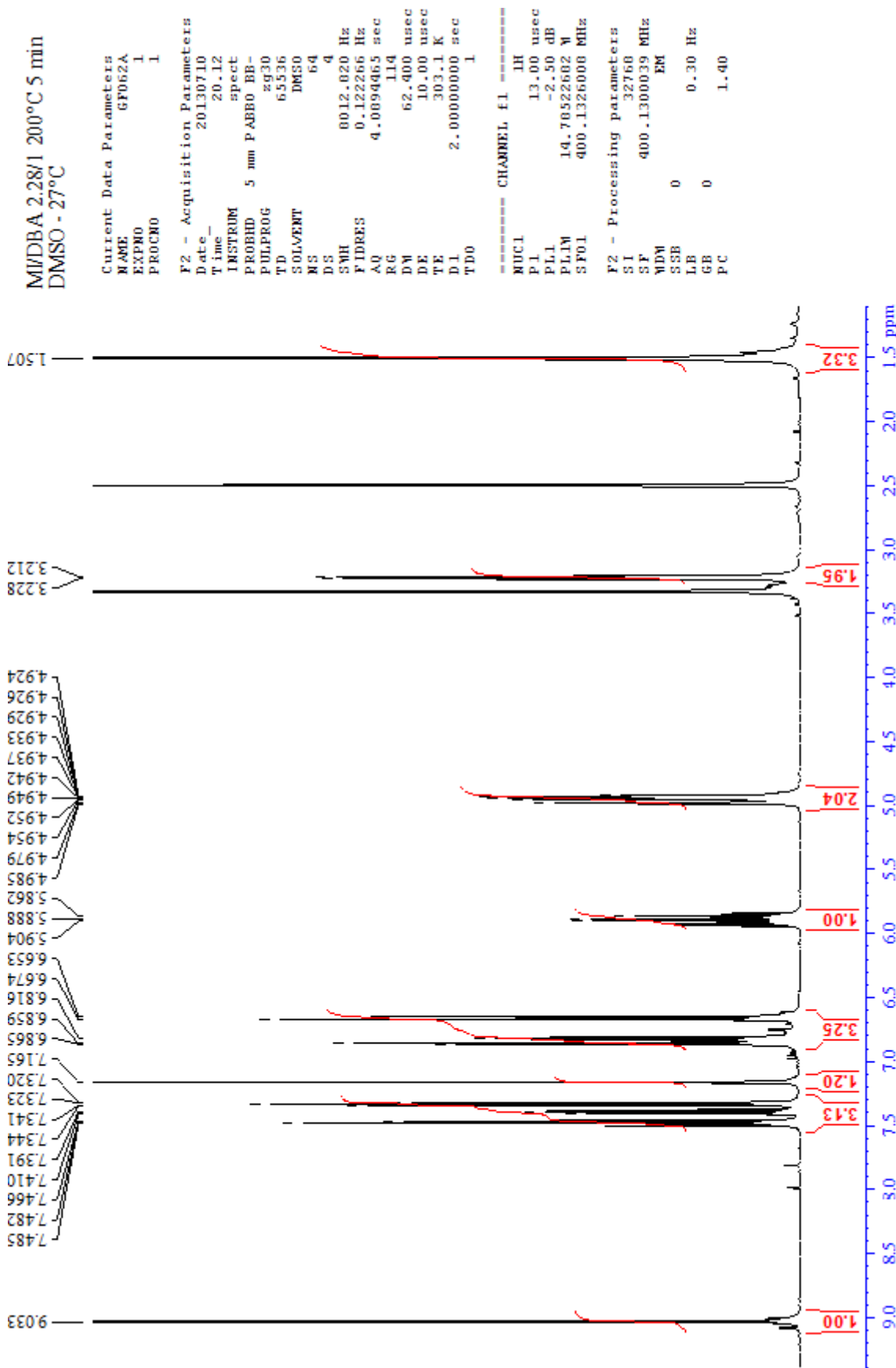


Appendix A: NMR spectra

BMI/AP 0.57:1 cured 40 min at 200°C, DMSO-d6, 27°C.

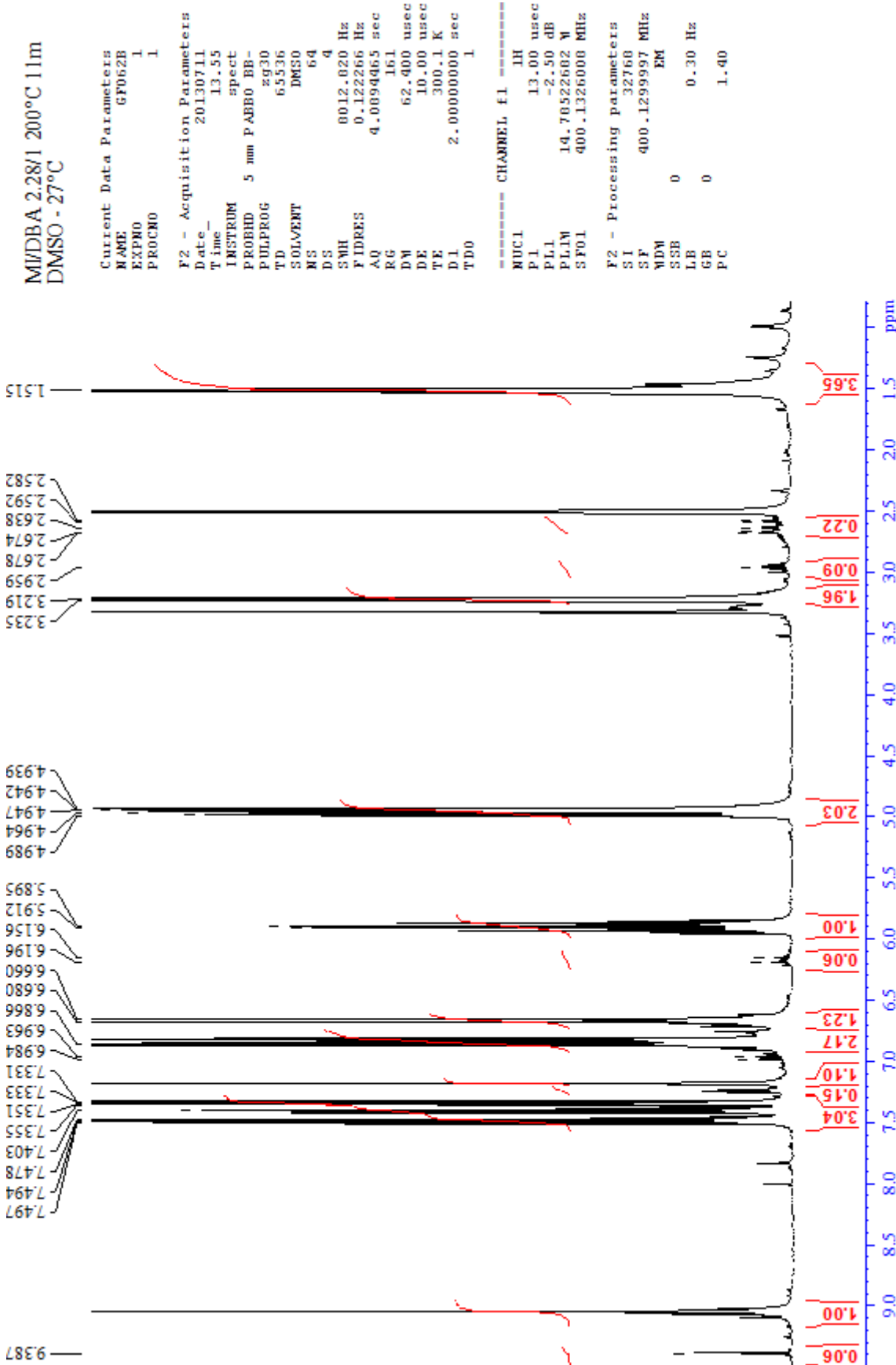


MI/DBA 2.28:1 cured 5 min at 200°C, DMSO-d6, 27°C.

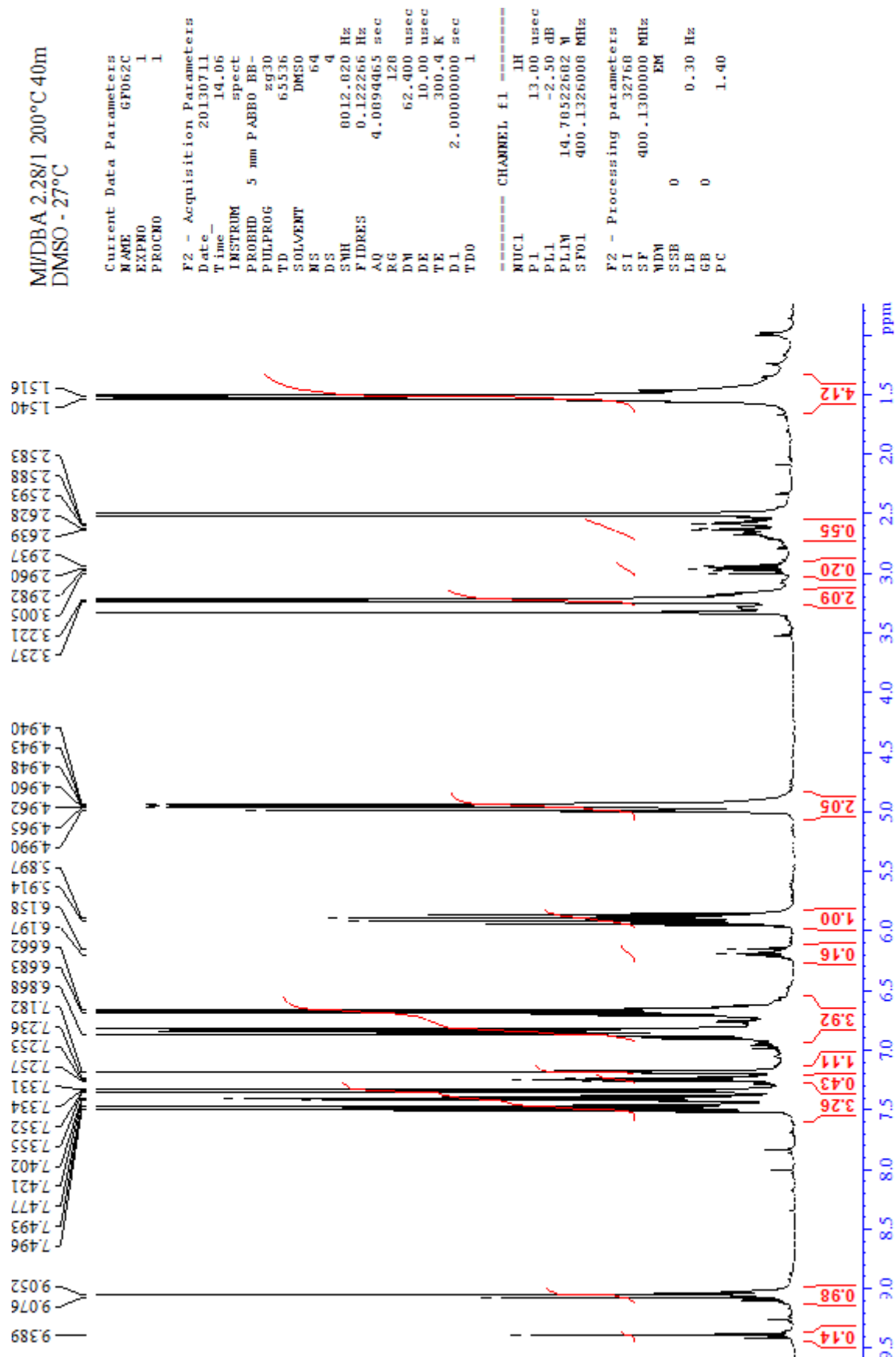


Appendix A: NMR spectra

MI/DBA 2.28:1 cured 11 min at 200°C, DMSO-d6, 27°C.

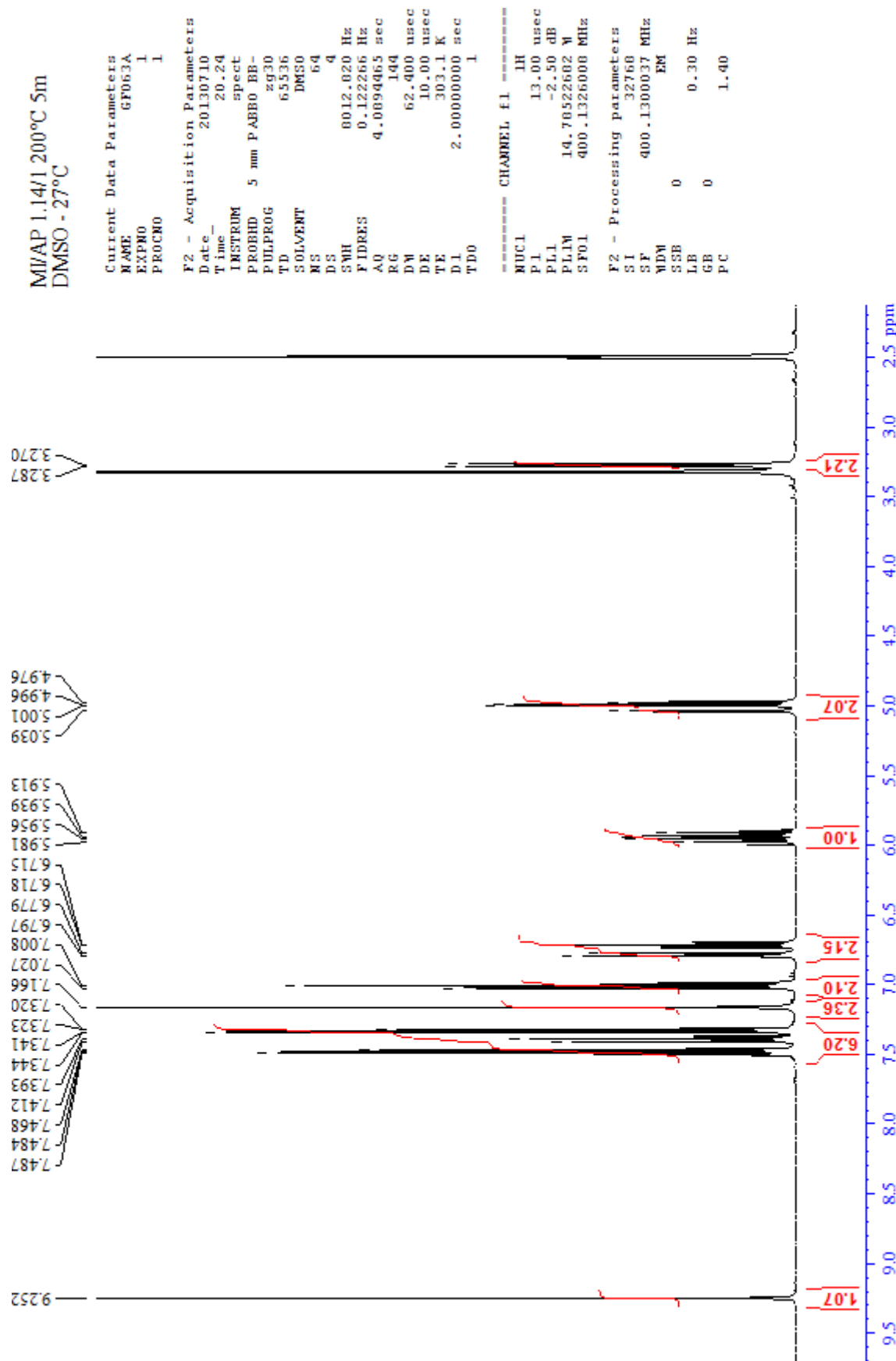


MI/DBA 2.28:1 cured 40 min at 200°C, DMSO-d6, 27°C.

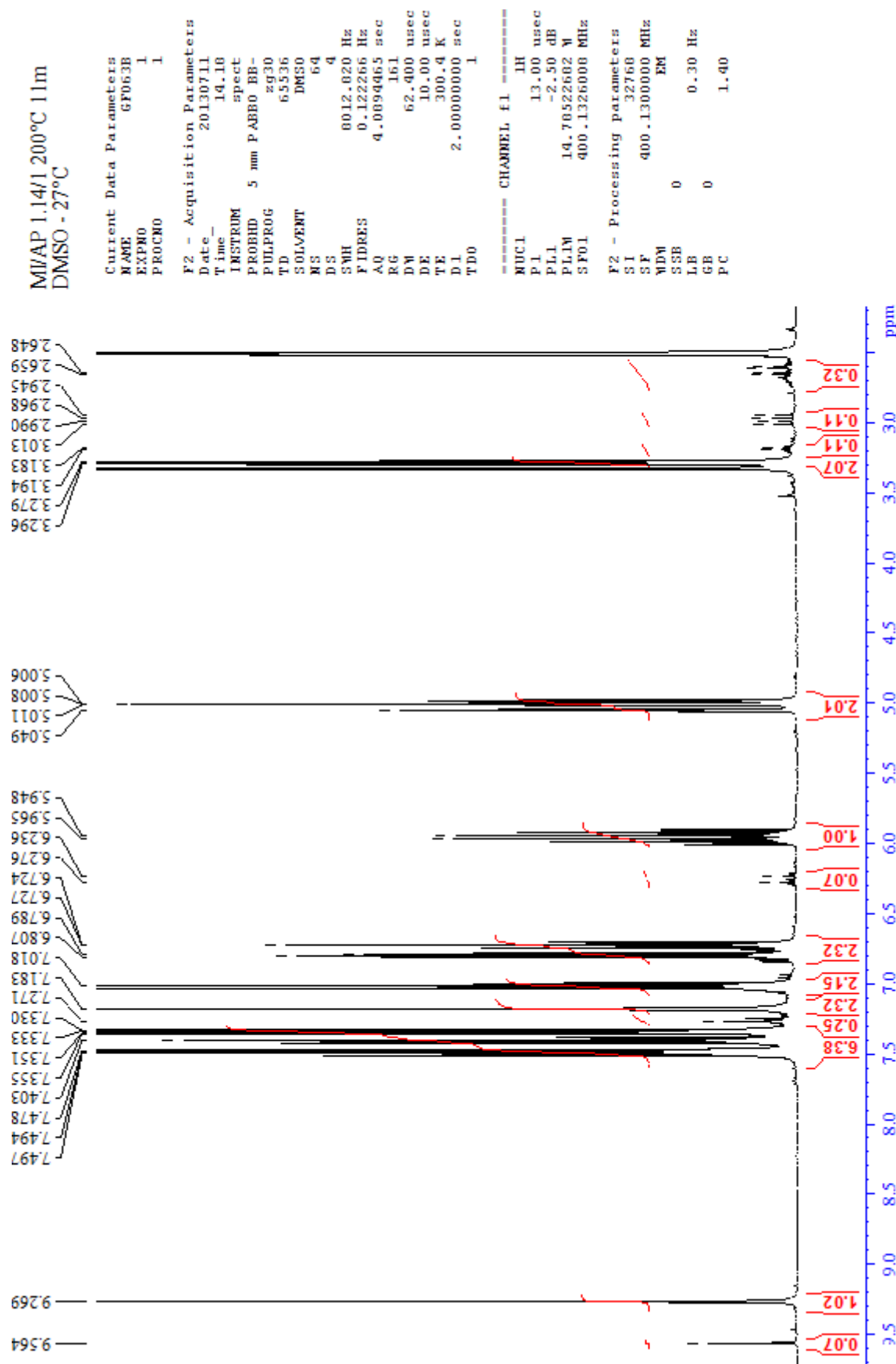


Appendix A: NMR spectra

MI/AP 1.14/1 200°C 5m
DMSO - 27°C.

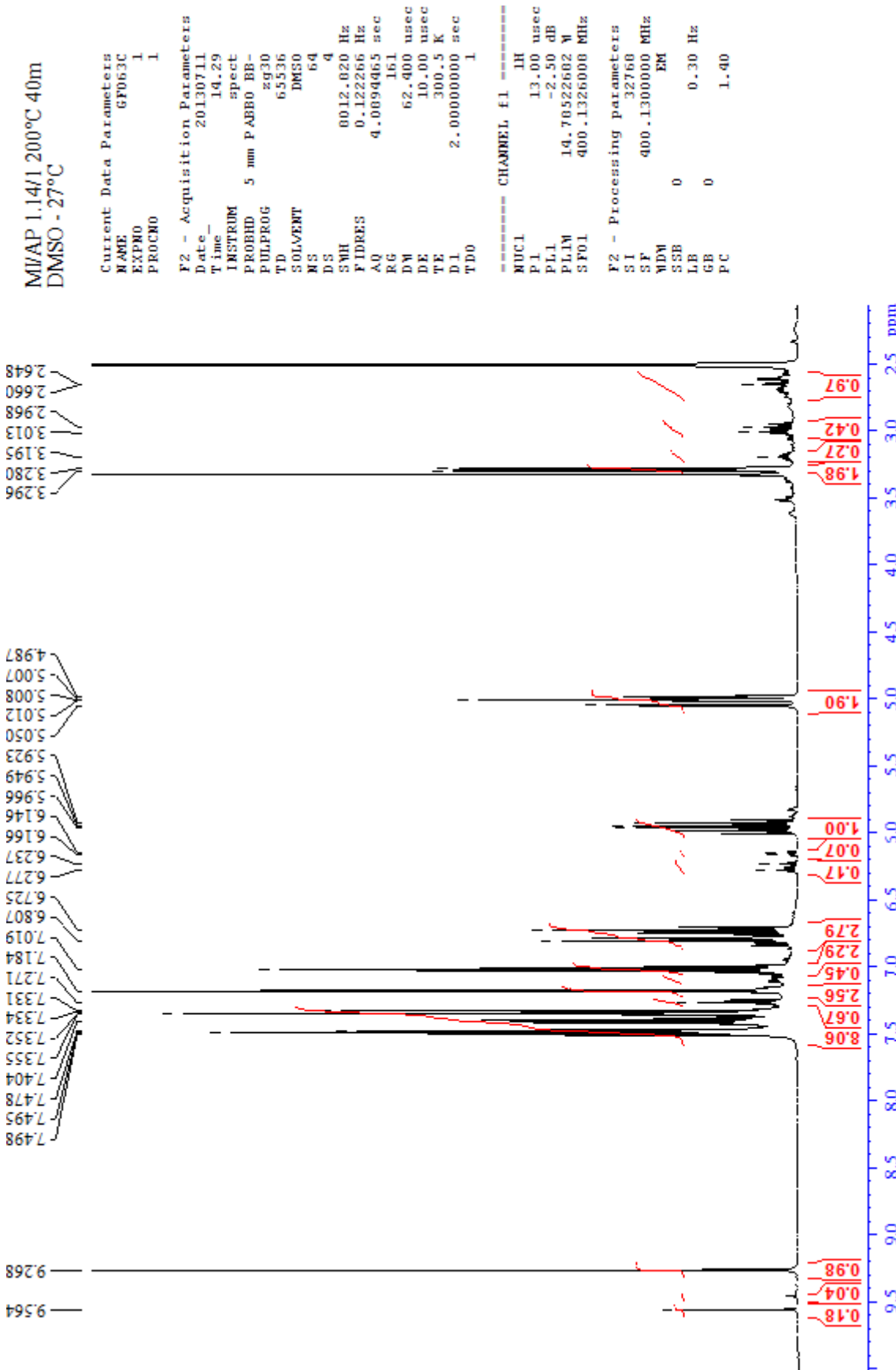


MI/AP 1.14:1 cured 11 min at 200°C, DMSO-d6, 27°C.

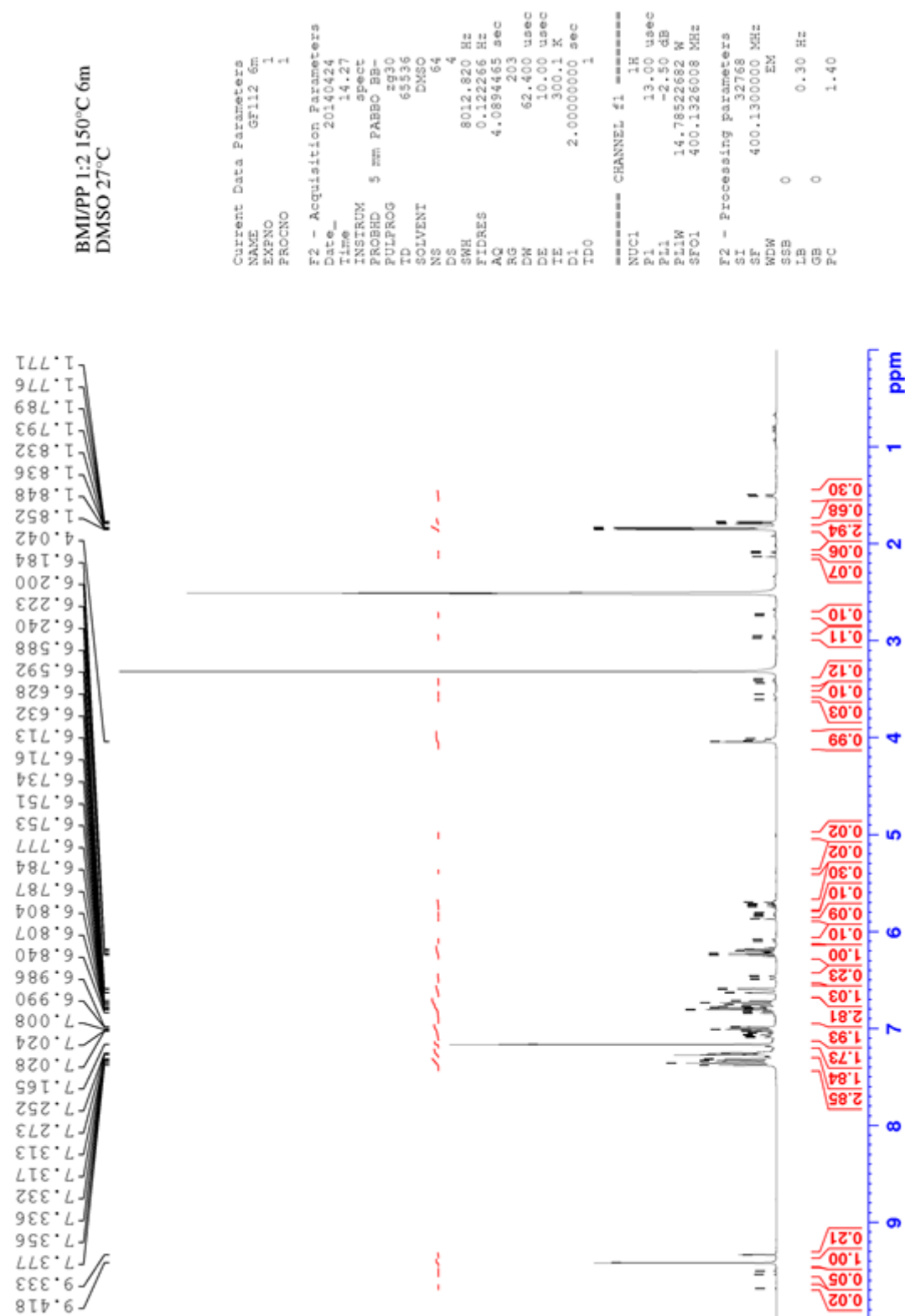


Appendix A: NMR spectra

MI/AP 1.14/1 200°C 40m
DMSO - 27°C



BMI/PP 1:2 150°C 6m DMSO-d6, 27°C.



Appendix B: Modulus loss calculation

Considering a simple mixing law for the longitudinal modulus:

$$E_c = V_m E_m + V_f E_f$$

With E being the Young modulus, V the volume fraction, c , m and f indexes referring to the composite, matrix and fibre respectively. A rough approximation with $E_m = 4$ GPa, $E_f = 240$ GPa, $V_m = 0.4$ and $V_f = 0.6$ gives $E_m = 145.6$ GPa. Considering no influence of the temperature on the fibres, the variation of the composite modulus can be approximated by:

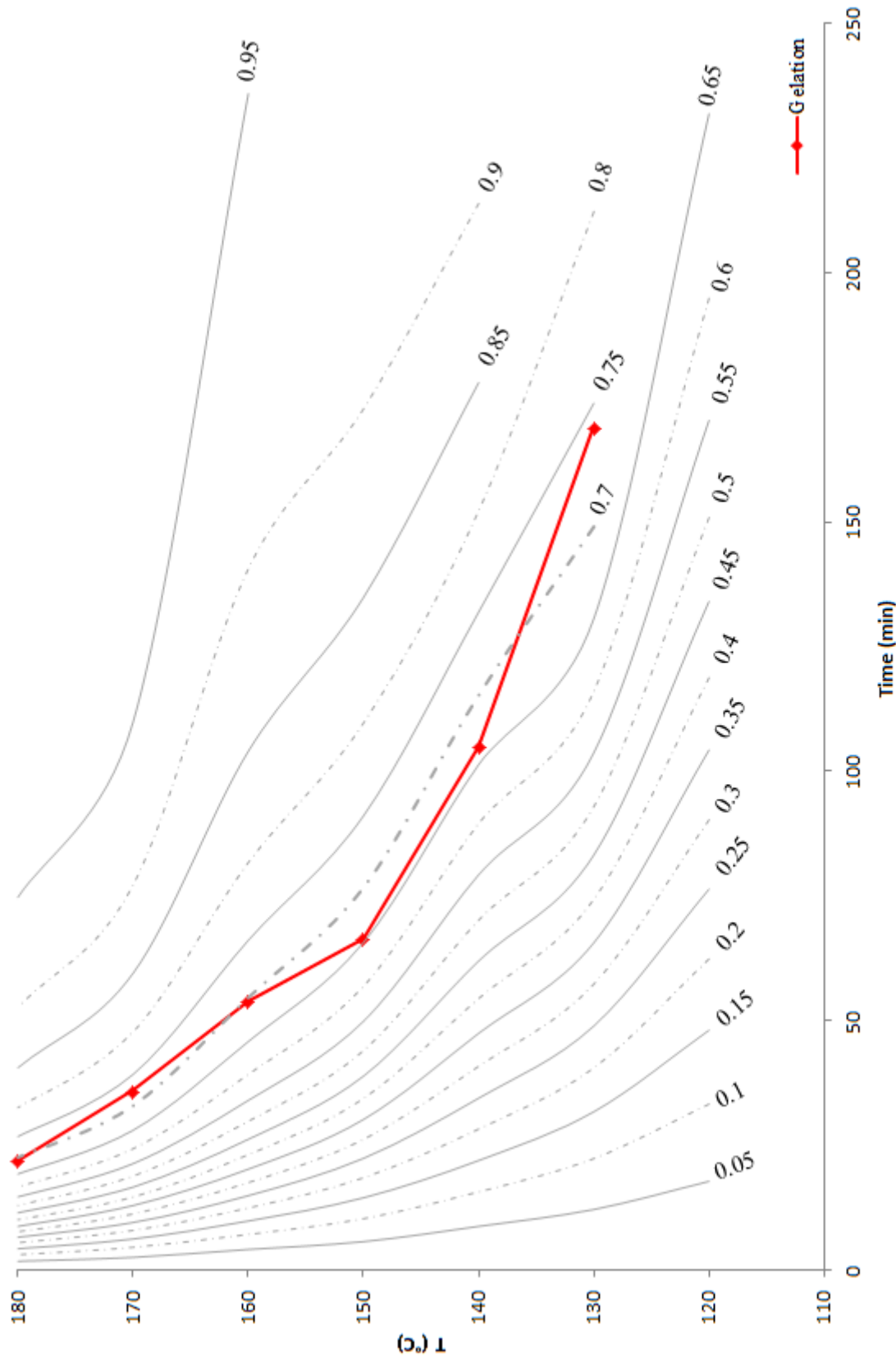
$$\frac{\Delta E_c}{E_c} \simeq V_m \frac{\Delta E_m}{E_c}$$

With the previous numerical values, if E_m drops by 25% (1 GPa), E_c only decreases of 0.3%.

Remark: a similar calculation leads to a greater effect on the transverse modulus (roughly 25%) but structures are usually designed to align fibres with the main stress axis.

Appendix C: Epoxy TTT diagram

DGEBA/DDS 1:1.



Appendix D: Simulation program

Line breaks are indicated by the tag \ Line Break\. They have to be delete for running the code.

Monomer class.

```
classdef Monomer < handle
    %monomer is the general superclass for BMI and DBA
    properties
        type
        doubleBond
        radical
        AlderEneCount
    end

    methods
        function PropagateRadical(monomer)
            if monomer.doubleBond > 0
                monomer.radical = monomer.radical+1;
                monomer.doubleBond = monomer.doubleBond-1;
            end
        end

        function TerminateRadical(monomer)
            if monomer.radical > 0
                monomer.radical = monomer.radical-1;
            end
        end
    end
end
```

BMI class.

```
classdef BMI < Monomer

    properties
    end

    methods
        function obj = BMI()
            obj.type = 'BMI';
            obj.doubleBond = 2;
            obj.radical = 0;
            obj.AlderEneCount = 0;
        end

        function initiate(monomer)
            if monomer.doubleBond > 0
```

```

monomer.radical = monomer.radical+1;
monomer.doubleBond = monomer.doubleBond-1;
end
end

function AlderEne(monomer)
if monomer.doubleBond > 0 & monomer.AlderEneCount < 2
    monomer.doubleBond = monomer.doubleBond-1;
    monomer.AlderEneCount = monomer.AlderEneCount+1;
end
end
end
end

DBA class.

classdef DBA < Monomer

properties
end

methods
function obj = DBA()
obj.type = 'DBA';
obj.doubleBond = 2;
obj.radical = 0;
obj.AlderEneCount = 0;
end

function AlderEne(monomer)
if monomer.doubleBond > 0 & monomer.AlderEneCount < 2
    monomer.AlderEneCount = monomer.AlderEneCount+1;
end
end
end
end

```

Neighbours finding function.

```

function tab = findNeighbours(P,L)
% find the neighbours of a point in a LxLxL matrix,
% taking edge points into account
i=1;
if P(1)>1
    tab{i}=[P(1)-1 P(2) P(3)];
    i=i+1;
end
if P(1)<L
    tab{i}=[P(1)+1 P(2) P(3)];
    i=i+1;
end

```

```

if P(2)>1
    tab{i}=[P(1) P(2)-1 P(3)];
    i=i+1;
end
if P(2)<L
    tab{i}=[P(1) P(2)+1 P(3)];
    i=i+1;
end
if P(3)>1
    tab{i}=[P(1) P(2) P(3)-1];
    i=i+1;
end
if P(3)<L
    tab{i}=[P(1) P(2) P(3)+1];
end
end

```

Function determining if two monomers are bonded.

```

function yn = Isbonded(monomer1,monomer2,BondMatrix)
    % Determines whether two monomers are bonded
% according a matrix containing bonds.
    % monomers are sets of coordinates
    x1 = monomer1(1);
    y1 = monomer1(2);
    z1 = monomer1(3);
    x2 = monomer2(1);
    y2 = monomer2(2);
    z2 = monomer2(3);
    if isempty(BondMatrix{x1,y1,z1}) & isempty(BondMatrix{x2,y2,z2})
        yn = 0;
    else
        yn = ismember(monomer1,cell2mat(BondMatrix{x2,y2,z2}(:)), 'rows',
        \ Line Break\
        'legacy') | ismember(monomer2,cell2mat(BondMatrix{x1,y1,z1}(:)),
        \ Line Break\
        'rows', 'legacy');
    end
end

```

Function determining if BMI monomer is among neighbours.

```

function output = NextToBMI(Neighbours,M)
    % Determines whether there is a BMI in Neighbours
% and returns its coordinates.
    % Returns (0,0,0) if no BMI is found
    for i=1:length(Neighbours)
        x = Neighbours{i}(1);
        y = Neighbours{i}(2);
        z = Neighbours{i}(3);
        if strcmp(M{x,y,z}.type,'BMI')

```

```

    yn = 1;
    break
else
    x = 0;
    y = 0;
    z = 0;
    yn = 0;
end
end
output = [x,y,z,yn];
end

```

Function determining if an unbonded BMI monomer is among neighbours.

```

function output = NextToUBMI(Neighbours,M)
% Determines whether there is an unbounded BMI in Neighbours
% and returns its coordinates.
% Returns (0,0,0) if no BMI is found
for i=1:length(Neighbours)
    x = Neighbours{i}(1);
    y = Neighbours{i}(2);
    z = Neighbours{i}(3);
    if strcmp(M{x,y,z}.type,'BMI') & M{x,y,z}.doubleBond == 2
        yn = 1;
        break
    else
        x = 0;
        y = 0;
        z = 0;
        yn = 0;
    end
end
output = [x,y,z,yn];
end

```

Function stocking vectors in a cell.

```

function c = pushInCell(M,x,y,z,v)
% push a vector in cell
A = cell2mat(M{x,y,z}(:));
dim = size(A,1);
V1 = [];
V2 = [];
V3 = [];
V4 = [];
V5 = [];
if dim>0
    V1=A(1,:);
end
if dim>1
    V2=A(2,:);

```

```

end
if dim>2
    V3=A(3,:);
end
if dim>3
    V4=A(4,:);
end
if dim>4
    V5=A(5,:);
end
c = {v,V1,V2,V3,V4,V5};
end

```

Script generating a network.

```

% Creates a matrix containing a random distribution of monomers.
steps = 7;
% Sample size
L = 50;
% BMI fraction
f = 1.14;
% limit for monomer attribution to generated random values
limit = L^3*f/(1+f);
% initial fraction of radical complexes (half of radical fraction)
%Cr = 0.01;
% probability to initiate radicals
pi = 0.0062;
% probability to propagate at each step
pp = 1;
% probability of Alder-ene reaction to occur
pa = 0.005;
% number of monomer double bonds that have reacted
dBMR = 0;
% number of double bonds that have reacted
dBR = 0;

% Initiates a random matrix support for initial monomer distribution
RL = randperm(L^3);
RM = reshape(RL,L,L,L);

% Initiate an empty matrix for bonds
MBonds = cell(L,L,L);

% Initial empty matrix
M = cell(L,L,L);

% Monomer attribution within the initial matrix
for i=1:L
    for j=1:L

```

```

for k=1:L
    if RM(i,j,k)<limit
        M{i,j,k} = BMI();
    else
        M{i,j,k} = DBA();
    end
end
end

% Creation of a radical table
% dimRTable = max([2,2*round(limit*Cr)]);
dimRTable = 0;
RTable = cell(1,dimRTable);

% % Initial random radical attribution on BMI monomers
% N = dimRTable/2;
% for l=1:N
%     tmp = 0;
%     a = 1+round((L-1)*rand);
%     b = 1+round((L-1)*rand);
%     c = 1+round((L-1)*rand);
%     Neighbours = findNeighbours([a,b,c],L);
%     ShuffleNeighbours = tabShuffle(Neighbours);
%     Po = NextToUBMI(ShuffleNeighbours,M);
%     while strcmp(M{a,b,c}.type,'DBA') | M{a,b,c}.radical ~= 0 | Po(4) ~=1
%         tmp = tmp+1;
%         a = 1+round((L-1)*rand);
%         b = 1+round((L-1)*rand);
%         c = 1+round((L-1)*rand);
%         Neighbours = findNeighbours([a,b,c],L);
%         ShuffleNeighbours = tabShuffle(Neighbours);
%         Po = NextToUBMI(ShuffleNeighbours,M);
%     % break criterion is not that all monomers have been tested.
%     % Limit value of tmp can be changed
%     if tmp==L^10
%         break
%     end
% end
% if tmp ~= L^10 & Po(4) ~=0
%     RTable{l} = [a,b,c];
%     RTable{N+l} = [Po(1),Po(2),Po(3)];
%     initiate(M{a,b,c});
%     initiate(M{Po(1),Po(2),Po(3)});
%     A(a,b,c)=3;
%     A(Po(1),Po(2),Po(3))=3;
%     MBonds{a,b,c} = pushInCell(MBonds,a,b,c,[Po(1),Po(2),Po(3)]);
%     dBMR = dBMR + 2;
%     dBR = dBR + 2;

```

```

%    else
%    break
% end
% end

for count=1:steps
% Termination step
N = size(RTable,2);
if N>0
    for m=1:N
        xM = RTable{m}(1);
        yM = RTable{m}(2);
        zM = RTable{m}(3);
        Neighbours = findNeighbours(RTable{m},L);
        % randomisation of the termination direction
        ShuffleNeighbours = tabShuffle(Neighbours);
        for n=1:length(ShuffleNeighbours)
            x = ShuffleNeighbours{n}(1);
            y = ShuffleNeighbours{n}(2);
            z = ShuffleNeighbours{n}(3);
            if M{xM,yM,zM}.radical>0 & M{x,y,z}.radical>0
                \ Line Break\
                & ~Isbonded([xM,yM,zM],[x,y,z],MBonds)
                    M{xM,yM,zM}.radical = M{xM,yM,zM}.radical-1;
                    M{x,y,z}.radical = M{x,y,z}.radical-1;
                    MBonds{xM,yM,zM} = pushInCell(MBonds,xM,yM,zM,[x,y,z]);
            end
        end
    end
    % remove non radical species from RTable
    ind = [];
    for m=1:N
        xM = RTable{m}(1);
        yM = RTable{m}(2);
        zM = RTable{m}(3);
        if M{xM,yM,zM}.radical == 0
            ind(end+1) = m;
        end
    end
    RTable(ind)=[];
end

% Propagation step
N = size(RTable,2);
inc = 0;
if N > 0
    for m=1:N
        reaction = rand;
        if reaction<pp

```

```

xM = RTable{m}(1);
yM = RTable{m}(2);
zM = RTable{m}(3);
Neighbours = findNeighbours(RTable{m},L);
ShuffleNeighbours = tabShuffle(Neighbours);
for n=1:length(ShuffleNeighbours)
    x = ShuffleNeighbours{n}(1);
    y = ShuffleNeighbours{n}(2);
    z = ShuffleNeighbours{n}(3);
    if M{xM,yM,zM}.radical>0 & M{x,y,z}.doubleBond>0
\ Line Break\
& ~Isbonded([xM,yM,zM],[x,y,z],MBonds)
    M{xM,yM,zM}.radical = M{xM,yM,zM}.radical-1;
    M{x,y,z}.radical = M{x,y,z}.radical+1;
    M{x,y,z}.doubleBond = M{x,y,z}.doubleBond-1;
    inc = inc+1;
    RTable{N+inc} = [x,y,z];
    MBonds{xM,yM,zM} = pushInCell(MBonds,xM,yM,zM,[x,y,z]);
    dBMR = dBMR + 1;
    dBR = dBR + 1;
end
end
end
end

% remove non radical species from RTable
ind = [];
for m=1:N
    xM = RTable{m}(1);
    yM = RTable{m}(2);
    zM = RTable{m}(3);
    if M{xM,yM,zM}.radical == 0
        ind(end+1) = m;
    end
end
RTable(ind)=[];
end

for i=1:L
    for j=1:L
        for k=1:L
% Alder-ene reaction step
        reaction = rand;
        if reaction < pa & M{i,j,k}.doubleBond > 0
\ Line Break\
& M{i,j,k}.AlderEneCount < 2
        Neighbours = findNeighbours([i,j,k],L);
        ShuffleNeighbours = tabShuffle(Neighbours);
        ind = [];% remove non compatible monomers
    end
end
end

```

```

        for n=1:length(ShuffleNeighbours)
            x = ShuffleNeighbours{n}(1);
            y = ShuffleNeighbours{n}(2);
            z = ShuffleNeighbours{n}(3);
            if strcmp(M{i,j,k}.type,M{x,y,z}.type)
\ Line Break\
| M{x,y,z}.doubleBond == 0 | M{x,y,z}.AlderEneCount>1
\ Line Break\
| Isbonded([i,j,k],[x,y,z],MBonds)
    ind(end+1)=n;
end
end
ShuffleNeighbours(ind)=[] ;
% cast Alder-Ene reaction
if ~isempty(ShuffleNeighbours)
    x = ShuffleNeighbours{1}(1);
    y = ShuffleNeighbours{1}(2);
    z = ShuffleNeighbours{1}(3);
    AlderEne(M{x,y,z});
    AlderEne(M{i,j,k});
    MBonds{i,j,k} = pushInCell(MBonds,i,j,k,[x,y,z]);
    dBR = dBR + 1;
end
end

% initiation step
reaction = rand;
Neighbours = findNeighbours([i,j,k],L);
ShuffleNeighbours = tabShuffle(Neighbours);
Po = NextToUBMI(ShuffleNeighbours,M);
if reaction < pi & strcmp(M{i,j,k}.type,'BMI') & Po(4) ~=0
\ Line Break\
& ~Isbonded([i,j,k],[Po(1),Po(2),Po(3)],MBonds)
    dimRTable = size(RTable,2);
    RTable{dimRTable+1} = [i,j,k];
    RTable{dimRTable+2} = [Po(1),Po(2),Po(3)];
    initiate(M{i,j,k});
    initiate(M{Po(1),Po(2),Po(3)});
    MBonds{i,j,k} = pushInCell(MBonds,i,j,k,[Po(1),Po(2),Po(3)]);
    dBMR = dBMR + 2;
    dBR = dBR + 2;
end
end
end
end
end

```

The commented loop starting with `Initial random radical attribution` is dedicated to free radical polymerization with a constant initial radical concentration `Cr`.

Function to plot bonds.

```
function plotBonds(M,L)
% draw bonds of a 3D bond LxLxL cell array
hold on
axis([1 L 1 L 1 L]);
axis square;
for i=1:L
    for j=1:L
        for k=1:L
            A = cell2mat(M{i,j,k}(:));
            dim = size(A,1);
            if dim ~=0
                for n=1:dim
                    line([i,A(n,1)], [j,A(n,2)], [k,A(n,3)]);
                end
            end
        end
    end
end
hold off
end
```

The following code is dedicated to percolation determination.

```
function [M,S] = nodes(BondMatrix,L,direction)
% Creates a matrix containing 4 columns.
% The first one is an index depending on direction.
% The last three are coordinates of non empty cells.
% Creates a matrix containing the indexes of linked cells.
M = [];
S = [];
for i=1:L
    for j=1:L
        for k=1:L
            if ~isempty(BondMatrix{i,j,k})
                if direction == 1
                    ID = i+(j-1)*L+(k-1)*L^2;
                elseif direction == 2
                    ID = i+(k-1)*L+(L-j)*L^2;
                else
                    ID = k+(j-1)*L+(L-i)*L^2;
                end
                Coord = cell2mat(BondMatrix{i,j,k}(:));
                v = [];
                for l=1:size(Coord,1)
                    x = Coord(l,1);
                    y = Coord(l,2);
                    z = Coord(l,3);
                    if direction == 1
```

```

v(1) = x+(y-1)*L+(z-1)*L^2;
elseif direction == 2
    v(1) = x+(z-1)*L+(L-y)*L^2;
else
    v(1) = z+(y-1)*L+(L-x)*L^2;
end
S = vertcat(S,[ID,v(1)]);
end
tmp = horzcat(v',Coord);
tmp = vertcat([ID,i,j,k],tmp);
M = vertcat(M,tmp);
end
end
end
M = unique(M,'rows');
S = horzcat((1:length(S))',S);
end

% test percolation of a bond matrix
dist = inf;

for direction = 1:3
    if dist == inf
        [nod,seg]=nodes(MBonds,L,direction);
        tmp = nod(:,1);
        start = tmp(tmp<=L^2);
        finish = tmp(tmp>=L^3-L^2);
        Sdim = length(start);
        Fdim = length(finish);
        if Sdim*Fdim ~= 0
            for s=1:Sdim
                if dist == inf
                    for f=1:Fdim
                        [dist,path] = dijkstra(nod,seg,start(s),finish(f));
                        if dist < inf
                            break
                        end
                    end
                end
            end
        end
    end
    if dist < inf
        for i=1:length(path)
            Pathperc(i,:) = nod(nod(:,1)==path(i),:);
        end
    end
end

```

```

hold on
plot3(Pathperc(:,2),Pathperc(:,3),Pathperc(:,4),'or')
hold off
end

```

The Dijkstra algorithm used is the following one.

```

function [dist,path] = dijkstra(nodes,segments,start_id,finish_id)
% DIJKSTRA Calculates the shortest distance and path between points
% on a map using Dijkstra's Shortest Path Algorithm
% [DIST, PATH] = DIJKSTRA(NODES, SEGMENTS, SID, FID)
% Calculates the shortest distance and path between start and finish
% nodes SID and FID
% [DIST, PATH] = DIJKSTRA(NODES, SEGMENTS, SID)
% Calculates the shortest distances and paths from the starting node
% SID to all other nodes in the map
% Note:
% DIJKSTRA is set up so that an example is created if no inputs are
% provided, but ignores the example and just processes the inputs
% if they are given.
% Inputs:
% NODES should be an Nx3 or Nx4 matrix with the format [ID X Y] or
% [ID X Y Z] where ID is an integer, and X, Y, Z are cartesian
% position coordinates)
% SEGMENTS should be an Mx3 matrix with the format [ID N1 N2]
% where ID is an integer, and N1, N2 correspond to node IDs from
% NODES list such that there is an [undirected] edge/segment between
% node N1 and node N2
% SID should be an integer in the node ID list corresponding with the
% starting node
% FID (optional) should be an integer in the node ID list
% corresponding with the finish
% Outputs:
% DIST is the shortest Euclidean distance
% If FID was specified, DIST will be a 1x1 double representing the
% shortest Euclidean distance between SID and FID along the map
% segments. DIST will have a value of INF if there are no segments
% connecting SID and FID. If FID was not specified, DIST will be a
% 1xN vector representing the shortest Euclidean distance between SID
% and all other nodes on the map. DIST will have a value of INF for
% any nodes that cannot be reached along segments of the map. PATH is
% a list of nodes containing the shortest route. If FID was specified,
% PATH will be a 1xP vector of node IDs from SID to FID. NAN will be
% returned if there are no segments connecting SID to FID. If FID was
% not specified, PATH will be a 1xN cell of vectors representing the
% shortest route from SID to all other nodes on the map. PATH will
% have a value of NAN for any nodes that cannot be reached along the
% segments of the map.
% Example:
% dijkstra; % calculates shortest path and distance between two nodes

```

```
% % on a map of randomly generated nodes and segments
%
% Example:
% nodes = [(1:10); 100*rand(2,10)]';
% segments = [(1:17); floor(1:0.5:9); ceil(2:0.5:10)]';
% figure; plot(nodes(:,2), nodes(:,3),'k.');
% hold on;
% for s = 1:17
%   if (s <= 10) text(nodes(s,2),nodes(s,3),[ ' ' num2str(s)]); end
%   plot(nodes(segments(s,2:3)',2),nodes(segments(s,2:3)',3),'k');
% end
% [d, p] = dijkstra(nodes, segments, 1, 10)
% for n = 2:length(p)
%   plot(nodes(p(n-1:n),2),nodes(p(n-1:n),3),'r-.','linewidth',2);
% end
% hold off;
%
% Author: Joseph Kirk
% Email: jdkirk630 at gmail dot com
% Release: 1.3
% Release Date: 5/18/07

if (nargin < 3) % SETUP
% (GENERATE RANDOM EXAMPLE OF NODES AND SEGMENTS IF NOT GIVEN AS
% INPUTS) Create a random set of nodes/vertices, and connect some
% of them with edges/segments. Then graph the resulting map.
num_nodes = 40; L = 100; max_seg_length = 30; ids = (1:num_nodes)';
nodes = [ids L*rand(num_nodes,2)]; % create random nodes
h = figure; plot(nodes(:,2),nodes(:,3),'k.') % plot the nodes
text(nodes(num_nodes,2),nodes(num_nodes,3),...
[ ' ' num2str(ids(num_nodes))],'Color','b','FontWeight','b')
hold on
num_segs = 0; segments = zeros(num_nodes*(num_nodes-1)/2,3);
for i = 1:num_nodes-1 % create edges between some of the nodes
  text(nodes(i,2),nodes(i,3),[ ' ' num2str(ids(i))],'Color','b',
\ Line Break\
'FontWeight','b')
  for j = i+1:num_nodes
    d = sqrt(sum((nodes(i,2:3) - nodes(j,2:3)).^2));
    if and(d < max_seg_length,rand < 0.6)
      plot([nodes(i,2) nodes(j,2)], [nodes(i,3) nodes(j,3)],'k.-')
    % add this link to the segments list
      num_segs = num_segs + 1;
      segments(num_segs,:) = [num_segs nodes(i,1) nodes(j,1)];
    end
  end
end
segments(num_segs+1:num_nodes*(num_nodes-1)/2,:) = [];
axis([0 L 0 L])
```

```
% Calculate Shortest Path Using Dijkstra's Algorithm
% Get random starting/ending nodes,compute the shortest distance
% and path.
start_id = ceil(num_nodes*rand);
disp(['start id = ' num2str(start_id)]);
finish_id = ceil(num_nodes*rand);
disp(['finish id = ' num2str(finish_id)]);
[distance,path] = dijkstra(nodes,segments,start_id,finish_id);
disp(['distance = ' num2str(distance)]);
disp(['path = [ ' num2str(path) ' ]']);
% If a Shortest Path exists,Plot it on the Map.
figure(h)
for k = 2:length(path)
    m = find(nodes(:,1) == path(k-1));
    n = find(nodes(:,1) == path(k));
    plot([nodes(m,2) nodes(n,2)], [nodes(m,3) nodes(n,3)],'ro-',
\ Line Break\
'LineWidth',2);
end
title(['Shortest Distance from ' num2str(start_id) ' to ' ...
num2str(finish_id) ' = ' num2str(distance)])
hold off

else %-----
    % MAIN FUNCTION - DIJKSTRA'S ALGORITHM
    % initializations
    node_ids = nodes(:,1);
    [num_map_pts,cols] = size(nodes);
    table = sparse(num_map_pts,2);
    shortest_distance = Inf(num_map_pts,1);
    settled = zeros(num_map_pts,1);
    path = num2cell(NaN(num_map_pts,1));
    col = 2;
    pidx = find(start_id == node_ids);
    shortest_distance(pidx) = 0;
    table(pidx,col) = 0;
    settled(pidx) = 1;
    path(pidx) = {start_id};
    if (nargin < 4) % compute shortest path for all nodes
        while_cmd = 'sum(~settled) > 0';
    else % terminate algorithm early
        while_cmd = 'settled(zz) == 0';
        zz = find(finish_id == node_ids);
        end
        while eval(while_cmd)
            % update the table
            table(:,col-1) = table(:,col);
            table(pidx,col) = 0;
            % find neighboring nodes in the segments list
```

```

neighbor_ids = [segments(node_ids(pidx) == segments(:,2),3);
    segments(node_ids(pidx) == segments(:,3),2)];
% calculate the distances to the neighboring nodes and keep
% track of the paths
for k = 1:length(neighbor_ids)
    cidx = find(neighbor_ids(k) == node_ids);
    if ~settled(cidx)
        d = sqrt(sum((nodes(pidx,2:cols) -
\ Line Break\
nodes(cidx,2:cols)).^2));
        if (table(cidx,col-1) == 0) || ...
            (table(cidx,col-1) > (table(pidx,col-1) + d))
            table(cidx,col) = table(pidx,col-1) + d;
            tmp_path = path(pidx);
            path(cidx) = {[tmp_path{1}] neighbor_ids(k)}];
        else
            table(cidx,col) = table(cidx,col-1);
        end
    end
end
% find the minimum non-zero value in the table and save it
nidx = find(table(:,col));
ndx = find(table(nidx,col) == min(table(nidx,col)));
if isempty(ndx)
    break
else
    pidx = nidx(ndx(1));
    shortest_distance(pidx) = table(pidx,col);
    settled(pidx) = 1;
end
% return the distance and path arrays for all of the nodes
if (nargin < 4)
    dist = shortest_distance';
    path = path';
else % return the distance and path for the ending node
    dist = shortest_distance(zz);
    path = path(zz);
    path = path{1};
end
end

```

Appendix E: Solubility parameters

Values are expressed in $(\text{cal}/\text{cm}^3)^{0.5}$. δ_{OH} is difficult to predict but expected positive from Coleman's work. For the oxygen alone $\delta_O = 18.6$, the unpredicted quite strong association contribution is expected to raise this value (a nitrogen alone is at $\delta_N = 0.6$ whereas adding a hydrogen with weak association contribution leads to $\delta_{NH} = 16.8$).

$$\delta_{BMI} = 162.3$$

$$\delta_{DBA} = 93.6 + 2\delta_{OH}$$

Consumption of maleimide and allyl with creation of a succinimide and propenyl gives:

$$\delta_{Alder-ene} = \delta_{BMI} + \delta_{DBA} + 5$$

For a typical PEI unit:

$$\delta_{PEI} = 206.2$$

Consequently:

$$\chi'_{copo,TP} \propto (\delta_{Alder-ene} - \delta_{PEI})^2$$

$$\chi'_{BMI,TP} \propto (\delta_{PEI} - \delta_{BMI})^2$$

Then:

$$\chi'_{BMI,TP} - \chi'_{copo,TP} \propto (2\delta_{PEI} - 2\delta_{BMI} - \delta_{DBA} - 5)(\delta_{DBA} + 5)$$

Finally:

$$\chi'_{BMI,TP} - \chi'_{copo,TP} \propto -10.8 - 2\delta_{OH} < 0$$

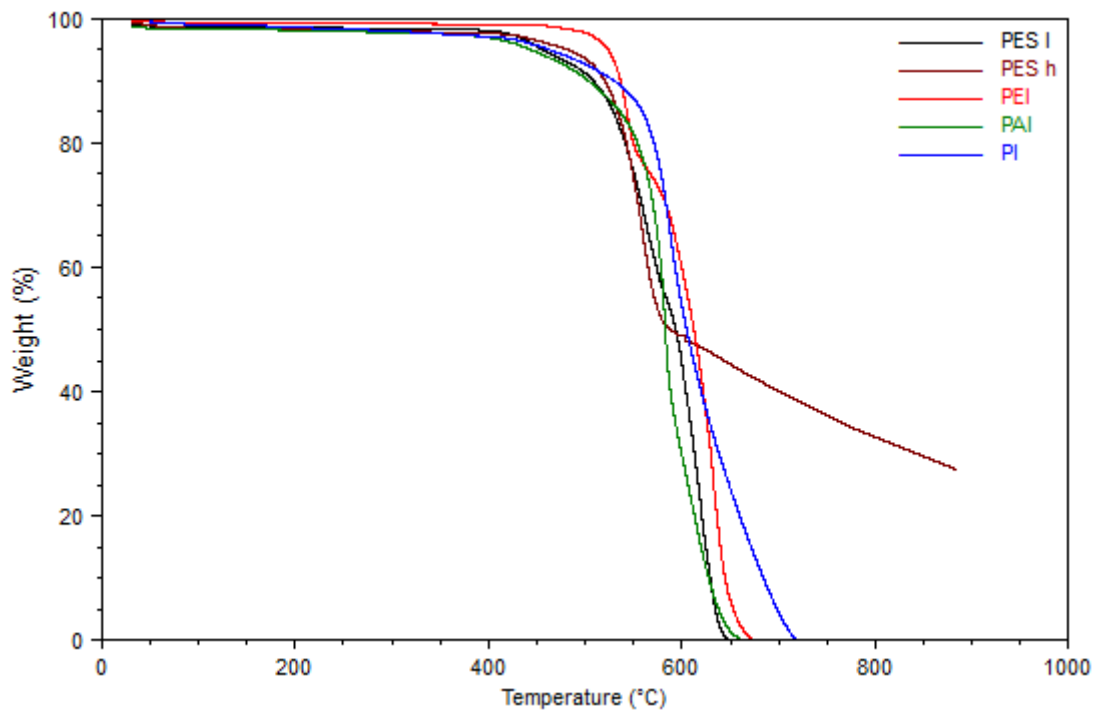
Similar calculation for $\chi'_{DBA,TP}$ strongly depends on the value of δ_{OH} :

$$\chi'_{DBA,TP} - \chi'_{copo,TP} \propto 57.9 - 2\delta_{OH}$$

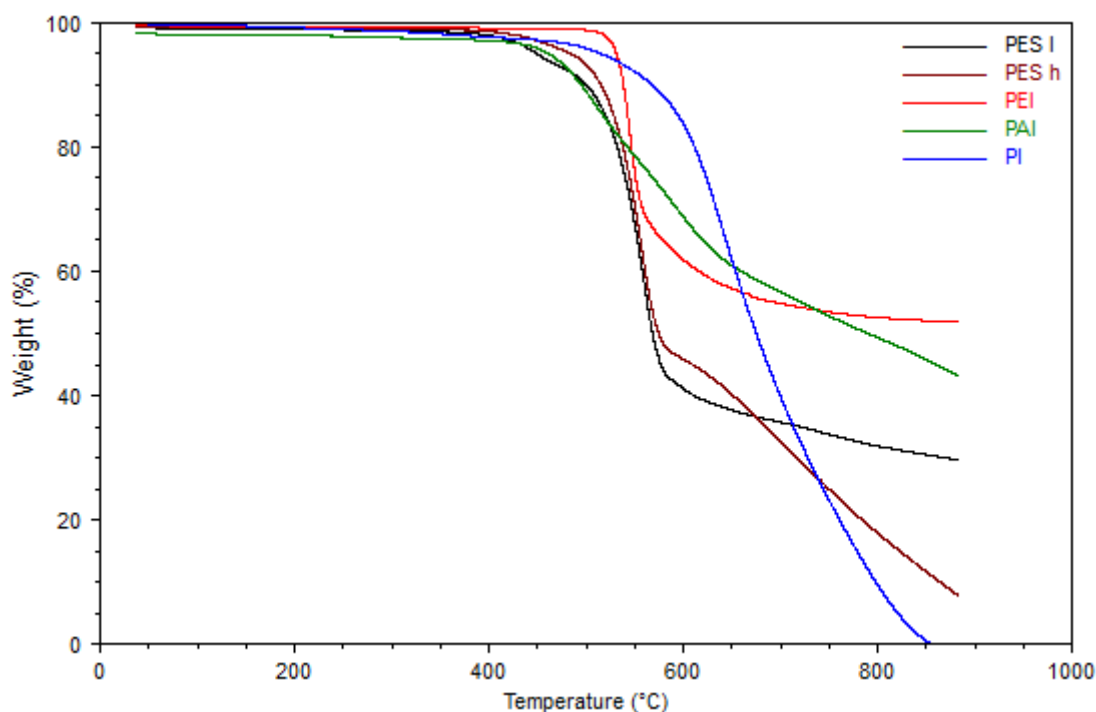
Experimentally DBA is a good solvent for thermoplastics and $\chi'_{DBA,TP} - \chi'_{copo,TP}$ is expected to follow the same behaviour as $\chi'_{BMI,TP} - \chi'_{copo,TP}$.

Appendix F: Thermoplastics TGA

Thermogravimetry under air.



Thermogravimetry under nitrogen.



Appendix G: Edge detection tools

8-bit images consist of pixels containing a value of intensity which varies from 0 to 255. Attributing a grey level to each intensity value (from black to white) allows bi-dimensional representation as a picture. These images I can also be considered as mathematical objects, functions f of spatial coordinates x and y , for which $f(x, y)$ is the intensity value of the pixel located at (x, y) . Using this formalism enables the use of classical mathematical operators.

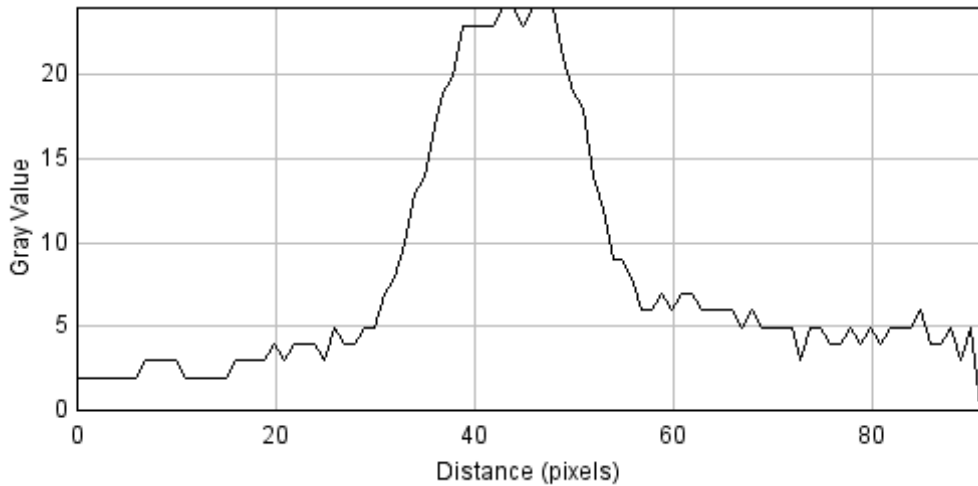


Figure 168: example of pixel intensity signal along a line.

Raw images obviously suffer from noise, as it can be seen on Figure 168. This can lead to local aberration when derivative operators are used because they involve neighbouring points, for which variations are not dominant over physical information. Most edge detection methods start to deal with noise reduction. This can be done using a convolution product with a Gaussian function (Equation 40) or more basically smoothing by replacing pixel intensity by a mean value of its neighbours. Figure 169 shows how the noise can be reduced with Gaussian convolution.

$$f_s(x, y) = \iint f(x - x', y - y') e^{-\frac{x'^2 + y'^2}{\sigma^2}} dx' dy' \quad \text{Eq. 40}$$

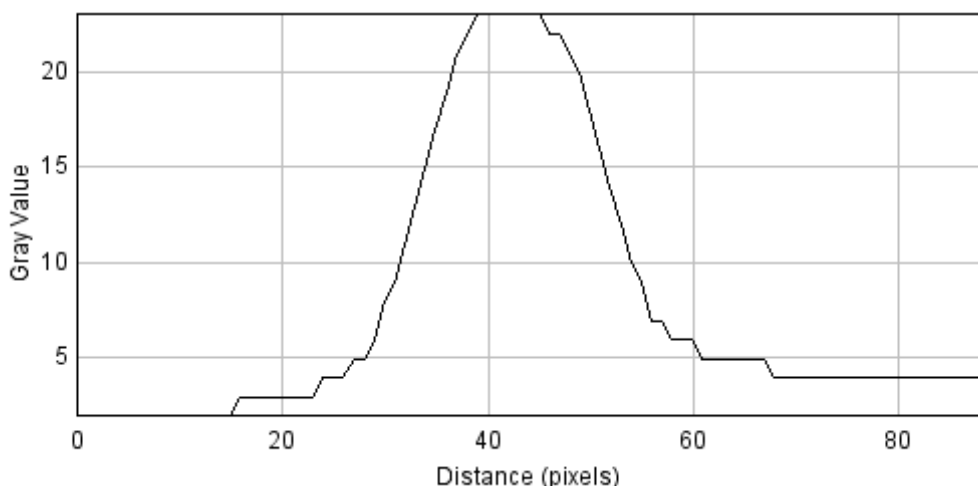


Figure 169: pixel intensity after image convolution with a Gaussian function.

Functions given by images being discontinuous, it is often more convenient to use approximated operators or masks. A mask can be written as a matrix, usually square, with odd dimensions. The central position of the matrix stands for the pixel at which the operator is applied, the other positions being attributed to its neighbours. Then the operation simply consists into multiplying each intensity value involved by the corresponding coefficient of the matrix. For instance, smoothing the image with the replacement of a pixel intensity by the mean value of its neighbours is done with the following mask:

$$\begin{matrix} 1 & 1 & 1 \\ 1 & 0 & 1 \\ 1 & 1 & 1 \end{matrix}$$

To keep the same intensity scale as the original image, the result has to be divided by the sum of the absolute value of matrix coefficients. For the sake of clarity, this operation does not appear here.

Edge detection can be achieved through many criteria. Basically, an edge is a strong variation of intensity. Therefore, derivative operators are fit for detection. Among them, the gradient gives a map of bi-dimensional variations, in which edges can be assimilated to local extrema. The Laplacian is a second order derivative operator, looking for its zeros should theoretically lead to the same result. The choice of the detection method depends on the resolution and the variation amplitude (contrast) of the images. Several operations can be combined with a single mask. For instance using the Laplacian of Gaussian (Marr-Hildreth method, also known as the Mexican hat operator, see Figure 170) deals with noise reduction and second order derivation in a single move.

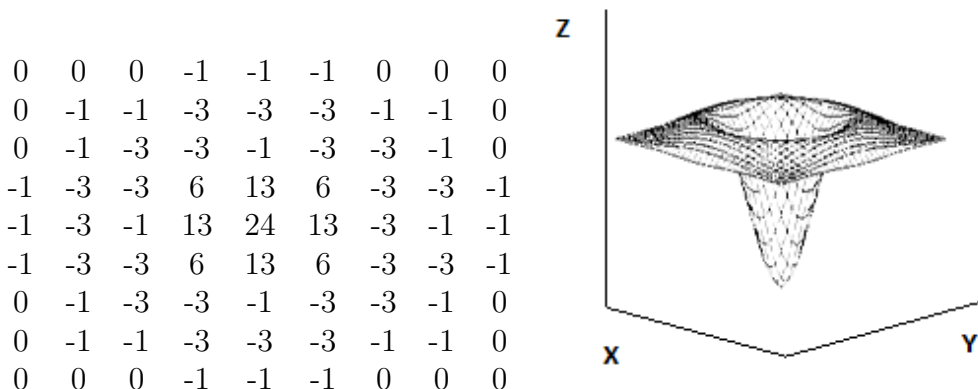


Figure 170: mask and surface plot of a Laplacian of Gaussian function.

Moreover, here the derivation is applied to the well-defined Gaussian function, then convolution with the image occurs. This is allowed because the derivative of a convolution product is the same as convolution with a derivative among the two product members. Derivation of the image is critical because it usually depends on resolution and quality, therefore it is easier to apply this operation to the Gaussian function.

Other methods rely on gradient calculation. Several approximations can be done to estimate local values of the gradient. It can be calculated in the two main directions (x and y) using a mean on neighbouring lines and columns (which is known as Sobel and Prewitt methods). General expressions are:

$$\frac{\partial f_s}{\partial x}(x, y) \simeq G_i(i, j) = \sum_{k=j_a}^{j_b} \alpha_k \frac{I(i+n, k) - I(i-n, k)}{2n}$$

$$\frac{\partial f_s}{\partial y}(x, y) \simeq G_j(i, j) = \sum_{k=i_a}^{i_b} \beta_k \frac{I(k, j+n) - I(k, j-n)}{2n}$$

The coefficients α_k and β_k allow to give more weight to the closest pixels (Sobel method). The parameter n is the step of derivation, often set to 1. The current definition uses a centred approximation. Approximations of derivation from left or right side are also possible. The sum boundaries i_a , i_b , j_a and j_b describe the number of lines and columns used to calculate the mean value. For instance, Sobel and Prewitt methods consider the eight pixels surrounding the (i, j) pixel, which leads to $i_a = i - 1$, $i_b = i + 1$, $j_a = j - 1$ and $j_b = j + 1$.

From these quantities the magnitude and the direction of the gradient can be calculated:

$$\|\overrightarrow{\text{grad}}(f_s)(x, y)\| \simeq \sqrt{G_i(i, j)^2 + G_j(i, j)^2}$$

$$\theta(i, j) = \arctan \left(\frac{G_j(i, j)}{G_i(i, j)} \right)$$

A local maximum value of the magnitude of the gradient is attributed to an edge. Maxima of G_i and G_j give the orientation of edges (through x and y respectively). More complex methods (Canny method) use local maximum detection in the direction of the gradient. Once θ is calculated, it is approximated to the closest of the four main directions (0° , 45° , 90° or 135°). The current pixel is then considered as an edge only if its gradient magnitude is maximum along this direction.

ImageJ macro for image derivation:

```
// Image dimensions
h = getHeight();
w = getWidth();

// Titles
ttr = getTitle();
titre = ttr + " derivative";

// Draw a vertical line
xa = 0;
ya = 0;
xb = xa;
yb = ya+h-1;
makeLine(xa, ya, xb, yb);

// Temporary table
Tsize = 3*h;
T = newArray(Tsize);
```

```

// Derivated image
newImage(titre, "8-bit black", w, h, 0);

for (k=1; k<w-1; k++){
// Coordinates initialisation
    xa = k-1;
    xb = xa;
    for (j=0; j<3; j++){
        makeLine(xa,ya,xb,yb);
    }
// Selection profile
    profil = getProfile();
    for (i=0; i<profil.length; i++){
        T[i+h*j] = profil[i];
    }
    xa = xa+1;
    xb = xa;
}
// Derivation and absolute value
selectImage(titre);
for (n=1; n<h-1; n++){
    val = abs(T[n-1]-T[n+1]+2*T[h+n-1]-2*T[h+n+1]+T[2*h+n-1]-T[2*h+n+1]);
    setPixel(k, n, val);
}
selectImage(ttr);
}

```

ImageJ macro detecting the maximum in each vertical half of images.

```

// Image dimensions
h = getHeight();
w = getWidth();
N = round(h/2);

// Titles
ttr = getTitle();
titre = ttr + " result";

// Resulting image
newImage(titre, "8-bit white", w, h, 0);

for (k=0; k<w-1; k++){
    makeLine(k,0,k,h-1);
// Selection profile
    profil = getProfile();
// First half
    max1 = 0;
    ymax1 = 0;
    for (i=0; i<N; i++){
        if (profil[i]>max1){
            max1 = profil[i];
        }
    }
    setPixel(k, N, max1);
}

```

```
    ymax1 = i;
}
}
// Second half
max2 = 0;
ymax2 = 0;
for (i=N; i<h-1; i++){
    if (profil[i]>max2){
        max2 = profil[i];
        ymax2 = i;
    }
}
// Set both maxima on the resulting image
selectImage(titre);
setPixel(k, ymax1, 0);
setPixel(k, ymax2, 0);
selectImage(ttr);
}
```